Supernova Neutrinos in AMANDA and IceCube
-
Monte Carlo Development and Data Analysis

Dissertation
zur Erlangung des Grades
„Doktor der Naturwissenschaften“
am Fachbereich Physik der
Johannes Gutenberg-Universität Mainz

Thomas Kowarik
geboren in Rüsselsheim

Mainz, den 22.07.2010

Supernova Neutrinos in AMANDA and IceCube: Monte Carlo Development and Data Analysis

Tag der Einreichung: 22.07.2010

Tag der mündlichen Prüfung: 22.11.2010

Thomas Kowarik
ETAP
Institut für Physik
Staudingerweg 7
Johannes Gutenberg-Universität
D-55099 Mainz
`thomas.kowarik@uni-mainz.de`

Abstract

Supernovae are among the most energetic events occurring in the universe and are so far the only verified extrasolar source of neutrinos. As the explosion mechanism is still not well understood, recording a burst of neutrinos from such a stellar explosion would be an important benchmark for particle physics as well as for the core collapse models. The neutrino telescope IceCube is located at the Geographic South Pole and monitors the antarctic glacier for Cherenkov photons. Even though it was conceived for the detection of high energy neutrinos, it is capable of identifying a burst of low energy neutrinos ejected from a supernova in the Milky Way by exploiting the low photomultiplier noise in the antarctic ice and extracting a collective rate increase. A signal Monte Carlo specifically developed for water Cherenkov telescopes is presented. With its help, we will investigate how well IceCube can distinguish between core collapse models and oscillation scenarios. In the second part, nine years of data taken with the IceCube precursor AMANDA will be analyzed. Intensive data cleaning methods will be presented along with a background simulation. From the result, an upper limit on the expected occurrence of supernovae within the Milky Way will be determined.

Kurzbeschreibung

Supernovae gehören zu den energiereichsten Ereignissen des Universums und stellen die einzig gesicherte extrasolare Neutrinoquelle dar. Da der Mechanismus der Explosion nicht ausreichend verstanden ist, wäre die Messung eines Ausbruchs von Neutrinos aus einem solchen Ereignis ein wichtiger Test, sowohl für die Explosionsmodelle als auch für die Elementarteilchenphysik. Das sich am Geographischen Südpol befindende Neutrinoteleskop IceCube weist Tscherenkow-Photonen im antarktischen Gletscher nach. Obwohl es für die Detektion hochenergetischer Neutrinos konzipiert wurde, ist es wegen des niedrigen Sensorrauschens im Eis möglich, den Neutrinoausbruch einer Supernova in der Milchstraße über eine kollektive Ratenerhöhung nachzuweisen. Mit einem speziell für Wasser-Tscherenkow-Teleskope entwickelten Signal-Monte-Carlo wird untersucht, inwiefern IceCube in der Lage ist, zwischen verschiedenen Supernovamodellen und Oszillationsszenarien zu unterscheiden. In einem zweiten Teil werden die mit dem IceCube-Vorläufer AMANDA aufgezeichneten neun Jahre an Informationen analysiert. Nach intensiver Datenbereinigung und Entwicklung einer Untergrundsimulation wird eine obere Grenze auf die erwartete Anzahl an Supernovae in der Milchstraße gesetzt.

Contents

Introduction

> Der gerade Weg ist der kürzeste,
> aber es dauert meist am längsten, bis
> man auf ihm zum Ziele gelangt.
>
> Georg Christoph Lichtenberg

Astronomy is the oldest of all natural sciences dating back to the very beginning of human history. It was revolutionized during the Renaissance with the proposal of the heliocentric system by Nicolaus Copernicus and the development of the telescope by Hans Lippershey, Sacharias Jansen and Jacob Metius. The mathematical and physical tools have continuously evolved, and nowadays, astronomy is a rich scientific field with many different approaches. In addition to classical astronomy with its optical telescopes, radio and gamma ray detectors are now among the most successful "eyes" pointed to the sky. In the past two decades fundamentally new techniques such as the search for gravitational waves or the detection of neutrinos have been developed and added to the repertoire.

Supernovae are the most prominent objects that can appear among the stars as they are capable of outshining whole galaxies for a few months before dimming out. The first sighting of a supernova dates back to 185 AD, when Chinese astronomers discovered a new light source near the direction of Alpha Centauri. Today we know that supernovae herald the final stage in the life of massive stars. When the fusion processes powering these cosmic furnaces fizzle out, they collapse and the density in their cores reaches nuclear levels. At this point, an incompressible object is formed and infalling matter is reflected; a shock wave ensues. Modern simulations indicate that this shock stalls due to energy losses and is only revived by momentum deposition from neutrinos. While little is known about the mechanism driving the supernova, it can be taken as granted that neutrinos play an important role in this process. In 1987, the first and so far only extrasolar neutrino source was discovered; the supernova SN1987A. This event marked the birth of neutrino astronomy.

As of today, there exist many neutrino detectors optimized for the identification of astrophysical sources. IceCube and its precursor AMANDA are among the most prominent, aiming at the detection of high energy neutrinos. Both experiments consist of light sensors brought deep down into the antarctic glacier to detect Cherenkov light indirectly produced by neutrinos. AMANDA consisted of 677 optical sensors and its construction was finished in the year 2000. It took data until the beginning of 2009, when it was decommissioned. The construction of IceCube started in 2005 and upon its completion in 2011, it will consist of 5160 light sensors. Even in its unfinished state it is already apparent that its capacity to outperform AMANDA is tremendous. Both neutrino telescopes are aimed at high neutrino energies. However, the dark noise rates of the light sensors deployed in the antarctic glacier are so low that it is possible to identify small rate changes by investigating the pulse distribution in all modules for collective deviations from their mean. As a supernova neutrino burst would increase the pulse rates in all sensors at the same time, its detection is feasible with both AMANDA and IceCube.

Little is known about the supernova mechanism, and the measurement of a neutrino signature would be a great scientific opportunity. It might help to determine the dynamics and processes driving the explosion and would even allow a closer investigation of the neutrino properties. IceCube would be able to reach the best statistical accuracy worldwide when measuring a neutrino light curve from a supernova at the galactic center. To investigate the possibilities, a simulation routine which implements numerous supernova models and allows the modulation of the neutrino fluxes with various oscillation effects was developed. Using this signal Monte Carlo, the ability to discern different supernova models as well as signatures of neutrino oscillations will be investigated.

AMANDA was running for nine years and recorded a large amount of information. As it was based on the same principle as IceCube, it can be considered a demanding test case for the supernova search. Careful quality checks and data cleaning of the complete set of nine years of data will be performed to ensure stable and reliable information. With background and signal simulations especially written for the supernova search, an upper limit on the number of supernovae in the Milky Way will be determined.

The field of activity of the author also included maintenance of the AMANDA supernova data acquisition in the years 2007-2008, extension of the system to enable more reliable message transfer to the Supernova Early Warning System (SNEWS) and creation of a monitoring system for the AMANDA supernova stream. An analysis of the AMANDA sensor pulse rates with respect to GRB 080319B was performed, but no correlated events were found. Furthermore, to understand the AMANDA noise behavior, the recorded data was subjected to Fast Fourier Transforms (FFT) and a profiling analysis where the average magnitude of data before and after high significance events were investigated. As neither of these approaches yielded results that were helpful in understanding the noise, they are not discussed here.

This thesis is ordered as follows. In chapter 1, we will lay the theoretical groundwork. First, the supernova process and the current models as well as the role of neutrinos will be described. Second, we will put our focus on neutrinos, describe them in the framework of the Standard Model and investigate their properties. A major part will be the investigation of neutrino oscillations in the supernova environment. In chapter 2, AMANDA and IceCube will be presented along with their detection principle and compared to competing experiments. We will then focus on the interaction processes which allow detection of supernova neutrinos. Chapter 3 will present the supernova simulation routine developed specifically for the supernova search. It will be used to investigate the performance of IceCube with respect to different models and oscillation scenarios. Finally, in chapter 4 the data taken with the AMANDA telescope will be examined. Careful quality considerations and a consistent background Monte Carlo including external perturbations from atmospheric muons will be presented. The chapter will close with the derivation of an upper limit for the number of supernova explosions in the Milky Way.

1 Theory

> A process cannot be understood by stopping it. Understanding must move with the flow of the process, must join it and flow with it.
>
> Frank Herbert

This chapter will lay some theoretical groundwork necessary to motivate and understand the analyses presented in this thesis. First, we will focus on the evolution of a massive stars ending in a supernova explosion. After presenting the current state of research, we will describe neutrinos and their interaction processes. Neutrino oscillations in the supernova environment will be considered in the last section.

1.1 Supernovae

The most energetic events observable in our universe are the cataclysmic deaths of massive stars, capable of outshining their whole host galaxy. In 1934, the astronomers and physicists Walter Baade and Fritz Zwicky coined the term *supernova* to describe these sudden luminous outbursts in the sky and hypothesized them being the transition phase between normal and neutron stars [1].

It was a supernova that marked the birth of neutrino astronomy. On February 24, 1987, the light of the dying blue supergiant Sanduleak (-69° 202a) reached the Earth from the Magellanic Cloud and could be seen with the naked eye. It was titled SN1987A, and its neutrinos were the first and so far only ever observed from an extrasolar source.

In this section we will shortly describe the evolution of a massive star up to its final stage, the supernova. The explosion mechanism is considered in more detail, and an overview of current research will be given.

1.1.1 The Life of a Star

1.1.1.1 The Birth

As this is a very complex subject, we will only shortly outline the formation of stars. For an extensive treatment, refer to e.g. [2].

Stars are born in interstellar clouds of gas and dust spanning many parsecs[1], called Giant Molecular Clouds (GMC). They consist mostly of hydrogen and, to a lesser extent, some heavier elements synthesized in previous stellar populations and supernova explosions.

When the gravitational pull exceeds the stabilizing thermal pressure of the gas, the cloud begins to collapse[2]; density and pressure increase. In the beginning, photons can still escape and carry away much of the energy released during contraction. At densities of $\sim 10^{-13}\,\mathrm{g/cm^3}$, the medium becomes opaque, preventing further cooling by radiative emission. Gas pressure increases due to rising temperatures and the collapse decelerates. A *proto-star* is formed.

When the temperature reaches $1800\,\mathrm{K}$, the molecular hydrogen is dissociated, using up kinetic energy and thus decreasing temperature and gas pressure. The equilibrium shifts to gravitational pull, and the collapse accelerates. After the complete dissociation of hydrogen, temperature and gas pressure rise again, and the collapse slows down. If temperatures reach $6000\,\mathrm{K}$, ionization of hydrogen reduces the pressure, and the collapse can proceed. Density and temperature increase, the collapse decelerates another time; a *young stellar object* (YSO) forms. Over the course of the next $\sim 10^6\,\mathrm{a}$, it slowly accretes matter, and the core temperature continues to rise. When it exceeds $\sim 10^6\,\mathrm{K}$, fusion of deuterium starts and the star enters its *T-Tauri* phase. At core temperatures of $\sim 3.5 \cdot 10^7\,\mathrm{K}$, hydrogen burning starts; the star enters its main phase.

1.1.1.2 Burning Stages

The stars of our universe have been observed to group according to their luminosity and surface temperature. Figure 1.1 shows the so-called Hertzsprung-Russel diagram.

For a star, the burning stages it will go through and which kind of death it must endure are primarily determined by the initial mass. A second, albeit less significant factor is its metallicity. The higher it is, the higher the photonic opacity and thus the higher the mass loss rate which determines the composition of the outer layers[3].

A star is governed by the struggle between gravitational pull on the stellar matter and the compensatory thermal pressure of the fusion processes at its core. During the stable burning phases, these forces are in equilibrium. However, if the fuel in the core runs out, the fusion in the central regions stops, and the star begins to contract. Pressure and temperature increase and depending on the previously burned fuel and the strength of the gravitational pressure, further burning stages can be ignited. Note that while a new fusion cycle is reached in the core, the former burning still continues in the envelope. The more massive the star, the higher the pressure inside the core that can be reached by contraction. Consequently, higher energy thresholds can be overcome to ignite the next burning phase as depicted in table 1.1. This cycle ends with the depletion of silicon as fusion processes for the iron group would be

---

[1] $1\,\mathrm{pc} \approx 3.26$ light-years.

[2] Mostly, the collapse is triggered by external influences such as shock waves of nearby supernovae or the radiative pressure of newly born stars.

[3] Stars can lose their hydrogen and even their helium envelope to stellar winds.

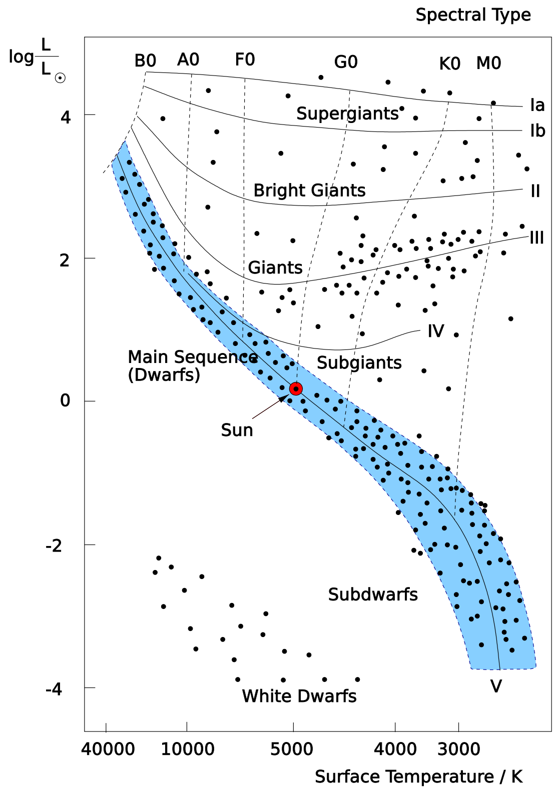

Figure 1.1: Hertzsprung-Russel diagram

The diagram, taken from [3] and slightly modified. L describes the luminosity of a star in solar units. The spectral type (B,A,...) is a classification based on the temperature of the stellar atmosphere. A star starts out on the main sequence. Upon igniting helium burning, it will leave its current branch and move to the next higher one. The White Dwarfs on the lower left were low mass stars like our sun that could not ignite the next burning phase; they collapsed to a compact object made up mostly of electron-degenerate matter. Stars of the O class are the hottest and most massive. The diagram does not show them as this spectral type is located left of the B class.

Fuel	Ash	Duration	$T/10^9\,\mathrm{K}$	$\rho/\mathrm{g/cm}$	$L_\gamma/L_{\gamma,\odot}$	$L_\nu/L_{\nu,\odot}$
H	He	11 My	0.035	5.8	28000	$1.8 \cdot 10^3$
He	C, O	2 My	0.18	$1.4 \cdot 10^3$	44000	$1.9 \cdot 10^3$
C	Ne, Mg	2 ky	0.81	$2.8 \cdot 10^5$	72000	$3.7 \cdot 10^5$
Ne	O, Mg	0.7 y	1.6	$1.2 \cdot 10^7$	75000	$1.4 \cdot 10^8$
O, Mg	Si, S, Ar, Ca	2.6 y	1.9	$8.8 \cdot 10^6$	75000	$9.1 \cdot 10^8$
Si, S, Ar, Ca	Fe, Ni, Cr, Ti	18 d	3.3	$4.8 \cdot 10^7$	75000	$1.3 \cdot 10^{11}$
core collapse	neutron star	$\sim 1\,\mathrm{s}$	> 7.1	$> 7.3 \cdot 10^9$	75000	$> 3.6 \cdot 10^{15}$

Table 1.1: Burning stages of a massive star. The values were taken from [4].

endothermic. With each new burning phase fuel usage, core temperature and density as well as photonic and neutrino luminosities increase[4] [4]. Stars with masses greater than $11\,\mathrm{M}_\odot$[5] can undergo the complete fusion cycle while stars with masses in the range of $8\,\mathrm{M}_\odot - 11\,\mathrm{M}_\odot$ are in a transition region [5].

The reactions going on during the different burning stages will be outlined in the following paragraphs. For more details, refer to e.g. [5, 6].

Main Sequence and Helium Burning

The spectral type (B,A,...) classifies stars by their surface temperature. The first two stages in the fusion cycle are the most common ones and not unique to massive stars. Our sun is still in the hydrogen burning phase and will start on helium after the current fuel is depleted. As its mass is not sufficient to reach the advanced stages, it will end as a white dwarf.

Hydrogen Burning is the most common fusion cycle going on in the universe. As depicted in table 1.1, it is the first and the longest stage; stars in this phase are on the main sequence branch. Hydrogen burning is governed by two separate reactions. The first one - the proton-proton chain - is most important for low mass stars, fusing hydrogen into helium without a catalyst. However, if the stellar mass exceeds $1.3\,\mathrm{M}_\odot$, the *CNO-cycle* (and side channels thereof) becomes dominant[6] [7] (the break-even is at $\sim 1.7 \cdot 10^7\,\mathrm{K}$). The cycle proceeds via the following steps:

$$\begin{aligned}
p + {}^{12}\mathrm{C} &\longrightarrow {}^{13}\mathrm{N} + \gamma \\
e^+ + {}^{13}\mathrm{N} &\longrightarrow {}^{13}\mathrm{C} + \nu \\
p + {}^{13}\mathrm{C} &\longrightarrow {}^{14}\mathrm{N} + \gamma \\
p + {}^{14}\mathrm{N} &\longrightarrow {}^{15}\mathrm{O} + \gamma \\
e^+ + {}^{15}\mathrm{O} &\longrightarrow {}^{15}\mathrm{N} + \nu \\
p + {}^{15}\mathrm{N} &\longrightarrow {}^{12}\mathrm{C} + \alpha \quad .
\end{aligned}$$

Helium Burning is the next stage in the fusion cycle. It is the last phase that can still be identified in the Hertzsprung-Russel diagram and drives stars populating the region above the main sequence. The two principal reactions are:

$$\begin{aligned}
\alpha + \alpha + \alpha &\longrightarrow {}^{12}\mathrm{C} \\
&\text{and} \\
\alpha + {}^{12}\mathrm{C} &\longrightarrow {}^{16}\mathrm{O} + \gamma \quad .
\end{aligned}$$

---

[4] More energy is lost through neutrinos in later burning stages, necessitating a faster burning of the fuel to maintain the equilibrium.

[5] $M_\odot = 1.99 \cdot 10^{30}$ kg describes the mass of the sun.

[6] In stars of the first generation (the earliest stars), the abundance of heavy elements was still insignificant so that hydrogen burning had to occur through the proton-proton chain.

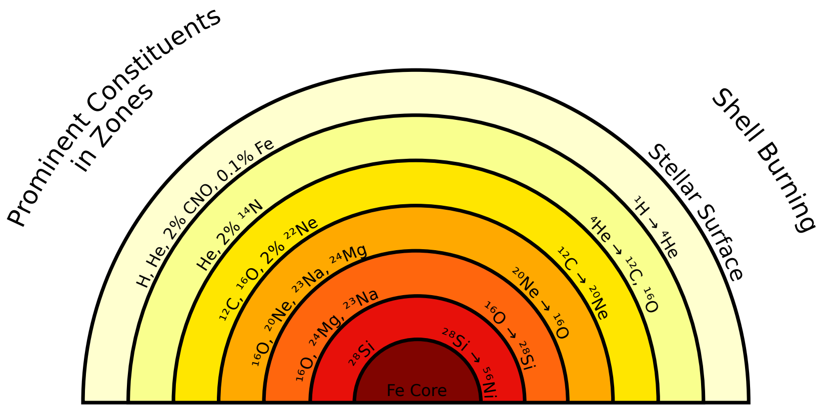

Figure 1.2: Onion model of a massive star at the end of its life

The figure depicts the internal structure of a star which has reached its final burning stage. While the growing iron core is inert, the fusion processes continue in the envelope. Of course, the fusion regions are not as cleanly separated as one might assume from the figure. They mix at the transition regions. The figure was inspired by [6].

Advanced Burning Stages

Of course, the fusion processes do not halt in the whole star when the fuel in the center is depleted. Rather, they relocate themselves into the envelope leading to an onion structure of the star (see figure 1.2). All following burning stages happen so quickly that the outside evolution of fails to keep up. To an observer, advanced stages are only identifiable through convection bringing up core material to the surface.

Carbon Burning follows up on the helium phase. The principal reaction fuses two ^{12}C into a highly excited ^{24}Mg* which primarily decays through

$$\begin{aligned} {}^{12}\mathrm{C} + {}^{12}\mathrm{C} \longrightarrow {}^{24}\mathrm{Mg}^* \quad &\longrightarrow \quad {}^{23}\mathrm{Mg} + n \\ &\longrightarrow \quad {}^{20}\mathrm{Ne} + \alpha \\ &\longrightarrow \quad {}^{23}\mathrm{Na} + p \end{aligned}$$

with the last two having about the same branching ratios and the first one only $0.1\% \sim 5\%$.

Due to interaction with protons, neutrons and α-particles, the core composition after carbon burning is dominated by ^{16}O (ashes from helium burning), ^{20}Ne and ^{24}Mg.

Neon Burning ignites before the temperature required for oxygen fusion is reached. The net reaction is given by

$$ {}^{20}\mathrm{Ne} + {}^{20}\mathrm{Ne} \longrightarrow {}^{16}\mathrm{O} + {}^{24}\mathrm{Mg} \quad . $$

The composition after neon burning is chiefly ^{16}O, ^{24}Mg and ^{28}Si.

Oxygen Burning is the next phase in the cycle. At the conditions governing a massive star ($T \sim 2 \cdot 10^9\,\mathrm{K}$), photodisintegration of $^{16}\mathrm{O}$ is less important[7] than oxygen fusion which proceeds via the following steps:

$$\begin{aligned} {}^{16}\mathrm{O} + {}^{16}\mathrm{O} \longrightarrow {}^{32}\mathrm{S}^* &\longrightarrow {}^{31}\mathrm{S} + n \\ &\longrightarrow {}^{31}\mathrm{P} + p \\ &\longrightarrow {}^{30}\mathrm{P} + d \\ &\longrightarrow {}^{28}\mathrm{Si} + \alpha \quad . \end{aligned}$$

At the end of the day, $^{28}\mathrm{Si}$ and $^{32}\mathrm{S}$ are the prime constituents of the core.

Silicon Burning heralds the end of the star. Instead of a straightforward fusion process, silicon burning is characterized by photodisintegration and subsequent rearrangement. $^{32}\mathrm{Si}$ is photodissociated into α-particles which then add up to the quasi-equilibrium group above $^{32}\mathrm{Si}$. Eventually, most of the material becomes concentrated in the tightly bound iron group. The silicon abundance decreases; burning stops.

1.1.2 The Death of a Star

After fuel at the stellar core is depleted, the star begins to collapse. If the conditions are right, its life ends in a cataclysmic explosion called supernova.

Observational Classification

Supernovae are classified by the characteristics of their observed light curves (see [8] for a detailed review). The first distinction is made between type I (no hydrogen lines) and type II (strong hydrogen lines).

Type I supernovae are subdivided in three categories. Type Ib (helium lines) are believed to be stars having lost their hydrogen envelope, while type Ic (no helium lines) are assumed to have lost their helium envelope as well. A very special case are the type Ia supernovae which are characterized by strong absorption from Silicon with no hydrogen or helium line. Their explosion mechanism is completely different from the core collapse discussed below. According to current research, a white dwarf in a binary system accretes matter from its partner until the Chandrasekhar mass[8] is reached; at this point the star undergoes a thermonuclear explosion from which no remnant remains. Due to the uniformity of their light curves, type Ia supernovae are used as standard candles in astronomy [9].

The most common supernovae are of type IIP. They show prominent Balmer lines[9] and a plateau in the light curve for $\sim 100\,\mathrm{d}$ in which the density of expanding envelope

---

[7] For explosive oxygen burning ($T \sim 3 \cdot 10^9\,\mathrm{K} - 4 \cdot 10^9\,\mathrm{K}$), both can occur at comparable rates.

[8] This is the limit up to which an inactive stellar core can support its own mass. When it is exceeded, the gravitational energy becomes to great and the object collapses.

[9] The Balmer series denominates the spectral line emissions of the hydrogen atom.

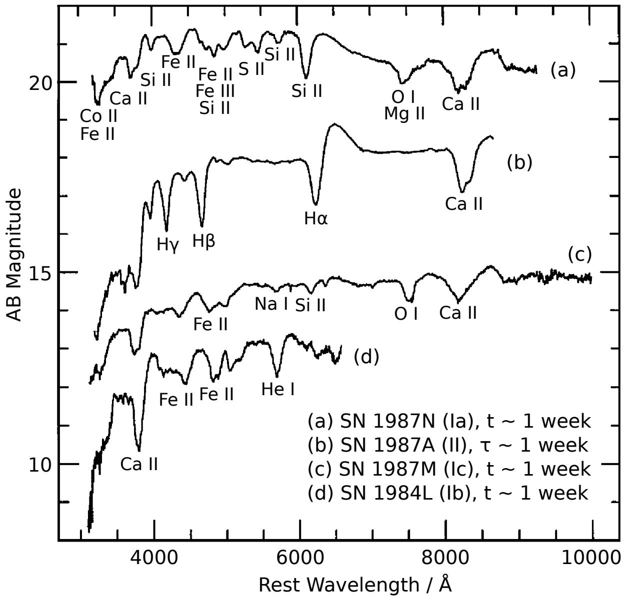

Figure 1.3: Spectra of supernova light emission [8]
AB magnitudes are defined as $-2.5 \log f - 48.6$ *with the flux* f *given in* $\frac{\mathrm{erg}}{\mathrm{s\,cm^2\,Hz}}$. *One can clearly see the different absorption lines described in the text.*

slowly decreases and becomes transparent, allowing the photons trapped inside to slowly escape. Also featuring hydrogen lines but lacking Balmer absorption lines are type IIL supernovae. As opposed to type IIP, their light curve drops in a linear fashion. It is believed that these stars have lost most of their atmosphere before the explosion sets in. See figure 1.3 for some light spectra.

Mass and Metallicity

Just as the life of a star is determined by initial mass and metallicity so is its death. While a certain mass is necessary to drive the collapse, the thickness of the stellar envelope shortly before the explosion is the primary factor defining the light curve of the ensuing supernova. As the metallicity “directly“ influences the mass loss rate (see e.g. [10]), it is a governing factor for the conditions in pre-supernova star. The dependence on the metallicity goes so far as to determine whether a star ends in a supernova or fails in its explosion, directly forming a black hole[10]. It also influences the kind of remnant that is left behind (see diagram 1.4 for more details and [11, 12] for a discussion).

---

[10] Note that while the term direct black hole is often used, it can be misleading. The star does not directly form a black hole but goes through the first stages of a supernova. As the proto neutron star collapses to a black hole before the shock revival, the supernova fails.

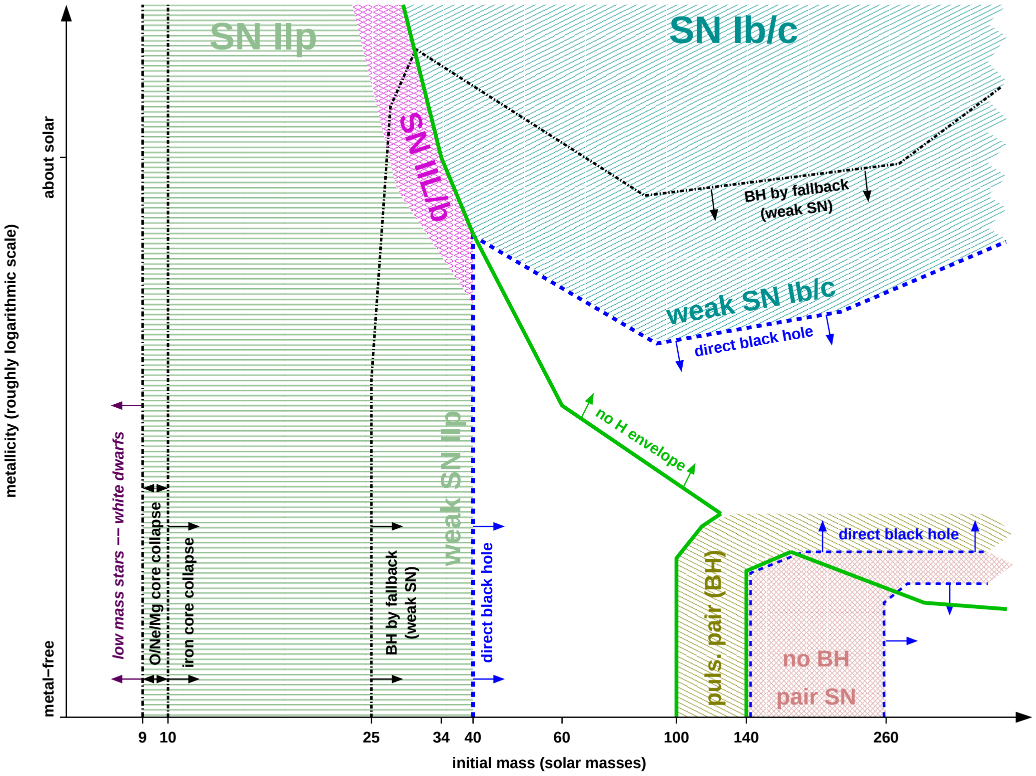

Figure 1.4: Supernova types of non-rotating massive single stars
Note that opposed to this picture, the lower mass limit for supernovae is not strictly at $9\,\mathrm{M}_\odot$. *Modern simulations show that stars with masses of* $8\,\mathrm{M}_\odot - 10\,\mathrm{M}_\odot$ *can undergo a electron capture supernova (titled O/Ne/Mg core collapse in the picture, see section 1.1.2.3 for more details). Rotation can further enhance the mass loss, therefore smearing out the transition regimes. Stars above* $100\,\mathrm{M}_\odot$ *and below* $260\,\mathrm{M}_\odot$ *experience pair-instability. During the contraction igniting oxygen burning, thermal pressure is dissipated into electron-positron pair production. Because of this sudden instability, the contraction is accelerated and the oxygen burning much enhanced, leading to a sudden increase of nuclear reaction rates. Abrupt bursts of counter-pressure lead to pulses for stars* $< 140\,\mathrm{M}_\odot$. *For stars* $> 140\,\mathrm{M}_\odot$, *complete disruption and explosion of the star, leaving no remnant [13], can be the consequence. The figure was taken from [11].*

1.1.2.1 The Neutrino-Driven Core Collapse Mechanism

In the following paragraphs, the standard model of core collapse will be presented.

When the fuel inside of the star is exhausted, an inactive core is formed and continues to grow until its internal pressure can no longer oppose the gravitational forces; the core contracts. This time, no further fusion cycle can be initialized so that the density increases up to the nucleon level where the collapse stops; a proto neutron star (PNS) is formed. The infalling envelope bounces on the PNS and reverses its momentum. A shock wave which propagates to the outside of the collapsing star forms. However, instead of leading to the final explosion, this shock stalls in all current simulations, discarding the so-called *prompt shock* scenario[11]. Of the different approaches to revive this shock, the neutrino-driven mechanism, first proposed in [14], is the most commonly accepted. This standard scenario of core collapse can be split in six stages which will be outlined in the following (see also [15, 4]).

Onset of the Core Collapse

In the inactive iron core, the pressure which opposes the gravitation is dominated by a degenerate gas of relativistic electrons. The core is stable up to the Chandrasekhar limit

$$M_{\mathrm{Ch}} = 5.83\bar{Y}_e^2\left[1+\left(\frac{\bar{s}_e}{\pi\bar{Y}_e}\right)^2\right] \tag{1.1}$$

with $\bar{Y}_e$ describing the mean electron fraction per baryon and $\bar{s}_e$ the mean electron entropy. Typical values place this limit at $\sim 1.44M_\odot$.

Due to the ongoing fusion processes, matter accumulates on the inactive core and its mass continues to grow. At densities of $\sim 10^{10}\,\mathrm{g/cm^3}$ and temperatures of $\sim 10^{10}\,\mathrm{K}$, the Fermi energy of the electrons $\mu_e = 11.1\,\mathrm{MeV}$ is higher than the mass difference between ^{56}Mn and ^{56}Fe and thus electron capture on the Fe nuclei occurs via the reaction

$$^{56}\mathrm{Fe} + e^- \longrightarrow {}^{56}\mathrm{Mn} + \nu_e - 3.7\,\mathrm{MeV} \quad .$$

The electron fraction is reduced; the Chandrasekhar limit decreases, and the star starts to contract. When Temperatures reach $T \gtrsim 5\cdot 10^9\,\mathrm{K}$, photo dissociation of iron nuclei occurs via

$$\gamma + {}^{56}\mathrm{Fe} \longrightarrow 13\alpha + 4n - 124.4\,\mathrm{MeV} \quad , \tag{1.2}$$

absorbing thermal energy and thus decreasing the electron entropy and thermal pressure. Consequently, electron degeneracy grows and electron capture on nucleon and protons becomes important:

---

[11] In the prompt explosion model the initial shock drives the explosion.

$$\begin{aligned} e^- + p &\longrightarrow n + \nu_e \quad , \\ e^- + N(Z,A) &\longrightarrow N(Z-1,A) + \nu_e \quad . \end{aligned}$$

During all these reaction, the produced neutrinos can still leave the core and thus reduce the electron fraction. Consequently, the Chandrasekhar limit drops further; the collapse is now irrevocable. This initial phase is illustrated in the first panel of figure 1.5.

Collapse and Neutrino Trapping

The iron core collapse starts out on a free-fall time scale of the order of $\sim 0.04\,\mathrm{s}$. The outer regions of the core are at first unaffected by the internal contraction. When pressure rises due to increasing density, the internal collapse velocity becomes proportional to the radius. At this time, the outer core is in free fall and reaches supersonic speeds.

Up to now, the electron neutrinos produced could freely escape from the star. As soon as the central density reaches $10^{11} - 10^{12}\,\mathrm{g/cm^3}$, coherent scattering on nuclei and nucleons,

$$\begin{aligned} \nu_e + A &\longrightarrow \nu_e + A \quad \text{and} \\ \nu_e + n,p &\longrightarrow \nu_e + n,p \quad , \end{aligned}$$

becomes important. Furthermore, the electron neutrinos fall into a β-equilibrium,

$$e^- + p \longleftrightarrow n + \nu_e \quad , \tag{1.3}$$

with the degenerate electron gas. The mean free path of the neutrinos drops significantly and the time scale on which they can leave the star exceeds the time scale of the collapse. Neutrinos become effectively trapped in the core and will be entrained by the infalling matter.

As density decreases to the outside of the star, it stands to reason that above a certain radius neutrinos can freely escape. This surface is called the neutrinosphere and is defined as the radius at which the "optical" neutrino depth (the mean number of times the neutrinos is scattered) is 2/3. It can be determined to

$$R_\nu \approx 1.0 \cdot 10^7\,\mathrm{cm} \left(\frac{E_\nu}{10\,\mathrm{MeV}} \right) \quad . \tag{1.4}$$

Neutrinos above this radius can freely escape and are responsible for the first rise in neutrino luminosities (see below).

This phase of the collapse is shown in the upper right diagram in figure 1.5.

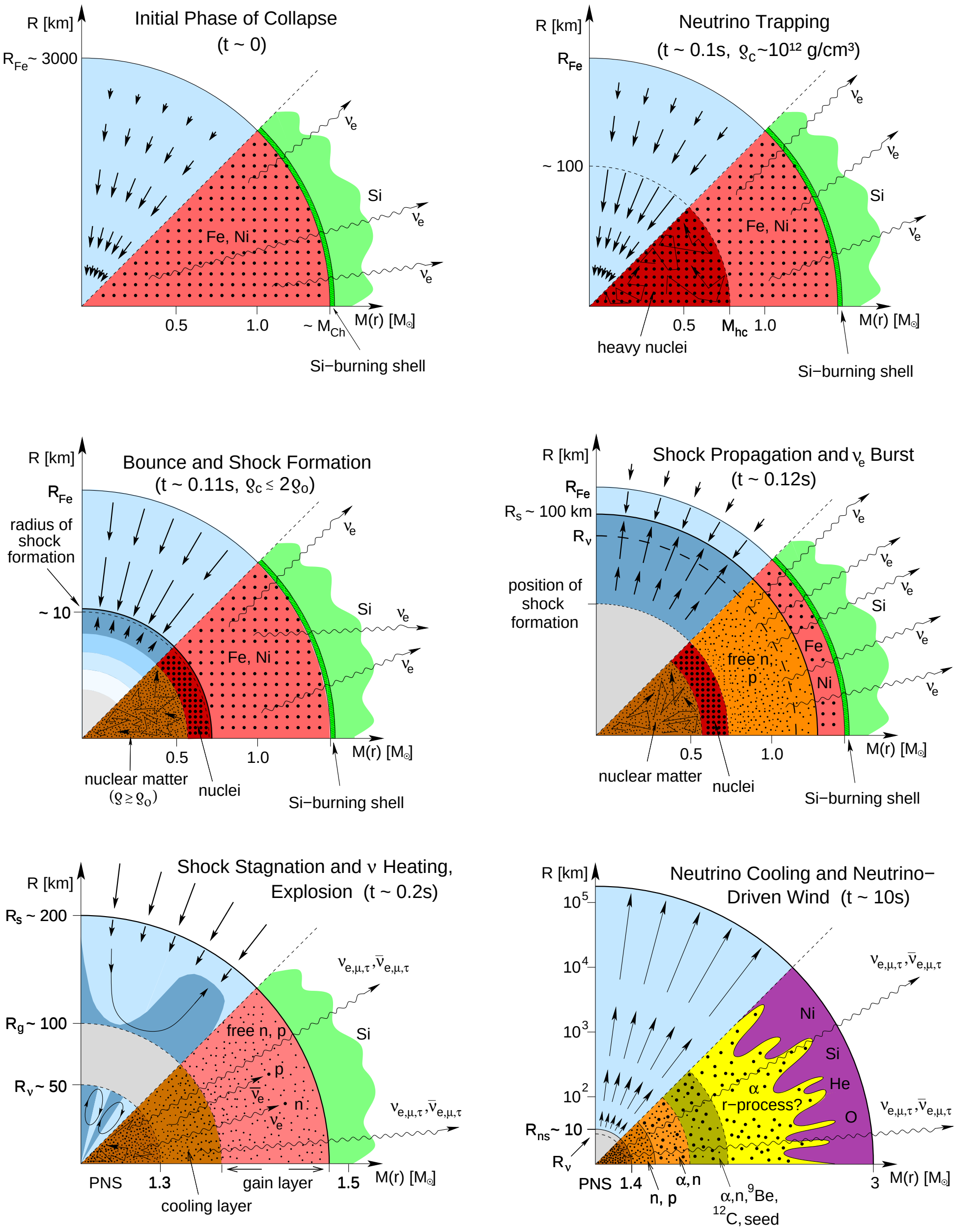

Figure 1.5: Schematic representation a core collapse

The panels (taken from [16]) describe the dynamical conditions in their upper halves with the arrow sizes describing the velocities and the y-axis the radius. The lower halves show the nuclear composition and the weak interaction indicated along with the mass information on the x-axis. R_{Fe}, R_s, R_ν, R_g *and* R_{ns} *describe the radius of the iron core, the position of the shock front, the neutrinosphere, the gain radius and the size of the neutron star, respectively. The individual panels are more closely discussed in the text.*

Core Bounce and Prompt Shock

When the density inside the collapsing core reaches nuclear levels ($\sim 3 \cdot 10^{14}\,\mathrm{g/cm^3}$), the degeneracy pressure[12] stops the collapse. An incompressible object - the *proto neutron star* (PNS) - forms in the center of the inner core. Matter falling on its surface is promptly stopped and its impulse is inverted; an outward moving shock forms (see the first diagram in the second row of figure 1.5).

On its way towards the outer core, the shock front traverses the infalling matter and dissociates the nuclei into free nucleons, consuming $\sim 8.8\,\mathrm{MeV}/A$. The shock is slowed down and a huge amount of ν_e generated by the electron capture on free protons,

$$e^- + p \longrightarrow n + \nu_e \quad ,$$

gathers just behind the shock front. As the shock moves past the radius of the neutrinosphere, the medium becomes permeable for the neutrinos, and they can escape. The neutrino eruption timescale is of the order of the shock propagation, and the so-called *deleptonization* or *breakout burst* has a typical full width half maximum of $5-7\,\mathrm{ms}$. It features in all modern supernova simulations (the models are considered more closely in section 1.1.2.3) and carries $3.3 - 3.5 \cdot 10^{53}\,\mathrm{erg/s}$ [17] (see the last diagram in the second row of figure 1.5).

As the electron degeneracy is not high in the hot post-shock region, pair-production and thus and positron capture on neutrons become possible:

$$e^+ + n \longrightarrow p + \bar{\nu}_e \quad . \tag{1.5}$$

In addition to these reactions, which can only produce electron neutrinos, processes such as

$$\begin{array}{rcl} e^- + e^+ & \longrightarrow & \nu_{e,\mu,\tau} + \bar{\nu}_{e,\mu,\tau} \quad \text{and} \\ N + N' & \longrightarrow & N + N' + \nu_{e,\mu,\tau} + \bar{\nu}_{e,\mu,\tau} \end{array}$$

increase the neutrino luminosities of all flavors in the region above the PNS.

Shock Stall and Delayed Explosion

Through dissociation of the infalling matter and the escaping neutrinos, most of the energy driving the shock front is lost, and the shock stalls at $100 \sim 200\,\mathrm{km}$. All current supernova models confirm this picture, discarding the prompt shock the model [18].

The proto neutron star at the center of the forming supernova is still very hot and continues accreting matter. Its cooling proceeds mainly by neutrino pair production which slowly diffuse to the outside of the star. On their way out, they pass through the stalled shock front and deposit energy via the reactions

---

[12] Due to the Pauli exclusion principle, fermions cannot occupy the same quantum states. Therefore, matter can no longer be compressed when all quantum states are filled. The exception to this rule is the formation of a black hole which cannot yet be quantum-mechanically described.

$$\begin{aligned} \nu_e + n &\longrightarrow e^- + p \quad \text{and} \\ \bar{\nu}_e + p &\longrightarrow e^+ + n \quad . \end{aligned}$$

If the energy transfer (typically ~ 10% [19]) is high enough, the shock is revived and the supernova explodes. This mechanism is called *delayed explosion* and it develops on a timescale ~ 100 ms. Initially, the idea of energy deposition via neutrino interactions was proposed by [14], and the *delayed explosion* was first simulated in [20].

The mechanism of the *delayed explosion* is highly sensitive to the competition of neutrino heating between neutrinosphere and *gain radius*[13] and neutrino cooling between *gain radius* and shock front. It is a self-energizing process. The stronger the heating, the more the velocity of the infalling matter is reduced by neutrino absorption and the time for reheating grows. Even more neutrinos can deposit their energy, and the shock front expands, again increasing the time the matter stays in the heating zone. On the other hand, if the cooling processes are too strong, the matter infall speeds up due neutrino emission and thereby the time available for reheating decreases; no explosion occurs (for a detailed discussion refer to [19]). See the first panel on the lowest row of figure 1.5 for a schematic view.

Proto Neutron Star (PNS) Cooling

After formation of the proto neutron star, the central object becomes gravitationally decoupled from the envelope. In the first 0.1 s to 0.5 s after bounce it shrinks from ~ 150 km to ~ 20 km due to neutrino emission from its low-density outer layer. Because of the compression, the exterior heats up. During this time, the PNS continues to accrete matter, adding to its mass and so its total neutrino emission.

Afterward follows the Kelvin-Helmholtz evolution[14], during which the PNS cools down. It can be split in two stages. While the heat on the outside propagates into the core, raising the temperature to a maximum of ~ 25 MeV within 10 s ~ 15 s, the excess neutrinos still trapped inside diffuse from the central region to the outer layers, leading to further deleptonization (see the last panel in figure 1.5). In the next ~ 10 s − 40 s the neutron star cools down to ~ 5 MeV and finally becomes transparent for neutrinos (references [21, 22] cover these processes in detail).

---

[13] The gain radius is the radial position where neutrino heating of the stellar matter by neutrino capture and cooling through neutrino emission are equal.

[14] The Kelvin-Helmholtz mechanism is an astronomical process that occurs while the surface of a star or planet cools down via the reactions

$$\begin{aligned} e^- + e^+ &\longrightarrow \nu_{e,\mu,\tau} + \bar{\nu}_{e,\mu,\tau} \quad \text{and} \\ N + N' &\longrightarrow N + N' + \nu_{e,\mu,\tau} + \bar{\nu}_{e,\mu,\tau} \end{aligned}$$

with the latter being dominant. Because the drop in temperature occurs through emission of e.g. neutrinos, the internal pressure of the object drops, and it contracts. Thus, the released gravitational energy leads to a rise of the temperature at the core.

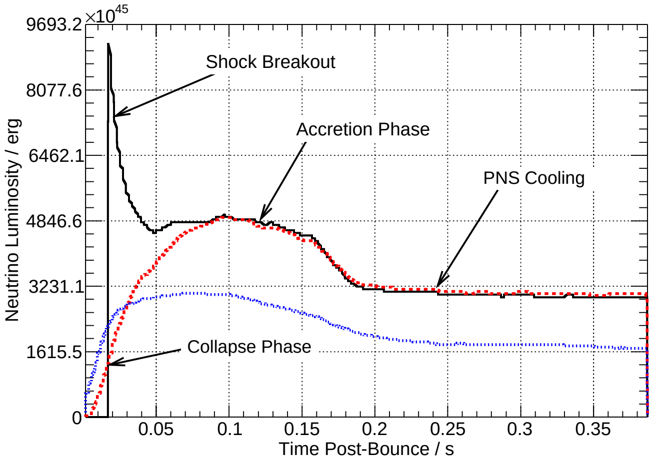

Figure 1.6: Neutrino luminosities of a one-dimensional supernova model
The graphic shows the calculated neutrino luminosities for all flavors. Solid black is the energy carried away by the electron neutrino and dashed red denotes the electron anti-neutrinos. The remaining flavors are depicted in dotted blue as current simulations make no difference between the non-electron flavors. For details, refer to the text.

Neutrino Signature

As we saw above, neutrinos play a strong role in the supernova process. It stands to reason that the neutrino emission during a supernova explosion carries important information on the physical processes during the core collapse. Figure 1.6 shows the neutrino luminosities taken from the one-dimensional simulation of a $15\,\mathrm{M}_{\odot}$ supernova [23]. While this is only one example for a model, it is useful to illustrate the fundamental features in the supernova neutrino emission.

The neutrinos created before the shock wave reaches the neutrinosphere are trapped in the core. Only those created above the neutrinosphere and those statistical exceptions that are able to leave the opaque region contribute to the neutrino luminosity; the emissions rise only slowly. When the shock wave reaches the neutrinosphere the neutrinos trapped before, especially those created by the deleptonization, can escape; we see a strong peak in the electron neutrino luminosity. During the accretion phase, neutrinos of all flavors are created. The luminosity rises for all neutrinos and due to the heating process and the infalling matter, a plateau forms. When the shock is driven out, the accretion drops and the proto neutron star cooling dominates the emissions.

As seen in figure 1.6, the neutrinos produced during the collapse are expected to carry energies $\mathcal{O}(10\,\mathrm{MeV})$. In the time directly after supernovae could also be the source of high energy neutrinos. Theory links supernova explosions of the types Ib and Ic to gamma-ray bursts (GRBs)[15] [24] which are expected to radiate neutrinos

---

[15] GRBs denote highly energetic flashes of electromagnetic radiation. They can last between a few seconds and some minutes.

with energies of $\mathcal{O}(100\,\text{TeV})$ [25]. Aside from this possibility, $\mathcal{O}(\text{TeV})$ neutrinos could be produced during the much later shock breakout from the progenitor star when the supernova becomes optically visible ($\sim 10\,\text{h}$ after the core collapse) [26]. Neither of these will be considered in this work.

1.1.2.2 Black Hole Formation

If a proto neutron star created in a supernova accretes enough matter, it can grow so heavy that internal pressure cannot support it against its gravitational pull[16]; it collapses into a black hole. The time at which this threshold is exceeded can significantly change the evolution of the supernova. For the current stellar population[17], the formation rate of black holes is expected to be in the order of $10\% - 25\%$ (see [29]). Two scenarios exist for the formation of black holes during supernova evolution.

As seen in figure 1.4, most current stars form black holes through fallback. After shock revival, the central object continues accreting matter until, $\sim 10 - 15\,\text{s}$ post-bounce [27], it grows heavier than the neutron star mass limit, and it collapses to a black hole. This marks an intense break in all emanations from the PNS; neutrino luminosity drops to zero. However, the optical emissions can still be observed because the explosion has already been triggered.

If a star has enough mass before collapse, it can take a more direct way to the formation of a black hole. Because of the large envelope, the matter infall during accretion is much more extreme than in the normal case and hinders the shock front expansion. As above, when the mass limit of the neutron star is reached, the object collapses to a black hole, halting all emanations. Here, however, this happens before shock revival and removes the engine driving the neutrino heating; the supernova fails. Figures 1.7 show neutrino luminosities and mean energies for this case as simulated in [30].

Note that from the considerations in section 1.1.2 failed supernovae would be much rarer than bright supernovae for several reasons. First, massive stars are much scarcer and burn out much faster, so the probability to detect one during our lifetime is significantly reduced. Second, as most stars currently formed are relatively metal-rich their outer layers are blown of by strong stellar winds, and thus, failed supernovae become even more unlikely. However, because failed supernovae are difficult to detect, the assumption of their scarcity is not yet confirmed. A survey of the disappearance of supergiants [32] is expected to shed some further light on this question.

1.1.2.3 Supernova Models

As the model of the *delayed explosion* due to neutrino heating is the most prominent at the moment, we will put our focus on this mechanism. Again, the initial mass of the star determines the details of the supernova explosion. For massive stars at the

---

[16] The maximal mass the neutron star can support is believed to be $\sim 1.5\,\text{M}_\odot - 3\,\text{M}_\odot$. However, it strongly depends on the composition of the neutron star (see [27, 28] for more details).

[17] These stars have about solar metallicity and are called *Population I* stars.

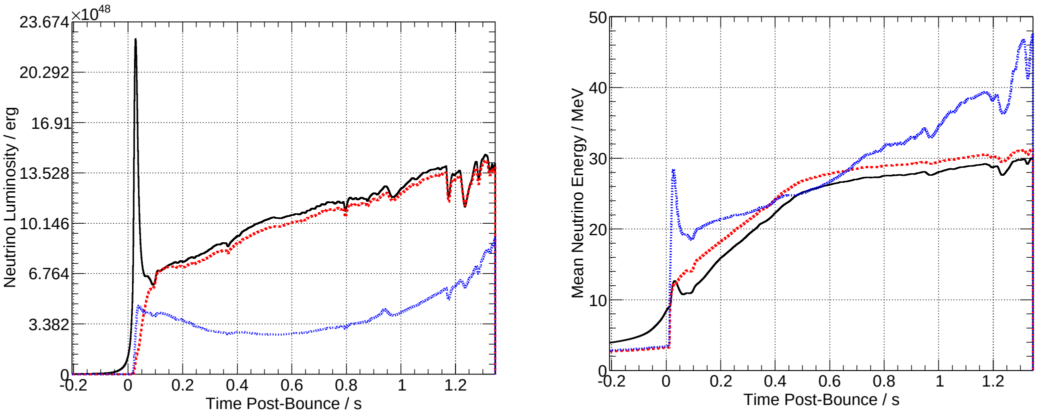

(a) Neutrino luminosities

(b) Neutrino mean energies

Figure 1.7: Neutrino emanations of a failed supernova
Above figures show the collapse of a $40\,\mathrm{M}_\odot$ *star, a failed supernova. In the beginning, the neutrinos show the same signatures as in figure 1.6. However, luminosities and energies drop to zero at the time of black hole creation. The data was kindly provided by K. Sumiyoshi [31]. Note that the simulation is stopped before the final black hole forms as the code cannot handle singularities. Electron neutrino luminosities and energies are depicted in solid black, the electron anti-neutrino characteristics in dashed red and the non-electron flavors in dotted blue. The Shen equation of state was used for this simulation (see later in this section).*

lower end of the mass spectrum ($8\,\mathrm{M}_\odot - 10\,\mathrm{M}_\odot$), already spherically symmetric one-dimensional models lead to an explosion. Higher mass stars only end in a supernova in multi-dimensional simulations with sophisticated neutrino transport, however, the different modeling groups see significant differences in this regime. The extension of the simulations to three dimensions is hoped to shed some further light. Note that in most discussed models, a non- or slowly rotating single star is used as progenitor.

Electron Capture Supernovae

In the case of stars with masses of $8\,\mathrm{M}_\odot - 10\,\mathrm{M}_\odot$, it was at first thought that the explosion would proceed through a *prompt shock* [33, 34]. However, new simulations show that these cores actually explode via the neutrino heating mechanism [35]. Technically, the collapse proceeds in the same manner as for iron core supernovae. Electron captures on oxygen and magnesium cores trigger the collapse by reducing the electron fraction and thus the Chandrasekhar mass. As the star mass is insufficient to trigger neon burning, no counter-force stops the contraction [36]. Just like in iron core supernovae, the shock front stalls due to mass accretion, however, because of the much thinner envelope, the infall of matter rapidly decreases, easing the expansion of the shock front. The neutrinos streaming of the PNS can now accelerate the shock front

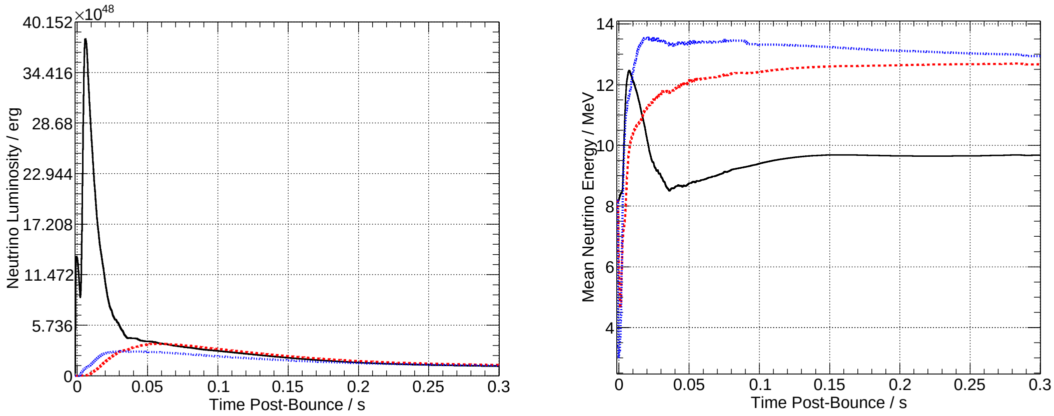

(a) Neutrino luminosities

(b) Neutrino mean energies

Figure 1.8: Neutrino emanations of an electron capture supernova
Above figures show the collapse of a $8.8\,\mathrm{M}_\odot$ *star; an electron capture supernova. The neutrino signatures was kindly provided H.-Th. Janka [38]. As before, electron neutrino luminosities and energies are illustrated in solid black, electron anti-neutrino characteristics in dashed red and non-electron flavors in dotted blue. Again, the Shen equation of state was used for the simulation (see below).*

more efficiently, and trigger the explosion even in one-dimensional models. Figures 1.8 show neutrino luminosities and mean energies as simulated in [37].

Standing Accretion Shock Instability (SASI)

Of course, the one-dimensional modeling of a supernova is a strong simplification of the real conditions. As first pointed out in [39], the hot bubble behind the shock front is bound to be convectively unstable as neutrino production is not uniform. The inclusion of hydrodynamic effects yielded some promising results, namely the faint explosion of a $11.2\,\mathrm{M}_\odot$ star. The larger mass infall of heavier stars, however, dampens the shock propagation and thus inhibits the supernova evolution [40].

As recently discovered, the explosion is aided by the instability of the shock towards non-radial deformation - the so called *standing accretion shock instability* (SASI) [41].

During reheating, an “advective-acoustic cycle” develops because vorticity perturbations at the shock front disrupt the matter falling onto the proto neutron star. Acoustic waves propagate back up to the shock front where they entail further perturbation in the infalling matter and thus reinforce the disturbances; a feedback loop develops (see [42] for more details). Bi-polar sloshing, driving the shock front to oscillate between contraction and expansion is the consequence. Since part of the matter in the shock front is pushed further out by this motion, the time it stays in the neutrino heating zone increases, strengthening the neutrino energy deposition and ultimately leading to an explosion. The SASI develops in all current two-dimensional simulations

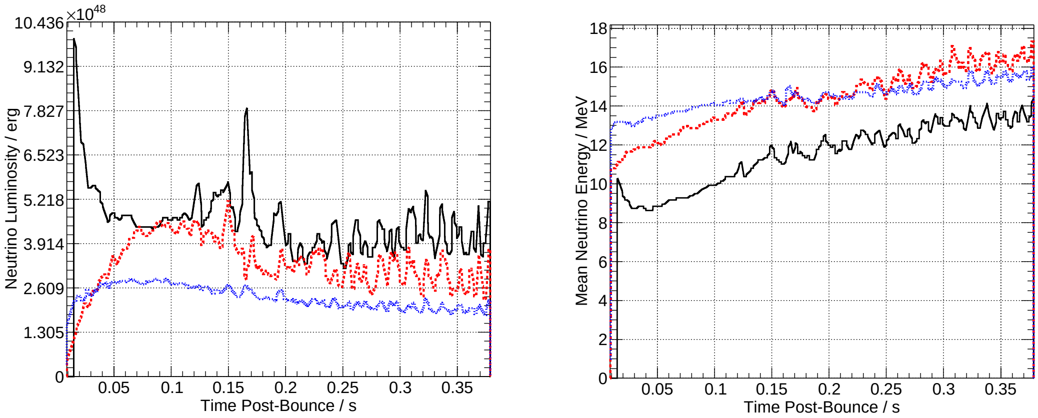

(a) Neutrino luminosities

(b) Neutrino mean energies

Figure 1.9: Neutrino emanations of a failed supernova
Above figures show the emanations of the simulated collapse of a 15 $\mathrm{M}_\odot$ *star. The data used was taken from [23]. Electron neutrino luminosities and energies are depicted in solid black, electron anti-neutrino characteristics in dashed red and all remaining in dotted blue. The Lattimer-Swesty equation of state was used for this simulation (see below).*

covering 180° (see e.g. [40, 43, 44, 45, 46]). Due to the strong oscillations inside the supernova, the explosion itself can be highly asymmetric (see [46]), leading to a large impulse transfer to the central object. Observations of high-velocity neutron stars support this mechanism (see e.g. [47]).

Some of the current simulation results featuring exploding stars $> 10M_\odot$ can be found in [48] ($15M_\odot$) and [49] ($12M_\odot$, $15M_\odot$, $20M_\odot$ and $25M_\odot$). However, the modeling results are quite different in explosion onset and strength. Figures 1.9 show neutrino luminosities and mean energies as simulated in [23].

Three-dimensional simulation efforts have just started and will certainly further the understanding of the supernova process (see e.g. [50, 49]).

Equation of State (EoS)

During the life of a star, its evolution is determined primarily by nuclear and electromagnetic reactions between the nuclei within. However, above a temperature of a few 100 keV, the reactions mediated by electromagnetic and strong interaction balance out with their reverse reaction, forming a nuclear statistical equilibrium (NSE). The nuclear composition is now independent on the interaction types. Only the weak force is able to change the conditions in the core as neutrinos can still leave the star. When the core becomes opaque for neutrinos, weak interactions go into equilibrium as well (see [16] for more detail).

The equation of state (EoS) describes the thermodynamical quantities as function of temperature, density and electron-to-nucleon ratio. Three are most commonly used in the supernova modeling community.

The Lattimer-Swesty equation of state describes leptons and photons as ideal Fermi and Bose gases, respectively. Nuclei are modeled in the compressible liquid drop picture. A heavy nucleus in a unit cell is surrounded by a gas made of protons, neutrons and alpha-particles. For more details refer to [51]. It has been the standard EoS for more than a decade.

Wolff and Hillebrandt derived an equation of state from temperature-dependent Hartree-Fock calculations and self-consistent mean field models for the nucleon-nucleon interactions (see [34] for details).

The third equation of state - the Shen EoS - is based on the relativistic mean field theory using a Thomas-Fermi spherical cell model and the relativistic Brückner-Hartree-Fock theory (details can be found in [52]).

For a more detailed discussion on the differences between the equation of states see [16].

1.1.2.4 Alternative Models of the Supernova Mechanism

While the neutrino heating mechanism is promising, there exist further approaches to explain the supernova explosion (see [15, 49] for a discussion).

Rotation and Magnetic Fields

So far, most supernova simulations consider only non- or slowly rotating stars without magnetic fields. Rapid rotation of the supernova precursor, however, would also lead to large anisotropies and explain the asymmetric explosion as well as fast-rotating neutron stars. A detailed discussion of the influence of rotation can be found in e.g. [53]. Another open question is the influence of strong magnetic fields on the supernova dynamics (see e.g. [54]) as they can significantly influence the dynamics of core collapse.

Acoustic Mechanism

In [43, 44] it was found that anisotropies inside the accretion regime drives the proto neutron star to oscillate which leads to the emission of sound waves into the supernova environment. By the momentum of the acoustic flux, the accretion streams are pushed to the other side of the PNS thus anti-correlating average sound emission and matter accretion. As in the case of the SASI (see above), a feedback loop develops with the oscillations of the PNS feeding turbulences and asymmetries in the accretion streams who in turn excite further oscillations of the PNS. The oscillations and thus the shock wave emissions of the proto neutron star grow so large that the stalled shock front of the supernova is driven out, leading to an explosion. Note that this mechanism has not been confirmed by other groups so far.

QCD Phase Transition

It has been theorized that white dwarfs and neutron stars contain new states of baryonic matter, such as a quark condensate (see e.g. [55]). The density of such a matter state would be higher than that of normal nuclear matter, thus leading to a smaller radius of the neutron star. If this phase transition happens shortly after the core bounce, a further contraction of the PNS and thus a second shock wave ensues which could trigger the explosion [56]. This mechanism has first been proposed in [57].

1.1.2.5 SN1987A

On February 24, 1987, two independent sightings of a bright object were made by Ian Shelton at the Las Campanas Station of Toronto University at about 05:31 and independently by Nelson Jones at the Aukland Observatory at about 8:53 [58]. It was the first supernova discovered in the year 1987 and was thus called SN1987A. The light curve characterized it as a type II explosion [59]. *Sanduleak -69° 202a*, a blue supergiant at a distance of $(51.4 \pm 1.2)\,\mathrm{kpc}$ [60] in the Large Magellanic Cloud (LMC), was noted to be its precursor [59]. It is believed to have had a binary companion [61]. Figure 1.10 shows the relevant sky section before and shortly after the supernova explosion.

As of this date, no remnant of the supernova explosion could be identified. A strong pulsar can be excluded as residue because matter fallback should now be so much reduced that such an object would no longer be obscured [62]. Possibilities that could not be ruled out yet are a black hole induced by later fallback with a weak accretion disk, a quark or strange star with low luminosity or a slowly rotating neutron star with a weak field [63, 64].

SN1987A is the best observed supernova in astronomy and the closest observed since Keplers supernova in 1604. It also marked the beginning of neutrino astronomy and is the only source of extrasolar neutrinos discovered up to date. The Irvine-Michigan-Brookhaven water Cherenkov experiment detected a burst of eight neutrinos with energies of $20 - 40\,\mathrm{MeV}$ spaced over an interval of $6\,\mathrm{s}$, the first event occurring at 7:35:41.37 UT [66]. Kamiokande-II recorded 11 neutrino signatures[18] in a time interval of $13\,\mathrm{s}$ with energies between 7.5 to $36\,\mathrm{MeV}$ with the first being at 7:35:35 UT [67, 68]. Unfortunately, the timing information between the two experiments is not certain. Figure 1.11 shows the recorded neutrino times and energies. Five coincident signal events within $9.1\,\mathrm{s}$ were reported by the Baksan collaboration [69]. However, this result remains questionable as the fiducial volume of the detector is an order of magnitude smaller than for the other two [70].

Just based on the 19 neutrinos observed from SN1987A, it was e.g. possible to pose the following constraints on the neutrino properties [15]:

$$m_\nu < (19 - 30)\,\mathrm{eV} \quad , \quad \tau_{\nu_e} \geq 1.25 \cdot 10^{-2} \frac{m_\nu}{E_\nu}\,\mathrm{s} \quad , \quad Q_{\nu_e} < 10^{-17}\,e \quad . \tag{1.6}$$

---

[18] Kamiokande-II detected 12 events, the sixth, however, was below the energy threshold of 7.5 MeV.

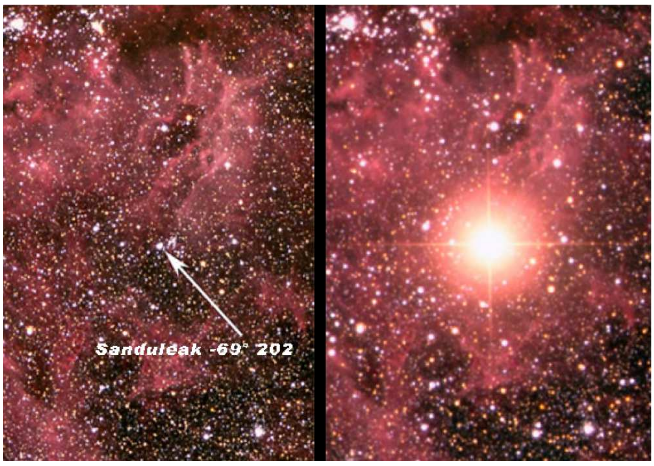

Figure 1.10: Optical Observations of Sanduleak -69° 202a
The two pictures from the Anglo-Australian Observatory have been taken from [65] and slightly modified. The right one was shot on February the 5th, 1987 and the right one at March the 10th, 1987.

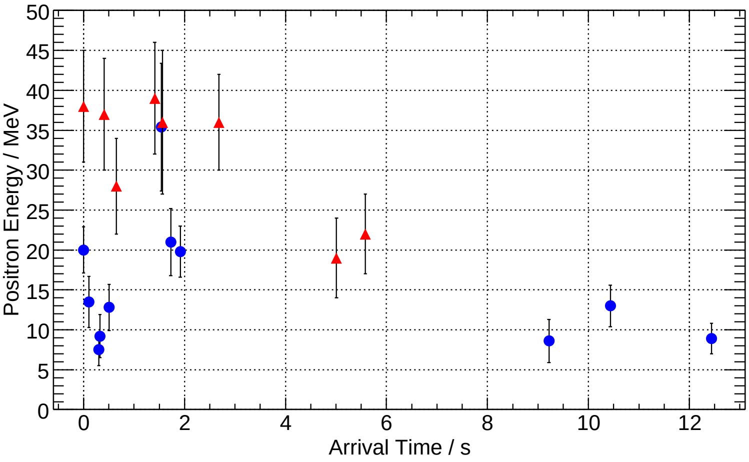

Figure 1.11: Neutrinos from SN1987A recorded by Kamiokande-II and IMB
The blue circles illustrate the neutrinos recorded by Kamiokande-II, the red triangles the ones recorded by IMB. In the figure it is assumed that the first neutrino events of the two experiments were synchronous. The difference in energies recorded by IMB and Kamiokande-II is due to different detection thresholds of the experiments.

1.1.3 Supernova Rate

The rate of supernovae is first and foremost dependent on the age of the galaxy under investigation as old galaxies feature few to no star forming regions. Because of their higher mass, supernova precursors have a much shorter lifetime than an average star and thus older galaxies (e.g. elliptical ones) have no heavy stars left which could end in a core-collapse. Of course, this reasoning holds only true for core collapses and not supernovae of type Ia.

When talking about the explosion rate in our galaxy, one has to take into account that much of the Milky Way is occluded from our point of view. In fact, it has been found by simulations that to explain the five supernovae observed in the last millennium[19], one has to assume 39 supernova explosions. From observation of other galaxies, the expected number of supernovae per century in the Milky Way can be derived to $1.6 - 3.2$ per century with the unknown shape of our galaxy being the main uncertainty [71]. [72] estimates the supernova rate by detecting gamma-rays from radioactive ^{26}Al to be 1.9 ± 1.1 per century. Considering that $\sim 85\%$ of these are due to a core-collapse, one can expect a neutrino burst every $\sim 47\,\mathrm{y}$ [71]. Faint and failed supernovae could of course raise this expectation. However, a value above six per century would lead to significant overproduction of iron compared to current measurements.

1.1.4 Supernova Precursor Distribution

To facilitate the search for neutrino bursts from core collapses with AMANDA and IceCube, the knowledge of the distance distribution of supernova precursors is very important. In [73] the distribution of stars in the Milky Way as given in [74] was used to estimate the supernova distance. However, this distribution is no clear indicator for the occurrence of supernovae as only few stars are massive enough to end in an explosion. [75] studied the distribution of pulsars and OB stars[20] and [76] used this data to derive a distribution of expected supernovae as seen from Earth. Figure 1.12 shows the two distributions.

---

[19] These were the SN1006 (appearing in the Lupus constellation, it was the brightest supernova ever observed; type Ia), SN1054 (Crab, type II), SN1181 (Cassiopeia, type II), SN1572 (Tycho's supernova, type Ib) and SN1604 (Keplers supernova, type Ia).

[20] OB stars are hot massive stars of spectral types O or B which are rather short-lived. Due to their low lifetime, their occurrence is expected to be correlated to supernovae.

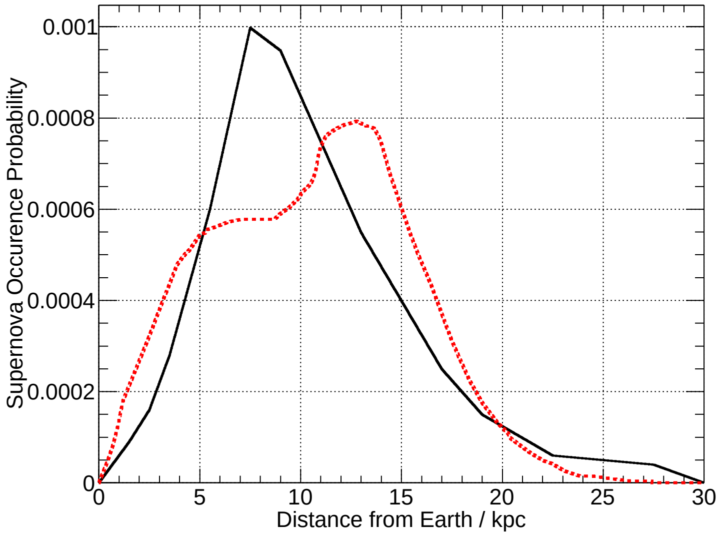

Figure 1.12: Distributions for stellar deaths

The solid black line displays the star distribution as calculated by Bahcall and Soneira (data taken from [77]). As stars ending their lives in supernova explosions are more massive than average stars, the supernova precursor distribution is expected to deviate from this function. The red distribution, given in [76], has been compiled using hot massive stars and neutron stars and should thus reflect the occurrence of core collapses more accurately. Note that the distribution do not take into account the spiral arms of the Milky Way.

1.2 Neutrinos

As AMANDA and IceCube are aimed at neutrinos, we will now put our focus on these particles.

We will start by placing neutrinos in the context of the Standard Model of particle physics and then describe their properties and interactions. Finally, we will examine neutrino oscillations in the context of supernovae.

1.2.1 Neutrinos and the Standard Model of Particle Physics

1.2.1.1 The Standard Model of Particle Physics

The Standard Model of particle physics (SM) is a quantum field theory describing the known elementary particles and their interactions. It includes the strong, electromagnetic and weak but not the gravitational coupling. The strong is the most powerful of the four, but due to self-coupling of its interaction particles, it is confined to small ranges. The coupling constant of the electromagnetic force is two orders of magnitude smaller with a strength decreasing as $\sim r^{-2}$, the massless photon being its carrier. A further three orders of magnitude separate the weak interaction from the electromagnetic one. Because of the heavy mass of its interaction particles, the $W^{\pm}$ and Z^0 bosons, it is also finite in range. The gravitation, with a coupling constant $\sim 10^{-38}$ times the strong one, can be neglected in the particle picture.

Mathematically, the Standard Model is a gauge theory[21] based on the local symmetry group $SU(3)_C \times SU(2)_L \times U(1)_Y$. The subscripts C, L and Y denote color, left-handed chirality and hypercharge. $SU(3)_C$ describes the color symmetry and is responsible for strong interactions. As it has eight generators, there are eight gauge bosons - the gluons - which mediate the strong coupling. From the three generators of the left-handed chirality symmetry group, $SU(2)_L$, and the one for the hypercharge symmetry, $U(1)_Y$, derive three massive - $W^{\pm}$ and Z^0 - and one massless - the γ - gauge bosons responsible for electroweak coupling. All interaction parameters, except for the coupling constants, are fixed by the respective symmetry groups.

The fundamental mathematical tools of the Standard Model are *Lagrange densities* $\mathcal{L}$. From these, equations of motions (e.o.m.) for the physical observables can be derived by inserting $\mathcal{L}$ in the Euler-Lagrange-Equations.

The Standard Model features twelve elementary spin 1/2 particles - the *fermions* - and thirteen particles with integral spin - the *bosons*. The fermions are divided in those carrying a color charge, the quarks, and the ones without, the leptons. Flipping the sign of the electric charge provides the anti-particles known in the SM. The spin 1 interaction bosons are the eight gluons, the photon, the $W^{\pm}$ and the Z^0. The scalar Higgs boson H has spin 0 and mediates no interactions. It is necessary in the SM to provide mass to the particle zoo. Figure 1.13 illustrates the model.

---

[21] In other words, a theory whose physical observables do not change under local transformations.

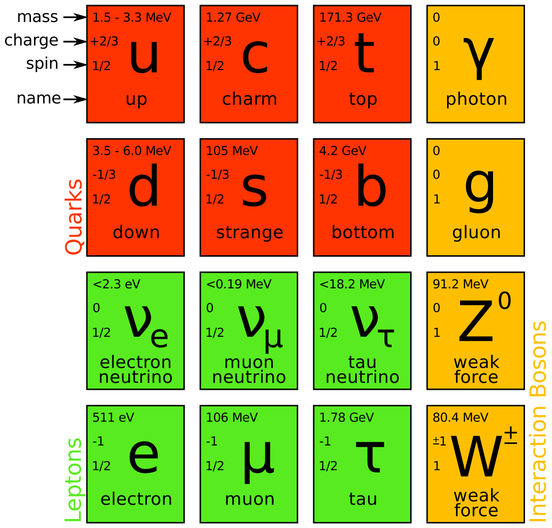

Figure 1.13: Standard model of particle physics
The left block (12 in all) shows the fermions with spin $1/2$ *and the right one the 12 vector bosons with spin* 1*, the gluon* g *featuring eight times. The scalar spin* 0 *Higgs is not shown in this picture. The values inscribed were taken from [78].*

1.2.1.2 Electroweak Coupling

The three generators of the $SU(2)_L$ group, called the *weak isospin*, are subsequently denoted as I_a with $a = 1, 2, 3$ and satisfy the angular momentum commutation relations. In the two-dimensional representation they can be described by the Pauli matrices σ_a. For the hypercharge symmetry group $U(1)_Y$, the generator Y is related to the charge operator Q by the Gell-Mann-Nishijima relation $Q = I_3 + \frac{Y}{2}$.

The weak force is different from all other interactions insofar as it only interacts with left-handed (negative helicity) particles and right-handed (positive helicity) anti-particles. Other interactions have not been observed, making this force maximally parity violating. It stands to reason to split fermion fields f in right- and left-handed fields:

$$f = f_L + f_R \quad \text{with} \quad f_{R/L} = \frac{1 \pm \gamma^5}{2} f \tag{1.7}$$

and $\gamma^5 = \gamma^0\gamma^1\gamma^2\gamma^3$ where γ^i represent the Dirac matrices. Neglecting the masses, the Lagrange density for the leptons in absence of fields can be written as

$$\mathcal{L}_{\text{lepton,free}} = \left(\bar{\nu}_l\,,\,\bar{l}\right)_L i\partial\!\!\!/ \begin{pmatrix} \nu_l \\ l \end{pmatrix}_L + \bar{l}_R\,\partial\!\!\!/\, l_R \tag{1.8}$$

with l being the lepton flavor, $\partial\!\!\!/ = \gamma^\mu\partial_\mu$ and $\bar{l}, \bar{\nu}_l = \gamma^0 l, \gamma^0\nu_l$.

As stated before, the Lagrange density must remain invariant under the local transformation

$$f(x) \rightarrow f'(x) = U_{SU(2)_L}(x)\, U_{U(1)_Y}(x)\, f(x) \tag{1.9}$$

with the operators

$$\begin{aligned} U_{SU(2)_L}(x) &= \exp\left(i\vec{\chi}(x)\cdot\frac{\vec{\sigma}}{2}\right) \quad \text{and} \\ U_{U(1)_Y}(x) &= \exp\left(i\lambda(x)\frac{Y}{2}\right) \quad . \end{aligned} \tag{1.10}$$

Here, we have chosen the two-dimensional representation of the $SU(2)$ by taking $\vec{\sigma} = (\sigma_1, \sigma_2, \sigma_3)$ as generators. The functions $\vec{\chi}(x)$ and $\lambda(x)$ govern the transformation and need to be differentiable.

Inserting the transformed fields into equation 1.8, we see that the Lagrange density does not remain unchanged. To ensure its invariance, we redefine the derivative as

$$\partial_\mu \longrightarrow D_\mu = \partial_\mu - ig\frac{\vec{\sigma}}{2}\cdot\vec{W}_\mu(x) - ig'\frac{Y}{2}B_\mu(x) \tag{1.11}$$

with the fields $\vec{W}_\mu(x)$ and $B_\mu(x)$ transforming as

$$\begin{aligned} \vec{W}_\mu(x) &\longrightarrow \vec{W}'_\mu(x) = \vec{W}_\mu(x) + \frac{1}{g}\partial_\mu\vec{\chi}(x) + \vec{\chi}(x)\times\vec{W}_\mu(x) \quad \text{and} \\ B_\mu(x) &\longrightarrow B'_\mu(x) = B_\mu(x) + \frac{1}{g'}\partial_\mu\lambda(x) \quad . \end{aligned} \tag{1.12}$$

The Lagrange density then reads as

$$\mathcal{L}_{\text{lepton}} = \left(\bar{\nu}_l\,,\,\bar{l}\right)_L i\not{D} \begin{pmatrix}\nu_l \\ l\end{pmatrix}_L + \bar{l}_R \not{D}\, l_R - \frac{1}{4}\vec{W}_{\mu\nu}\cdot\vec{W}^{\mu\nu} - \frac{1}{4}B_{\mu\nu}\cdot\vec{B}^{\mu\nu} \quad . \tag{1.13}$$

The gauge boson fields $\vec{W}_\mu(x)$ and $B_\mu(x)$ are related to the known bosons mediating the interactions by

$$\begin{aligned} W^\pm_\mu &= \frac{1}{\sqrt{2}}\left(W^1_\mu \pm iW^2_\mu\right) \quad , \\ Z^0_\mu &= \cos\theta_\text{W} W^3_\mu - \sin\theta_\text{W} B_\mu \quad \text{and} \\ A_\mu &= \sin\theta_\text{W} W^3_\mu + \cos\theta_\text{W} B_\mu \end{aligned} \tag{1.14}$$

with the Weinberg angle θ_W defined as $\cos\theta_\text{W} = \frac{M_W}{M_Z}$ and evaluated to $\sin^2\theta_\text{W} \approx 0.23119 \pm 0.00014$ [78]. Under these conditions, the photon described by A_μ does not couple to the neutrino.

1.2.2 Neutrino Properties

Because they only interact via the weak and the gravitational force[22] neutrinos take a special place in the standard model. As stated above, they have spin 1/2 and carry no electric charge. Neutrinos have a weak isospin of 1/2 with the third component being 1/2 for neutrinos and −1/2 for anti-neutrinos.

As they can be observed through the weak force alone, only left-handed neutrinos and right-handed anti-neutrinos are known so far. In theory, right-handed neutrinos and left-handed anti-neutrinos are possible, however, as they will only interact through gravitation, their direct detection remains impossible for the time being. They supply natural candidates for sterile neutrinos which, depending on their mass, abundance and variety, could compose a significant fraction of Dark Matter [81].

While neutrino masses are taken to be zero within the Standard Model, oscillation experiments have proven this to be incorrect[23], necessitating extensions to the SM. Just as quarks, the propagation eigenbasis is different from the one describing interactions through weak forces. In analogy to the CKM matrix in the quark sector, neutrino flavor eigenstates relate to mass eigenstates through a mixing matrix, the so-called Maki-Nakagawa-Sakata (MNS) matrix:

$$\begin{pmatrix} |\,\nu_e\rangle \\ |\,\nu_\mu\rangle \\ |\,\nu_\tau\rangle \end{pmatrix} = \begin{pmatrix} c_{12}c_{13} & s_{12}c_{13} & s_{13}e^{-i\delta} \\ -s_{12}c_{23} - c_{12}s_{23}s_{13}e^{i\delta} & c_{12}c_{23} - s_{12}s_{23}s_{13}e^{i\delta} & s_{23}c_{13} \\ s_{12}s_{23} - c_{12}c_{23}s_{13}e^{i\delta} & -c_{12}s_{23} - s_{12}c_{23}s_{13}e^{i\delta} & c_{23}c_{13} \end{pmatrix} \begin{pmatrix} |\,\nu_1\rangle \\ |\,\nu_2\rangle \\ |\,\nu_3\rangle \end{pmatrix} \tag{1.15}$$

with $c_{ij} = \cos\theta_{ij}$, $s_{ij} = \sin\theta_{ij}$, the mixing angles θ_{ij} and a phase factor δ responsible for CP-violation. As δ has only little impact on neutrino oscillations and is so far undetermined, we will take it as zero for the remainder of this work[24].

Note that we have taken the neutrinos to be Dirac particles. In the Majorana case[25], two additional phases would apply to the matrix. For supernova neutrino detection, the particle type is not expected to make a significant difference because it does not affect neutrino oscillations and has no measurable impact on the interactions in the detector.

The experimental values determined so far are (see [78] for a compilation and [84, 85, 86] for the experimental measurements):

---

[22] Of course, this is only the case if the neutrino has no magnetic moment (current upper limit: $0.54 \cdot 10^{-10}\,\mu_B$) and no electric charge (current upper limit: $3.7 \cdot 10^{-12}e$) ([79, 80, 78]).

[23] The first compelling experimental confirmation of neutrino oscillations was found by *SNO* [82].

[24] According to [83], a non-vanishing CP-violating phase could lead to modifications to the non-electron (anti-)neutrino fluxes and even to the electron (anti-)neutrino fluxes from supernovae if muon and tauon (anti-)neutrino fluxes differ at the neutrinosphere.

[25] A Majorana fermion is its own anti-particle. For neutrinos, this means that $\nu_L \equiv \bar{\nu}_L$ and $\bar{\nu}_R \equiv \nu_R$.

$$
\begin{aligned}
\sin^2 2\theta_{12} &= 0.87 \pm 0.03 \quad \left[\theta_{12} = (34.4^{+1.3}_{-1.2})^\circ\right] \quad , \\
\sin^2 2\theta_{23} &> 0.92 \quad [\,36.8^\circ < |\theta_{23}| < 53.2^\circ\,] \quad \text{and} \\
\sin^2 2\theta_{13} &< 0.19 \quad [\,|\theta_{13}| < 12.9^\circ\,] \quad .
\end{aligned}
\tag{1.16}
$$

The second set of parameters relevant for neutrino mixing and oscillation are the mass differences. Current experiments set them to (again, see [78] for a compilation and [84, 87] for the experimental results):

$$
\begin{aligned}
\Delta m^2_{21} &= 7.59^{+0.19}_{-0.21} \cdot 10^{-5}\,\mathrm{eV}^2 \quad , \\
|\Delta m^2_{32}| &= (2.43 \pm 0.13) \cdot 10^{-3}\,\mathrm{eV}^2 \quad \text{and} \\
|\Delta m^2_{31}| &\approx |\Delta m^2_{32}| \quad .
\end{aligned}
\tag{1.17}
$$

Note that the sign of Δm^2_{32} is yet unknown, leading to the hierarchy problem sketched in figure 1.14. The normal hierarchy is taken to be $m_1 < m_2 < m_3$ while the inverted is $m_3 < m_1 < m_2$.

Due to the small mass differences, the absolute masses are constrained by the smallest experimental limit given by the electron neutrino with $m_{\nu_e} < 2.3\,\mathrm{eV}$ [88, 78]. From cosmological constraints[26] one can derive a limit on the summed mass of all neutrino flavors. Depending on the cosmological model used, namely the standard model of cosmology, ΛCDM, or a more general model with a dark energy equation of state parameter w (wCDM), the neutrino masses can be restricted to 0.28 eV or 0.59 eV at 95% confidence [78, 90].

1.2.3 Neutrino Interactions

It is essential to understand the interactions of neutrinos with matter for production and detection processes. As mentioned above, neutrinos interact through the weak and gravitational forces only. For our purposes, only the former is relevant.

In the following paragraphs, we will shortly outline the theory behind the interaction processes. For a detailed review refer to specialized books such as [91].

1.2.3.1 Charged Current Interactions

The Lagrange density for the charged current interactions can be written as

---

[26] In the early universe neutrino energies decreased to non-relativistic levels much later than ordinary matter and thus did not influence the gravitational fields during radiation domination. Large scale structures formed during the matter-radiation equality time frame when dark matter collapsed gravitationally. For this reason, free streaming neutrinos lead to a suppression of small scale fluctuation compared to large scale fluctuations [89].

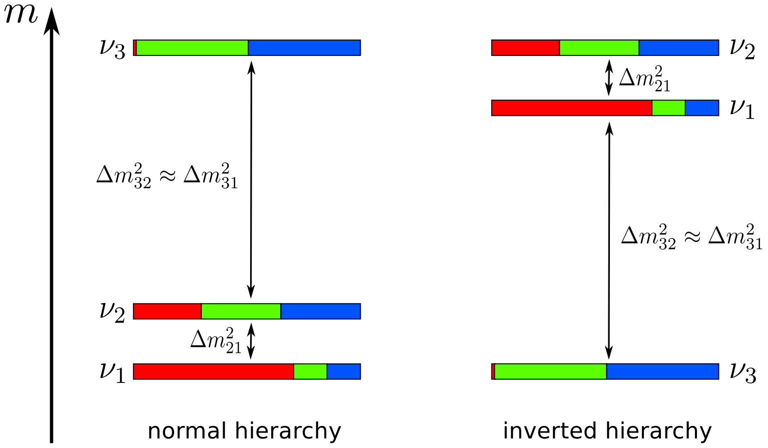

Figure 1.14: Neutrino hierarchy problem

The figure sketches the two possible cases for the hierarchy of the neutrino masses with the colors showing the contribution of the flavors to each vacuum state. Red (always at the left) depicts the electron, green (the middle) the muon and blue the tauon neutrino flavor.

$$\mathcal{L}_L^{\text{CC}} = \frac{ig}{\sqrt{2}}(j^{\mu}_{W^-} W^-_{\mu} + j^{\mu}_{W^+} W^+_{\mu}) \tag{1.18}$$

with the charged currents

$$j^{\mu}_{W^-} = \sum_{\alpha} \bar{\nu}_{\alpha}\, \gamma^{\mu}\, (1-\gamma^5)\, l_{\alpha} + \sum_{(q_+,q_-)} \bar{q}_-\, \gamma^{\mu}(1-\gamma^5)\, q_+ \quad \text{and} \tag{1.19}$$

$$j^{\mu}_{W^+} = (j^{\mu}_{W^-})^{\dagger} = \sum_{\alpha} \bar{l}_{\alpha}\, \gamma^{\mu}\, (1-\gamma^5)\, \nu_{\alpha} + \sum_{(q_+,q_-)} \bar{q}_+\, \gamma^{\mu}(1-\gamma^5)\, q_- \tag{1.20}$$

and summing over all lepton $\alpha = e, \mu, \tau$ and quark flavors $(q_+, q_-) = (u', d'), (c', s'), (t', b')$. The primes denote that we are dealing with the weak and not the mass quark eigenstates. The first term of the negatively charged current, equation 1.19, describes the conversion of a lepton to its corresponding neutrino and, by crossing symmetry, the conversion of an anti-neutrino into the respective anti-lepton, both under emission of a W^-. The hermitian conjugate completes the interaction by the positively charged current, equation 1.20, namely the conversion of an anti-lepton into an anti-neutrino and the conversion of a neutrino into the respective lepton under emission of a W^+. We get the reactions for the quark sector from the second terms of equations 1.19 and 1.20, namely $q_- \rightarrow q_+ + W^-$, $\bar{q}_+ \rightarrow \bar{q}_- + W^-$, $q_+ \rightarrow q_- + W^+$ and $\bar{q}_- \rightarrow \bar{q}_+ + W^+$. Note that the weak charged current is the only possibility for quark flavor conversion.

1.2.3.2 Neutral Current Interactions

The Lagrange density for the neutral current is given by

$$\mathcal{L}_L^{NC} = -\frac{g}{2\cos\theta_\mathrm{W}} j_Z^\mu Z_\mu + \mathcal{L}_L^\gamma \tag{1.21}$$

with the second term being the QED Lagrangian. The weak neutral current $j_{Z,L}^\mu$ is given by

$$j_{Z,L}^\mu = \bar{f}\,\gamma^\mu\,(g_V^f - g_A^f)\,f \tag{1.22}$$

for the fermion f. The vectorial and axial couplings are defined as

$$\begin{aligned} g_V^f &= g_L^f + g_R^f = I_3^f - 2q_f\sin\theta_\mathrm{W} \quad \text{and} && (1.23)\\ g_A^f &= g_L^f - g_R^f = I_3^f && (1.24)\end{aligned}$$

where g_L^f and g_R^f denote the coupling to the left- and right-handed particles respectively (e.g.: $g_R^\nu = 0$). q_f denotes the electric charge and I_3^f the third component of the weak isospin. Equation 1.22 describes all fermion annihilation and pair production processes and momentum transfers via the Z^0.

1.2.4 Neutrino Oscillations

In the case of neutrinos, the mass eigenstate is different from the weak interaction or flavor eigenstate. Because the detection process works only through weak forces and neutrinos travel the distance from source to detector as mass eigenstate, neutrinos can well be detected as another flavor than they were produced in.

Neutrinos ejected during the Supernova explosion undergo multiple oscillation phases. The most notable ones are induced by the matter potential and self-interactions. More exotic scenarios such as neutrino conversions due to interaction of a hypothetical neutrino magnetic moment with the magnetic field of the supernova (see e.g. [92]) will not be discussed in this work.

Precise predictions concerning the oscillations must remain incomplete as the smallest mixing angle θ_{13} and the mass hierarchy are still unknown. We will investigate the effect the different parameterizations can have on a supernova signal detected by IceCube. Studies already began in [93] will be expanded by further oscillation scenarios.

The goal of this section is to give basic theoretical insight in the oscillation mechanisms taking place in a supernova. We will start with the well known vacuum oscillations. From there, we will expand to the common description of the matter driven oscillations and its repercussions for supernova neutrinos. For the understanding of collective neutrino oscillations, a geometrical approach, the matrix density formalism and its associated neutrino flavor isospin (NFIS) picture, will be introduced.

The general considerations hereafter follow [91]. More specialized cases such as oscillations in supernovae and collective oscillations were taken from multiple references and are cited when relevant.

1.2.4.1 Vacuum Oscillations

The neutrino flavor eigenstates $\alpha = e, \mu, \tau$ relate to the neutrino mass eigenstates $k = 1, 2, 3$ in the following way:

$$\mid \nu_\alpha \rangle = \sum_k U^*_{\alpha k} \mid \nu_k \rangle \quad . \tag{1.25}$$

$U_{\alpha k}$ is the MNS matrix shown in equation 1.15. From the Schrödinger equation we know the time development of a neutrino flavor eigenstate to be:

$$\mid \nu_\alpha(t) \rangle = \sum_k U^*_{\alpha k} e^{-iE_k t} \mid \nu_k \rangle \quad . \tag{1.26}$$

The probability for a neutrino of the initial flavor α at $t = 0$ to be found in the state β at a given time t can be derived by combining equations 1.25 and 1.26. This yields:

$$\begin{aligned} P_{\alpha \to \beta}(t) &= |\psi_{\alpha\beta}(t)|^2 \quad \text{with} \\ \psi_{\alpha\beta}(t) &= \langle \nu_\beta \mid \nu_\alpha(t) \rangle = \sum_k U_{\alpha k} e^{-iE_k t} U^*_{\beta k} \quad . \end{aligned} \tag{1.27}$$

As we are only interested in the ultra-relativistic cases, $E_k \approx E + \frac{m_k^2}{2E}$, the conversion probability simplifies to (omitting some steps):

$$P_{\alpha \to \beta}(t) = \sum_{k,j} U^*_{\alpha k} U_{\beta k} U_{\alpha j} U^*_{\beta j} \exp\left(-i \frac{\Delta m^2_{kj}}{2E} t \right) \tag{1.28}$$

with $\Delta m^2_{kj} = m_k^2 - m_j^2$ (note: as $c \equiv 1$, the distance source detector $L \equiv t$).

Note that some simplifications made in this section break universality.

First, we assume that we are not sensitive to the different mass contributions (ν_1, ν_2, ν_3) to the flavor states $(\nu_e, \nu_\mu, \nu_\tau)$. This holds true for all present neutrino experiments.

All the massive neutrino components making up a neutrino flavor are presumed to have the same momentum. While this simplification need not hold true, the momentum is irrelevant for the derivation of oscillation probabilities.

The assumption of time and distance between source and detection being equal is also somewhat problematic. In quantum theory particles are generally described by wave packets. We imply a group velocity close to the speed of light. Due to different masses, the group velocities of the massive neutrinos differ which could again lead to oscillations. However, as the detection length is generally much smaller than the oscillation length L, the wave packets overlap coherently and the simplified approach is sufficient.

1.2.4.2 Neutrino Oscillations in Matter

In this section we will introduce the effect of matter on neutrino oscillations for the two flavor case and consider the repercussions in the supernova environment.

General Considerations

While neutrino oscillations in matter are in principal analogous to vacuum oscillations, the decisive parameters are dependent on the propagation medium. Due to forward scattering, the effective masses of neutrinos can change in matter. As the interaction potentials differ by neutrino type, the mass differences, the mixing angles and thus the oscillation behavior between the flavors change. At densities defined by the mixing parameters, the probability for flavor conversion can become large while it might normally be inhibited. This is the so-called *Michejew-Smirnow-Wolfenstein (MSW)* effect.

For illustration purposes, we will restrict ourselves to ν_e and ν_μ. Later in this section, it will become evident that this restriction is sufficient for the supernovae case.

Let us focus on the Schrödinger equation for the wave function $\psi_{\alpha\beta}(t)$ (see equation 1.27 for the definition):

$$i\frac{\mathrm{d}}{\mathrm{d}x}\vec{\psi}_\alpha(x) = \mathcal{H}_\mathrm{F}\vec{\psi}_\alpha(x) \tag{1.29}$$

with $\mathcal{H}_\mathrm{F}$ being the Hamiltonian in the flavor basis. When neutrinos travel through matter they are affected by charged and neutral currents. As NC interactions influence all flavors in the same way, their contributions to $\mathcal{H}_\mathrm{F}$ can be neglected when discussing neutrino oscillations. In ordinary matter forward scattering through the charged current can only occur for the electron flavor, and thus, the Hamiltonian has to be modified by the potential $V_\mathrm{CC} = \sqrt{2}G_\mathrm{F}N_e$. For two neutrinos, this equation can be written as (for details on the derivation, see appendix A.1):

$$i\frac{\mathrm{d}}{\mathrm{d}x}\begin{pmatrix}\psi_{ee}\\ \psi_{e\mu}\end{pmatrix} = \frac{1}{4E}\begin{pmatrix}-\Delta m^2\cos 2\theta + A_\mathrm{CC} & \Delta m^2 \sin 2\theta \\ \Delta m^2 \sin 2\theta & \Delta m^2 \cos 2\theta - A_\mathrm{CC}\end{pmatrix}\begin{pmatrix}\psi_{ee}\\ \psi_{e\mu}\end{pmatrix} \quad . \tag{1.30}$$

A_CC describes the charged current interactions and is related to the potential V_CC and the neutrino energy E by $A_\mathrm{CC} = 2EV_\mathrm{CC}$.

The Hamiltonian can be diagonalized to

$$\mathcal{H}_\mathrm{F} \rightarrow U_\mathrm{M}^\dagger \mathcal{H}_\mathrm{F} U_\mathrm{M} = \mathcal{H}_\mathrm{M} = \mathcal{H}_\mathrm{M}^\dagger = \frac{1}{4E}\mathrm{diag}(-\Delta m_\mathrm{M}^2, \Delta m_\mathrm{M}^2) \tag{1.31}$$

with the effective mass difference and the mixing angle in matter of

$$\begin{aligned}\Delta m_\mathrm{M}^2 &\equiv \sqrt{(\Delta m^2 \cos 2\theta - A_\mathrm{CC})^2 + (\Delta m^2 \sin 2\theta)^2} \quad ,\\ \sin 2\theta_\mathrm{M} &\equiv \frac{\Delta m^2 \sin 2\theta}{\Delta m_\mathrm{M}^2} \quad \text{and} \quad \cos 2\theta_\mathrm{M} \equiv \frac{\Delta m^2 \cos 2\theta - A_\mathrm{CC}}{\Delta m_\mathrm{M}^2} \quad .\end{aligned} \tag{1.32}$$

The neutrino eigenvectors of this Hamiltonian constitute an eigenbasis different from the vacuum one. Its base vectors will be called ν_1^M for the light and ν_2^M for the heavy neutrino in analogy to the vacuum basis.

Resonance Condition: At an electron density of

$$N_e^{\mathrm{R}} = \frac{\Delta m^2 \cos 2\theta}{2\sqrt{2} G_{\mathrm{F}} E} \quad , \tag{1.33}$$

we get a matter potential of

$$A_{\mathrm{CC}}^{\mathrm{R}} = \Delta m^2 \cos 2\theta \quad . \tag{1.34}$$

At exactly this point, $\cos 2\theta_{\mathrm{M}}$ becomes zero, the mass difference Δm_{M}^2 goes to its minimal value, and consequently, mixing becomes maximal. Whether the resonance exists in the neutrino or in the anti-neutrino sector depends on the value of θ. Since in normal matter $A_{\mathrm{CC}} \geq 0$, a mixing angle $\theta \leq \pi/4$ would allow for a resonance in the neutrino sector while for $\theta > \pi/4$ the resonance would be in the anti-neutrino sector.

We now consider the contribution of the flavor α to the matter eigenstate i at distance x, $P_{\nu_\alpha \to \nu_i}(x) = |\phi_{\alpha i}(x)|^2$, for $\alpha = e$:

$$\vec{\psi}_e(x) = \begin{pmatrix} \psi_{ee} \\ \psi_{e\mu} \end{pmatrix} = \begin{pmatrix} \cos\theta_{\mathrm{M}} & \sin\theta_{\mathrm{M}} \\ -\sin\theta_{\mathrm{M}} & \cos\theta_{\mathrm{M}} \end{pmatrix} \begin{pmatrix} \phi_{e1} \\ \phi_{e2} \end{pmatrix} = U_{\mathrm{M}} \vec{\phi}_e(x) \quad . \tag{1.35}$$

Putting this into equation 1.29, we get:

$$\begin{aligned} i\frac{\mathrm{d}}{\mathrm{d}x}\vec{\phi}_e(x) &= \left(\mathcal{H}_{\mathrm{M}} - iU_{\mathrm{M}}^\dagger \frac{\mathrm{d}}{\mathrm{d}x} U_{\mathrm{M}}\right)\vec{\phi}_e(x) \\ &= \frac{1}{4E}\begin{pmatrix} -\Delta m_{\mathrm{M}}^2 & -4iE\frac{\mathrm{d}}{\mathrm{d}x}\theta_{\mathrm{M}} \\ 4iE\frac{\mathrm{d}}{\mathrm{d}x}\theta_{\mathrm{M}} & \Delta m_{\mathrm{M}}^2 \end{pmatrix}\vec{\phi}_e(x) \quad . \end{aligned} \tag{1.36}$$

If matter density is not constant, $\frac{\mathrm{d}}{\mathrm{d}x}A_{\mathrm{CC}} \neq 0$ and therefore $\frac{\mathrm{d}}{\mathrm{d}x}\theta_{\mathrm{M}} \neq 0$. Transitions between ν_1^{M} and ν_2^{M} become possible.

Adiabatic Evolution: We define the adiabaticity parameter as:

$$\gamma \equiv \frac{\Delta m_{\mathrm{M}}^2}{4E\frac{\mathrm{d}}{\mathrm{d}x}\theta_{\mathrm{M}}} = \frac{(\Delta m_{\mathrm{M}}^2)^2}{2E\sin 2\theta_{\mathrm{M}} |\frac{\mathrm{d}}{\mathrm{d}x}A_{\mathrm{CC}}|} \quad . \tag{1.37}$$

If the matter density changes slowly $\gamma \gg 1$, and the transitions between ν_1^{M} and ν_2^{M} are negligible. The survival probability $P_{\nu_e \to \nu_e}$ can be derived to

$$\begin{aligned} P_{\nu_e \to \nu_e}^{\mathrm{adiabatic}} &= \frac{1}{2} + \frac{1}{2}\cos 2\theta_{\mathrm{M}}(0)\cos 2\theta_{\mathrm{M}}(x) \\ &\quad + \frac{1}{2}\sin 2\theta_{\mathrm{M}}(0)\sin 2\theta_{\mathrm{M}}(x)\cos\left(\int_0^x \frac{\Delta m_{\mathrm{M}}^2(y)}{2E}\,\mathrm{d}y\right) \quad . \end{aligned} \tag{1.38}$$

For most cases, the matter density at detection is neglectable and the oscillation parameters are given by $A_{\mathrm{CC}}(x_{\mathrm{det}}) \approx 0$, $\theta_{\mathrm{M}}(x_{\mathrm{det}}) \approx \theta$ and $\Delta m_{\mathrm{M}}^2(x_{\mathrm{det}}) \approx \Delta m^2$. Furthermore, due to the finite detector resolution, P has to be integrated over Δx and ΔE. It follows that

$$\langle P^{\text{adiabatic}}_{\nu_e\to\nu_e}\rangle = \frac{1}{2} + \frac{1}{2}\cos 2\theta_{\text{M}}(0)\cos 2\theta \quad . \tag{1.39}$$

Maximum Violation of Adiabaticity: While the adiabatic evolution is the one side of the medal, the other one is called maximal violation of adiabaticity. Here, γ from equation 1.37 has to be minimal, meaning $\frac{\mathrm{d}}{\mathrm{d}x}\gamma \approx 0$ which is the case for large density slopes. The resulting condition is:

$$\left(3\cos 2\theta_{\text{M}}\sin 2\theta_{\text{M}}(\frac{\mathrm{d}}{\mathrm{d}x}A_{\text{CC}})^2 + \Delta m^2 \sin 2\theta \frac{\mathrm{d}^2}{\mathrm{d}x^2}A_{\text{CC}}\right)\Bigg|_{x=x_{\text{MVA}}} = 0 \quad . \tag{1.40}$$

Note that generally the point of maximal violation of adiabaticity is not at the same coordinates as the resonance point, defined by $\cos 2\theta_{\text{M}}\big|_{x=x_{\text{res}}} = 0$. However, for small mixing one can approximate x_{MVA} by x_{R}.

If the propagation through the star is non-adiabatic, neutrino transitions $\nu_1^{\text{M}} \rightleftarrows \nu_2^{\text{M}}$ occur. They are maximal at x_{MVA} and with $\gamma \to 0$ we get full neutrino conversion. Neutrino evolution in matter can best be understood with the help of a level crossing diagram as shown in figure 1.15.

Matter Driven Oscillations in Supernovae

In this section we will consider matter driven oscillations in the supernova environment. We will first make some general comments and then follow up with the discussion of the simple case of a static density profile. However, as the assumption of a static profile is not tenable, we will also consider density changes due to the propagation of a simple shock wave through stellar matter.

All current detectors sensible to supernova neutrinos are unable to distinguish between muon and tauon neutrinos which is why mixing in this regime need not be considered. As most neutrino transitions in a supernova occur in the resonance layers, $\rho_{\text{res}} \pm \Delta\rho_{\text{res}}$, the treatment is much simplified. Equation 1.33 shows that the resonance densities are governed by the neutrino mass differences. This leads to [94]:

$$\rho_{\text{res}} \approx 1.4 \cdot 10^6\,\frac{\text{g}}{\text{cm}^3}\left(\frac{\Delta m^2}{1\,\text{eV}^2}\right)\left(\frac{10\,\text{MeV}}{E}\right)\left(\frac{0.5}{Y_e}\right)\cos 2\theta \tag{1.41}$$

with Y_e being the electron fraction, i.e. the number of electrons per nucleon.

Taking a look at the mass differences, we note that we need only consider two resonances: a heavy one, called H-resonance, determined by $|\Delta m^2_{32}| \approx |\Delta m^2_{31}|$ with

$$\rho_{\text{H},15\,\text{MeV}} \sim 2000 - 2300\,\frac{\text{g}}{\text{cm}^3} \tag{1.42}$$

and a light one, called L-resonance, governed by $|\Delta m^2_{21}|$ with

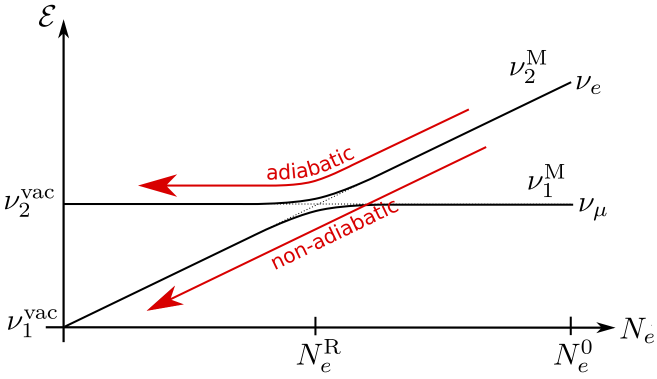

Figure 1.15: Level crossing diagram

$\mathcal{E}$ describes the eigenvalue of the Hamiltonian and N_e the electron density. The neutrinos are created in their flavor eigenstate at high density. Due to the matter interactions, the electron neutrino state consists mostly of the high mass eigenstate. During the propagation out of the star (from the right to the left), the density and therefore the effective potential acting on the electron neutrino decreases until the two states have approximately the same eigenvalues (at N_e^{R}). Depending on the vacuum mixing angles and the density slope, we then have adiabatic or non-adiabatic propagation transitions. In the first case, the neutrinos stay in their mass eigenstates and we follow the solid lines in the diagram (this is the case for solar neutrinos). In the case of maximally violated adiabaticity, full conversion occurs and the neutrinos follow the dotted line at the resonance density N_e^{R}.

$$\rho_{\mathrm{L},15\,\mathrm{MeV}} \sim 25\,\frac{\mathrm{g}}{\mathrm{cm}^3} \quad . \tag{1.43}$$

Note that these densities were calculated for neutrino energies of 15 MeV and an electron fraction of 0.5.

The probability for neutrino conversion to occur is called the crossing or flip probability and given by the modified Landau-Zener formula [95]:

$$P_c = \frac{\exp(-\frac{\pi}{2}\gamma F) - \exp(-\frac{\pi}{2}\gamma F/\sin^2\theta)}{1-\exp(-\frac{\pi}{2}\gamma F/\sin^2\theta))} \tag{1.44}$$

with F being a complicated function, defined by the density profile and the mixing angle.

Crossing Probability for a Simple Density Profile: The considerations in this paragraph closely follow reference [94]. From the conditions on the onset of the core collapse, an approximate density profile of the supernova precursor can be derived to be [96]:

$$\rho \propto r^{-n} \tag{1.45}$$

with $n \approx 3$. Equation 1.44 can be simplified by assuming $F = 1-\tan^2\theta$ as in the sun[27]. In the following discussion, we will focus on the H-resonance. The same argumentation can also be applied to the L-resonance. With

$$\gamma = \gamma(r = r_\mathrm{H}) = \frac{\Delta m_{13}^2 \sin^2 2\theta_{13}}{2E\cos 2\theta_{13}\left|\frac{\mathrm{d}}{\mathrm{d}r}\ln N_e\right|_\mathrm{H}} \tag{1.46}$$

the crossing probability is calculated to be

$$P_\mathrm{H} = \frac{\exp(\pi k_\mathrm{H} s_\mathrm{H}\cos^2\theta_{13}) - 1}{\exp(\pi k_\mathrm{H} s_\mathrm{H}) - 1} \tag{1.47}$$

with the neutrino wave number $k_\mathrm{H} = \Delta m_{13}^2/2E$ and the density scale factor at the resonance point of $s_\mathrm{H} = \left|\frac{\mathrm{d}}{\mathrm{d}r}\ln N_e(r)\right|^{-1}_{r=r_\mathrm{H}} = \left|\frac{\mathrm{d}}{\mathrm{d}r}\ln V(r)\right|^{-1}_{r=r_\mathrm{H}}$. For the simple density profile as in equation 1.45, the potential can be written as

$$V(r) = V_0\left(\frac{r}{R_\odot}\right)^{-n} \tag{1.48}$$

with the radius of the sun $R_\odot$.

As in [97], we assume $V_0 = 1.5\cdot 10^{-14}\,\mathrm{eV}$. Due to the large exponent, equation 1.47 reduces to the Landau-Zener limit which can be further simplified to:

---

[27] While the sun follows a density profile $\rho \propto e^{-r}$, the differences to the crossing probability are minimal [97].

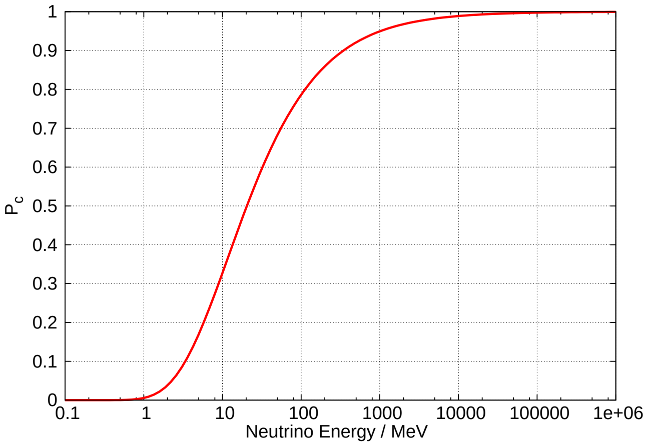

Figure 1.16: Energy dependence of the crossing probability for a fixed $\sin^2 2\theta_{13}$ of $2 \cdot 10^{-4}$

$$P_c \approx \exp\left(k_{\mathrm{H}} s_{\mathrm{H}} \sin^2\theta_{13}\right) = \exp\left(-A\left(\frac{\Delta m^2_{13}}{E}\right)^{\frac{2}{3}} \frac{\sin^2\theta_{13}}{(\cos 2\theta_{13})^{\frac{1}{3}}}\right) \tag{1.49}$$

with $A = 5.73 \cdot 10^6 \left(\frac{\mathrm{MeV}}{\mathrm{eV}^2/c^4}\right)^{\frac{2}{3}}$.

Figure 1.16 shows the energy dependence of the crossing probability for $\sin^2 2\theta_{13} = 2 \cdot 10^{-4}$. As only an upper limit is known for $\sin^2 2\theta_{13}$, we release this parameter in figure 1.17. Three regions become evident:

- Adiabatic region (I): If $\sin^2 2\theta_{e3} \gtrsim 10^{-3}$ then $P_c \approx 0$. In this case, most neutrinos stay in their respective matter eigenstate. Figure 1.17 shows this region in the color blue.
- Transition region (II): For $10^{-5} \lesssim \sin^2 2\theta_{e3} \lesssim 10^{-3}$, P_c changes with energy. Hence, neutrino conversion occurs. The color transition regime (blue to red) in figure 1.17 displays this case.
- Strong violation of adiabaticity (III): If $\sin^2 2\theta_{e3} \lesssim 10^{-5}$ then $P_f \approx 1$ and thus most neutrinos will switch their matter eigenstate. Figure 1.17 shows these transitions as red.

The energy spectrum of supernova neutrinos spans about one order of magnitude (see section 1.1.2.3). If one uses the restraints on the neutrino oscillation parameters (see section 1.2.2), one notes that the L-resonance always happens adiabatically. As the H-resonance depends on the yet unknown θ_{13} angle, it can fall into any of the three regions.

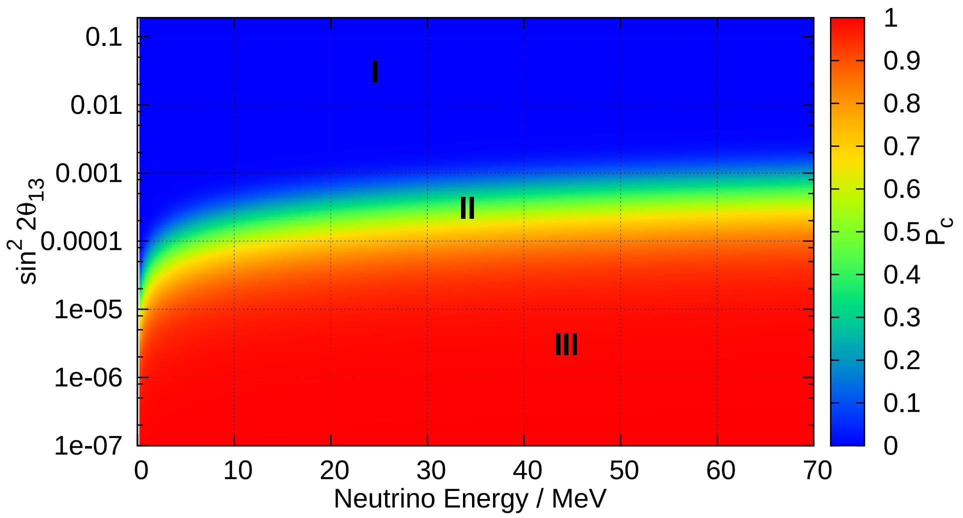

Figure 1.17: Crossing probability for neutrinos at the H resonance
The regions are the adiabatic regime (I), the transition region (II) and the case of maximal violation of adiabaticity (III).

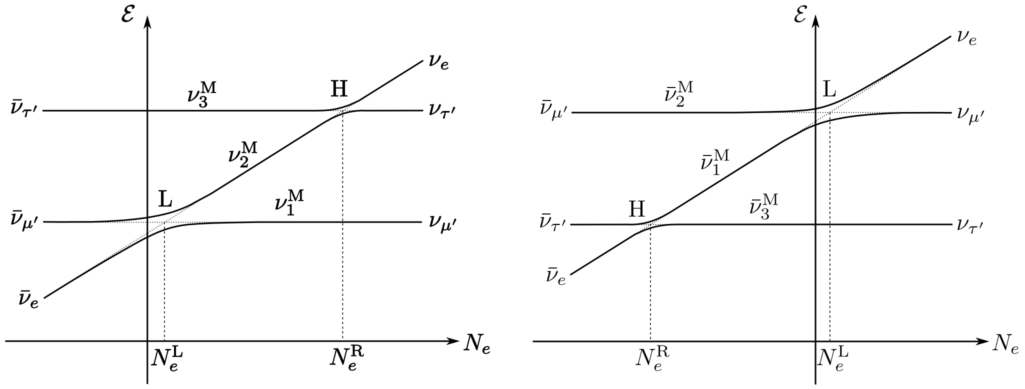

(a) Normal hierarchy

(b) Inverted hierarchy

Figure 1.18: Level crossing diagram for neutrino evolution in supernova
As before, $\mathcal{E}$ describes the eigenvalue of the Hamiltonian and N_e the electron density. Details on these diagrams can be found in the text.

Neutrino Evolution in a Star To understand the neutrino evolution through the star, let us examine the Hamiltonian:

$$\mathcal{H} = \frac{\mathcal{M}^2}{2E} + \mathcal{V} = \frac{1}{2E}\begin{pmatrix} m_{ee}^2 + 2EV & m_{e\mu}^2 & m_{e\tau}^2 \\ m_{e\mu}^2 & m_{\mu\mu}^2 & m_{\mu\tau}^2 \\ m_{e\tau}^2 & m_{\mu\tau}^2 & m_{\tau\tau}^2 \end{pmatrix} \quad . \tag{1.50}$$

Since rotations in the $(\nu_\mu - \nu_\tau)$ subspace do not affect the physics [98], the Hamiltonian can be simplified to:

$$\mathcal{H} = \frac{1}{2E}\begin{pmatrix} m_{ee}^2 + 2EV & m_{e\mu'}^2 & m_{e\tau'}^2 \\ m_{e\mu'}^2 & m_{\mu'\mu'}^2 & 0 \\ m_{e\tau'}^2 & 0 & m_{\tau'\tau'}^2 \end{pmatrix} \quad . \tag{1.51}$$

In high density, $V \gg m_{ij}^2/2E$, the mixing contributions to the electron neutrino mass can be neglected, yielding

$$\mathcal{H} = \mathrm{diag}(V, m_{\mu'\mu'}^2, m_{\tau'\tau'}^2) \quad . \tag{1.52}$$

Thus, $(\nu_e, \nu_\mu', \nu_\tau')$ are the matter eigenstates.

One can easily create the corresponding level crossing diagrams shown in figure 1.18. However, due to the unknown neutrino mass hierarchy two cases have to be considered.

Let us start with the normal mass hierarchy, $m_1 < m_2 < m_3$. The electron neutrinos get created inside the neutrinosphere (at the rightmost in the diagram) and travel in their flavor state which is at these high densities equivalent to the heaviest mass state ν_3^{M}. $\nu_{\mu'}$ and $\nu_{\tau'}$ are in the ν_1^{M} and ν_2^{M} mass states[28]. As the density decreases (we

---

[28] While the muon and tauon neutrinos start out in a coherent mixture of mass eigenstates, this coherence gets broken by a differing potential due to the different masses of the μ and τ leptons.

proceed to the left) so does the potential V, and we arrive at the first resonance region where $m^2_{ee} + 2EV \approx m^2_{\tau'\tau'}$. At lower densities, electron neutrinos consist mainly of the state ν^{M}_2 and the $\nu_{\tau'}$ of the ν^{M}_3 state. Further decreasing density leads to $m^2_{ee} + 2EV \approx m^2_{\mu'\mu'}$ where the same switch occurs between the mass states of ν_e and $\nu_{\mu'}$. In the anti-neutrino sector (sketched by the negative densities with propagation going from left to right) the potential V has a negative sign. The $\bar{\nu}_e$ get created as $\bar{\nu}^{\mathrm{M}}_1$ and the effective mass continuously stays below the masses of the other flavors. No crossings occur.

In the case of the inverted hierarchy, $m_3 < m_1 < m_2$, things look different. Again, the electron neutrinos are created in a state equivalent to the heaviest mass eigenstate, now ν^{M}_2. $\nu_{\mu'}$ and $\nu_{\tau'}$ are mainly made up of ν^{M}_1 and ν^{M}_3. With decreasing density, we reach the point $m^2_{ee}+2EV \approx m^2_{\mu'\mu'}$ and switch the mass states so that $\nu_{\mu'}$ is equivalent to ν^{M}_2 and ν_e to ν^{M}_1. However, we will reach $m^2_{ee} + 2EV \approx m^2_{\tau'\tau'}$ in the anti-neutrino sector only. Here, the $\bar{\nu}_e$ start out as being equivalent to the lightest $\bar{\nu}^{\mathrm{M}}_3$ state. After resonance, the $\bar{\nu}_e$ match $\bar{\nu}^{\mathrm{M}}_1$, having switched with $\bar{\nu}_{\tau'}$.

Using the level crossing diagrams, we can easily derive the neutrino composition leaving the star. Let us describe the neutrino fluxes emitted at the neutrinosphere by F^0_e for electron and $F^0_x = F^0_{\mu'} = F^0_{\tau'}$ for the muon and tauon neutrinos. Note that we assume the same fluxes for all non-electron neutrinos. Analogously, we describe the anti-neutrinos by $\bar{F}^0_e$ and $\bar{F}^0_x$. Within the star, the neutrinos travel in their matter eigenstates ν^{M}_i and due to the steady decrease in density leave the star in their vacuum mass eigenstates ν_i. The same goes for anti-neutrinos.

Generally, the neutrino fluxes leaving the star can be expressed as

$$\begin{aligned} F_i &= a_i F^0_e + (1-a_i) F^0_x \quad \text{and} \\ \bar{F}_i &= \bar{a}_i \bar{F}^0_e + (1-\bar{a}_i) \bar{F}^0_x \end{aligned} \tag{1.53}$$

with $\overset{(-)}{a_i}$ being the contribution to the vacuum eigenstate i from the initial electron neutrino flux.

Using the level crossing diagrams shown in figure 1.18, the contributions can easily be derived for all fluxes. All that needs to be done is to follow the respective lines and apply the crossing probability $P_{H/L}$ at each resonance. The results are shown in table 1.2.

	a_1	a_2	a_3	$\bar{a}_1$	$\bar{a}_2$	$\bar{a}_3$
Normal Hierarchy	$P_{\mathrm{L}}P_{\mathrm{H}}$	$P_{\mathrm{H}} - P_{\mathrm{L}}P_{\mathrm{H}}$	$(1-P_{\mathrm{H}})$	1	0	0
Inverted Hierarchy	P_{L}	$(1-P_{\mathrm{L}})$	0	P_{H}	0	$(1-P_{\mathrm{H}})$

Table 1.2: Contribution of the initial electron (anti-) neutrinos to the vacuum flux.

The flux of electron neutrinos at Earth is determined by

$$F_e = \sum_i |U_{ei}|^2 F_i \quad . \tag{1.54}$$

Using the unitarity condition $\sum_i |U_{ei}|^2 = 1$, we can write:

$$F_e = pF_e^0 + (1-p)F_x^0 \quad \text{with} \quad p \equiv \sum_i |U_{ei}|^2 a_i \tag{1.55}$$

and accordingly for the anti-neutrinos.

The fluxes for the non-electron neutrinos F_μ and F_τ are easy to calculate, thanks to flux conservation:

$$F_\mu + F_\tau = 2F_x = (1-p)F_e^0 + (1+p)F_x^0 \quad . \tag{1.56}$$

As already mentioned before, the L-resonance is always crossed adiabatically due to the mixing angle θ_{12} (see also figure 1.17). Therefore, $P_{\mathrm{L}} \approx 0$ (see figure 1.17 at the value given in equation 1.16).

Again distinguishing between normal and inverted hierarchy, we derive the results shown in table 1.3.

	p	$\bar{p}$
Normal Hierarchy	$P_{\mathrm{H}}\|U_{e2}\|^2 + (1-P_{\mathrm{H}})\|U_{e3}\|^2$	$\|U_{e1}\|^2$
Inverted Hierarchy	$\|U_{e2}\|^2$	$\bar{P}_{\mathrm{H}}\|U_{e1}\|^2 + (1-\bar{P}_{\mathrm{H}})\|U_{e3}\|^2$

Table 1.3: Contribution of the initial electron (anti-) neutrinos to the electron neutrino flux at Earth.

However, as θ_{13} still covers a wide range, the crossing probability P_{H} can fall into any of the regions depicted in figure 1.17. Remember, these were the adiabatic regime (I) where $P_{\mathrm{H}} \approx 0$, the non-adiabatic regime (II) where $0.1 < P_{\mathrm{H}} < 0.9$ and the maximally violated adiabaticity (III) with $P_{\mathrm{H}} \approx 1$. Under the assumption that $\cos\theta_{e3} \approx 1$ and $|U_{e3}|^2 \ll |U_{e2}|^2$, we arrive at the results in table 1.4

It must be stressed that while the results for region II are strongly dependent on the density profile and must be used with care, regions I and III can be used nearly universally.

	Region I		Region II		Region III	
	p	$\bar{p}$	p	$\bar{p}$	p	$\bar{p}$
Normal Hierarchy	$\|U_{e3}\|^2$	$\cos^2\theta_{e2}$	$P_{\mathrm{H}}\sin^2\theta_{e2}$	$\cos^2\theta_{e2}$	$\sin^2\theta_{e2}$	$\cos^2\theta_{e2}$
Inverted Hierarchy	$\sin^2\theta_{e2}$	$\|U_{e3}\|^2$	$\sin^2\theta_{e2}$	$\bar{P}_{\mathrm{H}}\cos^2\theta_{e2}$	$\sin^2\theta_{e2}$	$\cos^2\theta_{e2}$

Table 1.4: Contribution of the initial electron (anti-) neutrinos to the electron neutrino flux at Earth for different mixing angles θ_{13}

Region I is the adiabatic domain where $\sin^2 2\theta_{13} > 10^{-3}$, *Region II the non-adiabatic case with* $10^{-5} < \sin^2 2\theta_{13} < 10^{-3}$ *and Region III the completely non-adiabatic interval with* $\sin^2 2\theta_{13} < 10^{-5}$.

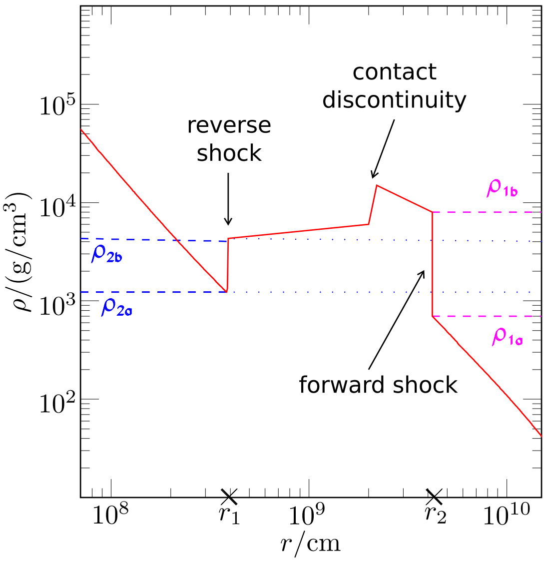

Figure 1.19: Schematic density profile in the presence of forward and reverse shock [99]

Supernova Shock Wave: Of course, the approximation of a static environment within the supernova is untenable. The first and most striking disruption is the propagation of the shock front through the stellar envelope. As matter falls inward to the proto neutron star, it is swept up by the outward moving shock, and steps form in the density profile. Seen from the outside, the first one is encountered directly at the shock front. Additional density steps develop behind it as stellar matter driven by neutrino-heating collides with the forward shock. Due to the negative velocity gradient caused by this clash, a reverse shock and thus a density step traveling back to the PNS forms when the wind speed starts exceeding the local speed of sound. In the collision region where the heated matter is reflected from the forward shock, a further density jump called the *contact discontinuity* can develop. Figure 1.19 shows a schematic of the shock front.

These features appear even in simple 1-D supernova models [100]. As one can expect, the multidimensional models show much more complex environments, featuring bubbles and turbulences due to hydrodynamics. However, in this work we will only investigate the simple case just specified.

The propagation of the shock front through the envelope can strongly influence the neutrino oscillation cases as the varying density gradients have a direct impact on the adiabaticity parameter. At the front of forward and reverse shocks and the contact discontinuity, the density gradients are very steep, leading to a large $\frac{\mathrm{d}}{\mathrm{d}x}A_{\mathrm{CC}}$ and thus a small γ. During the passage of the shock wave through the resonance region, full neutrino conversion will occur, and consequently, in all cases except the maximally violating one, we can expect changes to the crossing probability.

According to [101], the neutrino conversion during an abrupt change in density from ρ_a to ρ_b follows

$$P_c = \sin^2(\theta_a - \theta_b) \quad . \tag{1.57}$$

1.2.4.3 Collective Neutrino Oscillations

For the understanding of collective oscillation, the *Neutrino Flavor IsoSpin* (NFIS) formalism is essential. After a short sketch of the NFIS picture, we will introduce the effects of neutrino self-interactions. More details on this topic can be found in appendix A.2.

Neutrino Flavor IsoSpin (NFIS)

The NFIS formalism is derived from the description of neutrinos with the density matrix

$$\hat{\rho}(x) = \sum_\alpha \mid \nu_\alpha(x)\rangle W_\alpha \langle \nu_\alpha(x) \mid \quad . \tag{1.58}$$

As all 2×2 matrices can be decomposed into $X = \frac{1}{2}\left(\mathrm{tr}(X)\mathbb{1} + \sum_k \mathrm{tr}(X\sigma_k)\sigma_k\right)$ with the Pauli matrices σ_i, it becomes possible to describe neutrinos and their Hamiltonians by vectors. For neutrinos these are the neutrino flavor isospins $\vec{s}_\nu$ which are linked to the detection probabilities of a specific flavor at the point x via

$$\begin{aligned} P_{\nu_e}(x) &= \frac{1}{2} + \vec{s}_\nu \cdot \vec{e}_3^{\,\mathrm{F}} \quad \text{and} \\ P_{\nu_\mu}(x) &= \frac{1}{2} - \vec{s}_\nu \cdot \vec{e}_3^{\,\mathrm{F}} \quad . \end{aligned} \tag{1.59}$$

The Hamiltonian vectors are given by

$$\begin{aligned} \vec{H}_\mathrm{V}^\mathrm{F} &= (-\sin 2\theta,\ 0,\ \cos 2\theta) \quad , \\ \vec{H}_e^\mathrm{F} &= (0,\ 0,\ \sqrt{2}G_\mathrm{F}N_e) \quad \text{and} \\ \vec{H}_\mathrm{eff}^\mathrm{F} &\equiv \mu_\mathrm{V}\vec{H}_\mathrm{V} + \vec{H}_e \quad . \end{aligned} \tag{1.60}$$

Consistently applying the density matrix formalism and mapping it to the NFIS picture converts equation 1.29 to

$$\frac{\mathrm{d}}{\mathrm{d}x}\vec{s}_\nu = \vec{s}_\nu \times \vec{H}_\mathrm{eff} \tag{1.61}$$

which is equivalent to the precession of a gyroscope or a spin in a magnetic field.

This analogy will come in handy for the understanding of collective neutrino oscillations.

Generalities of Neutrino Self-Interactions

Due to the high neutrino density in the supernova environment, neutrino-neutrino interactions, which could normally be neglected, play an important role.

The two major oscillation modes will be considered in this section. Synchronized oscillation occur if the neutrino gas is dominated by a single flavor, leading to the ensemble behaving as a single neutrino with energy E_{sync}. The second case is the bi-polar mode where mixed neutrino gases form disparate blocks and may fall into an (anti-) aligned state. Last, we will examine the special case of the supernova environment. The depicted approach closely follows the one in [102].

If large numbers of (anti-)neutrinos propagate together, their Hamiltonian has to be modified by a contribution describing their forward scattering on each other. For the ith neutrino, this contribution is

$$\mathcal{H}_{\nu\nu,i} = -\frac{\vec{\sigma}}{2} \cdot \sum_j \mu_{ij} \left(n_{\nu,j} \vec{s}_{\nu,j} - n_{\bar{\nu},j} \vec{s}_{\bar{\nu},j} \right) \tag{1.62}$$

with $n_{\nu,i}$ being the number density of the flavor of neutrino i, $\mu_{ij} = -2\sqrt{2}G_{\mathrm{F}}(1 - \cos\Theta_{ij})$ and Θ_{ij} the angle between the ith and jth neutrino. Writing $\vec{s}_{\nu,j}$ and $\vec{s}_{\bar{\nu},j}$ as $\vec{s}_j$ and $-\vec{s}_j$ respectively and decomposing the Hamiltonian, we get

$$\frac{\mathrm{d}}{\mathrm{d}t}\vec{s}_i = \vec{s}_i \times \left(\mu_{\mathrm{V},i}\vec{H}_{\mathrm{V}} + \vec{H}_e + \sum_j \mu_{ij} n_j \vec{s}_j \right) \tag{1.63}$$

with the sum going over both neutrinos and anti-neutrinos and

$$\mu_{\mathrm{V},i} \equiv \begin{cases} +\Delta m^2/2E & \text{for neutrinos} \\ -\Delta m^2/2E & \text{for anti-neutrinos} \end{cases} \quad . \tag{1.64}$$

We further define the total effective energy

$$\mathcal{E} \equiv -\sum_i n_i \vec{s}_i \cdot (\mu_{\mathrm{V},i}\vec{H}_{\mathrm{V}} + \vec{H}_e) - \frac{1}{2}\sum_{i,j} \mu_{ij} n_i n_j \vec{s}_i \cdot \vec{s}_j \quad . \tag{1.65}$$

Note that $\mathcal{E}$ is not equivalent to the physical neutrino energies. From equation 1.63 follows $\frac{\mathrm{d}}{\mathrm{d}t}\vec{s}_i \perp \vec{s}_i$ and thus as long as $\frac{\mathrm{d}}{\mathrm{d}t}\vec{H}_{\mathrm{eff}} \approx 0$ one finds

$$\frac{\mathrm{d}}{\mathrm{d}t}\mathcal{E} \approx 0 \quad . \tag{1.66}$$

For simplification we will assume an isotropic neutrino gas, leading to

$$\mu_{ij} \rightarrow \mu_\nu \equiv -2\sqrt{2}G_{\mathrm{F}} \quad . \tag{1.67}$$

If we define

$$\vec{S} \equiv \sum_j n_j \vec{s}_j \quad , \tag{1.68}$$

the total effective energy simplifies to

$$\mathcal{E} = -\sum_i \mu_{\mathrm{V},i} n_i \vec{s}_i \cdot \vec{H}_\mathrm{V} - \frac{\mu_\nu}{2}\vec{S}^2 \quad . \tag{1.69}$$

Synchronized Oscillations

We will first discuss the simple case of a single neutrino flavor without matter background and then use the method of the co-rotating frames to generalize this picture.

Pure Neutrino Gas without Matter: We assume $N_e = 0$ and a finite energy range of $|\mu_{\mathrm{V},i}| \leq |\mu_{\mathrm{V},i}|_{\max}$. The equation of motion (e.o.m.) 1.63 for $\vec{s}_i$ thus results in

$$\frac{\mathrm{d}}{\mathrm{d}t}\vec{s}_i = \vec{s}_i \times (\mu_{\mathrm{V},i}\vec{H}_\mathrm{V} + \mu_\nu \vec{S}) \quad . \tag{1.70}$$

We obtain the respective e.o.m. for the NFIS of the combined gas $\vec{S}$ by summing over all neutrinos

$$\frac{\mathrm{d}}{\mathrm{d}t}\vec{S} = \sum_i \mu_{\mathrm{V},i} n_i \vec{s}_i \times \vec{H}_\mathrm{V} \quad . \tag{1.71}$$

We now assume a very dense neutrino gas so that $|\mu_\nu \vec{S}| \gg |\mu_{\mathrm{V},i}|_{\max}$. From equations 1.69, 1.66 and $|\vec{s}_i \cdot \vec{H}_\mathrm{V}| \leq \frac{1}{2}$ follows

$$\mathcal{E} \simeq -\frac{\mu_\nu}{2}\vec{S}^2 \simeq \mathrm{const} \quad . \tag{1.72}$$

Consequently, the magnitude of the total NFIS stays approximately the same. The e.o.m. of $\vec{s}_i$ reduces to

$$\frac{\mathrm{d}}{\mathrm{d}t}\vec{s}_i \simeq \vec{s}_i \times \mu_\nu \vec{S} \quad , \tag{1.73}$$

meaning that the individual $\vec{s}_i$'s precess around the total NFIS $\vec{S}$ with a common angular frequency of

$$\omega_\nu \equiv |\mu_\nu \vec{S}| \quad . \tag{1.74}$$

If we take a look at the time frame $2\pi/\omega_\nu \ll \delta t \ll 2\pi/\omega_{\mathrm{sync}}$, the individual NFIS average out to $\vec{s}_i \simeq (\vec{s}_i \cdot \vec{S})\vec{S}$. Inserting this into equation 1.71, the e.o.m. simplify to

$$\frac{\mathrm{d}}{\mathrm{d}t}\vec{S} \simeq \omega_{\mathrm{sync}} \vec{S} \times \vec{H}_\mathrm{V} \tag{1.75}$$

with

$$\omega_{\mathrm{sync}} = \langle \mu_\mathrm{V} \rangle \equiv \sum_i \frac{\mu_{\mathrm{V},i} n_i \vec{s}_i \cdot \vec{S}}{\vec{S}^2} \quad . \tag{1.76}$$

Thus, the neutrino ensemble behaves as a single neutrino with energy ω_{sync}.

General Synchronized Neutrino Systems Using co-rotating reference frames with angular velocity of e.g. $-\Omega\vec{H}_{\mathrm{V}}$, one can relate more general neutrino ensembles or even a matter background to the simple case just discussed. Essentially, the behavior in these cases is equivalent to a pure neutrino gas without matter background. Refer to appendix A.2.2 for more details.

Bi-Polar Oscillations

No synchronization occurs if we have equal numbers of say ν_e, ν_μ, $\bar{\nu}_e$ and $\bar{\nu}_\mu$. However, because the neutrino gas consists of two distinct NFIS blocks, collective oscillations can still occur.

Simple System without Matter: Consider a simple system consisting only of ν_e and $\bar{\nu}_e$ in equal number densities n_ν with energies $\mu_{\mathrm{V}+} = -\mu_{\mathrm{V}-} = \mu_{\mathrm{V}}$ for all (anti-)neutrinos. Summing equation 1.63 over all neutrinos and anti-neutrinos, respectively we get

$$\begin{aligned}\frac{\mathrm{d}}{\mathrm{d}t}\vec{S}_\nu &= \vec{S}_\nu \times \left(\mu_{\mathrm{V}}\vec{H}_{\mathrm{V}} + \mu_\nu \vec{S}_{\bar{\nu}}\right) \quad \text{and} \\ \frac{\mathrm{d}}{\mathrm{d}t}\vec{S}_{\bar{\nu}} &= \vec{S}_{\bar{\nu}} \times \left(-\mu_{\mathrm{V}}\vec{H}_{\mathrm{V}} + \mu_\nu \vec{S}_\nu\right)\end{aligned} \tag{1.77}$$

with the definitions

$$\vec{S}_+ \equiv \vec{S}_\nu + \vec{S}_{\bar{\nu}} \quad \text{and} \quad \vec{S}_- \equiv \vec{S}_\nu - \vec{S}_{\bar{\nu}} \quad . \tag{1.78}$$

The equations of motion for this case are given by

$$\begin{aligned}\frac{\mathrm{d}}{\mathrm{d}t}\vec{S}_+ &= \mu_{\mathrm{V}}\vec{S}_- \times \vec{H}_{\mathrm{V}} \quad \text{and} \\ \frac{\mathrm{d}}{\mathrm{d}t}\vec{S}_- &= \mu_{\mathrm{V}}\vec{S}_+ \times \vec{H}_{\mathrm{V}} + \mu_\nu \vec{S}_- \times \vec{S}_+ \quad .\end{aligned} \tag{1.79}$$

To investigate the evolution of a neutrino ensemble, it is expedient to examine its overall mass eigenstate given by $s^{\mathrm{V}}_{\nu,3} = \vec{S}_\nu \cdot \vec{e}^{\,\mathrm{V}}_3 \sim \cos\vartheta$. As the calculations are quite complex, we will discuss only the results at this point. For more details refer to appendix A.2.3.1.

In normal hierarchy as well as low neutrino densities ϑ is delimited by the vacuum mixing angle and the neutrinos stay in their initial state. At medium densities, the range the angle can take increases and neutrino conversion become more likely. The exceptional consequences of the self-coupling become only evident at high and very high neutrino densities. Here, the angle ϑ becomes large, allowing the neutrino ensembles to decouple from their initial state; oscillations can occur. This goes so far that the neutrinos can completely swap their states even for very small mixing angles.

General Bi-Polar Neutrino Systems: The modus operandi for the generalization in bi-polar case is the same as in the synchronized case. Details can be found in appendix A.2.3.2.

If one consistently applies this technique to mixed neutrino gases with two flavors and different energies, the swapping between the ensembles becomes dependent on the energies. Table 1.5 shows the possibilities.

Hierarchy	$\nu_e - \bar{\nu}_e$	$\bar{\nu}_\mu - \nu_\mu$	$\nu_e - \nu_\mu$	$\bar{\nu}_\mu - \bar{\nu}_e$
$\Delta m^2 > 0$	Never	Always	$E_{\nu_e} > E_{\nu_\mu}$	$E_{\bar{\nu}_\mu} < E_{\bar{\nu}_e}$
$\Delta m^2 < 0$	Always	Never	$E_{\nu_e} < E_{\nu_\mu}$	$E_{\bar{\nu}_\mu} > E_{\bar{\nu}_e}$

Table 1.5: Conditions for bi-polar neutrino swapping of mono-energetic neutrino systems.

Again, the presence of matter does not significantly modify the behavior of the neutrino ensembles.

Collective Neutrino Oscillations in the Supernova Environment

It should be noted that this is a very active and rapidly developing field, and the considerations hereafter are far from complete, even at the current time. Much is still unknown about these phenomena. For example, the current state-of-the-art supernova simulations do not include neutrino self-interaction processes or neutrino oscillations, and it is not at all certain that these effects can be neglected.

Shortly above the neutrinosphere, the neutrino density is so large that a synchronized ensemble forms which behaves as a single neutrino with the energy E_{sync}. However, in this region, the density of the ordinary matter is so high that the mixing angles are strongly suppressed and thus flavor-lepton numbers are nearly perfectly conserved. As the neutrinos propagate to the outside, the synchronized system breaks down and bi-polar alignment is achieved. As sketched before, in the case of inverted mass hierarchy full flavor conversion can occur even for very small mixing angles. Matter only slightly affects the bi-polar oscillation behavior in the supernova environment (see also [103]).

A further complication in the supernova picture is that the uniform distribution of the propagation directions breaks down. While so far we only considered neutrinos with a fixed emission angle Θ, this is only an approximation. However, the consideration of multiple trajectories does not seem to provide significantly new output [104]. As further investigations are not yet available, we will restrict ourselves to the single-angle approximation.

The considerations in this section closely follow [105].

We assume an isotropic neutrino gas described by neutrino flavor isospins $\vec{s}_i$. Unlike before, however, the neutrino energies have continuous spectra. We replace the NFIS vectors $\vec{s}_i$ by polarization vectors at given energies $\vec{P}_\omega$ with $\omega > 0$ describing the neutrinos and $\omega < 0$ the anti-neutrinos. In analogy to $\vec{S}_+$ we define

$$\vec{D} \equiv \int_{-\infty}^{\infty} \operatorname{sign}(\omega) \vec{P}_\omega \, \mathrm{d}\omega \quad . \tag{1.80}$$

Note that $\vec{D}$ is analogous to $\vec{S}_+$ and not $\vec{S}_-$ because $\vec{s}_{\bar{\nu}}$ has a minus sign in front when expressed in terms of $\vec{s}_\nu$ whereas $\vec{P}_\omega$ does not. The quantity D_z is linked to the net lepton number of the neutrino gas.

Starting from equation 1.63, we go to the co-rotating frame with angular velocity $-\vec{H}_e$ to eliminate the matter potential, replace $\vec{s}_i$ by $\vec{P}_\omega$, multiply the equation with $\operatorname{sign}(\omega)$ and integrate it over the whole spectrum. We arrive at

$$\frac{\mathrm{d}}{\mathrm{d}t} \vec{D} = \vec{H}_\mathrm{V} \times \vec{M} \quad . \tag{1.81}$$

We note the similarity between this result and the equation for $\vec{S}_+$ given in 1.79 if $\mu_\mathrm{V} \vec{S}_- \rightarrow \vec{M} \equiv \int_{-\infty}^{\infty} \operatorname{sign}(\omega)\, \omega\, \vec{s}_\omega \, \mathrm{d}\omega$. The differences originate from the continuous energy spectra.

From equation 1.81, we see that $\frac{\mathrm{d}}{\mathrm{d}t}(\vec{D} \cdot \vec{H}_\mathrm{V}) = 0$ at all times. As D_z describes the neutrino flavor lepton number, only pair-transformations are possible. Furthermore, the mixing angle shortly above the neutrino sphere is small so that interaction and mass eigenbasis practically coincide. Collective transformations in this regime can consequently only happen in the form $\nu_e \bar{\nu}_e \rightarrow \nu_x \bar{\nu}_x$.

Deleptonization Peak For the onset of core-collapse, one has to carefully examine the above argumentation as it strongly deviates from the later conditions. In the first milliseconds the luminosity is completely dominated by ν_e while all other neutrino types are strongly suppressed. The bi-polar condition, i.e. neutrino numbers of the same order, is not met and one expects only synchronized oscillations. Thus, we can assume the absence of collective effects in the starting signal.

Post-Breakout Phase Excluding the deleptonization burst, neutrinos are produced in approximately the same amounts within the star, with the only difference between the flavors being the spectra. As collective oscillations can only happen in pairs, a so-called spectral split can occur. For instance, the spectra of the ν_e and ν_x will swap up to a certain energy and above the original spectra obtain. Furthermore, multiple spectral splits can occur (see [106, 107]).

For the purposes of simulating the effects of these splits on our signal, we will use the results published in [107] and kindly provided by I. Tamborra [108]. The energy spectra in this simulation are assumed to be thermal:

$$\Phi_\alpha(E) = \frac{2\beta_\alpha}{3\zeta_3} \frac{(\beta_\alpha E)^2}{e^{\beta_\alpha E} + 1} \tag{1.82}$$

with $\beta_\alpha = \frac{c_+}{\langle E_\alpha \rangle}$ and $c_+ = \frac{7\pi^4}{180\zeta_3} = 3.151$ and mean energies of

$$\langle E_{\nu_e} \rangle = 10\,\mathrm{MeV} \quad , \quad \langle E_{\bar{\nu}_e} \rangle = 12\,\mathrm{MeV} \quad \text{and} \quad \langle E_{\nu_x} \rangle = 15\,\mathrm{MeV} \quad . \tag{1.83}$$

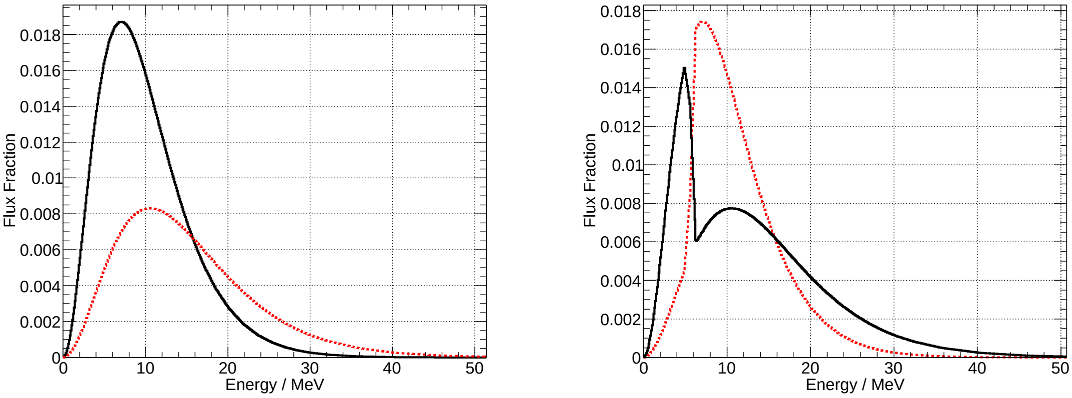

(a) No self-interactions

(b) Self-interactions

Figure 1.20: Collective oscillations of the supernova neutrinos
Solid black illustrates the energy spectrum of the electron flavor, dotted red the spectrum of the non-electron flavors. In the case of self-interactions, the spectra swap at $\approx 6\,\mathrm{MeV}$.

with a total luminosity of $L_{\text{tot}} = 10^{53}\,\mathrm{erg/s}$ exponentially decaying on a timescale of $\tau \simeq 3\,\mathrm{s}$. The luminosity fractions $l_\alpha = L_\alpha / L_{\text{tot}}$ were modified in steps of 10%.

The flavor evolution is investigated in the two neutrino case (comparison with [109] has shown that the three flavor evolution is essentially the same) with a mixing angle of:

$$\sin 2\theta_{13} = 10^{-6} \quad . \tag{1.84}$$

Figure 1.20 shows the spectra before and after oscillation for neutrinos and figure 1.21 the spectra for anti-neutrinos, both for luminosity equipartition $L_{\nu_e} = L_{\bar{\nu}_e} = L_{\nu_x} = L_{\bar{\nu}_x}$. In the neutrino case, one can clearly observe the spectral split at $\approx 6\,\mathrm{MeV}$. The anti-neutrinos are nearly completely converted as the split is at $\approx 1\,\mathrm{MeV}$.

1.2.4.4 Oscillation Sequence in the Supernova

The order by which neutrinos undergo oscillations inside a supernova is primarily determined by the density gradient of the precursor star. One can distinguish two cases.

Iron Core

In the case of most supernovae, the precursor stars have formed an iron core and feature large masses in a thick matter envelope. The H and L resonance regions are far above the neutrinosphere ($\sim 1000\,\mathrm{km}$ for the H resonance) while the collective effects dominate up to $\sim 200\,\mathrm{km}$. Close to the PNS, the neutrinos form a synchronized

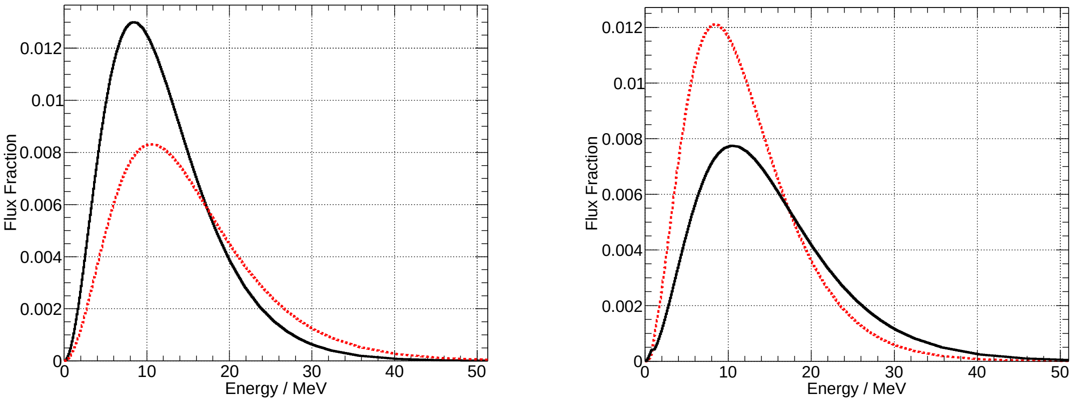

(a) No self-interactions

(b) Self-interactions

Figure 1.21: Collective oscillations of the supernova anti-neutrinos
Solid black illustrates the energy spectrum of the electron flavor, dotted red the spectrum of the non-electron flavors. In the anti-particle case, the spectra swap almost completely (the split is at $\approx 1\,\mathrm{MeV}$*).*

ensemble for which oscillation effects are strongly suppressed because of high matter densities. Above $\sim 50\,\mathrm{km}$, the synchronization breaks down and a bi-polar ensemble is formed. Spectral splits as discussed above can be the consequence [102].

O-Ne-Mg Core

While most supernovae have an iron core, about 30% of the progenitors have masses of $8\,\mathrm{M}_\odot - 10\,\mathrm{M}_\odot$ with cores consisting of oxygen, neon and magnesium. These feature only very small mass envelopes with steep density gradients where the H and L resonance will be passed before the neutrino ensemble breaks apart [110]. In such a case, the neutrinos pass the resonances while still in the synchronized mode. Naively seen, this would mean they oscillate like a neutrino with the energy E_{sync} would. However, as noted in [111], the interplay between matter and self-interaction can lead to special signatures in the neutronization burst. We do not consider this effect because IceCube is not able to discern the deleptonization peak for anything other than very close-by supernovae [93].

2 Detector

> Astronomy compels the soul to look upwards and leads us from this world to another.
>
> Plátōn

In the following chapter, we will first motivate and explain neutrino telescopes in general and then move to the examples of AMANDA and IceCube. A description of the supernova data acquisition (SNDAQ) setup follows. Thereafter, we will continue with a detailed examination of the interactions between neutrinos and ice which will help us to estimate the expected signal of a supernova.

2.1 Neutrino Telescopes

For astronomy, the small weak interaction cross section of neutrinos has its pros and cons.

Because neutrinos are hard to identify, telescopes aimed at their detection require huge effective masses to record even a few events. Furthermore, due to the detection principle, the angular resolution (e.g. $> 0.6°$ for IceCube) is much inferior to classical astronomy (e.g. $< 0.1\,\text{arcsec}$ for the Hubble telescope).

On the other hand, neutrinos allow us to look inside stars while photons are mainly radiated from their surface. Neutrinos would provide us with fundamentally new information, helping to better understand the processes driving the universe. Examples are supernovae as described in section 1.1 or neutrinos radiated from the sun. Moreover, the detection of extra-terrestrial neutrinos can provide a better understanding of the characteristics of these particles. Examples are the solution of the solar neutrino problem or the constraining of neutrino parameters with the supernova neutrinos recorded in 1987 (see section 1.1.2.5). Another advantage of neutrinos is that they are not diverted from their path. Photons can be absorbed by dust clouds or get lost in the light of other stars (e.g. no stellar objects behind the galactic core are visible). Looking for charged particles is no real alternative as they are deviated from their original track by galactic magnetic fields thus losing all direction information unless the energy exceeds $\sim 10^{19}\,\text{eV}$ [112].

2.1.1 Principle of Neutrino Telescopes

Neutrino telescopes are neutrino detectors aimed at astrophysics observations. In astronomy the most important observable is the source location, necessitating a good angular resolution. Contrary to photons, the direct observation of neutrinos remains unfeasible. They have to be identified via their reaction products.

When they travel through matter, neutrinos have a small chance of producing a lepton via charged current interaction with nuclei. Provided that the initial energy is sufficiently high, the charged lepton will then travel at nearly the vacuum speed of light and will normally exceed the speed of light in the medium. Due to the Cherenkov effect (see section 2.3.2), photons will be produced along the lepton track, allowing the reconstruction of its path by recording snapshots of the photon front.

These considerations set the key requirements for a neutrino telescope. For one, due to the small cross sections, a large amount of material is required to increase the interaction probability. As the detection principle is based on Cherenkov radiation, the material has to be optically transparent. To keep the costs manageable, it is best to use natural material as interaction mass and seed it with light sensors. Due to cost considerations and abundances, the most manifest candidate material for such an experiment is water, and thus, all neutrino telescopes past, present and planned are set either in water or ice. Neutrino telescopes are mostly placed deep below the surface to provide shielding from atmospheric radiation. Otherwise, the low neutrino reaction rates would be impossible to separate from the background of atmospheric muons.

Because the angle between neutrino and produced lepton decreases with the energy of the incoming particle, e.g. for $\nu_\mu \rightarrow \mu$ the angle is $< 1^\circ$ at $10\,\mathrm{TeV}$, neutrino telescopes are aimed at energies of $10\,\mathrm{GeV}$ and beyond [113].

The best candidate for astronomy are the muon neutrino and its anti-particle. High energy muons have a sufficiently long lifetime for detection and show a large penetration depth in matter. The much lighter electrons quickly lose their energy to electromagnetic cascades and bremsstrahlung. While this facilitates a reliable energy resolution, the angle is only poorly resolved. Another candidate would be tau neutrinos. However, tauons have a very short lifetime, greatly complicating their detection (their average track length is $\sim 50\,\mathrm{m}$ at $10^6\,\mathrm{GeV}$). Tau (anti-)neutrinos show a characteristic signature in the detector, initiating electromagnetic cascades at the tauon creation and decay points. If the two cascades can be separated, this phenomenon is called a *double bang*.

For the case of supernova neutrino detection, the electron flavor is the most relevant. Because the energies involved are in the order of $10\,\mathrm{MeV}$ (see section 1.1.2.3), no other leptons can be produced in charged current interactions.

2.1.2 Neutrino Telescopes in the Ice

We will now consider the neutrino telescopes AMANDA (Antarctic Muon And Neutrino Detector Array) and its successor IceCube. They are the only experiments of their type using ice as detection medium and are the tools of the same collaboration.

Both telescopes were built at the geographic South Pole for the following reasons:

- One of the purest natural deposits of optically transparent materials that can be found on Earth is the antarctic glacier. With a thickness of $\sim 3\,\mathrm{km}$ at the South Pole, it provides good shielding against charged atmospheric radiation, making neutrino astronomy possible.
- In 1956, the US Navy constructed the first station at South Pole. Since then, it has been continuously upgraded (with the Dome in 1975 and the Elevated Station in 2003) so that it supplies an extensive and reliable infrastructure. As of now it is run by the United States Antarctic Program (USAP) and continues to provide good support for scientific programs, facilitating the construction of the AMANDA and IceCube array.
- A further bonus of the southern location is its possibility to complement neutrino telescopes in the northern hemisphere such as ANTARES or the upcoming KM3NET (see section 2.1.3).

AMANDA and IceCube consist essentially of nothing more than Photomultipliers (PMTs) monitoring the ice for Cherenkov light induced by charged leptons. To install sensors in the ice, holes are drilled deep into the glacier. This is done in two steps. First, a hole is melted into the *firn ice*[1] using a heating coil. Once a depth of $50\,\mathrm{m} \sim 100\,\mathrm{m}$ is reached, the hole is extended down to $\sim 2.5\,\mathrm{km}$ with the main drill. This piece of equipment is nothing more than a nozzle spraying hot water on the ice. The melt water is pumped up to the surface where it is heated and pumped back into the drill, closing the loop. After the final depth has been reached, the light sensors are attached to thick wire ropes and lowered into the hole which then gradually refreezes over the next few weeks[2].

2.1.2.1 AMANDA

Construction History

Work on the AMANDA telescope started in the austral summer 1991/92, and it ran until the beginning of 2009 when it was decommissioned. The main constituents of the detector were Hamamatsu R5912-02 photomultipliers (PMTs) installed in a glass pressure housing and connected to the surface by an electrical cable, providing high voltage and transmitting the PMT signal. A more detailed description of the sensors will be provided later. The AMANDA telescope has been continuously extended up to the year 2000:

Test modules: In the antarctic summer of 1991/92, eight optical modules were brought into the ice. Four were deployed at a depth of 150 m and four at 800 m.

---

[1] The first $50 \sim 100\,\mathrm{m}$ of the glacier consist of a layer of packed old snow that has recrystallized and compacted into a substance denser than the surface snow.

[2] The refreezing process starts on top of the hole and slowly works its way downward. It can take anywhere between two weeks and two months.

AMANDA-A: 1993/94, the first four strings with 80 modules were installed at 800 m − 1000 m below the surface. Unfortunately, at these depths, the high density of air bubbles lead to scattering lengths $\lesssim 1\,\mathrm{m}$, inhibiting the reliable reconstruction of muon tracks. After installation of the later strings, AMANDA-A was no longer used.

AMANDA-B4: The next phase of the telescope was termed AMANDA-B and later AMANDA-II. During the austral summer of 1995/96, the collaboration installed four strings with 86 modules in total at depths of 1500 m − 2000 m. One string was placed at the center, the three others were deployed in a circle of 35 m radius. For the first section of the detector, the signal transfer was provided by coaxial cables which, due to their high dispersive properties, showed strong pulse distortion. The PMTs were put into glass spheres constructed by the company *Billings* and featured the lowest noise rates of all AMANDA modules ($200\,\mathrm{Hz} \sim 400\,\mathrm{Hz}$) albeit at a lower transparency in the UV-region. These sensors are termed the B4 generation.

AMANDA-B10: In the antarctic summer 1996/97, 216 optical modules on six strings were plunged into the glacier placed in a circle of 60 m radius with AMANDA-B4 at its center. For this phase, the PMTs were enclosed in glass spheres provided by the company *Benthos*, showing better transparency properties. Due to higher radioactive impurities in the glass, the background rates for these was much higher than in the B4-generation (1 kHz − 1.5 kHz). With the usage of twisted pair cables, pulse distortion and dead weight could be reduced although at the cost of strong cross talk in the transmission and inferior electromagnetic shielding.

AMANDA-B13: 1997/98, AMANDA was extended by 3 strings with 126 sensors in total. Together with the later B19 generation, B13 makes up the outer circle with a radius of 100 m. The modules have the same properties as the B10 generation. Signal transfer was done by optical fibers, eliminating cross talk, pulse distortion and electromagnetic interferences. However, the optical fibers proved vulnerable to the freezing process.

AMANDA-B19: AMANDA underwent the final construction phase in the antarctic summer of 1999/2000. It gained 249 additional optical modules on six strings. The type of PMTs remained the same; however, the glass was changed to a purer batch, decreasing the noise rates to $600\,\mathrm{Hz} \sim 1000\,\mathrm{Hz}$. Unfortunately, string 17 got stuck during deployment and froze above its final destination. Because of the low scattering lengths at its location, it could not be used for track reconstruction.

Figure 2.1 shows a schematic of the AMANDA detector. More details on the AMANDA telescope can be found e.g. in [114, 115, 116, 117].

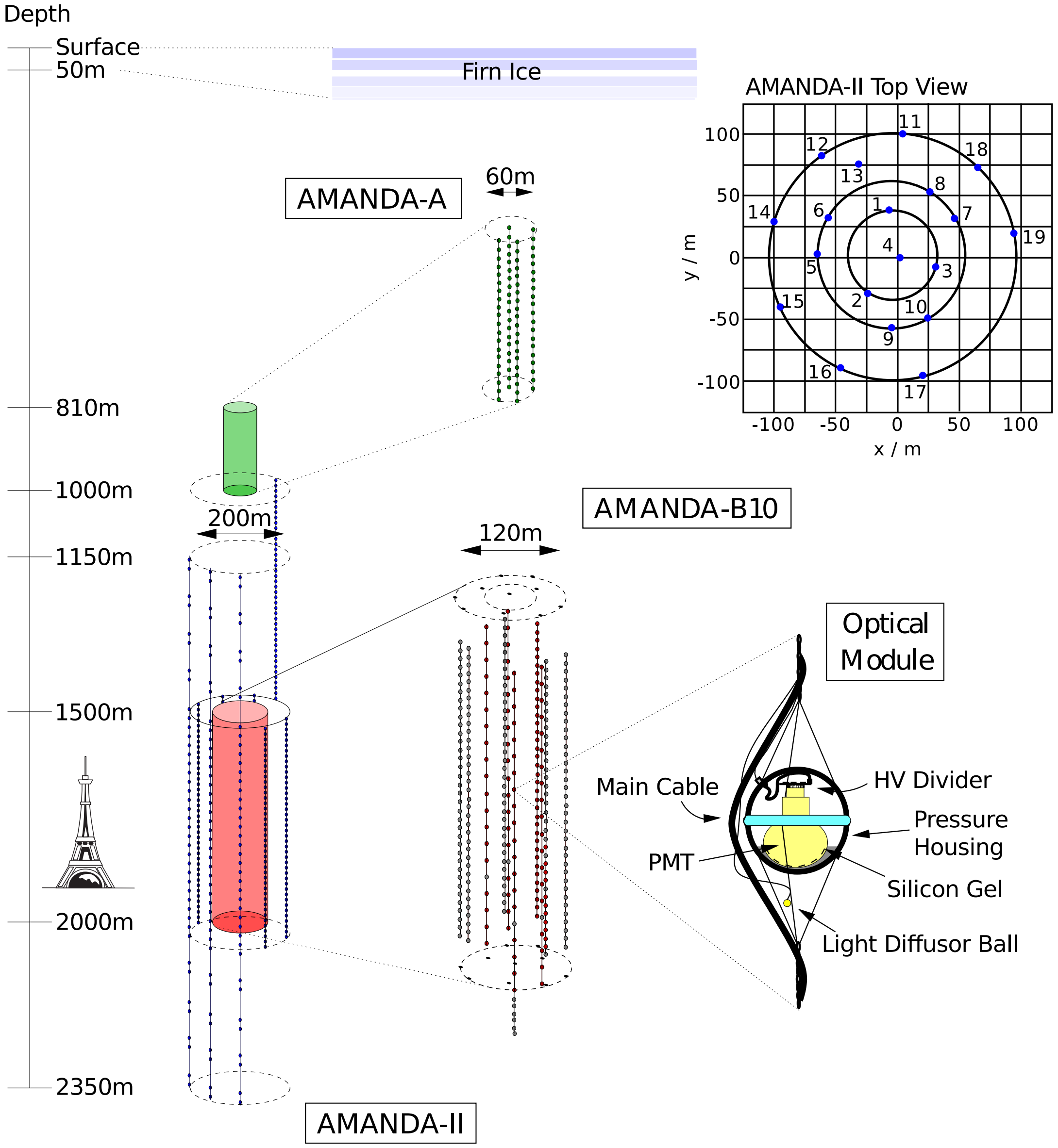

Figure 2.1: Schematic of the AMANDA detector, taken from [115] and slightly modified

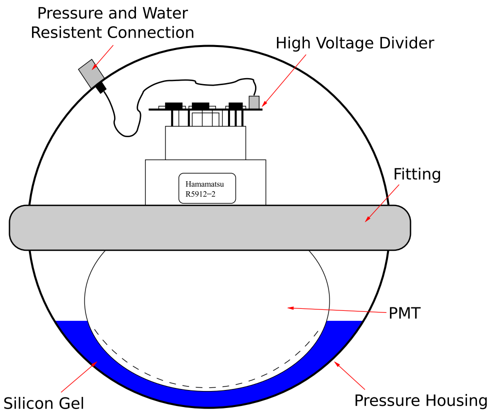

Figure 2.2: Schematic of an AMANDA OM, taken from [3] and slightly modified
The plug on the upper left of the schematic drawing provides the connection to the surface. It is also the Achilles' heel of the module. Water break-ins are most likely to happen here and the freezing process can damage this component. The wire rope holding the modules is attached to the fitting shown in the middle of the illustration.

The Optical Module (OM)

As stated before, the main components of a water Cherenkov telescope are the light sensors or PMTs. During deployment and later refreezing the optical module is exposed to extreme stress. The deepest sensors have to resist pressures of up to 250 bar and more during freezing. To resist the pressure and to protect the electronics, the 8 inch (20.3 cm) PMTs were encased into 12.5 mm thick glass spheres with materials chosen for their resistance as well as for their transparency and purity. The latter is especially important for supernova detection as already small traces of radioactive elements can significantly increase the dark noise rates. As mentioned above, three different glass types were used. When the collaboration switched from Billings to Benthos, the trade-off was between better transparency and higher radioactive contamination. While this substitution might have been worthwhile for track reconstruction, it was unfortunate for supernova detection. The reduced ^{40}K fraction of the B19 generation reduced the dark noise somewhat and lead to better supernova sensitivities for these modules.

Another important constituent of an optical module is a silicon gel that fixes the PMT and provides optical coupling between the sensor and its envelope. If the space between the glass sphere and the PMT were left empty, Fresnel losses[3] would have reduced the detection efficiency. The gel was chosen so that it remains viscous down to −93°C.

A schematic for an AMANDA optimal modules is shown in figure 2.2. More details on OMs can be found e.g. in [118, 119] and references therein.

---

[3] When light moves between media with different refractive indices, it is partially reflected on the transition regions. A clever choice of media can strongly reduce the losses.

2.1.2.2 IceCube

Due to the extensive experience collected during the construction of AMANDA, IceCube proceeded in a much more orderly fashion. The principle of the detector remains the same albeit with a few improvement mainly in the light sensors but also the installation planning. For AMANDA, the whole deployment phase, not counting the refreezing, took $\sim 7\,\mathrm{d}$ (e.g. string 16). In IceCube the strings can be installed in $\sim 2.5\,\mathrm{d}$.

Construction History

When finished, the main IceCube detector will feature 80 strings, placed at distances of $\sim 125\,\mathrm{m}$ and arranged in a hexagonal grid with light sensors at depths between $1450\,\mathrm{m} - 2450\,\mathrm{m}$. Each of these 80 strings holds 60 digital optical modules (DOMs) vertically placed in 17 m intervals. This spacing binds the detectable energy to be above $\sim 100\,\mathrm{GeV}$.

It was later decided to extend IceCube by a low energy extension called *DeepCore* which consists of six strings with 60 DOMs each. The first difference to the standard strings is the DOM spacing. Each string holds 10 modules at shallow depths between 1750 m and 1850 m and 50 between 2100 m and 2450 m at a 7 m spacing. The horizontal distance between the strings is $\sim 70\,\mathrm{m}$. Overall, this geometry lowers the muon detection threshold to $\sim 10\,\mathrm{GeV}$ [120]. For DeepCore, an improved PMT with higher quantum efficiency ($30\% \sim 40\%$ more compared to the standard DOMs) was chosen.

The deployment of IceCube started in the austral summer of 2004/05 with string 21. During the next season, this number was brought up to 9 and in 2006/07 to 22 strings, exceeding the whole AMANDA array. In 2007/08, 18 strings were installed, bringing the total to 40 and in 2008/09, 19 more were brought into the ice, among them the first DeepCore string. In 2009/10, the remaining 5 strings of the low energy extension were installed along with 15 additional standard strings. IceCube stands now at a total of 73+6 strings (IceCube+DeepCore) and will be completed during the upcoming season.

In addition to the in-ice setup, IceCube also features a surface array called *IceTop* aimed at cosmic ray air showers. It is made up of pairs of frozen water tanks, separated by $\sim 10\,\mathrm{m}$ and located $\sim 25\,\mathrm{m}$ around the top of each string. Their high noise rates make them uninteresting for the purpose of supernova detection.

Figure 2.3 shows a schematic of the IceCube array as of July 2010. For more detailed information on the detector, refer e.g. to [121, 93].

The Digital Optical Module (DOM)

In principle, the light sensors used in IceCube are the same as the ones integrated into AMANDA. However, they differ in important technical details.

The first and most striking distinction is the data handling. In AMANDA the PMTs sent their registered pulses directly to the surface where they were analyzed and processed. In IceCube this no longer holds true. Each IceCube module features

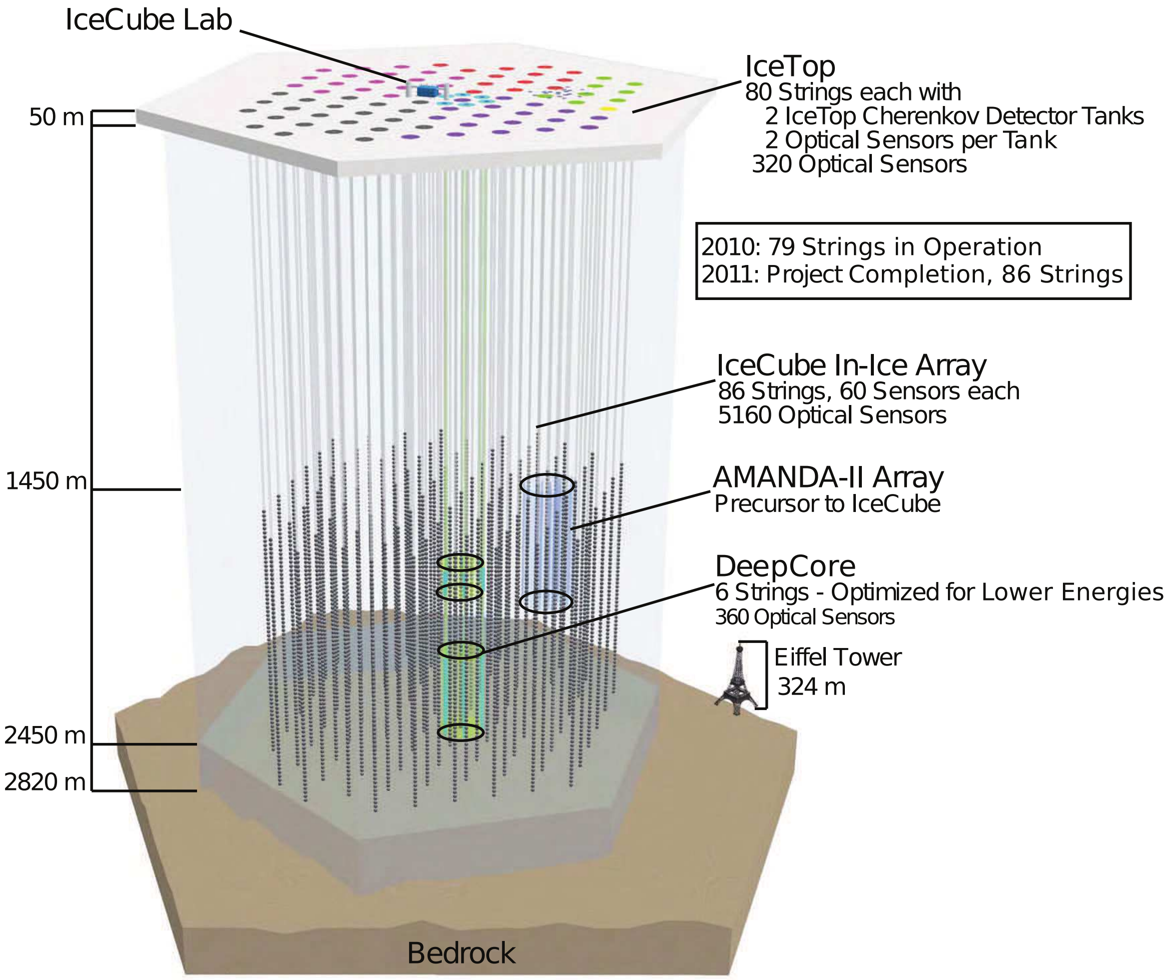

Figure 2.3: Schematic of the IceCube telescope, taken from [122] and slightly modified

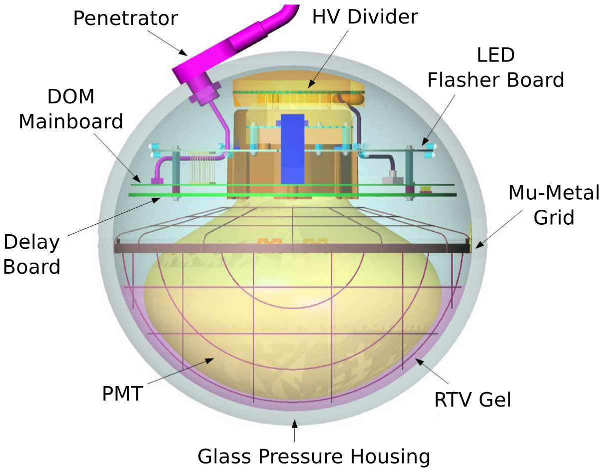

Figure 2.4: Schematic of an IceCube module, taken from [122]
In principle, an IceCube sensor is build the same as an AMANDA OM. Additional features are the electronics which digitize and preprocess the pulses, the flasher boards used for calibration purposes and the mu-metal mesh which is intended to shield the DOM from the ambient magnetic field of the Earth and its fluctuations. The HV divider transforms the incoming low voltage to the high voltage needed by the PMT.

an autonomous data acquisition and transmits the recorded data in digitized form. While this introduces a potential weakness in the module, this is more than offset by the absence of cross talk, electromagnetic interferences and pulse distortion on the way up. Furthermore, the introduction of local coincidence checks between neighboring DOMs becomes possible.

Second, larger PMTs with diameters of 10 inch (25.4 cm) have been used in IceCube. They are housed in glass spheres with a 13 inch (32 cm) diameter and 12.7 mm thickness. As stated before, the modules used in DeepCore are more efficient (30% $\sim$ 40% with respect to the standard DOMs [120]). The typical average dark noise rate of a standard IceCube DOM is $\sim$ 540 Hz. Each DOM is also equipped with a 12 on-board flasher LEDs which can emit predefined pulses of light and are used for calibration and verification tasks.

Third, the modules are only provided with low voltage (96 V) which is locally transformed to the high voltage necessary to power the PMT (1300 − 1500 V). This way, instabilities in the South Pole power plant do not transmit to the sensors.

Figure 2.4 shows a schematic drawing of an IceCube DOM. More details on the modules can be found e.g. in [93, 121, 123].

2.1.3 Neutrino Telescopes in Water

The first working neutrino telescope was set in the lake Baikal and is called *Baikal Deep Underwater Neutrino Telescope*. Construction was started in 1993 and finished in 1998. It sports 200 optical modules.

ANTARES (*Astronomy with a Neutrino Telescope and Abyss environmental RESearch*) has approximately the same size of AMANDA and is located in the Mediterranean Sea of the coast of Toulan in France. Its construction was finished in 2008, two years after deployment of the first string. It features 900 optical modules.

KM3NeT (*KM3 Neutrino Telescope*) will be the first km^3 neutrino detector constructed in water. In a way, it will be the northern cousin of IceCube. The technical design report has not been made public at the time of writing.

It has to be noted that of the neutrino telescopes discussed above, only AMANDA and IceCube are able to observe a supernova burst due to their low background noise rates. When constructed, KM3NeT may be able to identify supernovae in the Milky Way.

2.1.4 Neutrino Detectors Sensitive to Supernovae

The most prominent neutrino detector to be named at this point is *Super-Kamiokande.* Like Kamiokande-II, it is located in the Kamioka mine in Japan and consists of a large tank of 50000 t of water which was originally monitored by 11146 photomultipliers.

Similar in design was the *Sudbury Neutrino Observatory* (SNO). It consisted of 1000 t of heavy water, monitored by 9600 light sensors. It ran from 1999 to 2006 and is now being extended to SNO+, using a liquid scintillator as detection medium.

The BOREXino experiment is located at Gran Sasso and consists of a tank filled with 300 t liquid scintillator of the form $\mathrm{C_nH_{2n+2}}$. Its main goal is the study of the ^{7}Be neutrino flux from the sun.

A somewhat different setup has been used for the *Large Volume Detector* (LVD), also located in Gran Sasso. It consists of an array of 840 stainless steel tanks, sized $1.0 \times 1.0 \times 1.5\,\mathrm{m}^3$ and also filled with a liquid scintillator.

All of these experiments would be able to detect a neutrino burst from a supernova in the Milky Way. They are specifically set up for the detection of low energy neutrinos, making the determination of energy, flavor and even rough directionality possible. All detectors covered in this section, with the exception of SNO, contribute to the *Supernova Early Warning System* (SNEWS)[4].

2.2 Data Acquisition

As the amount of information produced by AMANDA and IceCube is very large, the data is reduced and only interesting events are stored. For AMANDA some, and for IceCube all the raw data has been saved to tapes which can be accessed in case of need.

---

[4] This network collects data from neutrino experiments and aims to alert the astronomical community to an upcoming supernova.

2.2.1 Muon Data Acquisition

As mentioned before, the main goal of neutrino telescopes is the reconstruction of muon tracks induced by neutrinos. To a lesser degree it can also be used to identify electromagnetic cascades induced by electron neutrinos, complex energy deposits typical for tau neutrinos or other signatures such as induced by e.g. magnetic monopoles. To this end, the arrival times of the Cherenkov front at the optical modules are recorded. Using different reconstruction methods, this information can be used to reconstruct the track of the charged particle. Note that unless the whole signature resides inside the detector only the local energy deposit can be ascertained.

The triggering conditions used for event storage are customizable. In AMANDA as well as IceCube the *multiplicity trigger* demanding a certain amount of PMT pulses within a preset time window is the main trigger.

One of the problems in identifying muon neutrino signatures is the atmospheric muon background. While most of the atmospheric radiation is shielded by the ice, highly energetic muons and muon bundles can still reach the detector array and induce light. Therefore, all neutrino telescopes try to reconstruct upward going tracks from particles having crossed the earth as only neutrinos or exotic particles can be expected from this direction. Unfortunately, the downgoing muons cannot always be distinguished from the upgoing tracks, even with complicated and computationally intensive filters. Most of the background in a neutrino search thus consists of misreconstructed atmospheric muons.

For more information on this topic, refer to e.g. [124, 117, 115] for AMANDA and [121, 125] for IceCube.

2.2.2 Supernova Data Acquisition (SNDAQ)

Supernova detection with a neutrino telescope is fundamentally different from the track reconstruction just described. The light sensors are too far apart to reconstruct the paths of charged leptons created by $\mathcal{O}(10\,\mathrm{MeV})$ neutrinos.

However, a supernova explosion within our galaxy would induce an intense burst of neutrinos crossing the ice and producing light. As the noise rates in AMANDA and IceCube are low, it becomes possible to identify the additional rate by using the optical modules not as separate units but as a large combined counter for coherent rate increase.

The principle is the same for both AMANDA and IceCube. The pulses are collected in scalers and sent to a computer where they are synchronized and combined. An analysis algorithm then extracts a collective rate increase by the method described in 4.1.1. If a significant number of pulses is seen in a predefined time window, we have a supernova candidate and the *Supernova Data AcQuisition* (SNDAQ) records the data in a finer time resolution and sends out alarms to the IceCube Collaboration as well as the SNEWS network. While the SNDAQ is essentially the same, the implementations are quite different for the two experiments.

AMANDA: In the AMANDA case, the pulses were counted on the surface and directly sent to an analysis computer which was independent of the standard data acquisition. The raw data was recorded in a 10 ms binning and rescaled to 0.5 s for real time analysis. If a supernova candidate was identified, it was stored in the 10 ms resolution; otherwise only the 0.5 s stream was kept. For more details on the data taking refer to [3] and for the analysis implemented in the SNDAQ refer to [73].

IceCube: For the IceCube array, the data pulses are recorded on the DOM itself and transmitted to the standard data acquisition. This provides a data file containing asynchronously counted pulses in 1.634 ms[5] from each DOM. The SNDAQ reads the file and rebins the rates to 2 ms to synchronize the data streams of the modules. From here on, the procedure is the same as it was for AMANDA with the exception that candidates are stored in 2 ms resolution. The raw files in 1.634 ms binning are archived on tape. More information on this system can be found in [93].

2.2.3 Artificial Dead Time

When looking at the background noise rates of the modules, it becomes apparent that $\sim 60\%$ of the pulses are correlated. Afterpulses up to 11 ms after the initial hits are due to gas ionization in the PMT. However, this is only one part of the picture as electrons or positrons created by radioactive decay traversing the glass with energies of $> 0.2\,\mathrm{MeV}$ can ionize or excite the respective atoms. This can entail consecutive photon emission, leading to delayed pulses.

Because it was assumed that this kind of correlation was restricted to noise pulses, it was decided to introduce an artificial dead time, suppressing the background relative to the expected signal. Extensive studies have been performed in [73, 126] for AMANDA, and an artificial dead time of $\sim 250\,\mu\mathrm{s}$ has been deemed optimal. A similar approach has been used for IceCube in [93]. However, recent examinations cast some doubt on the absence of afterpulses for signal hits. The upcoming thesis by T. Griesel [127] closely inspects the local coincidence data in which background plays little to no role. The studies indicate that signal pulses show a significant amount of correlation.

2.3 Low Energy Neutrino Detection in AMANDA/IceCube

We will now describe the processes which allow for the detection of low energy neutrinos.

2.3.1 Neutrino Interactions in the Ice

Since the detection principle is based on Cherenkov radiation, we are interested in reactions producing charged particles. For a detailed examination of the possible contributions refer e.g. to [128].

---

[5] This results from the size of the counter (2 bit) and the clock latency of 40 MHz.

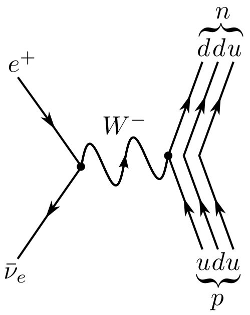

Figure 2.5: Feynman diagram of the inverse β^+ decay

As we will see below, the main rate stems from the electron anti-neutrinos. It is important to note that because of the energy scale involved in the supernova processes only electron neutrinos can interact via the charged current. The energies are just too low for the production of charged non-electron leptons.

2.3.1.1 Inverse β-Decay

The leading reaction channel for the neutrino detection by far, accounting for $\sim 96\%$ of the expected rate (using the model [35] and disregarding oscillations), is the inverse β-decay:

$$\bar{\nu}_e + p \longrightarrow n + e^+ \quad . \tag{2.1}$$

Figure 2.5 shows the corresponding Feynman diagram.

In the MeV range the calculation of the scattering matrix up to the third order is sufficient to reach an uncertainty smaller than 1%. A simple approximation for the cross section

$$\sigma(E_{\bar{\nu}_e}, E_{e^+}) = |\vec{p}_{e^+}|\, E_{e^+}\, E_{\bar{\nu}_e}^{-0.07056 + 0.02018 \ln E_{\bar{\nu}_e} - 0.001953 \ln^3 E_{\bar{\nu}_e}} \times 10^{-47}\,\mathrm{m}^2 \tag{2.2}$$

has been found to match this precision for neutrinos energies $E_{\bar{\nu}_e} \lesssim 300\,\mathrm{MeV}$ [129]. For the calculation of the rate, we will need the differential form of the cross section

$$\frac{\mathrm{d}}{\mathrm{d}E_{e^+}} \sigma(E_{\bar{\nu}_e}, E_{e^+}) = \sigma(E_{\bar{\nu}_e}, E_{e^+})\, \delta(E_{e^+} - \langle E_{e^+} \rangle) \quad . \tag{2.3}$$

The energy of the positron E_{e^+} and thus the respective momentum $|\vec{p}_{e^+}| = \sqrt{(E_{e^+}^2 - m_e^2)}$ is not discrete but has a continuous spectrum. Its mean energy can be derived to be

$$\langle E_{e^+} \rangle \approx (E_{\bar{\nu}_e} - \delta) \left(1 - \frac{E_{\bar{\nu}_e}}{E_{\bar{\nu}_e} + m_p}\right) \tag{2.4}$$

with the proton mass m_p, the electron mass m_e, the neutron mass m_n and

$$\delta = \frac{m_n^2 - m_p^2 - m_e^2}{2m_p} \quad . \tag{2.5}$$

Neutron Capture

The neutron produced by the inverse β-decay is quickly reabsorbed in ice. For thermal energies, neutron capture in water is dominated by reactions on hydrogen [130]:

$$n \, + \, {}^1\mathrm{H} \longrightarrow {}^2\mathrm{H} \, + \, \gamma \quad . \tag{2.6}$$

The reaction emits a photon with an energy of 2.225 MeV (the binding energy of the deuterium nucleus). When the photon travels through ice, it can undergo Compton scattering thereby inducing a relativistic electron whose energy follows the distribution [131]

$$\begin{aligned} p(E_{e^-}) \quad \sim \quad & (E_\gamma - E_{e^-})^{-2} E_\gamma^{-2} \\ & -(2 + 2\frac{E_\gamma}{m_e} - \frac{E_\gamma^2}{m_e^2})(E_\gamma - E_{e^-})^{-1} E_\gamma^{-3} \\ & + \left(1 + \frac{E_\gamma}{m_e}\right)^2 E_\gamma^{-4} \; - \; m_e^{-2} E_\gamma^{-3} E_{e^-} \quad . \end{aligned} \tag{2.7}$$

Just as the positrons from inverse β-decay, this electron will produce light. With the above energy distribution, it will be possible to estimate the photon production from neutron capture in section 2.4.3.1.

2.3.1.2 Electron Scattering

An additional contribution to the neutrino signal ($\sim 3\%$ for model [35] disregarding oscillations) is caused by the scattering of neutrinos on electrons in ice:

$$\overset{(-)}{\nu}_\alpha \, + e^- \longrightarrow e^- \, + \, \overset{(-)}{\nu}_\alpha \quad . \tag{2.8}$$

Figures 2.6 show the processes that have to be taken into account for the scattering on electrons.

For ν_e and $\bar{\nu}_e$, this reaction can be mediated by the charged as well as the neutral current. In the cases $\alpha = \mu, \tau$, only the neutral current can contribute as the weak force conserves the lepton number.

Under the assumption of momentum transfer $\ll m^2_{W^\pm, Z^0}$, the differential cross section in the leading order looks as follows [132]:

$$\frac{\mathrm{d}}{\mathrm{d}y} \sigma_{\nu(e^-,e^-)\nu}(E_\nu, E_e) = \frac{2G_\mathrm{F}^2 m_e E_\nu}{\pi} \left(\varepsilon_\mp^2 + \varepsilon_\pm^2 (1-y)^2 - \varepsilon_+ \varepsilon_- \frac{m_e}{E_\nu} y \right) \tag{2.9}$$

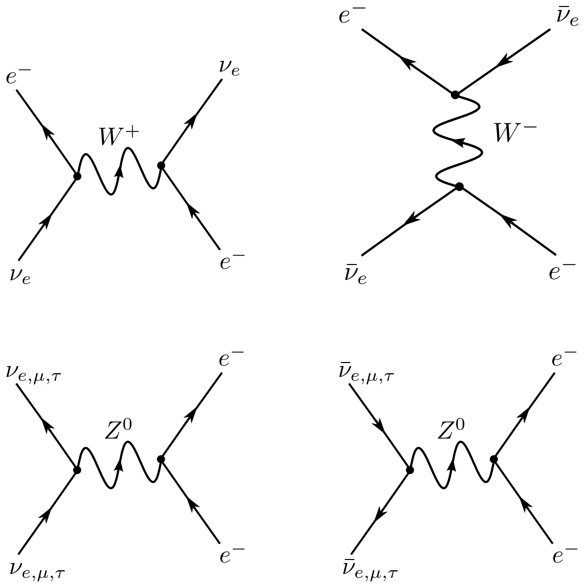

Figure 2.6: Feynman diagrams for the scattering of neutrinos on electrons

with $y = (E_e - m_e)/E_\nu$ and $0 \leq y \leq y_{\text{max}} = (1 + \frac{m_e}{2E_\nu})^{-1}$. The upper index on the ε stands for neutrino the lower one for anti-neutrino interactions, respectively. They are defined as

$$\varepsilon_+ = -\sin^2\theta_\text{W} \tag{2.10}$$

and

$$\varepsilon_- = \begin{cases} -\frac{1}{2} - \sin^2\theta_\text{W} & \text{for electron neutrinos} \\ \frac{1}{2} - \sin^2\theta_\text{W} & \text{for non-electron neutrinos} \quad . \end{cases} \tag{2.11}$$

Radiative corrections can be neglected at these energies as they only rise above $\sim 1\%$ at $\mathcal{O}(\text{GeV})$ [132].

2.3.1.3 Interaction with Oxygen

All interactions with ^{16}O contribute to the overall rate by $\sim 1\%$ (for model [35] disregarding oscillations). Of these, the most relevant reactions for the neutrino detection in a water Cherenkov telescope are the inverse β^+ and β^- decays (see figures 2.5 and 2.7):

$$\begin{aligned} \nu_e + \text{O} &\longrightarrow \text{X} + e^- \quad \text{and} \\ \bar{\nu}_e + \text{O} &\longrightarrow \text{X} + e^+ \quad . \end{aligned} \tag{2.12}$$

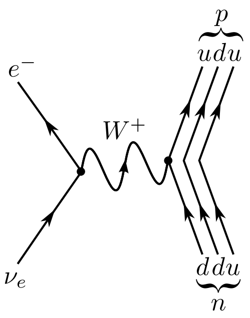

Figure 2.7: Feynman diagram of the inverse β^- decay

The most prominent interaction channels of neutrinos on ^{16}O have been calculated in [133] and it was found in [134] that $\nu_e(^{16}\mathrm{O}, \mathrm{X})e^-$ can approximately be described by the function

$$\sigma_{\nu_e(^{16}\mathrm{O},\mathrm{X})e^-} = 4.7 \cdot 10^{-44}\,\mathrm{m}^2 \left[\left(\frac{E_{\nu_e}}{\mathrm{MeV}} \right)^{0.25} - 15^{\,0.25} \right]^6 \quad . \tag{2.13}$$

For the energy threshold of these reactions we assume 15.4 MeV as given in [128] for the subreaction $\nu_e(^{16}\mathrm{O}, ^{16}\mathrm{F})e^-$.

As no analytic formula or fit for $\bar{\nu}_e(^{16}\mathrm{O}, \mathrm{X})e^+$ was found in the literature, the data from [133] was fitted by the author (see figure 2.8). The resulting function is

$$\sigma_{\bar{\nu}_e(^{16}\mathrm{O},\mathrm{X})e^+} = 2.1 \cdot 10^{-44}\,\mathrm{m}^2 \times \begin{cases} \left[\left(\frac{E_{\bar{\nu}_e}}{\mathrm{MeV}} \right)^{0.22} - 8.4^{\,0.22} \right]^{6.8}, & \text{for} \quad E_{\bar{\nu}_e} < 42.3\,\mathrm{MeV} \\ \left[\left(\frac{E_{\bar{\nu}_e}}{\mathrm{MeV}} \right)^{0.26} - 16.8^{\,0.26} \right]^{4.2}, & \text{for} \quad E_{\bar{\nu}_e} \geq 42.3\,\mathrm{MeV} \quad . \end{cases} \tag{2.14}$$

As energy threshold for all these reactions we assume 11.4 MeV as given in [128] for the subreaction $\bar{\nu}_e(^{16}\mathrm{O}, ^{16}\mathrm{N})e^+$.

For the lepton energy, we assume the initial neutrino energy minus the reaction threshold.

The uncertainty in the oxygen cross section is rather large and estimated to $\sim 30\%$ [135]. Charged current reactions on other isotopes like ^{18}O, ^{17}O and deuterium ($\sim 10\%$ of the total oxygen cross section) are not accounted for. Note that neutral current interactions on ^{16}O might be quite important, possibly increasing the light oxygen reactions by $3 \sim 4$ times. Because this would raise the detection efficiency for electron neutrinos and thus might facilitate the detection of the deleptonization burst, efforts to include these reactions in the simulation are currently ongoing.

The energy dependent cross sections discussed in the above section are shown in figure 2.9.

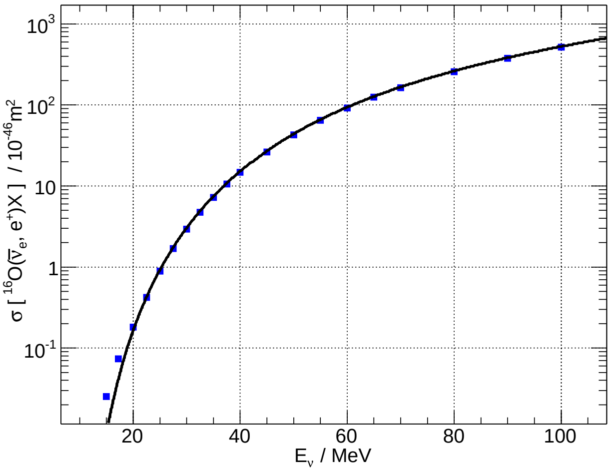

Figure 2.8: Cross section of $\bar{\nu}_e(^{16}\mathrm{O}, \mathrm{X})e^+$
The cross sections for $\bar{\nu}_e(^{16}O, ^{16}N)e^+$ *as calculated in [133] are shown as blue squares and the fit with function 2.14 as a black line.*

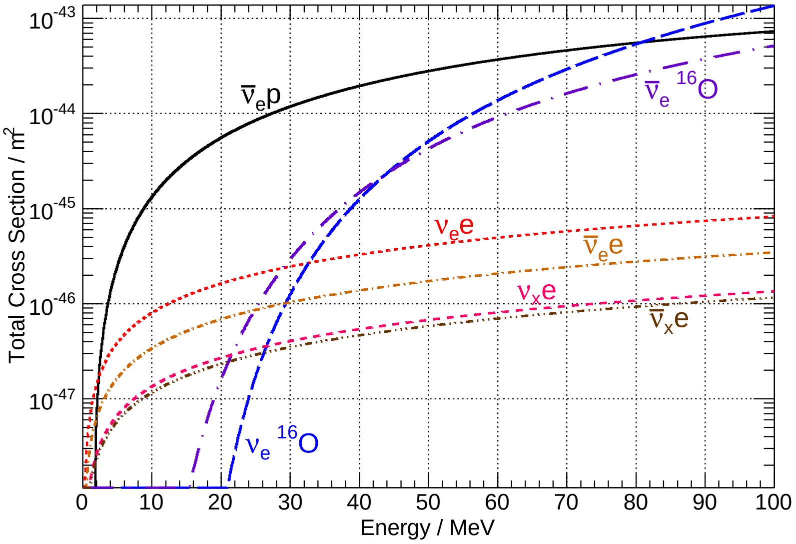

Figure 2.9: Neutrino interaction cross sections in the ice
The figure shows the cross section for the interaction of a single (anti-)neutrino with an H_2O *molecule. The values are scaled to the number of targets and* ν_x *stands for all non-electron flavor neutrinos.*

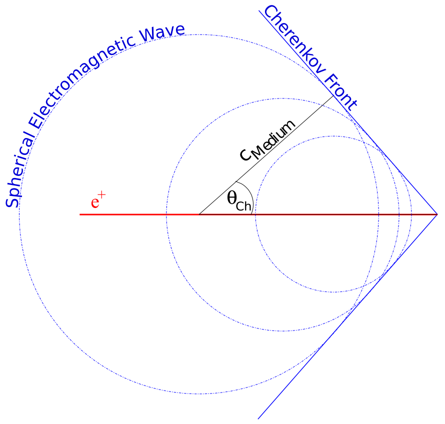

Figure 2.10: Schematic representation of the Cherenkov effect

2.3.2 Cherenkov Effect

While traversing a dielectric medium, a charged particle polarizes the surrounding atoms and/or molecules, leading to the emission of electromagnetic waves. If the charged particle travels faster than the *phase speed* of light of the medium, the waves overlap constructively under a characteristic emission angle of $\cos\theta_c = [\beta\, n(\lambda)]^{-1}$.

Here, c is the vacuum phase velocity of light, βc the speed of the particle and $n(\lambda)$ the refraction index which depends on the wavelength λ. Figure 2.10 illustrates the Cherenkov effect. In order to produce light the particle has to exceed the threshold $\beta_{\text{thr}} = 1/n(\lambda)$. With a refraction index of $n_{\text{ice}} = 1.3195$ at $\lambda = 400\,\text{nm}$ [136], this sets a minimum total energy for electrons in ice of $0.783\,\text{MeV}$.

The photons are emitted with a spectrum described by the Frank–Tamm formula:

$$\frac{\mathrm{d}N}{\mathrm{d}x\mathrm{d}\lambda} = \frac{2\pi\alpha}{\lambda^2}\left(1 - \frac{1}{\beta^2 n(\lambda)^2}\right) \quad . \tag{2.15}$$

$\mathrm{d}N$ is the number of photons emitted in a wavelength interval of $\mathrm{d}\lambda$ over a distance $\mathrm{d}x$. $\alpha \approx 1/137$ is the fine structure constant.

2.4 Signal Estimation

2.4.1 Effective Volume for Photon Detection

One of the most important ingredients for the estimation of a signal induced by supernova neutrinos is the effective volume for photons, V_{eff}^{γ}. Naively, it tells us in which volume a photon needs to be produced to be detected by an optical module. It is derived from the probability P to detect a photon depending on the distance $\vec{\rho}$ between light source and sensor and module acceptance $\mathfrak{a}$:

$$V_{\text{eff}}^{\gamma}(\vec{\rho}) = \int\int\int P^{\gamma}(\vec{\rho}, \mathfrak{a})\mathrm{d}V = 4\pi \int_0^{\infty} P^{\gamma}(\rho, \mathfrak{a})\rho^2 \mathrm{d}\rho \quad . \tag{2.16}$$

In the second step, we made the assumption of spherical symmetry for the detection probability which is not strictly true. However, for the case of supernova detection, we are interested in the mean signal increase and are thus able to account for the non-uniformity by using a sensor acceptance averaged over the detection angle. To determine an effective volume for photon detection, knowledge of the properties of antarctic ice and the DOM response is of paramount importance. Because the necessary inputs cannot be described analytically, the effective volume was determined with simulations as delineated in the following section.

2.4.1.1 Ice Properties

The AMANDA/IceCube Collaboration has developed a software package called Photonics which describes the propagation of photons from source to sensor [137].

Properties of Bulk Ice:

The bulk ice is the pristine glacial ice covering most of Antarctica. At the depths where the optical modules are placed, air bubbles are no longer a problem. In hundreds of millennia they have formed an air hydrate phase[6] nearly perfectly matching the refractive index of the ice. The main cause for scattering are dust molecules that accumulated over the past ages[7].

To get a handle on the ice properties, extensive measurements have been performed by the AMANDA/IceCube Collaboration. Light sources were embedded in the AMANDA telescope to emit well-defined photon bundles and their detection signatures were examined [139]. In IceCube each DOM has a *flasher board* capable of lighting up the detector and providing three dimensional information on light propagation in ice. These measurements were taken one step further with a *dust logger* shown schematically in figure 2.11 (for more details see [140]). Using this information, it was possible to map the absorption and scattering coefficients of the ice.

The IceCube detector extends over prominent dust layers, the one at 2050 m depth being the most pronounced. Figure 2.12 shows the coefficients describing the ice. Both are essential to describe the propagation of light in the detector.

Ice in the Drill Hole

A further complication is the ice in the drill hole. Contrary to the ambient bulk ice, it consists of water that has only just been frozen and retains many more bubbles; it has a much higher scattering coefficient than the ambient ice. Extensive analyses have been performed (see [141]) and the results have been implemented in *Photonics.*

---

[6] In this phase the gas molecule are trapped within the crystalline ice. For light, air hydrate and ice are nearly indistinguishable.

[7] They originate from Earth's deserts and volcanic activities and were carried to the deep south by strong winds in the upper atmosphere [138].

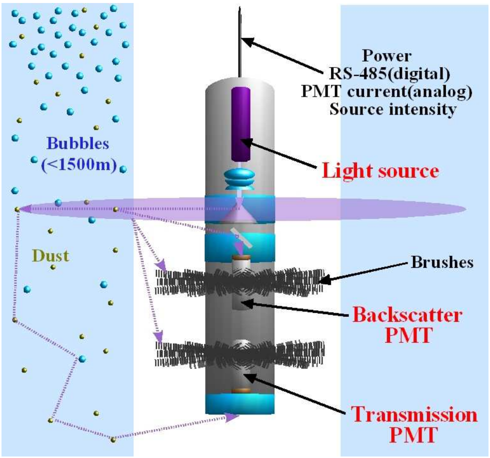

Figure 2.11: Schematic view of a dust logger in use
The figure, taken from [140], shows a dust logger in a drill hole. It sends out light into the ice, perpendicular to its axis. Light sensors in the device measure the photons reflected by back scattering off the ice or scattering on the dust particles and bubbles in the ice. Brushes keep the light from directly reaching the respective PMTs. Using the time and intensity differences between emitted and collected light, the dust and bubble concentrations can be extrapolated.

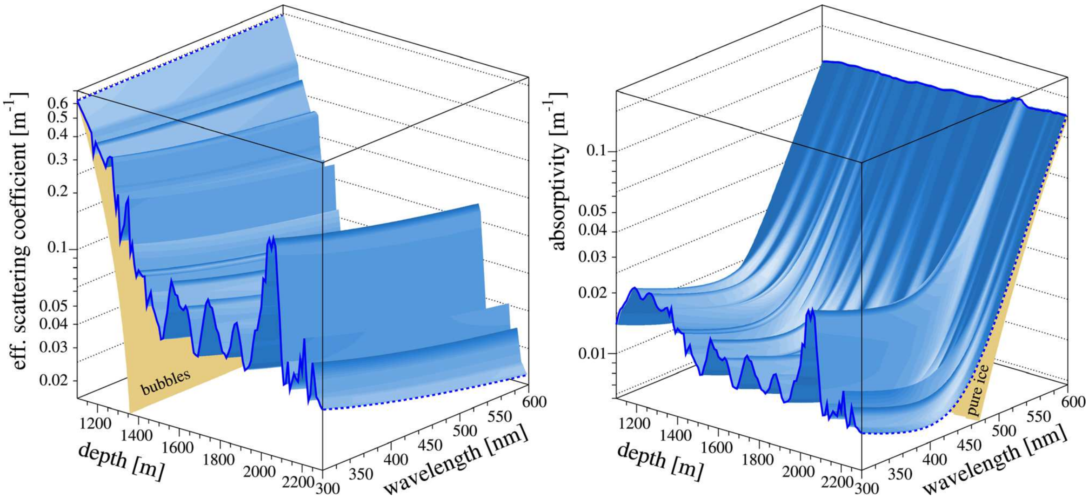

Figure 2.12: Properties of the deep ice at South Pole [139]

2.4.1.2 DOM Properties

As the state-of-the-art simulations are performed using the IceCube modules, we will focus on their properties and derive the conversion factors for AMANDA modules in section 4.5.

The simulation package used in the collaboration to generate the DOM response, ROMEO [142], includes the PMT quantum efficiencies, the detection threshold for photo electrons and the transmittances of glass and gel.

2.4.1.3 Photonics Result

To determine the effective volume for photons, light induced by 10 GeV muons (equivalent light production as $\mathcal{O}(10\,\mathrm{MeV})$ electrons) were generated. Propagation of the photons was then tracked with *Photonics* and the sensor response simulated using ROMEO [143]. The depth dependent results are shown in figure 2.13.

For the calculations in this thesis, we will use the mean effective volume as derived with the actual ice model *AHA* in 20 m resolution [144]:

$$V^{\gamma}_{\mathrm{eff,I3}} = 0.1575\,\mathrm{m}^3 \quad . \tag{2.17}$$

The error on the mean of 2% contributes to the systematics. Further sources of uncertainty are the hole ice ($\sim 1\%$) and the bulk ice properties ($\sim 6\%$) as well as the finite binning in *Photonics* ($\sim 1\%$) and the DOM sensitivity ($\sim 10\%$). Furthermore, there exists no consensus on how much signal is masked by DOM cables. The effects vary by $\sim 3\%$ in the simulations which we take as another uncertainty. Investigations to lower these uncertainties are ongoing. Pooling all of the above together, we arrive at a total of $\sim 12\%$. More details on the systematics can be found in [145].

2.4.2 Light Yield of an Electron/Positron

During its propagation through the ice, an electron or positron carrying $1\,\mathrm{MeV} \sim 100\,\mathrm{MeV}$ loses its energy mainly to ionization and bremsstrahlung, creating delta electrons and photons. The light quanta interact dominantly through Compton scattering, photo effect and pair production.

When trying to determine the light yield of an electron or positron, one has to take into account all of the above reactions and the resulting particles (e.g. the photons from positron annihilation). Charged secondary particles can produce Cherenkov light just as well as the initial lepton. In [73], a GEANT4 based simulation was written to solve this problem and a linear correlation between the distance the charged leptons travel while being above the Cherenkov threshold and the initial mean kinetic energy was found (see figure 2.14).

The relationship was determined to be [73]

$$d(E_{e^+}) = (0.577 \pm 0.005)\frac{\mathrm{cm}}{\mathrm{MeV}} \cdot \Theta(E_{e^+} - E_{\mathrm{ch}}) \cdot (E_{e^+} - E_{\mathrm{ch}}) \tag{2.18}$$

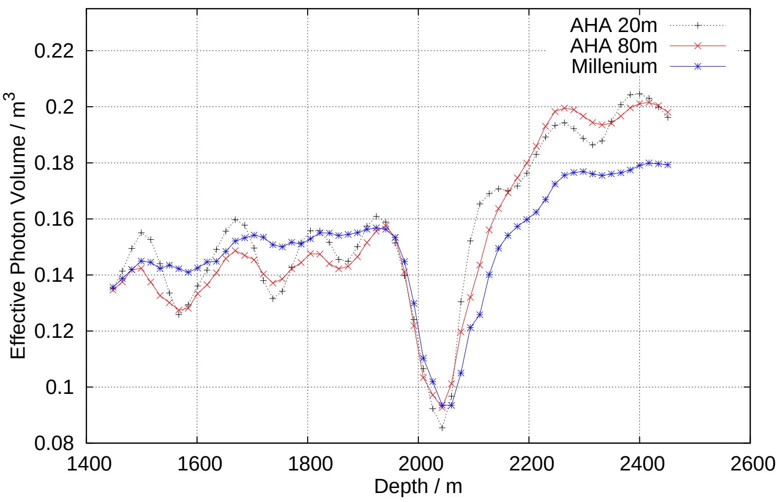

Figure 2.13: Effective volume for photon detection
The depth dependent effective volumes were calculated using two different ice models; the most recent (the AHA model [144]) is displayed in two different resolutions of the ice properties. One can easily distinguish the dust layers where the effective volumes drop. The simulation results include -25% *to take into account differences between deployed and testing modules, shadowing effects caused by cables and* μ*-metal mesh* (-10%) *and the detection threshold for photo electrons* (-15%)*. Efficiency losses due to reduced sensitivity at the PMT edges are not yet included as investigations are still ongoing.*

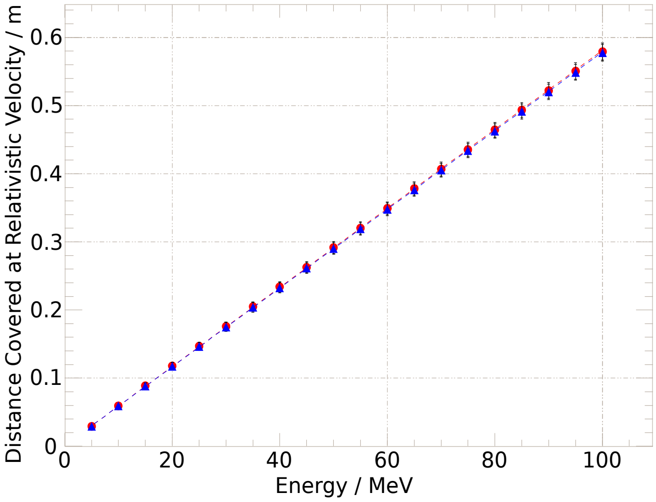

Figure 2.14: Distance covered above Cherenkov threshold
The figure shows the distance an electron (blue circles) or a positron (red triangles) covers while producing Cherenkov photons in function of its kinetic energy. Both have been fitted with a straight line in [73].

with the Cherenkov threshold E_{ch}. For electrons, the factor is slightly larger with $(0.580 \pm 0.005)\frac{\mathrm{cm}}{\mathrm{MeV}}$. Comparisons between GEANT4 and ESTAR as well as the intrinsic cross section uncertainties place the systematic error at $\lesssim 5\%$ [145]. Note that the simulation was only run for leptons with kinetic energies above 1 MeV, and consequently, the behavior close to the Cherenkov threshold is unclear. However, as leptons with these low energies contribute little to the signal, the overall uncertainty due to the linear extrapolation is of the order of $\sim 1\%$.

With the formula for the Cherenkov radiation given in equation 2.15 and the assumption $\beta \approx 1$, one can determine the number of photons with wavelengths between 300 nm − 600 nm produced per positron:

$$N_{\gamma_C} = (187.7 \pm 1.7)\frac{1}{\mathrm{MeV}} \cdot \Theta(E_{e^+} - E_{\mathrm{ch}}) \cdot (E_{e^+} - E_{\mathrm{ch}}) \quad . \tag{2.19}$$

From the effective volume for photon detection (see equation 2.17) and the number of photons produced by a lepton, we can easily derive the detection efficiency for an electron or positron by making a few assumptions. First, we take the probability for a sensor to be hit more than one photon from the same source as zero. In most datasets this is trivially true, because an artificial dead time $\tau \geq 8\,\mu\mathrm{s}$ is applied. For the remaining data, this case can still be neglected since the probability to detect two or more photons from the same source is more than one order of magnitude smaller than the probability for the detection of a single photon, even below distances of one meter. Second, we assume that the effective volumes do not overlap. For a typical case of a 15 MeV positron, the maximal probability for two modules to detect light from the same source is $2 \cdot 10^{-5}$ (for more details refer to [127]).

When combining equation 2.17 with 2.19, the effective volume for positron detection can be determined to

$$\begin{aligned} V^{e^\pm}_{\mathrm{eff,I3}}(E_{e^\pm}) &= V^{e^\pm}_{\mathrm{eff,0}} \cdot \Theta(E_{e^\pm} - E_{\mathrm{ch}}) \cdot (E_{e^\pm} - E_{\mathrm{ch}}) \quad \text{with} \\ V^{e^+}_{\mathrm{eff,0}} &= (29.6 \pm 0.7 \pm 3.8)\,\frac{\mathrm{m}^3}{\mathrm{MeV}} \end{aligned} \tag{2.20}$$

The systematic uncertainty of 13% is derived by combining all uncertainties from DOM description, ice model (see section 2.4.1.3) and lepton propagation.

2.4.3 Expected Rate

To estimate the rate increase expected for a supernova neutrino burst, we need the neutrino flux emitted by the star Φ_ν, the energy dependent differential cross sections $\frac{\mathrm{d}}{\mathrm{d}E_e}\sigma(E_\nu, E_e)$ and the energy distribution of the neutrinos $f_\nu(E_\nu)$. These inputs have to be combined and integrated, first, over the possible electron/positron energies to weight the effective volume with the electron/positron spectrum and second, over the neutrino energies accounting for the spectra emitted from the supernova. For the rate seen by a single optical module we obtain

$$R = n_{\text{ice}}\, \Phi_\nu \int_{E_{\text{thr}}}^{\infty} \mathrm{d}E_\nu f_\nu(E_\nu) \int_0^\infty \mathrm{d}E_{e^\pm} \frac{\mathrm{d}}{\mathrm{d}E_{e^\pm}} \sigma(E_\nu, E_{e^\pm})\, V_{\text{eff,I3}}^{e^\pm}(E_{e^\pm}) \tag{2.21}$$

with E_{thr} being the energy threshold for the reaction.

We now separately consider the contributions for each interaction.

2.4.3.1 Inverse β-Decay

We insert the differential cross section 2.3 in 2.21 and obtain

$$R_{\bar{\nu}_e(p,n)e^+} = n_{\text{ice}}\, \Phi_{\bar{\nu}_e} \int_{E_{\text{thr}}}^{\infty} f_{\bar{\nu}_e}(E_{\bar{\nu}_e})\, \sigma_{\bar{\nu}_e(p,n)e^+}(E_{\bar{\nu}_e}, \langle E_{e^+} \rangle)\, V_{\text{eff,I3}}^{e^+}(\langle E_{e^+} \rangle)\, \mathrm{d}E_{\bar{\nu}_e} \tag{2.22}$$

with the mean positron energy $\langle E_{e^+} \rangle$ as given in equation 2.4.

The electron anti-neutrino spectrum and the energy dependent cross sections are multiplied and integrated numerically. We thus avoid a restriction to analytical spectral functions and further allow for the incorporation of neutrino oscillations which alter the shape of the spectrum (e.g. the spectral split due to collective oscillations considered in section 1.2.4.3).

Neutron Capture

We assume that each neutron produced in an inverse β-decay leads to a capture process on a ^{1}H atom, emitting a gamma with 2.225 MeV which in turn transfers a significant amount of energy to an electron. With the energy distribution from equation 2.7, the derivation of the mean energy is straightforward. However, we need to account for the Cherenkov threshold E_{ch} as electrons below will not produce light. First, we derive the mean energy the electron carries while producing Cherenkov photons:

$$\langle E_{e^-} \rangle_{\text{ch}} = \int_{E_{\text{ch}}}^{\infty} p(E_{e^-})\, (E_{e^-} - E_{\text{ch}})\, \mathrm{d}E_{e^-} \quad . \tag{2.23}$$

Not all electrons will be scattered in this energy interval. It is therefore necessary to derive the ratio above the threshold:

$$\epsilon = \frac{\int_{E_{\text{ch}}}^{\infty} p(E_{e^-})\, \mathrm{d}E_{e^-}}{\int_0^\infty p(E_{e^-})\, \mathrm{d}E_{e^-}} \quad . \tag{2.24}$$

Knowing the mean kinetic energy above the Cherenkov threshold and the ratio of relevant electrons, the effective average energy for the detection can be determined to be

$$E_{e^-,\text{eff}} = \epsilon\, \langle E_{e^-} \rangle_{\text{ch}} \quad . \tag{2.25}$$

Note that this estimation only works because the photon production is linearly dependent on particle energy (see equation 2.19). For the case of a photon with 2.225 MeV we determine

$$\langle E_{e^-} \rangle_{\mathrm{ch}} = 1.057\,\mathrm{MeV} \quad \text{and} \quad \epsilon = 0.899 \quad . \tag{2.26}$$

The weighted mean kinetic energy is:

$$E_{e^-,\mathrm{eff}} = 0.951\,\mathrm{MeV} \quad . \tag{2.27}$$

In the simulation this value can simply be added to the total energy of the positron from inverse β-decay.

We estimate the total uncertainty on the light production of neutron capture to be $\sim 10\%$. As it contributes only slightly to the light production of a supernova burst ($< 10\%$), it does not increase the overall error of $\sim 1\%$ on the light from inverse beta decay.

2.4.3.2 Electron Scattering

In case of neutrino-electron scattering, the situation is more complicated. The differential cross section given in equation 2.9 is not linearly dependent on the electron energy [132].

Let us consider the integral over the electron energies:

$$\int_{E_{\mathrm{ch}}}^{\infty} \frac{\mathrm{d}y}{\mathrm{d}E_{e^-}} \frac{\mathrm{d}}{\mathrm{d}y} \sigma_{\nu(e^-,e^-)\nu}(E_\nu, E_e)(E_\nu, y)\,(E_{e^-} - E_{\mathrm{ch}})\,\mathrm{d}E_{e^-} \quad . \tag{2.28}$$

We used ν to represent all neutrino and anti-neutrino flavors.

As $y = (E_e - m_e)/E_\nu$, we can insert $E_{e^-} = yE_\nu + m_e$ and $\mathrm{d}y/\mathrm{d}E_{e^-} = 1/E_{e^-}$. y is restrained within $y_{\mathrm{ch}} \leq y \leq y_{\max} = (1 + \frac{m_e}{2E_\nu})^{-1}$ with $y_{\mathrm{ch}} \geq 0$. The integral transforms to

$$\int_{y_{\mathrm{ch}}}^{y_{\max}} \frac{\mathrm{d}}{\mathrm{d}y} \sigma_{\nu(e^-,e^-)\nu}(E_\nu, E_e)(E_\nu, y)\,(y - y_{\mathrm{ch}})E_\nu\,\mathrm{d}y \quad . \tag{2.29}$$

For now, we discard the coefficients and perform the integral

$$\int_{y_{\mathrm{ch}}}^{y_{\max}} \left(\varepsilon_\mp^2 + \varepsilon_\pm^2 (1-y)^2 - \varepsilon_+ \varepsilon_- \frac{m_e}{E_\nu} y \right) (y - y_{\mathrm{ch}})E_\nu\,\mathrm{d}y \quad . \tag{2.30}$$

The integration is pretty straightforward and results in

$$\begin{aligned} \int \ldots \; = \; & \left[\frac{y^4}{4} \varepsilon_\pm^2 - \frac{y^3}{3} \left(2\varepsilon_\pm^2 + \varepsilon_+ \varepsilon_- \frac{m_e}{E_\nu} + \varepsilon_\pm^2 y_{\mathrm{ch}} \right) \right. \\ & + \frac{y^2}{2} \left(\varepsilon_\mp^2 + \varepsilon_\pm^2 + 2\varepsilon_\pm^2 y_{\mathrm{ch}} + \varepsilon_+ \varepsilon_- \frac{m_e}{E_\nu} y_{\mathrm{ch}} \right) \\ & \left. - y \left((\varepsilon_\pm^2 + \varepsilon_\mp^2) y_{\mathrm{ch}} \right) \right]_{y_{\mathrm{ch}}}^{y_{\max}} E_\nu \quad . \end{aligned} \tag{2.31}$$

As above, the rate increase of a single OM is derived to be

$$R_{\nu(e,e)\nu} = n_{\text{ice}} V^{e^-}_{\text{eff},0}\, \Phi_\nu \int_0^\infty \mathrm{d}E_\nu\, f_{\bar{\nu}_e}(E_{\bar{\nu}_e})\, \frac{2G_{\text{F}}^2 m_e E_\nu}{\pi} \int \ldots \quad . \tag{2.32}$$

2.4.3.3 Interaction with Oxygen

The energy of the lepton resulting from the interaction E_e is taken to be discrete and the differential cross section is approximated in the same way as done in equation 2.3 for the inverse β-decay. We insert the mean positron energy instead of the whole spectrum and estimate the rate to be

$$R_{\nu(O,X)e} = n_{\text{ice}} V^{e}_{\text{eff},0}\, \Phi_\nu \int_{E_{\text{thr}}}^\infty f_\nu(E_\nu)\, \sigma_{\nu(O,X)e}(E_\nu, \langle E_e \rangle)\, (E_\nu - E_{\text{thr}} - E_{\text{ch}})\, \mathrm{d}E_\nu \quad . \tag{2.33}$$

2.4.4 SN 1987a

In previous works [73, 146, 114] the signal recorded from the supernova 1987a has been used as data based estimate for a signal. We will do the same in this section.

Kamiokande-II recorded $N_{\text{KII}} = 11$ positrons in a time span of 15 s. As the inverse β-decay is by far the most important reaction type and all detected leptons were positrons, we disregard other possibilities. To rescale the signal of SN 1987A to the rate increase seen by an AMANDA/IceCube OM in the case of a supernova at distance d, we compare the expected event rates and then modify them by the supernova distance:

$$N_{\text{AII/I3}} = N_{\text{KII}}\, \frac{R_{\bar{\nu}_e(p,n)e^+,\text{AII/I3}}}{R_{\bar{\nu}_e(p,n)e^+,\text{KII}}} \left(\frac{d_{52\,\text{kpc}}}{d} \right)^2 \quad . \tag{2.34}$$

To correctly reweight the events to AMANDA/IceCube, one has to take into account the neutrino energy spectrum and the trigger efficiency of Kamiokande. The estimated rate increase due to inverse β-decay for an AMANDA/IceCube OM is given by equation 2.22. For the case of Kamiokande-II, one has to modify the approach because the effective volume for detection of charged leptons is not linearly dependent on the energy but proportional to Kamiokande's detection efficiency $\epsilon(E_e)$.

$$R_{\bar{\nu}_e(p,n)e^+,\text{KII}} = n_{\text{KII}} V^{e}_{\text{eff},0,\text{KII}}\, \Phi_{\bar{\nu}_e} \int_0^\infty f_{\bar{\nu}_e}(E_{\bar{\nu}_e})\, \sigma_{\bar{\nu}_e(p,n)e^+}(E_{\bar{\nu}_e}, \langle E_{e^+} \rangle)\, \epsilon(\langle E_{e^+} \rangle)\, \mathrm{d}E_{\bar{\nu}_e} \quad . \tag{2.35}$$

Note that instead of using the effective volume of Kamiokande-II $V^{e}_{\text{eff},0,\text{KII}}$, we will use the detector mass $m_{\text{KII}} = 2140\,\text{t}$. For the AMANDA/IceCube case, the corresponding value is $V^{e}_{\text{eff},0}\rho_{\text{ice}}$ with a density of the antarctic ice of $\rho_{\text{ice}} = 916.8\,\text{kg/m}^3$ [147].

The electron trigger efficiency was taken from [68] and fitted with the function

$$\epsilon(E_e) = \Theta(E_e - E_0)\, \epsilon_{\max}\, (1 - e^{-a(E_e - E_0)}) \quad . \tag{2.36}$$

The parameters of the fit were determined to be $E_0 = 5.9\,\mathrm{MeV}$, $\epsilon_{\max} = 0.92$ and $a = 0.38\,\mathrm{MeV}^{-1}$. In addition, Kamiokande-II had a trigger threshold of 20 detected photons which corresponded to a minimum electron/positron energy of 7.5 MeV.

A further uncertainty in the scaling is the energy distribution of the neutrinos. A strong discrepancy exists between the Kamiokande-II and the IMB measurements, making a joint fit problematic. There exists currently no consensus on the spectrum of the neutrinos. One Suggestion is a Maxwell-Boltzmann spectrum with a pinching factor α [148]:

$$f_{\bar{\nu}_e}(E_{\bar{\nu}_e}) = \frac{(\alpha+1)^{(\alpha+1)}}{\Gamma(\alpha+1)} \frac{E_{\bar{\nu}_e}^{\alpha}}{\langle E_{\bar{\nu}_e}\rangle^{(\alpha+1)}} \exp\left\{-(\alpha+1)\frac{E_{\bar{\nu}_e}}{\langle E_\nu \rangle}\right\} \tag{2.37}$$

with the possible parameter settings ($\alpha = 0, \langle E_{\bar{\nu}_e}\rangle = 5.4$), ($\alpha = 2, \langle E_{\bar{\nu}_e}\rangle = 11.2$) or ($\alpha = 4, \langle E_{\bar{\nu}_e}\rangle = 14.2$).

Another proposal is a modified Fermi-Dirac distribution [149]:

$$f_{\bar{\nu}_e}(E_{\bar{\nu}_e}) = \frac{1}{T^3} \frac{E_{\bar{\nu}_e}^2}{1+\exp\{E/T-\eta\}} \tag{2.38}$$

with $T = 3.77\,\mathrm{MeV}$ and $\eta = 0.531$.

Due to the complicated shape of the combined functions, the integrations were performed numerically. The expected signals per IceCube DOM for a SN 1987A type supernovae at 10 kpc distance are shown in table 2.1.

Fit Performed	[148], $\alpha = 0$	[148], $\alpha = 2$	[148], $\alpha = 4$	[149]
Additional Hits	128.9	122.2	121.5	122.5

Table 2.1: Additional hits counted per IceCube DOM in the first 15 s caused by a SN 1987A like supernova at 10 kpc distance
The first line denotes the reference the fit was taken from (with a characterizing parameter if necessary) and the second the increase in rate over 15 s. *More information can be found in the text.*

The overall error from the counting statistics of 11 hits amounts to ~ 30% and has to be applied to all of the values in the table. As the energy spectra also influence the rates, we assume a further systematic uncertainty of 10%.

3 Supernova Signatures in IceCube

> Opportunities multiply as they are seized.
>
> Sūn Wǔ

Many different models and predictions exist for the neutrino flux from supernovae. A major task of this work was the design, revision and extension of the so-called Unified Supernova Simulation Routine (USSR). In the following chapter, we will first present the software suite and describe the approach used to simulate the detector response for supernova neutrinos. Next, a likelihood technique to discriminate models is introduced and applied to several signal predictions. Last, we determine the resolution of the neutrino burst arrival time.

3.1 Unified Supernova Simulation Routine (USSR)

To simulate supernova signatures in IceCube, one first has to decide which level of simulation detail is necessary. There exist two main approaches in the collaboration.

One is the simulation of the individual interaction vertices and the propagation of the produced particles within the detector volume. It is the most precise and thorough ansatz, but it is also slow and thus unsuitable for the investigation of many different models and scenarios.

A simpler and much faster way of estimating the signal is to predetermine an effective volume for the detection of leptons and use it to derive an average detector response. This Ansatz follows the standard IceCube procedure for photon propagation and is well tested in many analyses. We feel these benefits far outweigh the possible loss of precision.

It should be stressed that the main uncertainties for both approaches reside in the ice description, the knowledge of the (D)OM properties, the interaction cross sections and - most important - the supernova model.

The *Unified Supernova Simulation Routine* is a *C++* based, object-oriented framework intensively using the ROOT analysis library [150]. It provides the average expected signal a light sensor submerged in water or ice detects during an arriving supernova burst. The software suite was written by A. Piégsa [93], T. Griesel [127] and the author. Its mode of operation is schematically shown in figure 3.1 and will be described in the following section.

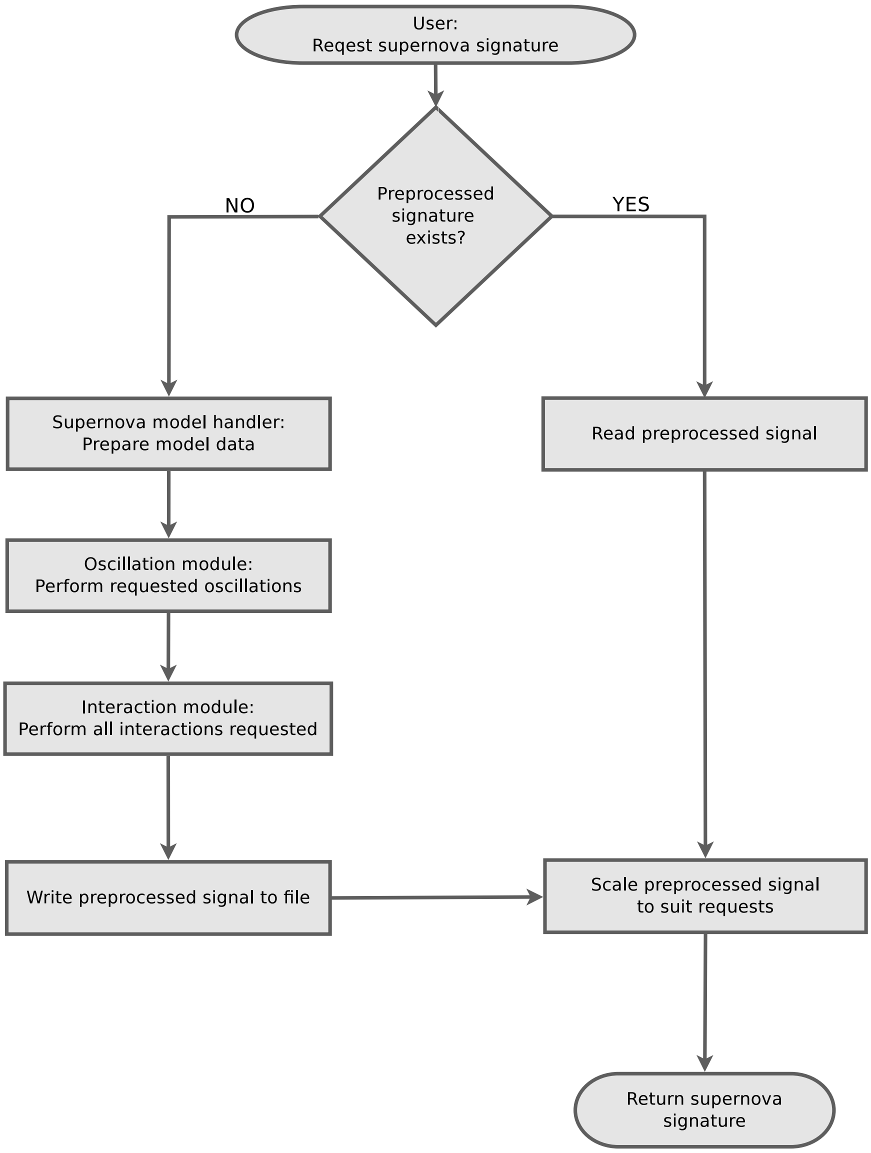

Figure 3.1: Flowchart of the supernova simulation routine
The boxes correspond to the respective software modules and are explained in more detail in the text.

3.1.1 Supernova Model Processing

At the most basic level, the simulation routine needs the neutrino flux properties of the supernova, namely the luminosity and the spectral information for each neutrino flavor.

3.1.1.1 Luminosities and Mean Energies

In its current release[1] the data is read in from ASCII files[2]. Luminosities L_ν should be furnished in erg/s and the mean energies $\langle E_\nu \rangle$ in MeV as function of time t in s. The requested input format is

$$[t]\ [L_{\nu_e}]\ [L_{\bar{\nu}_e}]\ [L_{\nu_x}]\ [\langle E_{\nu_e}\rangle]\ [\langle E_{\bar{\nu}_e}\rangle]\ [\langle E_{\nu_x}\rangle]$$

or

$$[t]\ [L_{\nu_e}]\ [L_{\bar{\nu}_e}]\ [L_{\nu_x}]\ [L_{\bar{\nu}_x}]\ [\langle E_{\nu_e}\rangle]\ [\langle E_{\bar{\nu}_e}\rangle]\ [\langle E_{\nu_x}\rangle]\ [\langle E_{\bar{\nu}_x}\rangle] \quad .$$

Elements of a line are separated by a space character and lines starting with a # are ignored.

As the internal binning of the USSR is not necessarily correlated to the timings of the input, the model data is interpolated linearly and stored internally. The time binning of the USSR is customizable (default is 0.1 ms).

3.1.1.2 Neutrino Spectra

At present, the simulation supports two ways of reading in neutrino spectra.

First and most commonly used is the description of the spectra with the analytic function [151]

$$f_\alpha(E) = \frac{(\alpha+1)^{-(\alpha+1)}}{\Gamma(\alpha+1)} \frac{E^\alpha}{\langle E\rangle^{(\alpha+1)}} e^{-(\alpha+1)\frac{E}{\langle E\rangle}} \quad . \tag{3.1}$$

As before, the necessary parameters are read from ASCII files. The energy distribution is specified with the keyword "function:" followed by a string conforming to a one-dimensional ROOT function (*TF1*) [150]. This allows an easy implementation of new spectral forms. Note that the first parameter is always the mean energy read in from the luminosity file (see above). Further parameters $p_1, p_2, \ldots$ are specified in the following lines in the format

---

[1] The inclusion of shock wave propagation and collective oscillations required the handling of numerical energy spectra. A major code revision was necessary to accommodate these demands. Furthermore, the new version also allows for mixing angles in the ranges of $10^{-5} < \sin^2 2\theta_{13} < 10^{-3}$ and signal preprocessing to reduce CPU time and enable mass production. In parallel, the code was moved to an object-oriented, modular design. Development of the *Khrushchev* release was a major task of this thesis.

[2] The *American Standard Code for Information Interchange* is a character-encoding scheme based on the ordering of the English alphabet. ASCII files are also referred to as plain text files.

$$[t]\ [p_{1,\nu_e}]\ [p_{1,\bar{\nu}_e}]\ [p_{1,\nu_x}]\ [p_{2,\nu_e}]\ [p_{2,\bar{\nu}_e}]\ [p_{2,\nu_x}]\ \cdots$$

or

$$[t]\ [p_{1,\nu_e}]\ [p_{1,\bar{\nu}_e}]\ [p_{1,\nu_x}]\ [p_{1,\bar{\nu}_x}]\ [p_{2,\nu_e}]\ [p_{2,\bar{\nu}_e}]\ [p_{2,\nu_x}]\ [p_{2,\bar{\nu}_x}]\ \cdots$$

It should be noted that the time bins of the spectral information do not have to be synchronous with the luminosity and energy information. Missing data is interpolated.

The second possibility is the inclusion of a time independent spectrum. While this approximation is not realistic, it was introduced to study the effect of collective oscillations as no time-dependent spectra were available at the time. Again, the data is read in from ASCII files and should be in the format

$$[E]\ [F_{\nu_e}]\ [F_{\bar{\nu}_e}]\ [F_{\nu_x}]\ [F_{\bar{\nu}_x}] \tag{3.2}$$

with the energy E given in MeV and the fluxes F_ν given in $1/(\mathrm{MeVcm^2s})$. An extension to spectral information available in tabulated form would only require extensions to the read-in mechanism. However, at the time being no input data requiring such a step is available.

All spectra are either calculated or interpolated to match the energy resolution requested (default is 0.1 MeV). Note that the neutrino energy distributions can also be arbitrarily combined with other models.

3.1.1.3 Model Buffer

Internally, the simulation buffers the neutrino luminosities, fluxes and mean energies for ν_e, $\bar{\nu}_e$, ν_x and $\bar{\nu}_x$ as well as the total flux for all time bins (default resolution is 0.1 ms).

The spectral information is filled into histograms with customizable energy range and resolution (default is the interval $[0, 100]$ MeV in steps of 0.1 MeV) for each time bin.

3.1.1.4 Available Models

At the time of writing, the USSR has 16 different model predictions available (see section 1.1.2.3 for a general explanation):

- The *Lawrence Livermore* model is a one-dimensional simulation of a $20\,\mathrm{M}_\odot$ star and one of the few that extends up to large times post-bounce (15 s). Its explosion had to be aided by external influences. For more information on this model refer to [152]. Only rough spectral information is available.
- Next is a collapsing $8.8\,\mathrm{M}_\odot$ star simulated by the Garching group in two-dimensions up to ~ 0.8 s post-bounce. It has been processed with the Lattimer-Swesty and the Wolff-Hillebrandt equations of state. More information on this model can be found in [35].

- In [23] a 15 $\mathrm{M}_\odot$ star was simulated up to ~ 0.38 s post-bounce. Calculations were run in one and two dimensions for the Lattimer-Swesty and Wolff-Hillebrandt equations of state. For the two-dimensional case, the available luminosities are the average over the northern hemisphere and the emission from the north pole. No specific spectral information is available up to date.
- Objects with stellar masses of 40 $\mathrm{M}_\odot$ which end in failed supernovae were modeled in [30]. The simulations run up to the point where a singularity, a black hole, develops. At this point, the processing is stopped to avoid a program crash. The model is available for the Shen and the Lattimer-Swesty equations of state.
- A 10 $\mathrm{M}_\odot$ star was simulated in [56] with and without a QCD phase transition. Again, no spectral information is available.
- The neutrino signal of a type Ia supernova was predicted in [153]. Unfortunately, the signal turns out to be far to small to be detected at distances above 100 pc. No spectral information is available.
- The last model included so far is also the newest. Again, it is the collapse of a 8.8 $\mathrm{M}_\odot$ star, but this time simulated in one dimension and still leading to an explosion. A Shen equation of state was used in the calculations and the simulations were run with a reduced and a full set of neutrino interactions (neutrino opacities). The models extend up to 25 s and 9 s, respectively. A detailed description can be found in [37]. The parameters of the spectral function 3.1 were provided by the simulation authors [38].

If nothing else is specified, the energy spectra were provided with the model and fitted with function 3.1. For the case that no spectral information is available, the mean energies of the requested model are combined with the distribution parameters of a reference model (default is [35] in the Lattimer-Swesty equation of state).

Adding new models to the USSR is a simple and straightforward process. Model and spectrum have to be prepared according to sections 3.1.1.1 and 3.1.1.2 and supplied to the USSR.

3.1.2 Neutrino Oscillations

Details on the oscillation of neutrinos in the supernova environment can be found in section 1.2.4.

MSW effect, shock wave propagation and vacuum mixing is accounted for by iteratively applying the probabilities derived in section 1.2.4.2 to the neutrino fluxes. As the conversion probabilities can depend on the neutrino energies, they are handled as histograms and multiplied bin by bin with the neutrino flux spectra. The simulation allows for normal and inverted hierarchies and any value of θ_{13}. If $10^{-5} < \sin^2 2\theta_{13} < 10^{-3}$, the density profile given in equation 1.45 is used for derivation of the MSW effects. For shock propagation, time dependent density gradients are provided by [99, 154] in 0.1 s steps up to 15 s after bounce. The effects of forward and reverse shock as well as the contact discontinuity are included in the USSR. Oscillation effects induced by the propagation through the Earth are also included (refer to [93]).

As collective oscillations require careful tracking and modeling of the neutrino propagation in the supernova, no consistent mechanism to account for the self-interactions can be implemented in the USSR. To estimate the effects, modified neutrino spectra were included in the simulation. In [107], neutrino self-interactions were simulated for 37 different partitions of neutrino luminosity ($L_{\nu_e} : L_{\bar{\nu}_e} : 4L_{\nu_x}$) in the early supernova phase for an inverted neutrino hierarchy with $\sin^2 2\theta_{13} = 10^{-6}$. For each case, we were provided with the initial and final spectra [108]. Assuming these are constant over time, they can be used to estimate the effect of collective oscillations in IceCube.

3.1.3 Neutrino Interactions

The simulation includes all cross sections presented in section 2.3.1 as histograms. To estimate the expected signal, the cross sections are multiplied bin by bin with the neutrino spectra and integrated over the energies (see section 2.4.3).

3.1.4 Signal Preprocessing

Estimating the signal for the requested time and energy resolution can take quite a while. Therefore, the model signatures are preprocessed and stored in a *root* file. When requesting the expectation for a supernova, the preprocessed signature is read from file and multiplied by the number of H_2O molecules in ice, the effective volume constant $V^{e}_{\mathrm{eff},0}$ and divided by $4\pi R^2_{\mathrm{SN}}$ with R_{SN} being the supernova distance in meters. This enables fast usability of the models and allows the generation of large statistics.

3.2 Simulating a Detector Response

The USSR provides the signal expectations of a given supernova model for any available oscillation scenario. For the simulation of a detector response, specific parameters like the number of DOMs or the dead time have to be applied afterward. As already shown in [93], the investigation of the summed DOM rates is a good observable for supernova signature in IceCube.

3.2.1 DOM Rates

The first ingredient necessary to estimate the detector response is the DOM noise.

For the average IceCube sensor we extract a mean rate of

$$\mu_{\mathrm{I3}} = 284.9\,\mathrm{Hz} \quad \text{and} \quad \sigma_{\mathrm{I3}} = 26.2\,\mathrm{Hz} \tag{3.3}$$

from the data of 2008. Studying the first DeepCore string deployed (string 83), we extract

$$\mu_{\mathrm{DC}} = 358.9\,\mathrm{Hz} \quad \text{and} \quad \sigma_{\mathrm{DC}} = 36.0\,\mathrm{Hz} \tag{3.4}$$

from the year 2009 for high efficiency modules.

Assuming 4800 standard and 360 DeepCore PMTs and correcting by an estimated failure rate of 2%, we obtain an average detector noise of

$$\mu_{\mathrm{all}} = 1.4669 \cdot 10^6\,\mathrm{Hz} \quad \text{and} \quad \sigma_{\mathrm{all}} = 1.9 \cdot 10^3\,\mathrm{Hz} \quad . \tag{3.5}$$

3.2.2 Dead Time

Next, the effect of dead time has to be taken into account. For each PMT hit, a dead time window opens during which no further events can be registered. Assuming a time interval ΔT, an overall mean rate of μ in and a dead time τ, we experience a sensitivity loss of

$$\varepsilon = \frac{\Delta T - \mu \Delta T \tau}{\Delta T} = 1 - \tau\mu \quad . \tag{3.6}$$

The overall mean rate is given by $\mu = \mu_{\mathrm{BG}} + \mu_{\mathrm{SN}}$. Note that while we know the background noise level μ_{BG} of the DOMs after dead time, this is not the case for the signal estimation. From our simulation routine, we are provided with the raw PMT signal μ'_{SN} before τ has been applied. To obtain the expected rate seen by the DOMs, we have to modify the simulation output to accommodate $\mu_{\mathrm{SN}} = \varepsilon\mu'_{\mathrm{SN}}$. We insert this relation in equation 3.6 and obtain

$$\varepsilon = 1 - \tau(\mu_{\mathrm{BG}} + \varepsilon\mu'_{\mathrm{SN}}) \quad . \tag{3.7}$$

The dead time efficiency factor results in

$$\varepsilon = \frac{1 - \tau\,\mu_{\mathrm{BG}}}{1 + \tau\,\mu'_{\mathrm{SN}}} \quad . \tag{3.8}$$

3.2.3 Finalizing the Detector Response

Now we have all we need to generate the detector response. We estimate the supernova signal using the program described above (section 3.1) and assume the effective volume from equation 2.20. Calculating the average rate increase for the whole detector is straightforward. For the standard PMTs, we multiply the individual rate estimation μ_{SN} by the number of sensors N_{I3}, and for DeepCore, we apply a factor of $\epsilon_{\mathrm{DC}} = 1.35$ before scaling the signal to all high efficiency modules N_{DC}. Note that N_{I3} and N_{DC} are already corrected by the estimated module failure rate of 2% as in section 3.2.1. The expected detector signal is then

$$\mu_{\mathrm{SN,I3+DC}} = N_{\mathrm{I3}}\,\mu_{\mathrm{SN}} + \epsilon_{\mathrm{DC}}\,N_{\mathrm{DC}}\,\mu_{\mathrm{SN}} \tag{3.9}$$

Using a normal distribution with the parameters given in equation 3.5, we first generate background rates and add a random number drawn from a Poisson distributed around $\mu_{\mathrm{SN,I3+DC}}$.

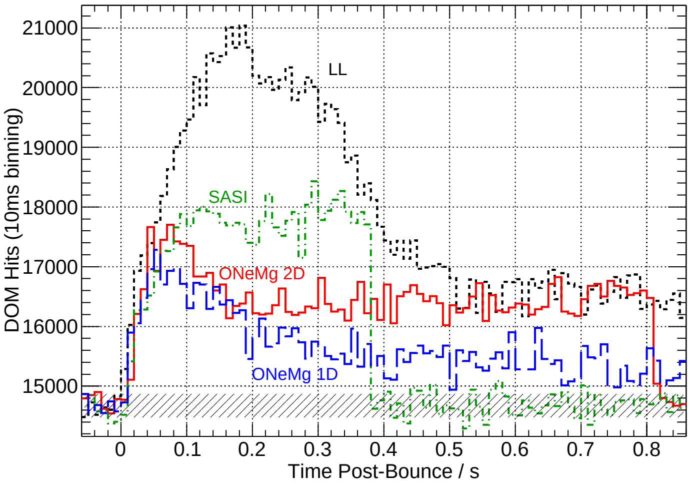

Figure 3.2: Detector response to supernovae of different masses (10 kpc)
The supernova signatures follow the Lawrence-Livermore model (LL) with $20\,\mathrm{M}_\odot$*, a SASI simulation by Garching with* $15\,\mathrm{M}_\odot$ *(SASI) ending at* $0.38\,\mathrm{s}$ *post-bounce and two ONeMg cores with* $8.8\,\mathrm{M}_\odot$ *calculated in one and in two-dimensions also by Garching (ONeMg 1D and ONeMg 2D). For more details and pertaining references, refer to section 3.1.1.4. All signatures are shown for a normal hierarchy.*

3.2.3.1 Model Signatures

We will now take a look at the IceCube signatures of some of the models.

Figure 3.2 compares the detector signals for the Lawrence-Livermore model, a SASI driven explosion simulated by the Garching group and two electron capture supernovae also simulated by Garching. We see that the SASI simulation shows stronger signals than the ONeMg cores which is likely due to the higher precursor mass. Of course, the Lawrence-Livermore model has an even higher mass and features a stronger signal still, however, this might well be due to different codes used to simulate the explosion.

In figure 3.3 we take a closer look at the SASI fluctuations for the averaged flux as well as the emissions from the north pole of the star. At close distances the modulations in the signal are evident. If one moves to e.g. 10 kpc, the fluctuations are difficult to distinguish from the noise (see also [127]).

Figure 3.4 shows the neutrino signals induced by failed supernovae. They are much stronger than all of the exploding models investigated so far, and we see a clear difference between the two equations of state.

3.2.3.2 Response to Oscillation Scenarios

As investigated in [93], the assumed neutrino mass hierarchy and the value of the θ_{13} mixing angle can have a serious impact on the detector response. In this section

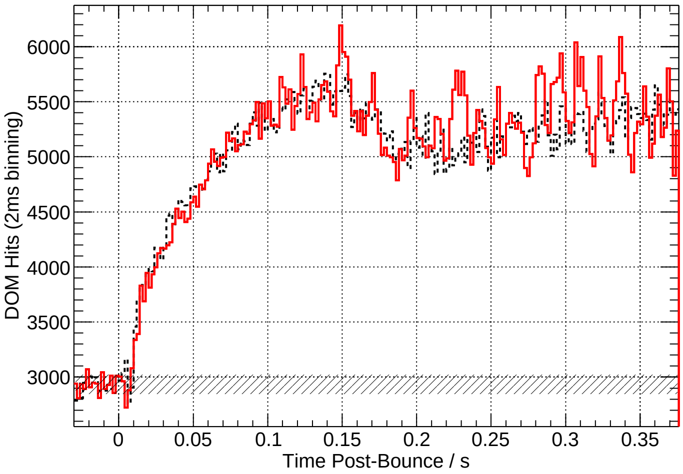

Figure 3.3: Detector response to supernovae showing the SASI (5 kpc)
Both lines display a Garching simulation with $15\,\mathrm{M}_\odot$ *at (*5 kpc*). Black dotted denotes the averaged neutrino luminosity over the northern hemisphere of the star. Solid red shows the emissions from the North Pole only, where fluctuations from the SASI are more apparent. A closer investigation of this model is performed in [127]. Details and references can be found in section 3.1.1.4. All signatures assume normal hierarchy.*

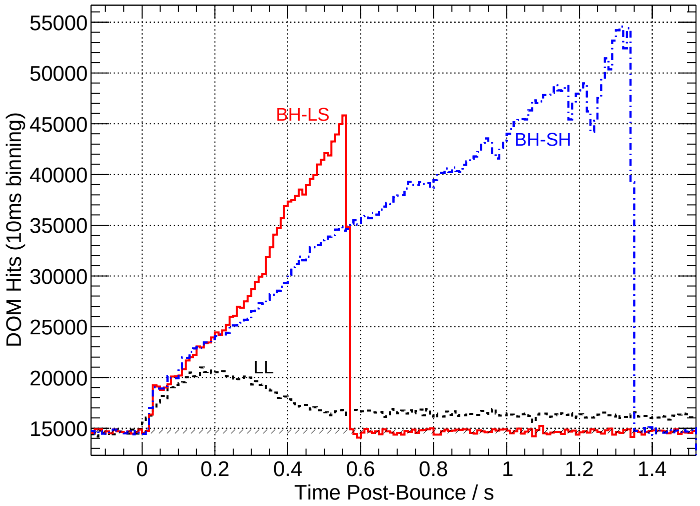

Figure 3.4: Detector response to failed supernovae (10 kpc)
The illustration displays the signatures of two failed supernovae assuming the equations of state from Shen (BH-SH) and Lattimer-Swesty (BH-LS) along with the detector response to a Lawrence-Livermore (LL) explosion. See section 3.1.1.4 for details on the models. All signatures assume a normal mass hierarchy.

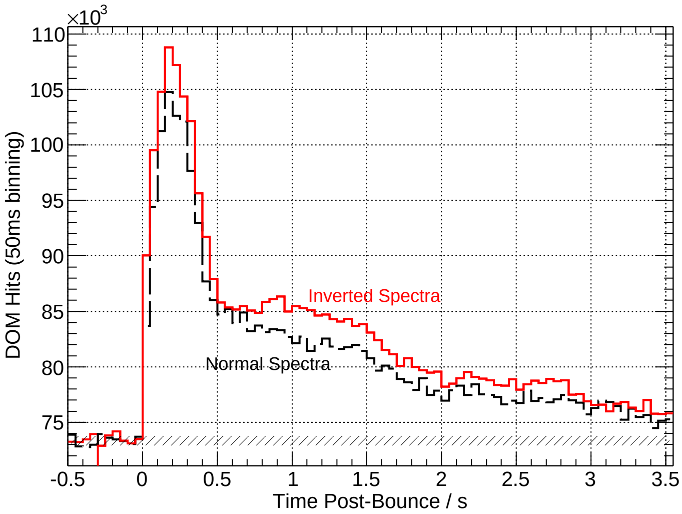

Figure 3.5: Matter oscillations for different neutrino mass hierarchies
The lines show a Lawrence-Livermore like supernova at $10\,\mathrm{kpc}$ *distance under the assumption of a normal mass hierarchy or a mixing angle conforming to* $\sin^2 2\theta_{13} < 10^{-5}$ *as well as an inverted hierarchy with* $\sin^2 2\theta_{13} > 10^{-3}$*. It is neutrinos leaving the star in the* $\bar{\nu}_1$ *state that will primarily be detected. In case of an inverted mass hierarchy with* $\sin^2 2\theta_{13} > 10^{-3}$*, the spectra of* $\bar{\nu}_e$ *and* $\bar{\nu}_x$ *are swapped, and thus, a stronger signal is induced in IceCube.*

the repercussion of some of the oscillation scenarios discussed in section 1.2.4 will be illustrated.

Figure 3.5 displays the effect of MSW oscillations. For an inverted mass hierarchy paired with a large θ_{13} mixing angle ($\sin^2 2\theta_{13} > 10^{-3}$) the neutrinos undergo adiabatic evolution. This means that neutrinos produced as $\bar{\nu}_x$ arrive at Earth in the $\bar{\nu}_1$ state, and because this state has the highest $\bar{\nu}_e$ contribution, they dominate the signal. For the Lawrence-Livermore model as well as most others, neutrinos created in the non-electron flavor have higher energies than neutrinos created in the electron flavor. Consequently, the signal is stronger than for e.g. a small mixing angle ($\sin^2 2\theta_{13} < 10^{-5}$).

Figure 3.6 displays the effects of shock wave propagation in a Lawrence-Livermore model. Again, the interesting features reveal themselves for the inverted mass hierarchy paired with a large θ_{13} mixing angle ($\sin^2 2\theta_{13} > 10^{-3}$). Note that the considerations in the following paragraph assume these neutrino properties. As the shock wave changes the density profile, it breaks adiabaticity and neutrino conversions will occur when the shock passes the resonance layers. This leads to time modulated oscillation probabilities and thus changes in the neutrino luminosity. For the single forward shock, $\bar{\nu}_x$ convert to the $\bar{\nu}_3$ state when the shock reaches the H-resonance. Because they would normally leave the star as $\bar{\nu}_1$, the signal decreases. When the reverse shock is switched on, neutrinos can switch their state twice, raising the signal when compared to the

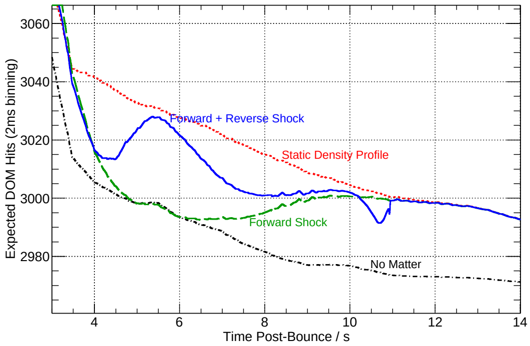

(a) Expectation at 10 kpc

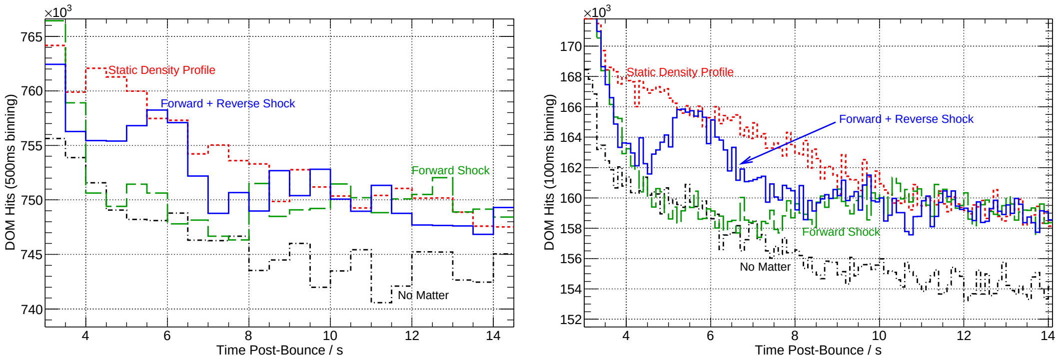

(b) Detector response at 10 kpc

(c) Detector response at 5 kpc

Figure 3.6: Neutrino oscillations due to shock wave propagation
Again, the simulations show the Lawrence-Livermore model. For a discussion, see the text.

forward shock.

Figure 3.7 illustrates the changes due to self-interaction for the case of luminosity equipartition ($L_{\nu_e} : 4L_{\nu_x} : L_{\bar{\nu}_e} = 1 : 4 : 1$). As described in section 1.2.4.3, high neutrino densities can lead to swaps in the energy spectra and thereby modulate the neutrino signature. Because of the approach used to estimate the effects of collective oscillations (see section 3.1.2), we see only a difference in scale and not in shape.

3.3 Separating Supernova Signals

To determine the performance of IceCube, a quantitative measure for the discrepancies between detector signatures of different models or oscillation scenarios is necessary.

Assume that we have signal hypotheses s_A and s_B. Further assume a recorded number of hits (n_A) for hypothesis A. We calculate the logarithmic likelihood sums

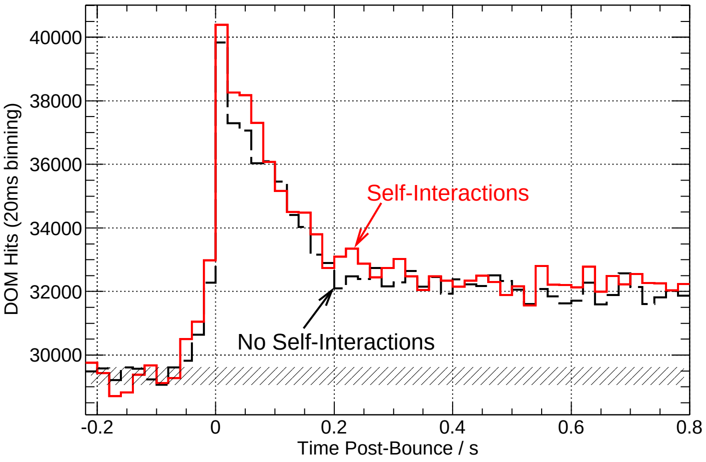

Figure 3.7: Signature of collective oscillations

The figure shows the effect of collective oscillations for an ONeMg supernova according to [35] with a Lattimer-Swesty equation of state and luminosity equipartition ($L_{\nu_e} : 4L_{\nu_x} : L_{\bar{\nu}_e} = 1 : 4 : 1$)*. Assuming "no self-interactions" is equivalent to a normal hierarchy. As stated in section 1.2.4.3, a mixing angle of* $\sin^2 2\theta_{13} = 10^{-6}$ *and fixed neutrino spectra were assumed.*

$$-\ln \mathcal{L}_A = \frac{1}{N}\sum_{i=1}^{N}\left(\frac{n_i^A - s_i^A}{\sigma_i^A}\right)^2 \quad \text{and} \quad -\ln \mathcal{L}_B = \frac{1}{N}\sum_{i=1}^{N}\left(\frac{n_i^A - s_i^B}{\sigma_i^B}\right)^2 \tag{3.10}$$

where N is the number of bins to be tested and σ^2 the expected variance, i.e. $\sigma^2_{\text{background}} + \sigma^2_{\text{signal}}$. Before calculating the likelihood sums, we subtract the background expectation μ_{BG} from n as well as s and scale both signatures to the same number of entries. We are thus independent on the absolute normalization. Figure 3.8 shows an example for this approach.

To exclude a model, we first have to find a hypothesis A which describes the data. We determine the distributions of $-\ln \mathcal{L}$ for the description (hypothesis A) as well as the model to be tested (hypothesis B) by running toy Monte Carlos. Having the two distributions, we next investigate how well they are separated. For this purpose, we determine the width σ_A and the mean μ_A of the distribution for hypothesis A and the 10% quantile $l_{B,10\%}$ of the distribution for hypothesis B (see figure 3.9). We define the separability or discrimination power $\mathfrak{s}$ as

$$\mathfrak{s} = \frac{l_{B,10\%} - \mu_A}{\sigma_A} \quad . \tag{3.11}$$

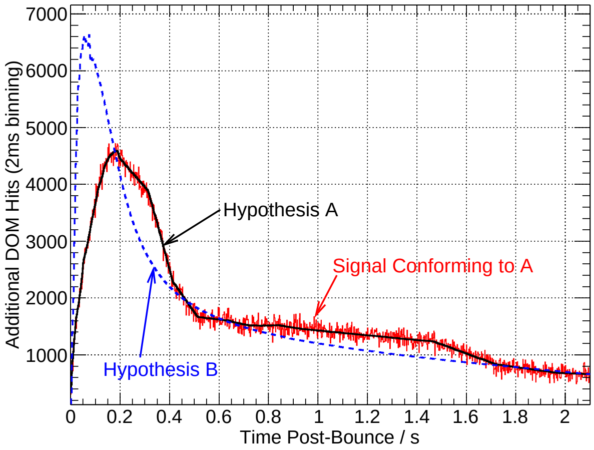

Figure 3.8: Comparison between hypotheses
The figure shows a simulated detector response to a Lawrence-Livermore model. Hypothesis A is the signal prediction given by the USSR Monte Carlo. We want to compare it to the assumption of a one-dimensional ONeMg core collapse model (hypothesis B). To do this, we calculate the differences between detector response and hypothesis for both expectations bin by bin. When summed over all bins, this gives us the logarithmic likelihood for each hypothesis (see figure 3.9).

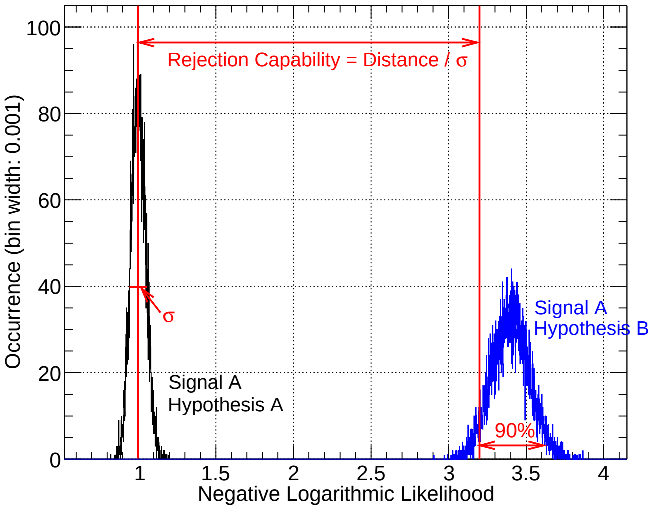

Figure 3.9: Example for a distribution of $-\ln\mathcal{L}$
The distributions show the logarithmic likelihood differences for 10000 simulations at 13 kpc *for the detector response and hypotheses conforming to figure 3.8. A detailed description of the method is given in the text.*

3.3.1 Model Comparisons

To demonstrate the capabilities of IceCube, we compare several model predictions. As test cases, we take the predictions for Lawrence-Livermore (LL), the failed supernovae with both equations of state and two ONeMg core collapse models, one in 1D with full neutrino opacities and one in 2D with a Lattimer-Swesty equation of state (for details, see section 3.1.1.4). The models are simulated with the USSR and then compared using the likelihood technique as described above. For a given detector response, we derive the capability to reject a wrong hypothesis in function of the distance. Figure 3.10 shows the rejection power for different kinds of supernovae. Note that these values are the optimal case, as the method assumes a perfect knowledge of the model shapes.

When looking at failed supernovae, the luminosity cutoff makes an identification much easier when comparing over large enough time spans (see figure 3.11). However, because of the stellar void in-between the edge of the Milky Way ($\sim 30\,\mathrm{kpc}$) and the Large Magellanic Cloud ($\sim 50\,\mathrm{kpc}$), one does not really profit from the good separability.

We can clearly see that IceCube would be quite helpful in testing supernova models. While ONeMg collapses would lead to small signals, they could still be used to exclude supernova hypotheses up to $> 10\,\mathrm{kpc}$ at 5σ at 90% confidence. If the explosion of a heavy star conforming to the Lawrence-Livermore signal would be recorded, the rejection capabilities would exceed $> 20\,\mathrm{kpc}$ at 5σ. Detection of a failed supernova with high mass would extend this range up to the Small Magellanic Cloud at $\sim 61\,\mathrm{kpc}$. More model comparisons, especially the SASI and the QCD phase transition, are covered in [127].

3.3.2 Shock Wave Comparisons

In section 1.2.4.2 we saw that neutrino oscillations can alter the detector signature of a core collapse and we showed some examples in section 3.2.3.2. The impact of the matter oscillations in case of static density profiles of supernovae was already examined in [93] and will be extended by [127]. However, an investigation of neutrino properties with the MSW effect alone is quite model dependent.

Shock waves on the other hand, are common to all supernovae. However, the way the shock wave develops and then travels to the outside is largely unknown since asymmetric propagations and turbulences as well as bubbles are likely. As no simulations in two or three dimensions exist for these late times, we restrict ourselves to the simple 1D example calculated in [99].

Because the shock wave modulation only becomes apparent at times $\gtrsim 4\,\mathrm{s}$ post-bounce, we need a model which includes the cooling phase. The only available candidates are the Lawrence-Livermore and the 1D ONeMg simulations. As the shock wave was simulated for an iron core, its propagation is much slower than it would be in the ONeMg case[3]. We will use the Lawrence-Livermore model as a baseline and modify it

---

[3] The envelope of the precursor to an ONeMg supernova is thinner and, therefore, features a steeper density gradient. A shock wave will consequently travel much faster than in an iron core collapse.

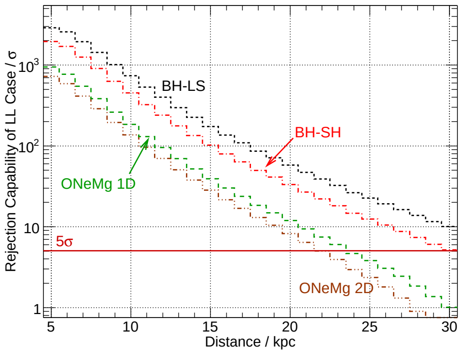

(a) Lawrence-Livermore model

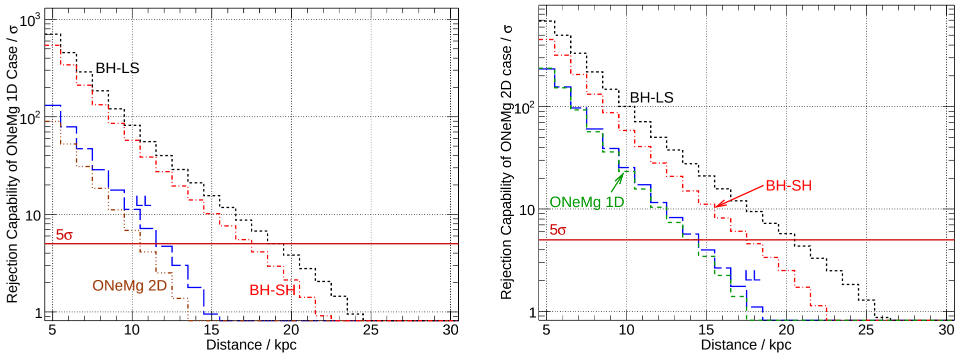

(b) 1D ONeMg core collapse (full ν-opacities)

(c) 2D ONeMg core collapse (LS-EoS)

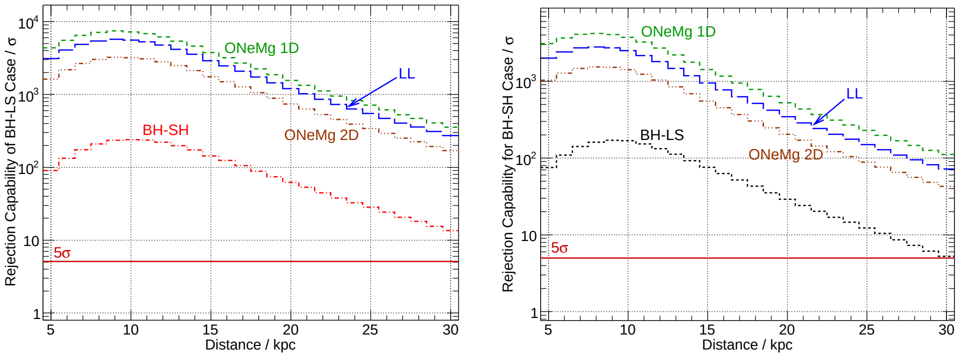

(d) Failed supernova (LS-EoS)

(e) Failed supernova (Shen-EoS)

Figure 3.10: Capability to reject supernova models
Each plot demonstrates the rejection capabilities for a supernova of a certain type. The tests were performed for the first 0.55 s *of the signal. As the dead time can modify the shapes at close distances, the separation power of strong signals from failed supernovae increases up to* 10 kpc. *For each model 10000 detector responses were simulated in* 1 kpc *steps.*

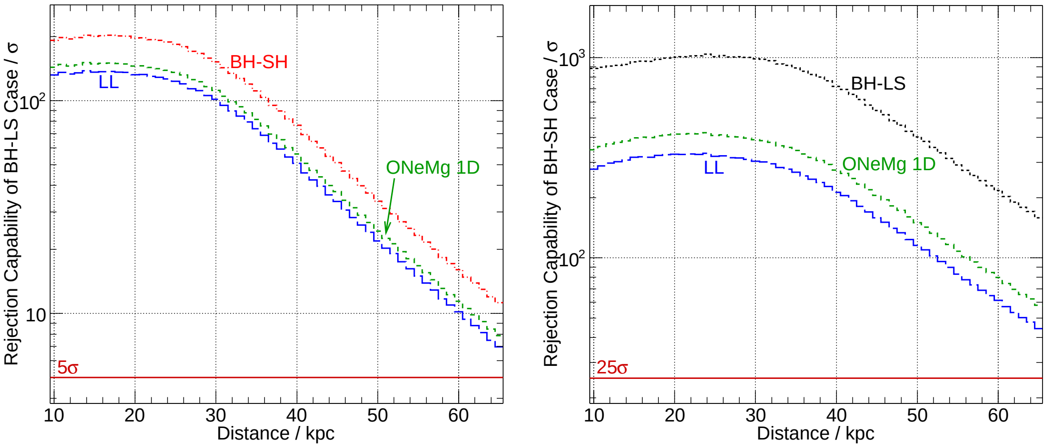

(a) Failed supernova (LS-EoS)

(b) Failed supernova (Shen-EoS)

Figure 3.11: Capability to reject supernova models
The figures can be interpreted in the same way as figure 3.10. Here, the initial 1.8 s *of the burst were compared. As we now include the neutrino luminosity cutoff at black hole formation, slight timing mismatches between hypothesis and signal caused by binning effects can lead to increased likelihood values and thus lower separabilities for very close-by supernovae. However, even in the worst case scenario the rejection capability never drops below* 90σ*. Again, 10000 detector responses were simulated per model in* 1 kpc *steps.*

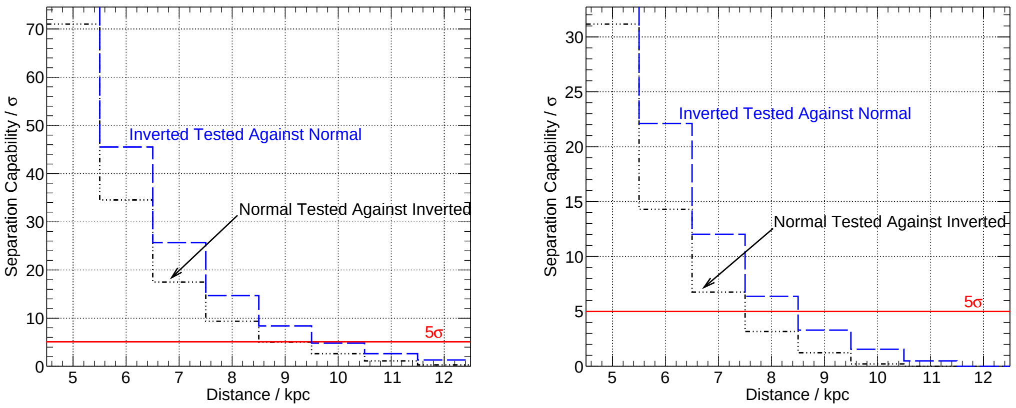

(a) Forward shock

(b) Forward + reverse shock

Figure 3.12: Discernability of neutrino properties through the supernova shock wave *These figures show the ability to discriminate against a certain neutrino oscillation scenario. Normal denotes the case of normal hierarchy or* $\sin^2 2\theta_{13} < 10^{-5}$ *while inverted stands for inverted mass hierarchy paired with* $\sin^2 2\theta_{13} > 10^{-3}$*. We always simulate a certain scenario, e.g. the inverted case, and test it against its opposite. Thus, we could reject the normal hierarchy and* $\sin^2 2\theta_{13} < 10^{-5}$ *at* 5σ *if we would detect a signal conforming to the inverted case for a supernova at* 10 kpc*. As above, for each scenario 10000 detector responses were simulated in* 1 kpc *steps.*

accordingly.

To investigate the neutrino properties, we consider four scenarios. In case of a normal hierarchy or a small θ_{13} mixing angle ($\sin^2 2\theta_{13} < 10^{-5}$), the detector signature is unchanged. However, in case of an inverted mass hierarchy and large mixing ($\sin^2 2\theta_{13} > 10^{-3}$), the propagating shock wave changes the detector response from the static density case. Figure 3.6 showed the expected signals. The rejection capabilities are shown in figure 3.12.

Using this method, the determination of the neutrino hierarchy is possible for close-by supernovae. Assuming an inverted mass hierarchy and large mixing, one would be able to reject the cases of normal hierarchy and small mixing with $> 5\sigma$ up to supernova distances of 10 kpc for a single forward shock and 8 kpc for a combination of forward and reverse shock. If one assumes normal hierarchy or small mixing, the case of inverted hierarchy with large mixing could be rejected at $> 5\sigma$ up to 9 kpc and 7 kpc, respectively.

Note that we assume that the neutrino signature is smooth during the cooling phase of the PNS. Model predictions seem to support this, however, simulations of these late times have only been done in 1D so far.

3.3.3 Comparing Collective Oscillation Scenarios

As stated in section 3.1.2, the current implementation of collective neutrino oscillations has to assume constant energies and flux fractions. Therefore, neutrino flavors will not retain the characteristic features by which it was so far possible to separate them. Comparing the signal shapes is therefore pointless.

Another possibility would be to compare the signal at different time intervals. As mentioned in section 1.2.4.3, bi-polar oscillations do not emerge during the deleptonization peak. The detector response would therefore remain the same, independent of whether collective oscillations occur or not. Comparing the first $\sim 10\,\text{ms}$, to the accretion phase, $t \in [0.1\,\text{s}, 0.8\,\text{s}]$, it might be possible to separate the scenarios if the models are known in detail. Unfortunately, there are only few DOM hits during the deleptonization phase, and thus, the counting error inhibits such an approach. Even at 1 kpc the statistical errors would be larger than the estimated effect.

The one method that remains is the comparison of the total number of hits, i.e. including the absolute normalization of the models. As the self-interaction modulated spectra available to the USSR were compiled for the early supernova phase only, we investigate an interval of $t \in [0.1\,\text{s}, 0.8\,\text{s}]$. We use the 2D ONeMg simulation with the Lattimer-Swesty equation of state as a reference model. For each of the 37 different sets of modulated spectra (see section 3.1.2), we derive the relative the differences between oscillated and non-oscillated counts, n_{coll} and n_{norm}:

$$\mathfrak{f} = \frac{n_{\text{norm}} - n_{\text{coll}}}{n_{\text{norm}}} \quad . \tag{3.12}$$

The relative flux differences for all luminosity ratios assuming model [35] as reference can be found in table 3.1.

l_{ν_e} \ $4l_{\nu_x}$	1	2	3	4	5	6	7	8
1	-43%	-38%	-31%	-23%	-13%	0%	0%	0%
2	-61%	-58%	-53%	-46%	-35%	-10%	0%	X
3	-69%	-65%	-59%	-46%	-18%	-1%	X	X
4	-73%	-65%	-52%	-27%	16%	X	X	X
5	-69%	-57%	-35%	-14%	X	X	X	X
6	-63%	-44%	-1%	X	X	X	X	X
7	-54%	-16%	X	X	X	X	X	X
8	-34%	X	X	X	X	X	X	X

Table 3.1: Differences between signals with and without collective oscillations
The table shows the differences in DOM counts when comparing oscillated with non-oscillated fluxes according to equation 3.12. l_{ν_e} and $4l_{\nu_x}$ describe the luminosity fractions of ν_e and ν_x. $l_{\bar{\nu}_e}$ can be derived from the equation $l_{\nu_e} + l_{\bar{\nu}_e} + 4l_{\nu_x} = 1$. In case of equipartition, we would expect a signal difference of 9%.

When comparing $\mathfrak{f}$ to its uncertainty $\sigma_{\mathfrak{f}}$, we can derive the resolution we could achieve

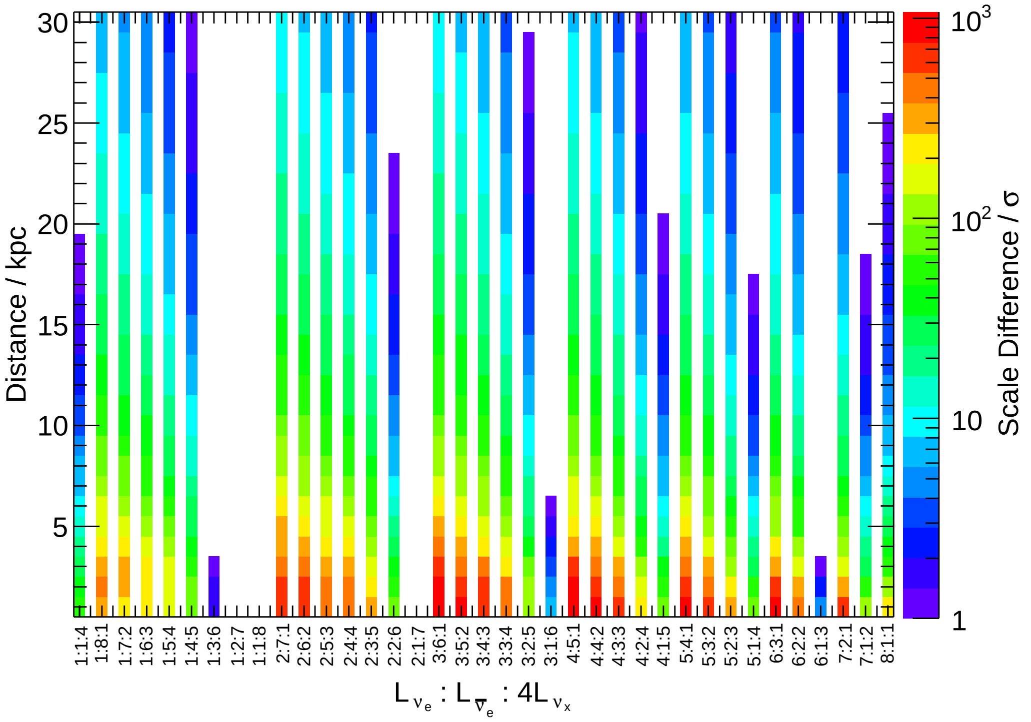

Figure 3.13: Separability for collective oscillations
The x-axis denotes the neutrino luminosity ratios which are an important factor when determining the consequences of collective oscillations. The colors show the relative flux difference $\mathfrak{f}$ *in units of* $\sigma_{\mathfrak{f}}$*. With increasing distance,* $\mathfrak{f}$ *decreases with respect to the counting errors. Thus, the difference in DOM hits becomes less noticeable.*

with IceCube if a reliable supernova model was found and the distance could be fixed. Figure 3.13 shows the optimal separabilities versus supernova distance. Depending on the neutrino luminosity fractions, differences in DOM hits can be observed for all stars in the Milky Way. However, most models show equal luminosities in all neutrino flavors and can therefore only be separated up to 8 kpc at 5σ.

When comparing only the number of PMT hits, one is strongly dependent on the understanding of the model and the detector. A systematic error in the derivation of the expected detector response will limit the possibility to distinguish signatures that only differ by a small overall normalization. E.g. if the expected difference in PMT hits is smaller than the systematic error, collective oscillation effects cannot be discerned in IceCube (this is the case for luminosity equipartition).

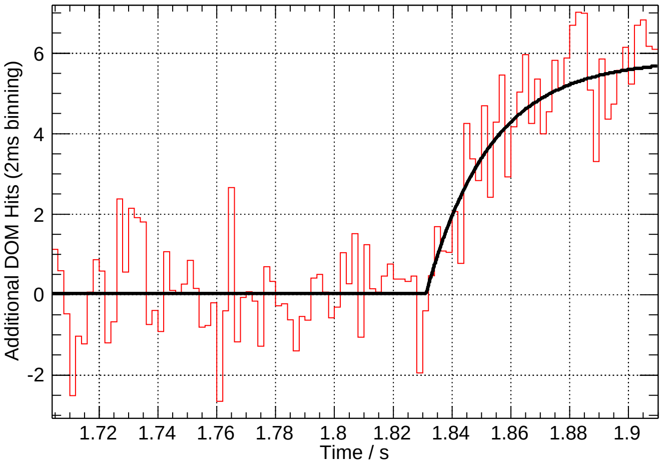

Figure 3.14: Start time reconstruction for an ONeMg core collapse at 5 kpc distance

3.4 Signal Start Reconstruction

In a future supernova signal the precise knowledge of the burst arrival time would be a very important parameter. It could be used for a triangulation with two or three detectors or the reconstruction of supernova properties such as the duration of the accretion phase.

To derive the time resolution of the signal onset, we simulate a large number of supernovae at varying distances and apply a fit of the form

$$\theta(t-t_0)\left(1-e^{(t-t_0)\tau}\right) \quad . \tag{3.13}$$

Here, τ is a free parameter and t_0 is the signal start. Figure 3.14 shows an example in the 2 ms binning.

Automatically fitting the signatures of supernovae at varying distances is not straightforward. For the fit to succeed, sensible starting parameters have to be found. The most successful approach was to fit the signal with a combined function consisting of a rising exponential as in equation 3.13 and a decaying exponential from the signal maximum on. Using the resulting parameters as a seed, the signal reconstruction lead to much better results.

Several models were simulated with normal and inverted hierarchies, mixing angles and distances and the signal onsets reconstructed. These were compared to the simulated start times and filled into histograms. The resolution is then determined from the width of the resulting distribution (see figure 3.15). Figure 3.16 shows that the resolution is a function of distance and can be described by

$$\Delta t(d) = a\Delta t + b\Delta t^2 \quad . \tag{3.14}$$

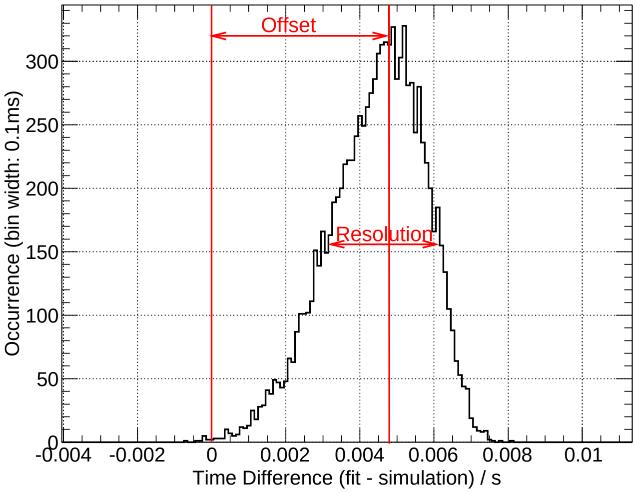

Figure 3.15: Difference between reconstructed and simulated start times for an ONeMg collapse at 5 kpc.

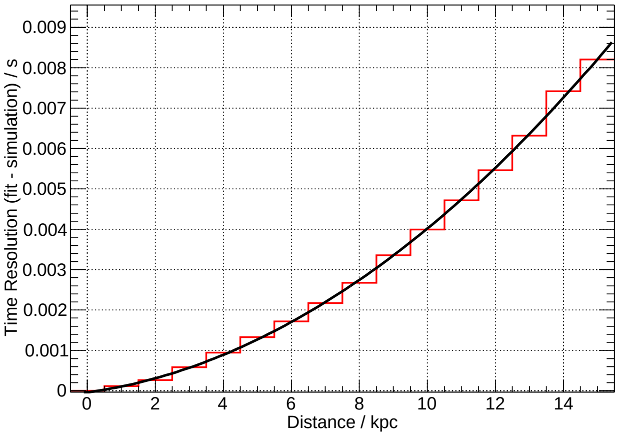

Figure 3.16: Time resolution with fit
This graph displays the time resolution of fits performed on ONeMg core collapse (2D) detector responses for normal neutrino mass hierarchy. It was fitted with the polynomial given in equation 3.14.

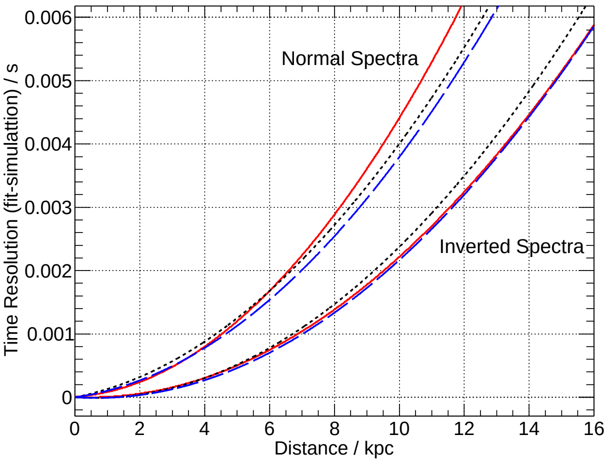

Figure 3.17: Fitted time resolutions for ONeMg collapses
Solid red denotes the 1D model with full neutrino opacities, broken blue the 1D model with the reduced interaction set and dashed black the two-dimensional model (for details, see section 3.1.1.4). The lower set of lines shows the inverted hierarchy case with large mixing and the upper set the time resolution for normal hierarchy (equivalent to a small mixing angle). The higher precision for the inverted case is due to a steeper gradient during signal start (see also [93]).

In the simulation only electron capture supernovae were used as they show the lowest signal and thus provide the most conservative resolution. The fit results are shown in figure 3.17 and in table 3.2.

Simulation Type	Normal Spectra		Inverted Spectra	
	$a/\frac{\mathrm{ms}}{\mathrm{kpc}}$	$b/\frac{\mathrm{ms}}{\mathrm{kpc}^2}$	$a/\frac{\mathrm{ms}}{\mathrm{kpc}}$	$b/\frac{\mathrm{ms}}{\mathrm{kpc}^2}$
2D Simulation	0.098	0.030	-0.031	0.027
Reduced Neutrino Interactions	0.072	0.031	-0.032	0.025
Full Neutrino Opacities	0.036	0.040	-0.023	0.024

Table 3.2: Parameters of the fits to the onset times
Normal and inverted spectra denote the cases of normal hierarchy or small mixing and inverted hierarchy with large mixing, respectively.

Finally, we need to take a look at the relative offset between fitted and simulated signal start. Figure 3.18 shows the differences for the one-dimensional simulation with full neutrino opacities. The offset depends on the distance of the supernova because small structures like the deleptonization peak vanish at larger distances, and will therefore not influence the fit anymore. At large distances, the signal disappears in the noise. The shape and even the relative differences are very similar for all simulations examined. For a supernova at unknown distance, one would have to assume a systematic

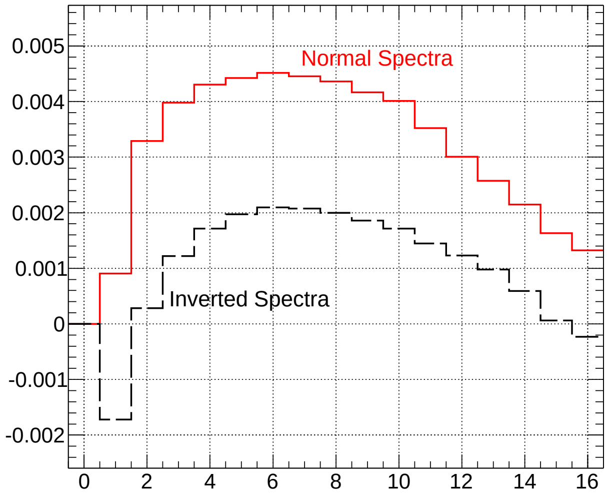

Figure 3.18: Offset of time reconstruction

uncertainty of $\sim 4\,\text{ms}$. If, however, the distance can be determined (typically 5%-10% using optical methods and $\sim 5\%$ using the deleptonization burst [17]), the offset can be corrected for.

3.5 Systematic Uncertainties

The detector specific uncertainties are shown in table 3.3. Earth matter oscillations, which were not considered in this thesis, can lead to a reduced number of PMT hits depending on neutrino mass hierarchy, θ_{13} mixing angle and direction of the supernova. [93] considered these effects in great detail.

As no benchmark exists for the supernova models, we do not estimate a systematic uncertainty. It is expected to be quite large.

Systematical uncertainty	Estimate / %	Source
Effective photon volume	~ 12	2.4.1.3
$e^{\pm}$ track length	~ 5	2.4.2
Cross section for $\bar{\nu}_e(p,n)e^+$ (scaled to total rate)	~ 1	2.4.3.1
Cross section for $\nu(e,e)\nu$ (scaled to total rate)	~ 1	2.3.1.2
Cross section for $\nu(O,X)e$ (scaled to total rate)	~ 3	2.3.1.3
Earth matter oscillations	-8	[93]
Total	$+13$ / -16	-

Table 3.3: Uncertainties on the signature predictions

4 AMANDA Supernova Search

> All things appear and disappear
> because of the concurrence of causes
> and conditions. Nothing ever exists
> entirely alone; everything is in
> relation to everything else.
>
> Siddhārtha Gautama

AMANDA collected a large amount of supernova data in its nine years of operation. One of the main goals of this work was the implementation of effective filtering methods to clean the data sample and search for supernova signatures.

4.1 Analysis Approach

To identify a supernova neutrino burst, a robust observable that effectively describes collective rate increases in the light sensors is essential. While the simple sum of sensor rates is a reasonable observable in the case of IceCube (see [93]), the same cannot be said for AMANDA (see section 4.4). The method described in the following was first introduced in [146] and later applied by [73]. It is optimized for signals small compared to the background level which is true for most supernova explosions in our galaxy.

4.1.1 Theory

We measure a pulse rate r_i of a given optical module i by counting a number of pulses n_i in a time window Δt:

$$r_i = \frac{n_i}{\Delta t} \tag{4.1}$$

with i ranging from 1 to the total number of optical modules N_{OM}. Figure 4.1 shows the distribution of pulses within 10 min and demonstrates that it can satisfactorily be described by a normal distribution. In section 4.2 it will become clear that this is not the case if the observed time frame extends beyond $\mathcal{O}(10\,\mathrm{min})$. However, for the calculation of the collective rate deviation, the approximation with Gaussian shapes is essential.

The collective rate deviation $\Delta\mu$ of all OM noise rates r_i from their individual mean rate μ_i is obtained by maximizing the likelihood function

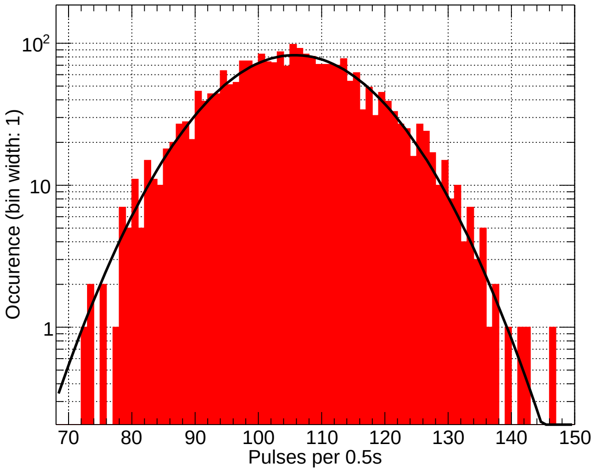

Figure 4.1: Pulses recorded by OM #001 during 10 min
The Gaussian fit to the pulse distribution results in $\mu = 105.8$, $\sigma = 11.3$ *and a reduced* $\chi^2 = 1.2$.

$$\mathcal{L}(\Delta\mu) = \prod_{i=1}^{N_{\text{(D)OM}}} \frac{1}{\sqrt{2\pi}\,\sigma_i} \exp\left\{-\frac{(r_i - (\mu_i + \epsilon_i\,\Delta\mu))^2}{2\sigma_i^2}\right\} \tag{4.2}$$

for the fluctuation hypothesis $\Delta\mu$. ϵ_i denotes the relative sensitivity in-between the modules[1] and σ_i the standard deviation of the OM rates. Minimizing $-\ln\mathcal{L}$ leads to

$$\Delta\mu = \sigma_{\Delta\mu}^2 \cdot \sum_{i=1}^{N_{\text{OM}}} \frac{\epsilon_i\,(r_i - \mu_i)}{\sigma_i^2} \quad , \quad \text{with} \quad \sigma_{\Delta\mu}^2 = \left(\sum_{i=1}^{N_{OM}} \frac{\epsilon_i^2}{\sigma_i^2}\right)^{-1} \quad . \tag{4.3}$$

For simplicity, we will later investigate the significance of the collective rate deviation defined as

$$\mathfrak{s} \equiv \Delta\mu/\sigma_{\Delta\mu} \quad . \tag{4.4}$$

As a supernova signal is expected to produce light in the whole detector, we will need a measure for the compatibility of a collective rate deviation $\Delta\mu$ with an isotropic and homogeneous illumination. The logical choice for such a value is the χ^2:

$$\chi^2(\Delta\mu) = \sum_{i=1}^{N_{\text{OM}}} \left(\frac{r_i - (\mu_i + \epsilon_i\,\Delta\mu)}{\sigma_i}\right)^2 \quad . \tag{4.5}$$

---

[1] For the case of AMANDA, the differences in glass transmittances between the first OM generation (B4) and the later generations are crucial. For IceCube, it will account for the different quantum efficiencies of the DeepCore and the standard modules.

In order to suppress high rate deviations due to anisotropic illuminations, we will later place a cut on the χ^2-confidence of data point.

All necessary values are described by simple, well defined sums and can easily be calculated during run time[2]. In [73] three different time binnings have been implemented:

0.5 s: This is the finest binning available to the analysis.

4 s: As argued in [155], the neutrinos of SN1987A are roughly compatible with an exponentially decaying rate of $\tau = 3\,\mathrm{s}$. The optimal time frame for the detection of such a signal is $\approx 3.8\,\mathrm{s}$. With 0.5 s binning, a value of 4 s is closest.

10 s: The largest binning was chosen in accordance to the time frame where most neutrinos from SN1987A were detected.

These time windows are not necessarily optimal for current supernova models. We will later rebin the data to obtain a better detection efficiency.

As already mentioned before, the formulas given in this section are optimal for the case of small signals, i.e. $\Delta\mu \ll \mu_i$. If the rate deviation reaches the order of the noise level or above, the following replacement has to be made:

$$\sigma_i^2 \rightarrow \sigma_i^2 + (\epsilon_i \sigma_{\Delta\mu})^2 \quad . \tag{4.6}$$

Unfortunately, $\Delta\mu$ can no longer be determined analytically for this case. Investigations looking for the best approach to deal with large signals are currently ongoing. We will neglect the repercussions for now as in most supernova scenarios, the rate increase becomes only problematic at very short distances (e.g. 1 kpc for the Lawrence-Livermore model), corresponding to a very small fraction of explosions ($< 1\%$).

4.1.2 Estimates for Mean and Standard Deviation

For the calculation of collective rate deviations via equation 4.3, the mean μ_i and the standard deviation σ_i need to be determined. Effective estimates can be derived by calculating the mean value $\langle r_i \rangle$ and the variance $\langle (r_i - < r_i >)^2 \rangle$.

These statistical estimates provide insight on the background characteristics of the modules. A dataset used for average estimation should fulfill three criteria:

- If possible, the data should be symmetrical around the bin being analyzed.
- The time frame around the investigated data point should be excluded.
- While the reference set should be much longer than the expected signal, it should also be sufficiently short to follow slow rate changes, e.g. from seasonal variations in the muon rates.

---

[2] Unfortunately, this is not the case for the smaller time binnings of 10 ms for AMANDA and 2 ms for IceCube. Here, the pulse distributions have to be described by the Poisson function and the resulting equations can no longer be be solved analytically (see [116]).

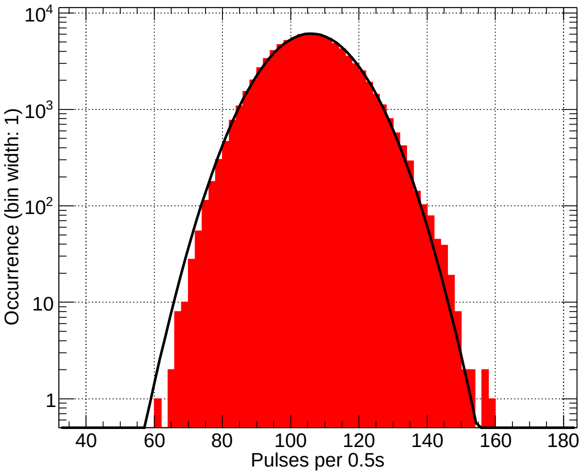

Figure 4.2: Recorded pulses of OM #001 during run 1000 in year 2002
The reduced χ^2 *of the fit with the Gauss function is* 7.2 *with parameters of* $\mu = 105.9$ *and* $\sigma = 11.2$.

In this and previous works a data buffer of 10 min length was used. It is large compared to the expected signal length of ~ 15 s and still compatible with the Gaussian expectation (see figure 4.1). In most cases, the buffer will be symmetrically placed around the bin being investigated with the exception of run start and stop. At present, 60 s around the analyzed data point are symmetrically excluded from the average building.

4.2 OM pulse distribution

If one examines the OM pulses in a time windows significantly larger than 10 min, asymmetries become evident. Figure 4.2 shows the same OM as before, now for 12 h of data taking. The pulses show a clear skewing to the right and can no longer be approximated by a normal distribution.

Let us increase the relevant time span even further. From the pulses recorded for OM #001 in the year 2002 (see figure 4.3), the skewing to the right becomes more obvious. We also notice that a Poissonian distribution would be to slim to describe the measurements.

Figure 4.4 shows the fano factors $\sigma/\sqrt{\mu}$ of the pulse distributions for the B10-19 generations for three different settings of the dead time τ. We see that a higher τ leads to a more Poissonian shape and thus conclude that the broadening of the pulse distributions is related to afterpulses (see section 2.2.3).

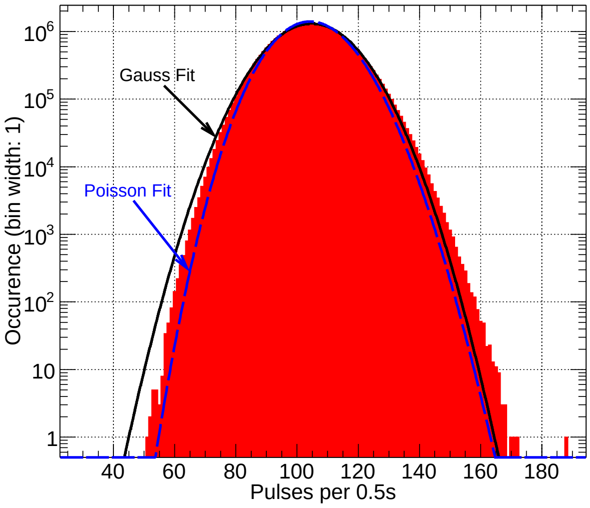

Figure 4.3: Recorded pulses of OM #001 during the year 2002
For a mean pulse rate of $\langle r_{001} \rangle = 104.8$ *as in this example, we would expect a standard deviation of* $\langle (r_{001} - \langle r_{001} \rangle)^2 \rangle = \sqrt{\langle r_{001} \rangle} = 10.2$ *which is too small when compared with the actual value of* 11.4*.*

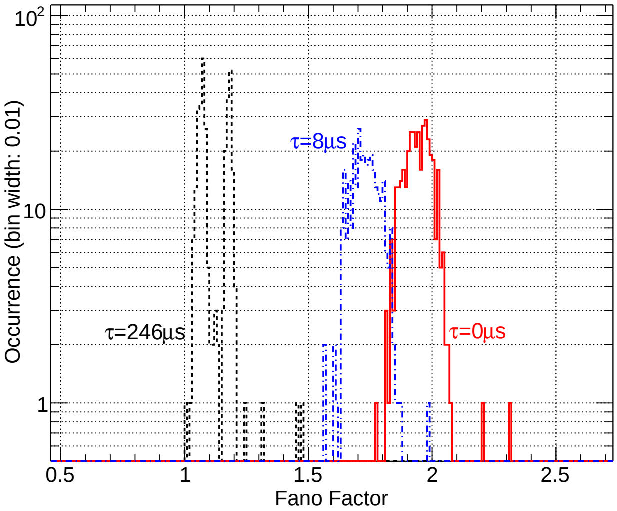

Figure 4.4: Distribution of the OM pulse fano factors for the years 2001 ($\tau = 8\mu s$), 2002 ($\tau = 246\mu s$) and 2003 ($\tau = 0$)

4.3 The Dataset

The available data spans the years 2000 to 2008. Not all of this data has been taken under the same conditions.

In the years 2000 and 2001, only a fraction of the B13 modules were attached to the SNDAQ and the artificial dead time was set to $\tau = 8\,\mu$s. In 2003, strings 11-13 and 17 were included in the supernova stream. 2003, most of 2005 and the beginning of 2006 the data taking did not use any artificial dead time at all due to software instabilities[3]. Table 4.1 shows the dead times τ for the available data. Furthermore, trigger settings of the DAQ hardware have been changed from time to time, introducing further differences into the data. Unfortunately, most of these reconfigurations were not properly recorded so that they could only be reconstructed from rate changes of the individual OMs.

Year	τ / μs
2000 & 2001	0.008
2002	0.246
2003	0.0
2004	0.256
2005	0.256 / 0.0
2006	0.0 / 0.256
2007 & 2008	0.256

Table 4.1: Dead time settings for the available data.

Note that for 2005 we will not investigate the data taken with $\tau > 0$, because it only extended from January 1 to March 14. The maintenance phases and construction works (see section 4.4.1.2) leave us with 14 days of data; an insufficient period to do reliable quality estimations.

Adding up the data from all years, we arrive at a total detector uptime of 6.3 a.

4.4 Quality Inspection

Unfortunately, the AMANDA data shows strong fluctuations and a poor stability. For all datasets, a careful inspection of many quality parameters is necessary to ensure a stable and reliable data stream. As many changes to the detector were made over the years, each set can be quite different (see section 4.3), and thus, separate checks are necessary for each data taking period.

The majority of the cut optimizations has to be done visually because the large differences in the data stability between the years do not allow an automatized approach.

---

[3] In 2003, a completely new version of the SNDAQ was installed [3] which had to be patched in 2005 to handle messages to SNEWS [73]. In the process a bug in the artificial dead time setting was introduced.

4.4.1 OM Stability Checks

Qualification or disqualification procedures of optical modules discard sensors when their behavior differs from the bulk of all OMs. Depending on the cut, modules are removed only for a single bin, for a whole run or the entire dataset.

4.4.1.1 Online Tests

The first cuts applied to the datasets are performed online [73] and aim at enforcing compatibility between the pulse distributions and the expected Gaussian shape. Modules failing these checks are removed from the analysis for the investigated bin and rechecked for the next one.

Mean Rate

Modules with averages μ_i strongly deviating from the bulk of the data is marked as bad. Due to the exclusion window around the analyzed bin, a signal would not affect the average rates at the time of interest. The cuts applied to the mean rates of all the datasets are shown in table C.1 with the percentage of OMs disqualified (refer to figure C.1 for an example).

Fano Factor

The fano factor or broadening factor $\sigma_i/\sqrt{\mu_i}$ can be seen as a measure for the compatibility of a distribution with a Poissonian shape. For a simple counting experiment, one would expect a fano factor close to unity. However, due to correlated afterpulses (see also section 2.2.3), the broadening factors are mostly larger than one. Table C.2 shows the cuts applied over the years.

Skewness

Last of the OM quality checks performed in real time are cuts on the skewness. It is the third standardized central moment of a distribution and defined by

$$s_i = \frac{(r_i - \mu_i)^3}{\sigma_i^3} \quad . \tag{4.7}$$

A skewness of zero describes a perfectly symmetrical distribution such as the normal distribution. The cuts applied on the absolute skewness are shown in table C.3.

4.4.1.2 Scaler Malfunction During Run

While investigating the fluctuations of the number of active channels, it became evident that during data taking the number of channels sending no data (rate smaller than 10 Hz) increased. The state was always back to normal at the beginning of each SNDAQ run. Figure 4.5 shows a representative case.

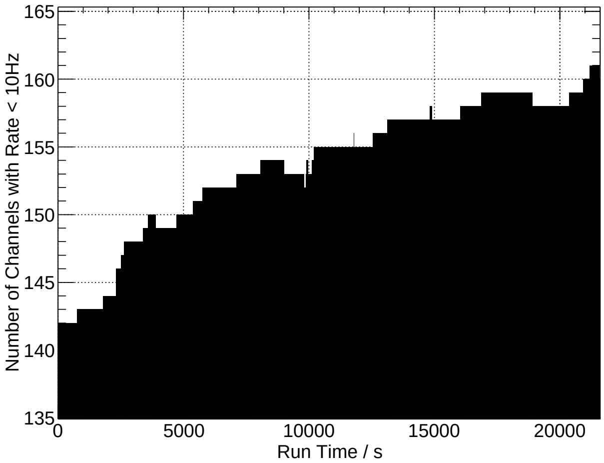

Figure 4.5: Number of OMs with fewer than 10 Hz in run 6201 from year 2006 versus the time after run start

Regrettably, this always happened with different channels and scalers. As this problem does not occur within IceCube, we suspect it was hardware-induced. Bugs in the DAQ code are unlikely, because the supernova data acquisition software of both experiments is all but identical. The only AMANDA hardware that could directly be affected by the SNDAQ were the supernova scalers.

Stability in the analysis is enforced by demanding a minimal pulse rate for each OM. Any sensors which drop below 10 Hz are excluded for the complete run.

4.4.1.3 Offline Requirements on OM Distributions

In the next step, we will place additional requirements on the individual pulse distributions to remove OMs which deviate from the norm. Note that the raw rates cannot be used for the investigation of the noise distributions because they are highly unstable. Typical examples are OMs falling silent during a run (see section 4.4.1.2) or rate jumps induced by a VLF (Very Low Frequency) antenna in 2004 (see figure 4.6). We therefore use data cleaned by the online cuts from section 4.4.1.1 and remove the dead channels mentioned in section 4.4.1.2. As the online analysis and the raw data streams are separate, a program was written which synchronizes them, enabling one to investigate the raw rates of OMs being tagged as stable.

OM Uptime

The first step is to take a look at the amount of data collected by each OM. Only if enough data is available, an investigation of the pulse distribution is done (see figure 4.7). A minimal lifetime was required for each OM (see table C.4).

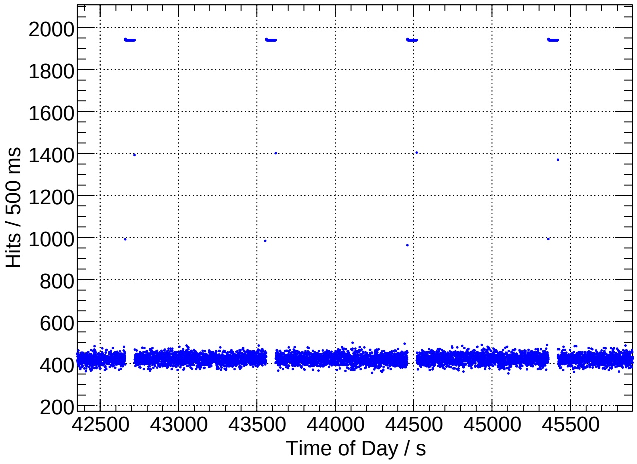

Figure 4.6: VLF jumps of OM 200 in the year 2004

During 2004, a VLF antenna was installed at pole which induced strong rate jumps in a large part of the optical modules. As the signal was periodic it could easily be removed from the data. By the end of 2004, a VLF filtering was installed and later data was no longer affected.

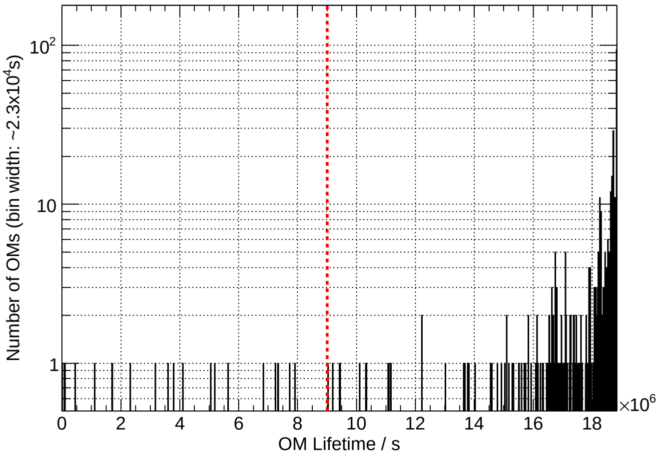

Figure 4.7: Uptime of the OMs in the year 2002

Shown is the time the individual modules were active, judged stable and thereby contributing to the online analysis. Using this histogram, a minimum uptime of $9 \cdot 10^6$ s *was required for each OM.*

Fits

As demonstrated in 4.2, neither Gauss nor Poisson functions can be used to properly describe the pulse distributions. Many different statistical functions were tried and it was found that shifted, broadened Poisson and shifted lognormal functions are best at describing the OM pulse distributions.

The first candidate, the modified Poisson, is described by:

$$p(x;\lambda,s,a) = \frac{\lambda^{a(x-s)}e^{-\lambda}}{\Gamma(a(x-s))} \quad . \tag{4.8}$$

Fixing the broadening at $a = 1$ much improved the results compared to a Poissonian, but still only about half of the OMs could be fitted sufficiently well. Allowing the broadening as a fit parameter lead to much better results. However, the given function is unable to fit the pulse distributions for datasets without dead time and its central moments can not be easily derived.

We now take a closer look at the other candidate, the lognormal distribution. It performed well during all fits (independent of τ) especially after introducing a shift parameter s:

$$p(x;\mu,\sigma,s) = \frac{1}{(x+s)\sigma\sqrt{2\pi}} \exp\left\{-\frac{(\ln(x+s)-\mu)^2}{2\sigma^2}\right\} \quad . \tag{4.9}$$

Contrary to the modified Poisson, the central moments of the lognormal distribution can be easily derived (see appendix B). Expectation value and variance are given by equation B.6:

$$\begin{aligned} \langle x \rangle &= e^{\mu+\frac{\sigma^2}{2}} - s \quad \text{and} \\ V(x) &= (e^{\sigma^2}-1)e^{2\mu+\sigma^2} \quad . \end{aligned}$$

Applying a lognormal fit to the pulses recorded with OM #001 in the year 2002 yields figure 4.8.

While most of the time, lognormal fits to the rates perform well, there are exceptions to this rule. Some OMs show increased or decreased rates during prolonged periods, leading to warped distributions. Said OMs seem otherwise well behaved which is why their complete disqualification from the dataset would be unjustified. Instead of investigating the absolute rates we subtracted the rate average of each individual run, $\langle r_i \rangle_{\text{run}}$, from the data before performing the fits. Figure 4.9 shows the two distributions for OM #211 of year 2002.

For each dataset, lognormal fits were applied, their reduced χ^2 plotted into separate histograms and a maximal reduced χ^2 determined (figure 4.10 shows the reduced χ^2 for the year 2002). Table C.5 shows the maximal allowed reduced χ^2 for each dataset along with the number of OMs lost.

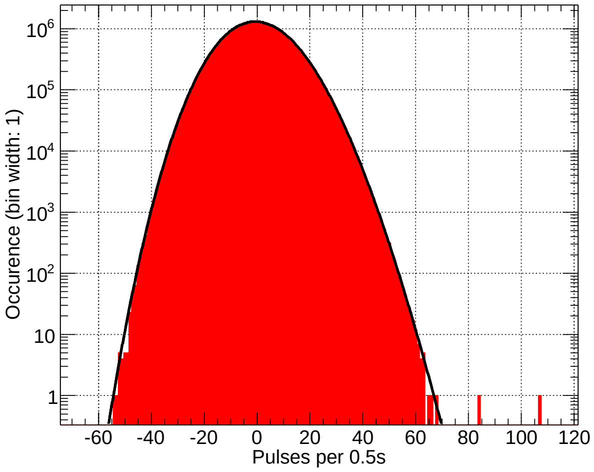

Figure 4.8: Lognormal fit to rate deviations of OM #001 from year 2002
The fit resulted in a reduced χ^2 *of 2.1 and yielded the parameters* $\mu = 5.57$, $\sigma = 0.043$ *and* $s = 261.3$. *Note that it was applied only to the central* $\pm 5\sigma$ *of the distribution.*

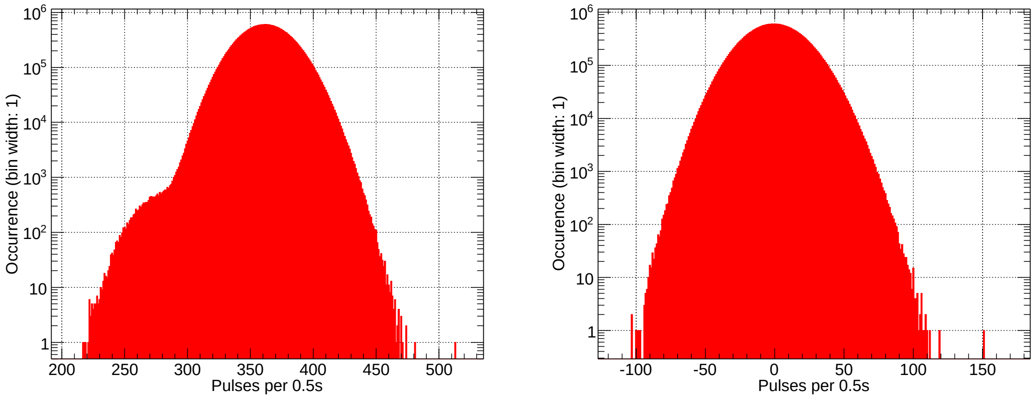

(a) Pulses

(b) Pulse deviations from average

Figure 4.9: Rates and rate deviations of OM #211 in the year 2002
Clearly a lognormal fit on the left-handed distribution would disqualify the OM. However, the right-handed histogram shows that this module is quite usable.

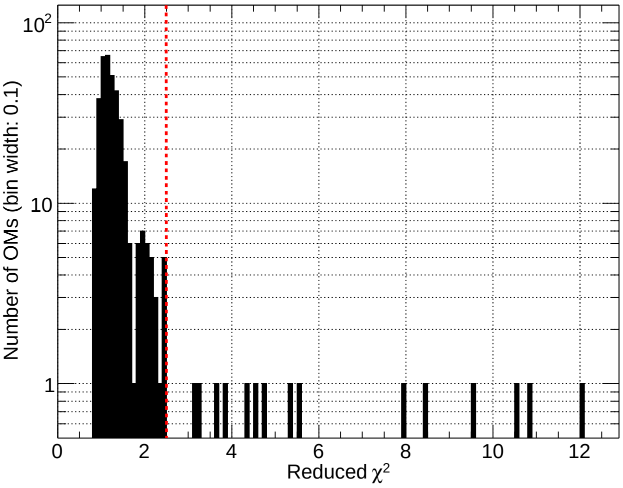

Figure 4.10: Reduced χ^2 of lognormal fits of the year 2002
The dashed red line shows the cut at χ^2/n.d.f. = 2.5*. This requirement removes 28 of 390 OMs for the year 2002.*

Tails

While the lognormal fits generally perform quite well on the data, they are insensitive to effects in the tails. However, strong fluctuations outside the bulk of the data can significantly influence our collective rate deviation observable. We therefore decided to place another cut based on the perturbation of the data.

Figure 4.11(a) shows OM #056 where an acceptable fit could be performed, but strong perturbations remain. To quantify these, we remove the inner 99.99% of the lognormal distribution from the recorded pulse distribution (see 4.11(b)). The absolute of the remaining data is summed up and divided by the number of entries of the initial pulse distribution. We get the probability for data lying outside 99.99% of the expected lognormal. For each dataset, these probabilities are histogrammed and cuts are applied (see figure 4.12 for the year 2002).

Table C.6 shows the cuts applied to all datasets with the number of OMs removed.

4.4.1.4 OM Activity

As seen in section 4.4.1.1, the number of OMs active in the SNDAQ can change within a run. Because we want to keep the data as stable as possible, it is important to restrict the number of OM fluctuations. Figure 4.13 shows the number of times OMs were reactivated during the runs of year 2002. To increase stability, we demand that no OM gets requalified more than a given number of times during a run. If an OM exceeds its allowed number of activations, it is disqualified for the whole run. Table C.7 shows the requirements for all the datasets.

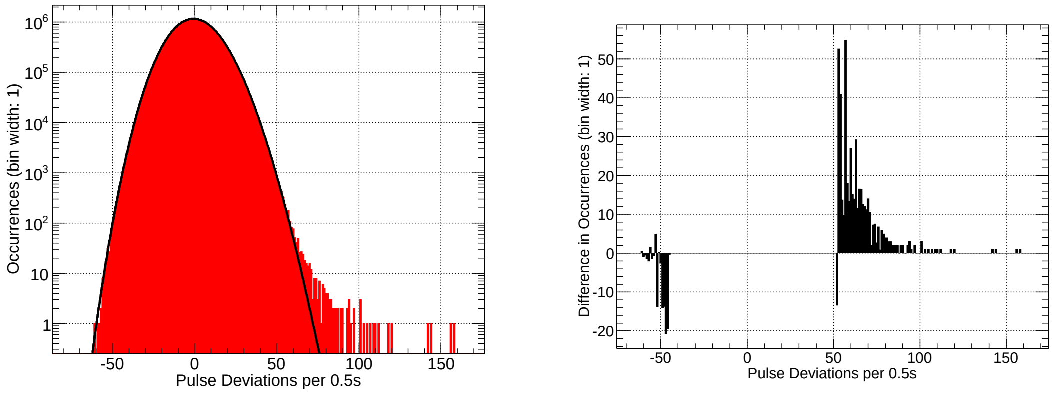

(a) Recorded pulses with a lognormal fit applied

(b) Differences in the occurrences between recorded data and lognormal approximation

Figure 4.11: OM #211 in the year 2002
Just from the fit to the pulse distribution (see left figure) the OM would be qualified for the analysis with a reduced χ^2 *of 2.2. However, the distribution shows a long tail. The picture on the right side displays the difference between the recorded pulses and the lognormal expectation. As we are only interested in perturbances in the tails, entries in the inner 99.99% of the distribution, the interval* $[-45.6, 52.0]$, *have been set to zero.*

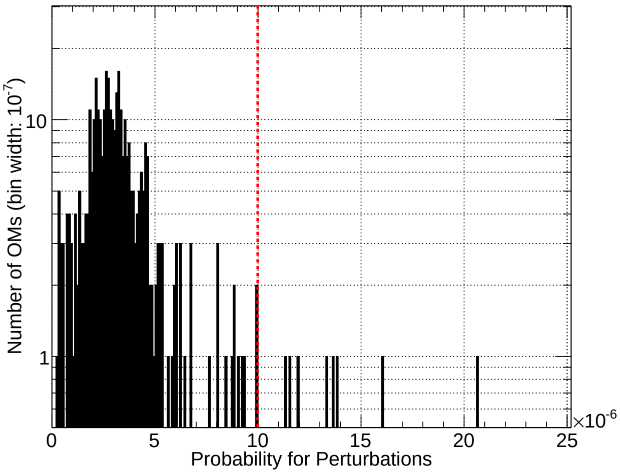

Figure 4.12: Perturbation Probabilities for the OMs of the year 2002
The dotted red line shows the cut of 10^{-5}, *removing 8 OMs from this dataset.*

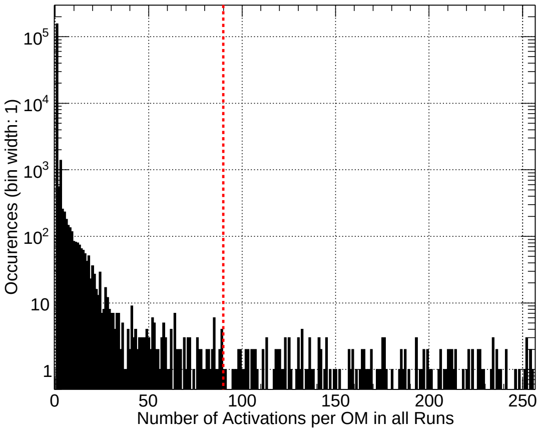

Figure 4.13: Number of times an OM is activated during a run in 2002
The histogram shows the number of activations for each OM in each run of the year 2002. The more often an OM is switched on or off, the more it fluctuates. For 2002, a cut has been placed at 90 activations per OM during a run.

4.4.1.5 Rate Drops in OMs

During the investigation of the data, it was found that from time to time the rates dropped significantly below the expectation, but did not go all the way down (see figure 4.14). Generally, OMs showing this sort of behavior should be excluded by the online cuts. However, at the fringes of the moving average window, and in the exclusion zone at its center, the data will not be disqualified. Such drastic drops of the OM rates influences the statistical observables and the collective mean rate deviations.

To eliminate this problem, an additional OM disqualification process is applied. With the lognormal fits from above, we have an expectation for the pulse rate of each OM. With these, we define a minimal allowed rate such that measuring a number of counts below this value happens in average once every ten years. In the example given in figure 4.14, the lower rate limit would result in 144 pulses per 0.5 s.

Sometimes the rates of a very large number of OMs drop simultaneously, leading to them all being removed. Due to the cut on the number of OMs qualified in the next section, the whole run might be dropped. To avoid this, the data is cleaned around the offending times by removing the related moving average window (10 min) if more than ten OMs show intense rate drops.

4.4.2 Active channels

As the number of OMs qualified during the analysis is another measure of detector stability, a minimal number of active channels is required. Figure 4.15 shows the number of active channels during the year 2002, and table C.8 summarizes the cuts applied to all datasets with and amount of data lost.

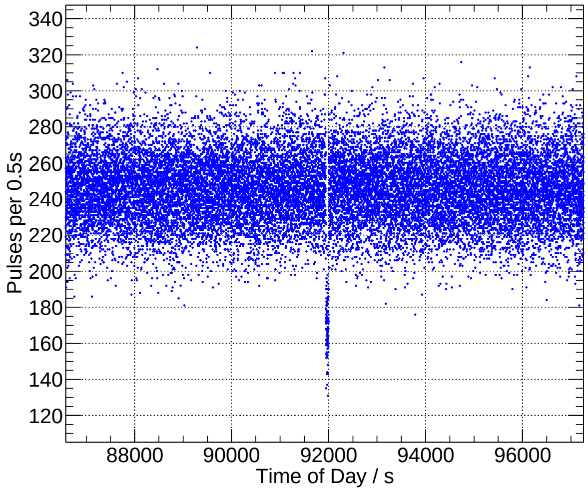

Figure 4.14: OM #440 during run 0939 of year 2002

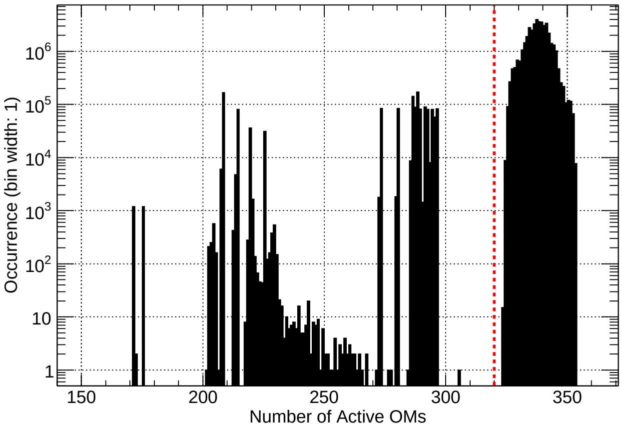

Figure 4.15: Number of OMs active in the analysis during 2002
The cut at 320 OMs applied to the dataset of 2002 is depicted by the dashed red line.

4.4.3 Cuts on Anisotropic Illuminations

A strong rate increase in a single qualified OM will raise the collective rate deviation, and consequently, an indication for the isotropy of an illumination in the ice is essential. The χ^2 defined in equation 4.5 is one possibility. However, it must be investigated whether this method is sufficiently sensitive for the supernova search.

To test the performance of the χ^2 cut, background was simulated and random rate outbursts were added. By modifying the strength of the signal and the number of modules chosen to burst, it was possible to investigate the pros and cons of the χ^2-method. The signals were applied starting from 10 OMs and were raised in steps of 10 modules. The burst strengths were varied from 10 Hz to 150 Hz in 10 Hz increments. As we are interested in the number of times the system is triggered by an anisotropic signal, we look for data with a significance $\mathfrak{s}$ higher than 6.0 with a χ^2 residing in 100%, 99.9% and 90% intervals. Figure 4.16 shows the results. While the χ^2 cut is very efficient for a few loud modules, it is less so if a significant amount of OMs contribute. In case of AMANDA already 40 bursting modules can lead to a false trigger. At first glance this might seem like a statistically unlikely number, however, it is little more than the number of OMs on a single string. This might become a problem when fluctuations in the power supply or static discharges due to strong surface winds influence the equipment.

A further problem that immediately meets the eye, is the reduction of triggers for large numbers of modules bursting at high rates when constraining the χ^2 confidence. Because the supernova search is primarily aimed at small signals from distant supernovae, we assumed an illumination small compared to the noise level in the χ^2 definition. As already stated in section 4.1.1, the equations for the collective rate deviation and the χ^2 (equations 4.3 and 4.5) should be modified in the case of larger signals. As the resulting formulas are not analytically solvable and the bulk of all potential supernovae are quite distant, we will stick to the current method.

To improve on the χ^2 discrimination, many different approaches were tried:

- Modules with extreme rates were removed from the data sample; the differences between the original and the cleaned significance was investigated.
- The difference between median and mean of the individual rate deviations $\epsilon_i(r_i - \mu_i)$ was tested.
- For each signature, the extreme 50% (minimal and maximal) were compared to the inner 50% of the rate deviation distributions.
- The width, skewness and kurtosis of the individual rate deviation distribution were examined.
- Kolmogorov-Smirnoff tests of the rate deviations with a Gaussian and reference data points were performed.
- Spatial isotropy was examined with a center of gravity test and a clustering approach.

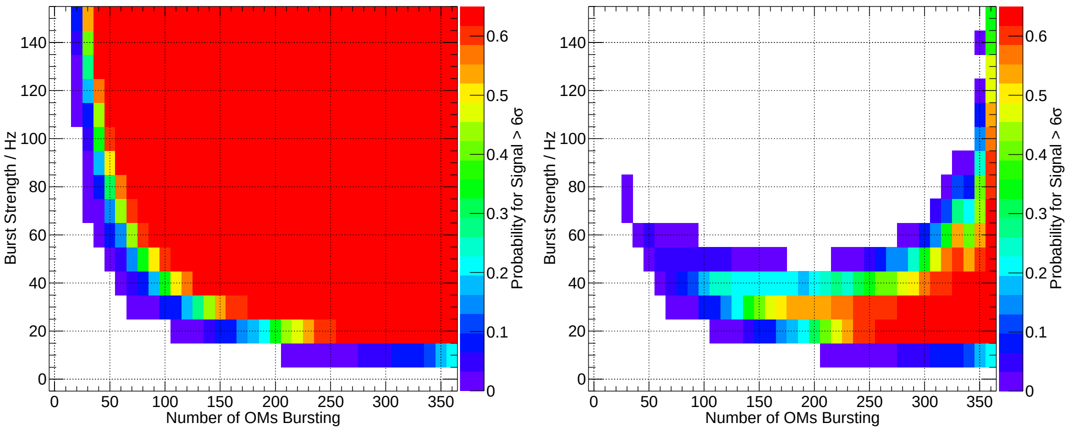

(a) No χ^2 cut (b) $\chi^2 \in 99.9\%$

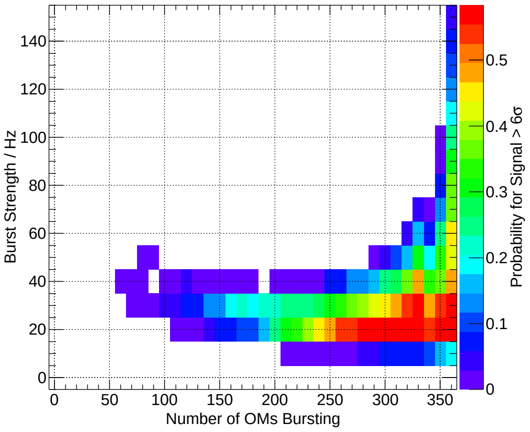

(c) $\chi^2 \in 90\%$

Figure 4.16: Performance of the χ^2 discrimination
The probability for a burst to reach a significance $\mathfrak{s}$ *higher than* 6.0 *while remaining in the requested* χ^2 *interval is given by the color. White denotes a probability of zero. During the investigation, 358 number of modules were simulated.*

Neither of these methods performed better than the χ^2 cut which is why it will be used in the supernova search.

4.4.4 Time Stamps

In this step, we place some basic requirements on the timing information of the data.

First, the time stamps are required to show sensible numbers. Especially at run start, the timings are often out of range (e.g. the day of year becomes greater than 1000). Second, the bins are required to have the correct time difference from their neighbors, i.e. 500 ms. Approximately $\sim 4.6\%$ of the data is discarded in this way.

4.4.5 Run Disqualification

Pole Seasons

During the austral summer, many maintenance and calibration operations were performed, leading to unstable data during these periods. For this reason, only data from beginning of March to end of October was used. While the polar season is usually finished by mid-February, work on the detector hardware and software often continued for a few weeks. Unfortunately, very few of these operations were logged, so a precise exclusion is impossible.

Time Instabilities

Runs which loose more than 30% of their data to the time stamp cleaning described in section 4.4.4 are rejected. 71 files, most of them from 2008, did not pass this test.

Flasher Runs

For the muon track search, the correct knowledge of detector geometry and ice properties is essential. Therefore, calibration runs using artificial light sources as described in section 2.1.2.2 are routinely performed for the IceCube detector. As these can illuminate the ice around AMANDA, the respective periods have to be excluded from the analysis. Since installment in 2005, 252 runs from the AMANDA SNDAQ were synchronous to flasher activities.

Scanning Runs

Unfortunately, even after the above quality requirements, many runs still show unexpected and pathological behavior. Some examples are shown in figure 4.17.

Obviously, data of this kind should be excluded from any analysis. Many approaches for an automatic discrimination of unstable runs have been tried, but none performed satisfactorily. Unfortunately, the monitoring written for the standard data taking [156] was not synchronous with the supernova data and does not cover the same times (e.g. the years 2007 and 2008 do not feature at all). It was therefore decided to scan the

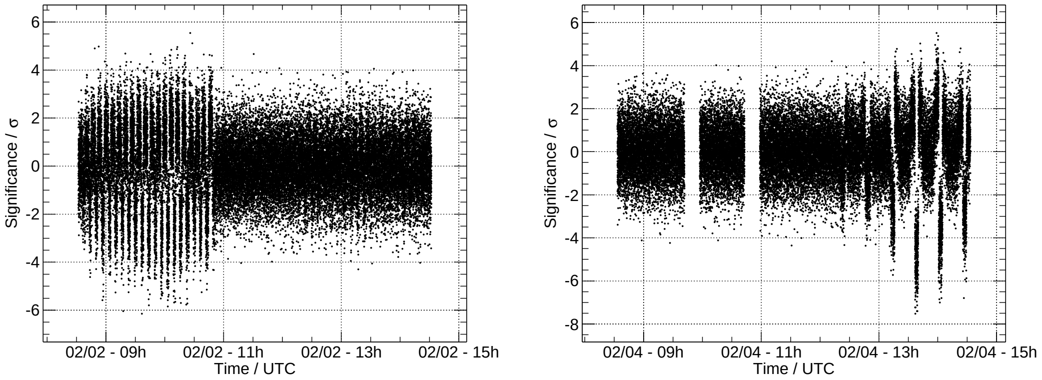

(a) Run 6943

(b) Run 6951

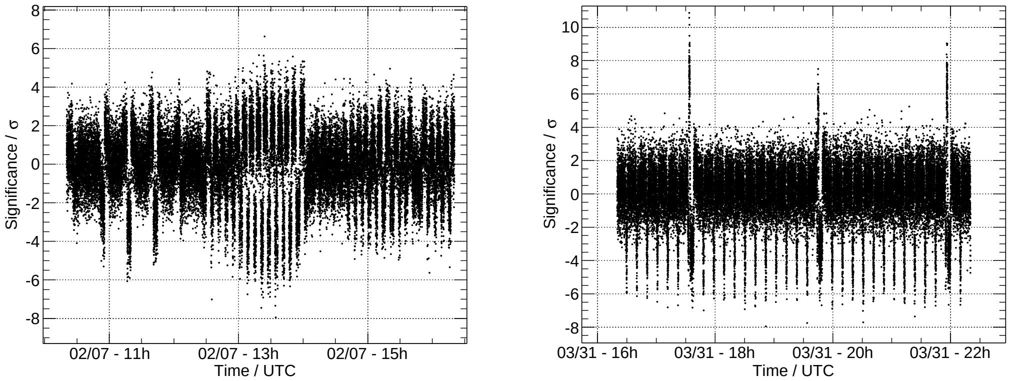

(c) Run 6965

(d) Run 7152

Figure 4.17: Significance over time for some unstable runs from the year 2007

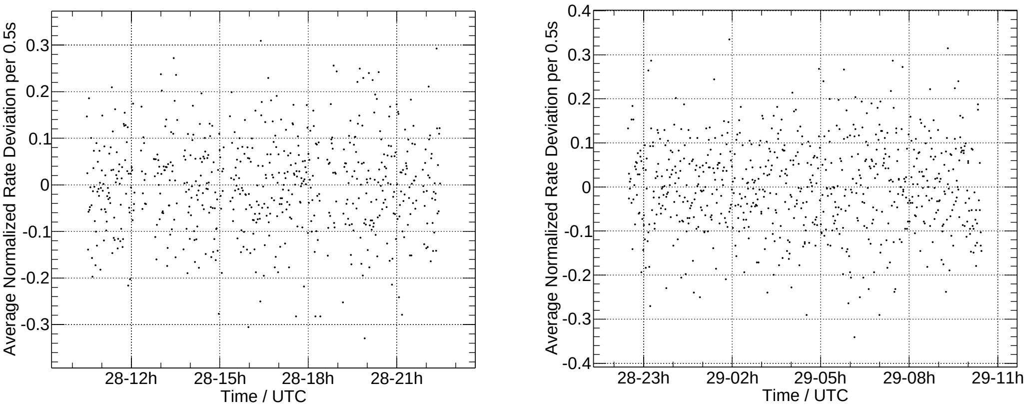

Figure 4.18: Normalized rate sum of simulated toy supernovae averaged over 1 min using only data with $\mathfrak{s} \in [-3, 3]$.
The runs contain more than ten supernova candidates with significances $\gtrsim 15$.

AMANDA supernova runs by eye. As one needs to stay unbiased with respect to supernova candidates, a direct check of rate deviation or significance is excluded.

Instabilities in the data taking can be expected to last longer than a few seconds, i.e. longer than the relevant timescale for a supernova and might influence the moving averages μ_i to which the actual rates are compared (see equation 4.3). The most direct and thorough approach would be the examination of the noise behavior of all OMs as a function of time. Such a method would have to be automatized and might be introduced in the future. At present, however, we will restrict ourselves to the examination of the sum of raw rates, excluding data above a predefined significance.

The simple ansatz $R = \sum_{i=1}^{N_{\mathrm{(D)OM}}} r_i$ is not a robust quantity in AMANDA. Instead of the simple sum of raw rates, we will take the rate deviation from their mean $(r_i - \mu_i)$, weighted with their relative efficiency ϵ_i and normalize the sum to the number of active modules N_{AC}:

$$\mathcal{R} = \frac{1}{N_{\mathrm{AC}}} \sum_{i=1}^{N_{\mathrm{AC}}} \epsilon_i (r_i - \mu_i) \quad . \tag{4.10}$$

For the stability examinations, we rebin the data to 1 min. To ensure that no potential supernova candidates are included, we require that all data points contributing have a significance inside the interval $\mathfrak{s} \in [-3, 3]$.

Before the checks, we run a toy Monte Carlo to ensure that supernova candidates are not affected. As a test signal, an exponentially decaying signal with a decay constant of $\tau = 3\,\mathrm{s}$ was used. About 1000 runs were simulated, each containing $5 \sim 10$ supernovae with signal strengths up to 60 kHz. As seen in figure 4.18, the typical average normalized rate deviations are unaffected.

We then proceed to exclude all runs which show steep rises, drops, significant clusters

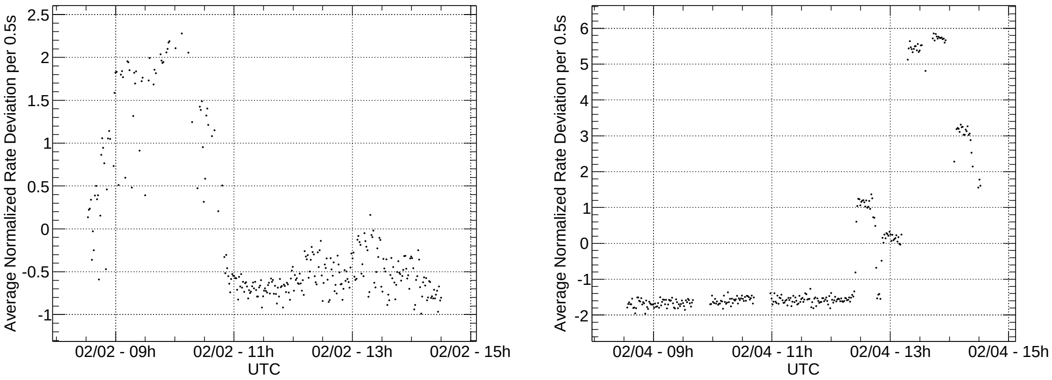

(a) Run 6943

(b) Run 6951

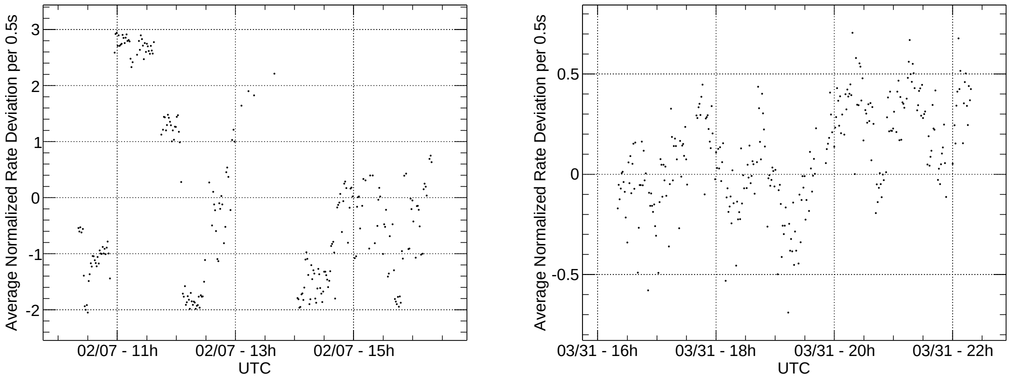

(c) Run 6965

(d) Run 7152

Figure 4.19: Normalized rate deviation averaged over 1 min for the unstable runs shown in figure 4.17

of outliers or periodic fluctuations. The average normalized rate deviations of the unstable runs shown in figure 4.17 are displayed in figure 4.19.

Out of 5664, 883 runs were excluded from the data due to unstable rates.

4.5 Longterm Rate Development

As mentioned in section 4.3, the conditions of the data taking changed with the years. To quantify the differences, be they man-made or naturally induced, we take a look at the average pulse rates. We notice jumps between datasets taken with different dead times τ but also between rates recorded with the same τ (see figure 4.20). These latter are caused by altered settings in the muon DAQ, such as increased pulse discrimination

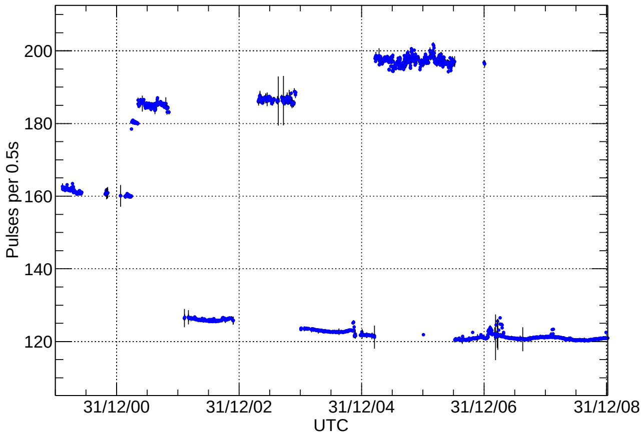

Figure 4.20: Mean pulse rates of OM #006, averaged over 24 h, for all the years

thresholds[4]. Years 2007 and 2008 yield the only datasets that are consistent, because work on the AMANDA muon data acquisition was discontinued at the end of 2006.

In spite of the jumps in the data, one notices slight changes as function of the seasons. Figure 4.21 shows the mean pulse rates of OM #003 using the dataset from the years 2007 and 2008 in a resolution of 24 hours. One observes a clear seasonal variation which is caused by the changing conditions in the atmosphere. With the antarctic summer, temperature increases, leading to expansion of the air and, therefore, lower density. Accordingly, pions produced by charged cosmic radiation have a larger mean free path in the upper atmosphere and therefore a higher decay probability. The number of atmospheric muons, the decay products of pions, is about 10% larger in summer than in winter (for more information on this subject see [157]). As the background pulses registered by the OMs also includes Cherenkov light caused by high energy muons, the OM rates will necessarily change with the seasons.

It was found that the variation of the pulse rates can be well described by a cosine function plus a constant and an exponential decay [93]:

$$\langle n_{\mathrm{OM}} \rangle(t) = n_{\mathrm{const}} + n_{\mathrm{dec}}\, e^{-\frac{t}{\tau}} + n_{\mathrm{atm}} \cos\left(\frac{2\pi}{T}(t - t_0)\right) \quad . \tag{4.11}$$

n_{const} describes the constant part of the background. It is composed of thermal noise, radioactive decay of long-lived isotopes and the average muon noise. The second element of the equation 4.11 denotes a slowly decreasing component of the background, which is not yet clearly understood. Parts are due to the freezing process, hereafter radioactive decay of isotopes with small lifetimes and degradation of the optical gel may also play a role. Last, the cosine function describes the fluctuations due to the changing muon rates. Figure 4.21 shows an OM fitted with this function.

---

[4] The pulse discrimination thresholds define the level above which a pulse will be counted. They were the same for both data acquisitions, and if they were altered, the noise rates changed accordingly.

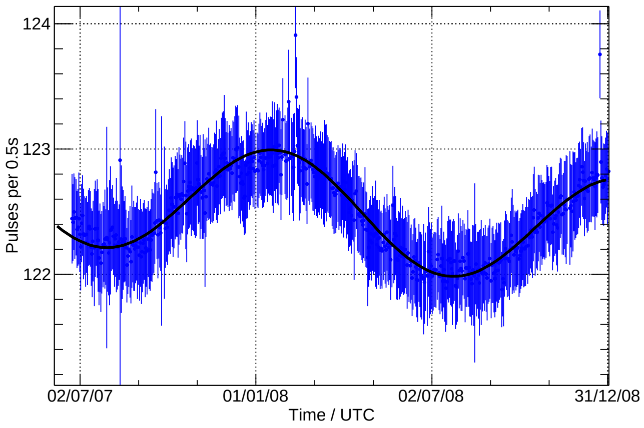

Figure 4.21: Mean pulse rates of OM #003 with cosine fit
The figure shows the mean pulse rate of OM #003 from mid 2007 to end 2008 in a resolution of 24 h. *One sees a strong seasonal variation due to changing muon rates. The data has been fitted with function 4.11.*

Unfortunately, only data taken with the modules of the B4 generation are stable enough to apply these longterm fits. The B10 and B13 modules have much larger spreads and are notoriously unstable, making them unusable for this purpose (figure 4.22 shows typical OMs of this generation). Another option would be the less noisy B19 OMs, however, their rates were quite erratic in the years 2007 and 2008. After selecting the OMs by visual inspection, only 30 of 112 B19 OMs remain (for comparison: 36 of 40 are usable in the case of the B4 generation).

Since the only seasonal variation known to affect the OM rates is in the muon production, the size of the constant n_{atm} should be directly proportional to the detection efficiency of the modules and the transparency of the surrounding ice. As few AMANDA modules are sufficiently stable, the efficiency cannot be determined individually for all modules. In [93] similar fits have been performed on data from the years 2007 and 2008 for IceCube DOMs. Figure 4.23 shows the mean variation amplitude versus depth for AMANDA and IceCube modules.

As expected, the amplitudes and thus the efficiencies are depth dependent because of the dust layers segmenting the ice (see section 2.4.1.1). The more dust in the vicinity of a module, the less light it can detect.

As the IceCube data is much more reliable due to better longterm stability and higher statistics, the IceCube depth dependence will later be used to determine the relative muon efficiencies of the modules for the background Monte Carlo. One can further use this data to determine a conversion factor between the IceCube DOMs and the AMANDA sensors. For this purpose, the AMANDA modules are replaced by IceCube modules at the relevant depths and a weighted average is calculated. It is then compared with the average of the original modules. The mean effects from seasonal variations for the AMANDA modules is given by:

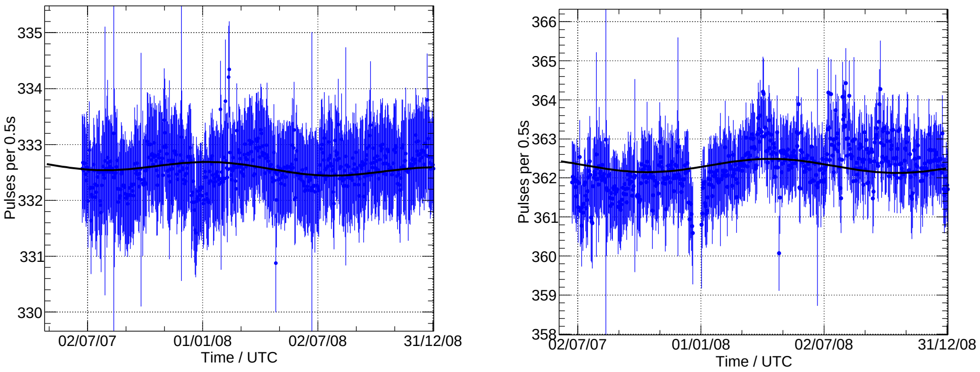

(a) OM #169

(b) OM #202

Figure 4.22: Mean pulse rates in 24 h resolution of typical B10/13 OMs
Fits according to equation 4.11 were applied and succeeded with reduced χ^2 *of* ≈ 0.3. *However, in both cases, the rate development shows large instabilities and thus, the fits cannot be seen as reliable.*

$$\begin{aligned} \langle n_{\mathrm{atm,B4}} \rangle &= 0.46 \pm 0.02 \quad \text{and} \\ \langle n_{\mathrm{atm,B19}} \rangle &= 0.61 \pm 0.04 \quad . \end{aligned} \tag{4.12}$$

Replacing the AMANDA modules with IceCube DOMs, we get:

$$\begin{aligned} \langle n_{\mathrm{atm,B4\rightarrow I3}} \rangle &= 0.80 \pm 0.02 \quad \text{and} \\ \langle n_{\mathrm{atm,B19\rightarrow I3}} \rangle &= 0.82 \pm 0.04 \quad . \end{aligned} \tag{4.13}$$

This yields the conversion factors:

$$\begin{aligned} \epsilon_{\mathrm{I3/B4}} &= 1.75 \pm 0.08 \quad \text{and} \\ \epsilon_{\mathrm{I3/B19}} &= 1.34 \pm 0.10 \quad . \end{aligned} \tag{4.14}$$

$\epsilon_{\mathrm{I3/B4}}$ reflects the difference between the cathode areas of 8 inch and 10 inch, the AMANDA and IceCube discriminator thresholds and differences in optical transmittances.

One can also determine the conversion factor between B4 and B19 of $\epsilon_{\mathrm{B4/B19}} = 0.76 \pm 0.07$. This compares well with a calculation based glass transmittances of $\epsilon_{\mathrm{B4/B19}} = 0.745$ [73].

Using these two determinations of $\epsilon_{\mathrm{B4/B19}}$, we estimate the systematic uncertainty to be $\sim 5\%$.

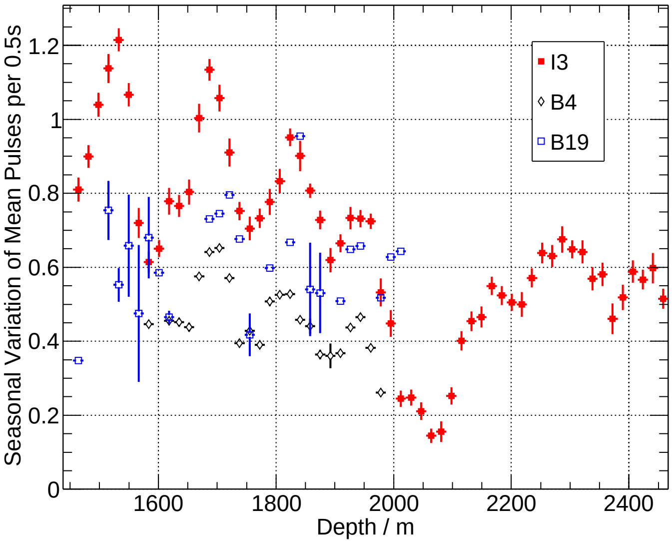

Figure 4.23: Seasonal variations of sensor pulses per 0.5 s versus module depth
Shown is the average constant of the cosine describing the seasonal muon variation, n_{atm}*, over its depth. The plot is segmented in* 17 m *bins because the IceCube DOMs have exactly this distance from each other. The red squares show the average seasonal variation of the IceCube modules deployed up to season 06/07, with roughly 20 entries per bin (according to 22 strings). The thick black lines show the B4 modules and the empty blue squares the B19 modules. For the AMANDA modules we obtain mostly only one entry per bin with a maximum of three. The ice structures are apparent. One also sees that the effect of muons is smaller in B19 and even smaller in B4 OMs when compared to IceCube.*

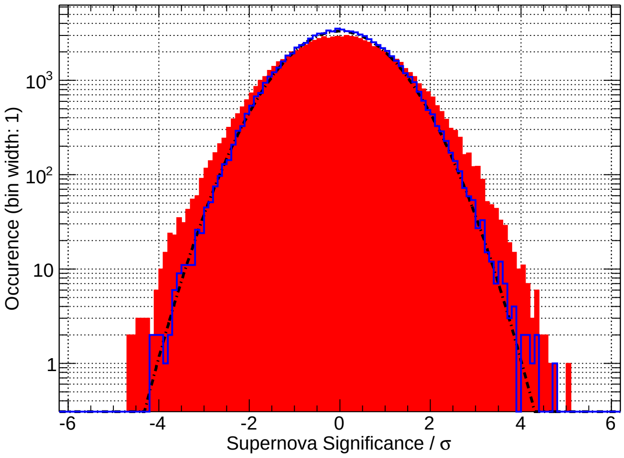

Figure 4.24: Significances of a run from 2002 with a simple background Monte Carlo *The filled red area shows the recorded supernova significances of run 0990, the blue line is the result from a simple Monte Carlo based on lognormal OM rate distributions only and the dash-dotted black line is a fit with a normal function with a fixed $\sigma = 1$.*

4.6 Background Simulation

One fundamental problem in most experiments is understanding the background.

In a first approach to understand the noise behavior, we simulate the distribution of the significance $\mathfrak{s}$ (as defined in equation 4.4) using only the lognormal functions found to describe the individual OM pulse (see section 4.4.1.3). In absence of external signals one would naively expect $\mathfrak{s}$ to follow a normal distribution with unit width centered at zero. Figure 4.24 compares the recorded significances to a normal distribution with $\sigma = 1$ and to the simple background simulation just described. As we see, neither the naive expectation nor the simple background simulation match the data. Simulating the detector background is not straightforward because the recorded pulse distributions do not only contain uncorrelated thermal and radioactive noise but also correlated illuminations from muons. While the seasonal of the muon rates changes can be neglected in our examinations, the statistical fluctuations can not.

The broadening in the data can be ascribed to fluctuations in the muon rates by synchronizing the muon data acquisition (μDAQ) and the SNDAQ. The μDAQ stores the full sample of muon tracks detected, except for the hit patterns, as nanoDST data. We count the amount of muons recorded during one 0.5 s SNDAQ bin and compare this number to the normalized rate deviation $\mathcal{R}$ as defined in equation 4.10. In figure 4.25 one can clearly see a strong correlation between these two measurements[5].

---

[5] While this approach turned out to be simple for the year 2004, it was not so for all datasets. At first, no correlation could be found in 2002. It later turned out that the time stamps of the supernova data preceded the muon data by 1 s, hiding any connection.

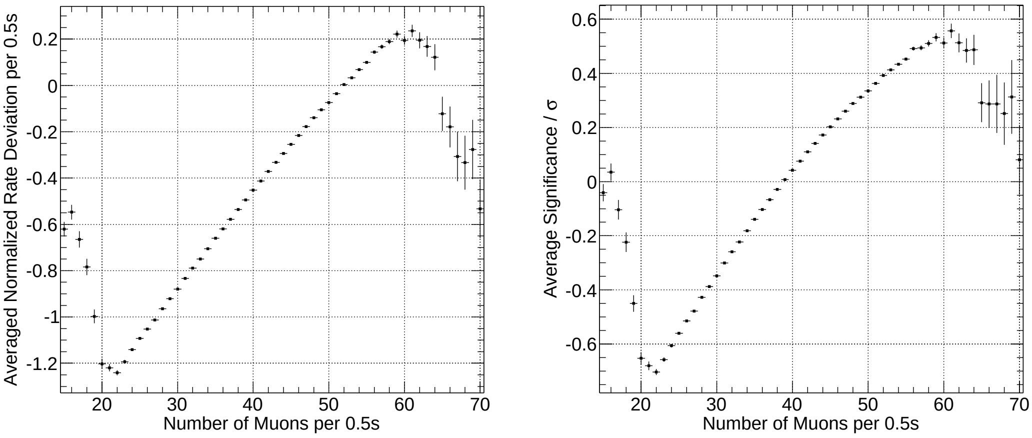

(a) Average normalized rate

(b) Supernova significance

Figure 4.25: Average normalized rate deviation and average significance versus the number of muons counted in a 0.5 s SNDAQ bin for the year 2004
For this figure, the muon measurements have been synchronized with the supernova data stream. Average values have been calculated for each number of muons detected and plotted into a profile histogram. The left figure confirms that more muons in the detector lead to collectively higher rates recorded by the SNDAQ which in turn leads to an increased significance as seen on the right. Because the significance is determined from comparison of the rates with a moving average of 10 min*, seasonal variation do not play a role. The different behavior in the tails is likely due to quirks in the detector. Examples are problems in the* μ*DAQ, cross-talk in the cables or OMs with unphysically high or low rates. Those perturbations do not always reflect back on the SNDAQ because of the completely separate data cleaning.*

It follows that the OM background distribution is a combination of the dark noise generated by its direct environment and the inherent noise behavior of the sensor on the one side and the Cherenkov light produced by atmospheric muons on the other. While the first phenomena are completely uncorrelated between the OMs, the latter can cause an overall rate increase in the whole detector. Fluctuations in the muon rates can therefore lead to a broadening of the significance distribution. Hence, one cannot simply use the lognormal shapes for single OMs as they have been derived earlier. A simulation using only these functions to generate the sensor hits, while correct for a single module, does not account for the correlated hits caused by muons. In addition, it is not possible to simply add the muon hits, because the individual OM distributions already include them, just not in a correlated fashion.

The optimal way to run a background simulation would be to simulate the dark noise of each OM individually and then add the correlated hits induced by cosmic radiation. While the underlying dark noise distribution is unknown, it can be estimated.

4.6.1 Estimation of Dark Noise Distribution

Let us consider the following scenario: We have two distributions from which random numbers are drawn. These are added up, and lead to a resulting lognormal distribution describing our OM noise.

We assume that the unperturbed noise distribution follows a lognormal function while the muon hit distribution follows a Poisson distribution. We further assume that the combination of a dominating lognormal and a subdominant Poisson distribution again yields a lognormal (numerical simulations show that this approach is sufficient for our purposes).

A complication found in the data is that the expectation value of the Poisson distribution will change over time. The muon rate is known to have an overall variation of 20% over the whole year (for more details, refer to [157]). However, this is easily overcome as the muon rate changes little over the time of a single run. The background simulation can, therefore, determine the dark noise distribution for each run individually.

In the case at hand, we have a sum of two independent random variables. Such a problem is best investigated with the method of characteristic functions. $\Phi_x(k)$ is defined as the Fourier transform of the probability density function $f(x)$ [158],

$$\Phi_x(k) = \int_{-\infty}^{\infty} e^{ikx} f(x) \mathrm{d}x \quad . \tag{4.15}$$

Note that there is a one-to-one correspondence between the p.d.f. and the characteristic function so that knowledge of one is equivalent to the other.

Consider a counting experiment governed by N independent distributions $f_1(x_1), f_2(x_2), ..., f_N(x_n)$ with the observable being defined by $z = \sum_{i=1}^{N} x_i$. The corresponding characteristic function $\Phi_z(k)$ is then calculated as follows:

$$\begin{aligned}
\Phi_z(k) &= \int_{-\infty}^{\infty} \ldots \int_{-\infty}^{\infty} \exp\left(ik \sum_{i=1}^{N} x_i\right) f_1(x_1) \ldots f_N(x_N) \mathrm{d}x_1 \ldots \mathrm{d}x_N \\
&= \int_{-\infty}^{\infty} e^{ikx_1} f_1(x_1) \mathrm{d}x_1 \ldots \int_{-\infty}^{\infty} e^{ikx_N} f_N(x_N) \mathrm{d}x_N \\
&= \Phi_1(k) \ldots \Phi_N(k) \quad .
\end{aligned} \tag{4.16}$$

The combined p.d.f. can then be obtained from $\Phi_z(k)$ using the inverse Fourier transform:

$$f(z) = \frac{1}{2\pi} \int_{-\infty}^{\infty} e^{-ikz} \Phi_z(k) \mathrm{d}k \quad . \tag{4.17}$$

In the present case, we have two underlying randomly distributed variables, namely the dark noise rates x and the muon hits y, which are summed up to the total noise z. We know the distribution of z and have a good estimate for y. Using equation 4.16, we can, derive the characteristic function of x:

$$\Phi_x(k) = \frac{\Phi_z(k)}{\Phi_y(k)} \quad . \tag{4.18}$$

Note that the characteristic function of the lognormal is not clearly defined and the above equation cannot be reduced to a simple distribution. Even though this method does not provide an analytical solution, it could be applied numerically. Unfortunately, this approach would require a factor ~ 100 more statistics than available.

However, if we assume that the OM dark noise can be described by a lognormal function, we can take a different approach. Using the description of the OM pulses $f(z)$ (see section 4.4.1.3) and the Poisson distribution of the muon hits $f(y)$ (see sections 4.6.2 and 4.6.3), we can derive the central moments of the dark noise distribution $f(x)$ from the equations (see appendix B.2):

$$\begin{aligned} \mu_z &= \mu_x + \mu_y \quad , \\ \sigma_z^2 &= \sigma_x^2 + \sigma_y^2 \quad \text{and} \\ S(z) &= \frac{S(x)V(x)^{\frac{3}{2}} + S(y)V(y)^{\frac{3}{2}}}{V(x)^{\frac{3}{2}}} \quad . \end{aligned} \tag{4.19}$$

With the knowledge of the three relations derived in appendix B.3,

$$\begin{aligned} \mu &= \frac{1}{2}\left(\ln V - \ln(e^{\sigma^2} - 1) - \sigma^2\right) \quad , \\ \sigma^2 &= \ln\left(\sqrt[3]{\frac{S^2 + 2 + S\sqrt{S^2+4}}{2}} + \sqrt[3]{\frac{S^2 + 2 - S\sqrt{S^2+4}}{2}} - 1\right) \quad \text{and} \\ s &= -E + e^{\mu + \frac{\sigma^2}{2}} \quad , \end{aligned} \tag{4.20}$$

the parameters of the dark noise lognormal can be calculated.

To test the validity of this approach, we randomly generated lognormal functions with parameters $\mu \in [5, 7]$ and $\sigma \in [0.015, 0.08]$, following the distribution of the fit results of the year 2002. The shift s was chosen so that the mean would be within 100 and 900. Values were randomly drawn from this distribution and added to values drawn from a Poisson distribution with a mean varied between 2 and 10. These values were filled into a histogram which was in turn fitted by a lognormal. Using the above approach, the initial lognormal was "retro-engineered" and used to generate yet another histogram. This histogram was compared to one generated from the initial lognormal with a χ^2 test. For each histogram, $2 \cdot 10^7$ entries, equivalent to $\approx 116\,\text{d}$ of data taking, were simulated. Figure 4.26 shows the reduced χ^2 of ~ 500 such tests. While the "retro engineered" and initial parameters can show differences, especially in the shift s, the derived functions describe the initial ones well.

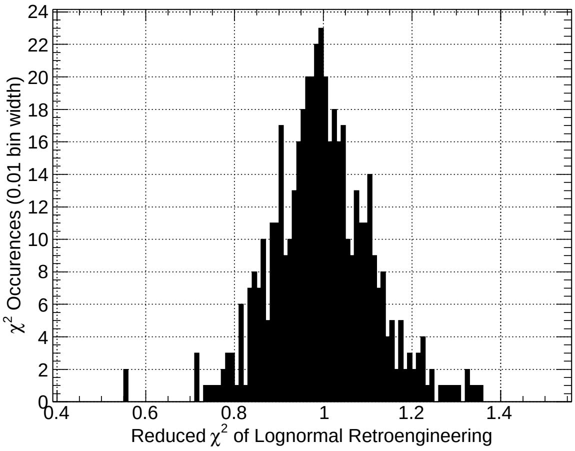

Figure 4.26: Reduced χ^2 difference between initial and retro engineered lognormal

4.6.2 Muon Influence on OM Pulse Rates

Next, the light induced by muons has to be considered by the simulation. Again, this is not straightforward. The nanoDST data composes only a subsample of the muons traversing the detector because the μDAQ is subject to an inherent dead time of $\approx 1.8\,\mathrm{ms}$, and each track has to feature at least 24 hit modules. Furthermore, hit selections and hit cleaning methods are used on the data sample before storing.

4.6.2.1 Mean Muon Rate

The first input needed to simulate the muon influence on the SNDAQ background is the number of muons lighting up the detector.

The mean muon rate seen by AMANDA-II depends on the time of the year. To derive the relative size of the seasonal fluctuation we used the cleaned and filtered nanoDST datasets of 2003, 2004 and 2005 that were prepared for the correlation of muon and meteorological data. The year 2002 was excluded as it features a steep rise in mid-September due to an unusual splitting of the ozone hole. More information on the meteorological analysis can be found in [157]. Each dataset was fitted with the function

$$R_\mu(t) = R_0 + \varepsilon R_0 \cos\left(\frac{2\pi}{T}(t - t_0)\right) \quad . \tag{4.21}$$

The resulting parameters can be found in table 4.2, and the fit for the year 2005 is shown in figure 4.27.

As the μDAQ provides only an estimate of the muons traversing the detector, this fit provides us with the relative variation of muons but not the total number. To derive the absolute normalization, we need to simulate the detector response to atmospheric

year	ε	T/d	t_0/d
2003	0.078	407	1
2004	0.072	382	11
2005	0.081	429	−19
average	0.077 ± 0.004	406 ± 19	-2 ± 13

Table 4.2: Fit parameters to mean muon rate measurements.

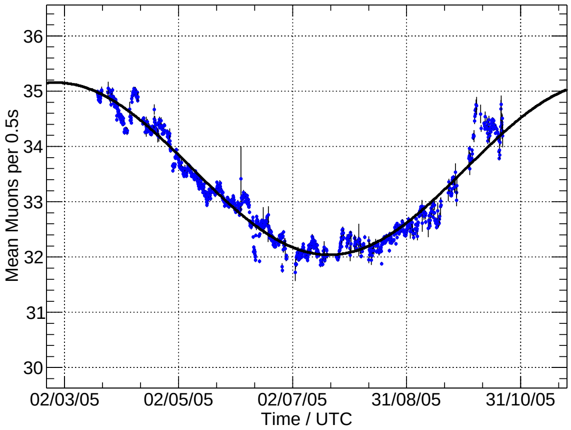

Figure 4.27: Seasonal variation of mean muon rate in the year 2005

muons without trigger thresholds or μDAQ dead time. The Monte Carlo written for the AMANDA-II standard analysis[6] simulates lepton production in the atmosphere using dCORSIKA[7] and propagates the resulting muons through the ice using the *Muon Monte Carlo* (MMC, for more information refer to [163]). The detector response is simulated with AMASIM [164] and the OM hit pattern stored in a so-called *f2k*-file (for more details on the simulation chain, refer to e.g. [159]). Four settings for the atmosphere are available in dCORSIKA: antarctic spring (October 1), summer (December 31), autumn (March 31) and winter (July 1). Running the Monte Carlo with these configurations using the detector setup of 2005 and fitting the results with the relative variation of muon rates, we determine R_0 to be $R_0 = 279.4 \pm 0.5$ muons per 0.5 s bin.

Note that the assumed cosine function is only a rough estimate for the seasonal muon rate fluctuation. It would be more precise to use the average muon rate counted by the μDAQ and rescale it to the total muon rate. Unfortunately, there are two major

---

[6] This refers to point source searches like [124], investigations of cosmic rays (e.g. [159]) and other track related analyses such as [160, 117].

[7] COsmic Ray SImulations for KAscade is a software package which simulates air showers induced by cosmic rays. It was initially written for the KASCADE experiment [161]. dCORSIKA is an adaption to the AMANDA/IceCube experiments [162].

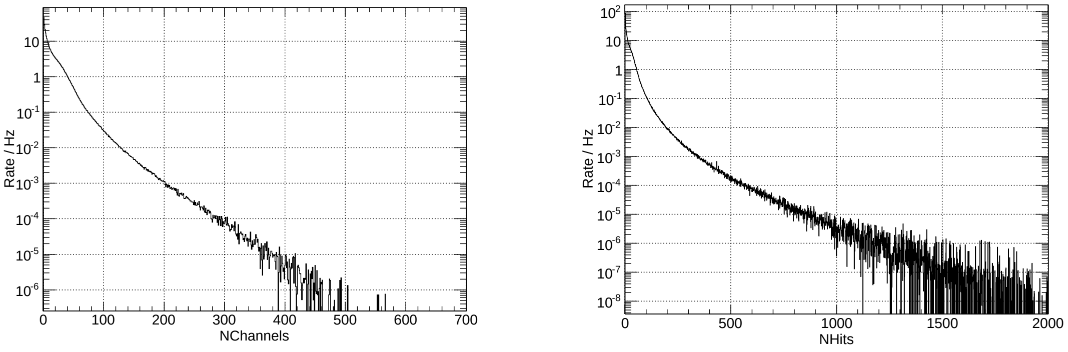

(a) NChannels

(b) NHits

Figure 4.28: Distribution of OMs triggered by muons
Depending on whether the dataset to be simulated was taken with or without dead time, the NChannel or the NHit distribution is relevant.

caveats to such an approach, especially with AMANDA. First, the factor to scale the recorded tracks to the actual number of muons in the detector is unknown, and the programs necessary to fully run the Monte Carlos with its reconstruction and filtering algorithms have compatibility issues with modern computer systems[8]. Second, even if this factor would be known, a rescaling would face the problem that the muon data is not as exhaustive as the supernova data. A significant fraction of the muon stream is missing or only present in bad quality when compared to the supernova stream. Such an approach might be feasible with IceCube were the two DAQs are synchronous, the simulation software well maintained and the data much cleaner.

4.6.2.2 OM Pulses Induced by Muons

Next, we must determine the number of OMs that are triggered by a muon. Contrary to point source analyses, it is unimportant to know which OM is triggered by which track. We only need to count the number of OMs hit by photons induced from muons within a time bin and distribute the counts among the modules taking their relative efficiencies into account.

The number of OM hits per muon is described by the *NChannel* and *NHit* distributions[9], can be determined from the simulation chain described in section 4.6.2.1. Figure 4.28 shows the distributions of sensors triggered within $32\mu s$. The distributions were fitted with rather complex functions, consisting of up to eight exponentials.

---

[8] The utility controlling the simulation chain, *simuperl*, uses modules compiled for 32 bit machines. As modern systems are based on 64 bit, the standard installation is not usable anymore. Unfortunately, recompiling the whole program is inhibited by software incompatibilities on up-to-date computer configurations.

[9] While the *NChannel* distribution includes only the first photon hit in each OM, the *NHit* distribution contains also subsequent ones. Both values store only pulses within a trigger window of $32\,\mu$s.

To determine the relative muon detection efficiencies of the OMs, one can use the longterm behavior as discussed in section 4.23. An OM which has a higher efficiency will necessarily show higher seasonal fluctuations than one which is less sensitive. The efficiencies depend chiefly on the OM depth (due to muon absorption and dust layers) and the module type.

4.6.3 Background Simulation Procedure

In summary, the background simulation needs the following input quantities:

- The lognormal functions describing the rate deviations which were determined for the OM quality checks introduced in section 4.4.1.3.
- The development of the mean muon rate (see section 4.6.2.1).
- The distribution of OMs triggered by light from muons as presented in section 4.6.2.2.
- The relative muon efficiencies of all modules derived from their longterm behavior (see section 4.5).

We go through the following steps for each run:

1. We reconstruct the individual OM distributions by adding the OM run averages $\langle r_i \rangle_{\text{run}}$ to the rate deviation lognormals 4.4.1.3..
2. With the cosine fit determined in section 4.6.2.1, we deduce the mean muon rate for the simulated run.
3. The mean pulses caused by muons in each OM $\langle N_{\mu,i} \rangle$ are deduced by multiplying the relative muon efficiencies $\epsilon_{\mu,i}$ with the mean muon rate μ_μ and the average number of OMs triggered by a muon $\langle N_{\text{PMT}} \rangle$, i.e. $\langle N_{\mu,i} \rangle = \mu_\mu \epsilon_{\mu,i} \langle N_{\text{PMT}} \rangle$.
4. Assuming a Poisson distribution with an expectation value of $\langle N_{\mu,i} \rangle$, the dark noise distributions are "retro-engineered" according to section 4.6.1.

Now, the simulation can start with the Monte Carlo production. For each bin, we

- simulate the dark noise of all OMs (using the dark noise lognormal),
- draw the number of muons in the detector (assuming a Poisson distribution),
- draw the number of OMs hit for each muon (assuming the distributions in figure 4.28 according to the dead time setting),
- distribute the muon hits among the OMs (according to their relative efficiencies) and
- apply the analysis.

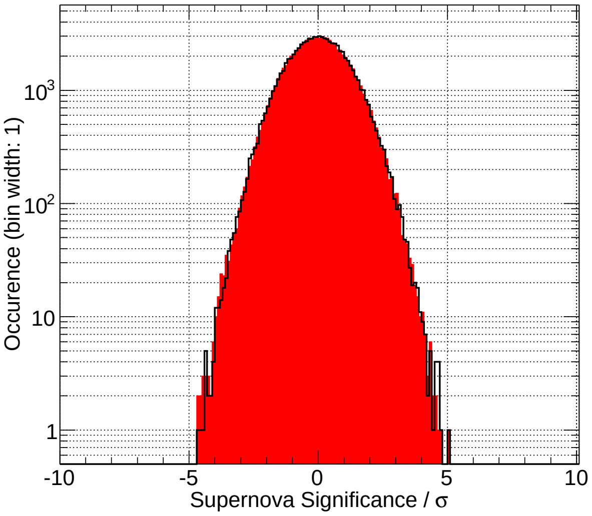

Figure 4.29: Supernova significances of run 0990 from year 2002 with muon modulated Monte Carlo

Figure 4.29 shows the comparison of the sample data from run 0990 from year 2002 with the muon modulated Monte Carlo and figure 4.30 the significance distribution of 2002 with Gaussian fits and background Monte Carlo as well as a more detailed comparison.

4.6.4 Adjustments to the Background Simulation

While the new Monte Carlo performs well for most datasets, discrepancies remain. As stated above, the *NChannel* and *NHit* distributions were simulated for the detector configuration of 2005. However, the performance in the years can be quite different because important settings were changed between the seasons (e.g. the muon DAQ trigger thresholds). Running the full simulation chain for all datasets is in principle feasible but not meaningful for two reasons. First, work on the μDAQ was discontinued end of 2006 and consequently, no configurations for 2007 and 2008 are implemented in the Monte Carlo. Second, the uncertainties are rather large. The programs do not use *Photonics*, raising the ice systematics to $\sim 12\%$. Uncertainties in OM sensitivity and calibration are $\sim 7.8\%$ and $\sim 5\%$, respectively [117]. Furthermore, the error on the description of the primary cosmic ray spectrum can be as large as $\sim 30\%$ [160]. Adding up these numbers, we obtain a total uncertainty of $\sim 34\%$. To be independent of these systematics we chose to optimize the Monte Carlo year per year.

As an adjustment, we introduce a multiplier scaling the number of OM hits triggered by muons and optimize this factor for each dataset separately. A subsample of runs was chosen as reference from each year ($\sim 3\%$), and for each run the background was simulated using multiple adjustment settings. Then, the difference between standard

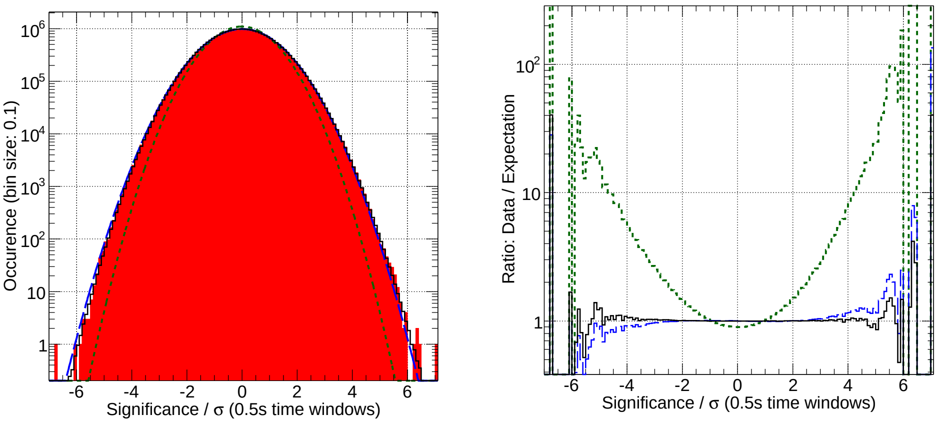

Figure 4.30: Significance distribution for 2002 and the expected background
The left figure shows the significance distribution (filled red area) along with the naively expected Gaussian with $\sigma = 1$ *(dotted green line), a Gaussian fit with* $\sigma = 1.15$ *(broken blue line) and the background Monte Carlo (solid black line). On the right, the data is divided by the Monte Carlo expectations. The muon modulated Monte Carlo best describes the measurements.*

deviations of the simulated and the measured significance distributions, $\sigma_{\text{data}} - \sigma_{\text{bg}}$, was calculated for each factor tested and an average determined. Next, the difference in standard deviations was plotted against the multiplier and fitted with a polynomial of second order (see figure 4.31 for an example). The factor setting where $\sigma_{\text{data}} - \sigma_{\text{bg}} = 0$ was taken as optimal. With this approach the background is tuned only for the bulk of the distribution but not in the tails which are sensitive to supernova signals. Table 4.3 shows the adjustment factors determined for the respective datasets.

Year	Factor
2000	1.30
2001	1.44
2002	0.98
2003	1.34
2004	0.89
2005 ndt	1.34
2006 ndt	0.70
2006 dt	0.86
2007	0.77
2008	0.92

Table 4.3: Adjustments to the number of hits in the background simulation

For the most part, the differences in the adjustment factors can be well understood

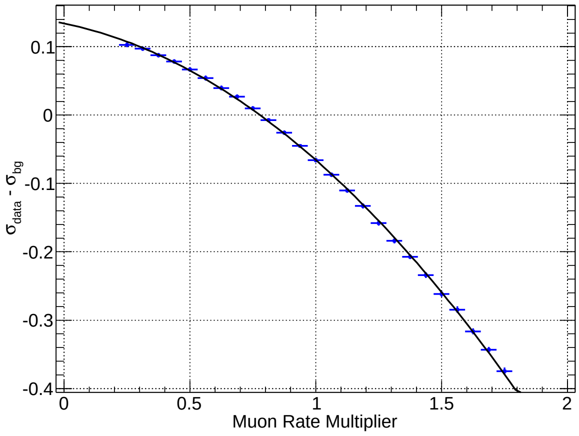

Figure 4.31: Tuning the background Monte Carlo for the year 2007
The difference of the standard deviations between data and background Monte Carlo, $\sigma_{\text{data}} - \sigma_{\text{bg}}$*, is calculated for multiple settings of the muon rate multiplier. Each adjustment factor is averaged over* ~ 15 *runs, and with the help of a polynomial of second order, the optimal value where* $\sigma_{\text{data}} - \sigma_{\text{bg}} = 0$ *is determined.*

by looking at the changes in detector configuration and thresholds. In the year 2000, we start with a dead time of 8 ms and a mean muon rate of 54 Hz. For 2001, the μDAQ trigger thresholds were changed, so that this year shows an average rate of 61 Hz, and consequently, the adjustment factor increases. 2002, a dead time of 246 μs was introduced and so it is not surprising that the factor for this dataset is completely different. A change in 2003 when compared to 2001 or 2002 is also to be expected, knowing that four more strings were read out by the SNDAQ and that no dead time was applied. The drop in factor between 2002 and 2004 can be retraced to a new detector setup (more OMs) and the decreased muon rate (66 Hz instead of 69 Hz). The rise from 2004 to 2005 doesn't come as a surprise either because no dead time was applied in 2005. The drop to 2006, however, is not as easily understood. As opposed to the other years the 2006 data taken without dead time expands only from March to mid June (the first two months are discarded because of quality requirements). Consequently, the optimization can only be performed for a much smaller interval than the other years which might be one reason for the low value. By the end of 2006, the muon DAQ was switched off and one can only speculate to what extend this affected the trigger thresholds. From 2007 to 2008, part of the SNDAQ electronics had to be disconnected because of power shortage and thus the number of OMs contributing to the supernova stream was reduced, resulting in the last change of factor.

Keep in mind that we optimized the background Monte Carlo only for a small subsample and that the function we use to describe the seasonal changes in the muon rate is not ideal. The data available from AMANDA is not stable enough for a more exhaustive approach as might be possible with IceCube. For more information on the muon rates in both detectors, refer to [157].

A second caveat is that the Monte Carlo does not simulate external perturbations from anything other than muons. While one tries to remove detector instabilities with the quality inspection discussed earlier, it cannot be guaranteed that the final data sample is clean. Unfortunately, the repercussions of some external influences such as instabilities of the power plant or static discharges in cables caused by gusty winds are unknown; no data is available to allow for a closer inspection.

4.6.5 Environmental Influences on the Module Rates

Muons are not the only external influences that lead to modulated rates. In the scope of this work, the sensor rates have been correlated with magnetic field strengths and photometric measurements of the ionosphere.

The electrodynamics of the upper atmosphere at South Pole is studied by the AGO project[10] using optical and radio wave auroral imagers, magnetometers and narrow and wide band radio receivers [165]. For our purposes, we access the available magneto- and photometer data and synchronize it with the supernova stream. The measurements are available in 10 min resolution and consist of the vertical and horizontal components for the magnetic field and optical emissions at 427.8 nm and 630 nm wavelengths. Due to the large time binning, it is unlikely that we will see dependencies between the supernova significances and the AGO data. We will therefore calculate the normalized rate sums according to equation 4.10 and plot them as a profile histogram.

Figure 4.32 shows the dependence of the mean normalized rate deviation versus the recorded magnetic field strength. The photometer measurements are shown in figure 4.33. A correct quantification of these dependencies would only be possible using data in finer time resolution. As these are not available, only muon modulations are included in the background Monte Carlo.

4.7 Signal Simulation

To determine the detection probability for supernovae in the Milky Way, we need to simulate the signatures core collapse would induce in AMANDA.

As signal input, we will use the simulation routine USSR presented in section 3.1. The average signal expectation per OM will be modified by the dead time (if applicable) and OM efficiency and then used as a basis to generate a random Poisson number which is added to the background simulation documented in section 4.6 and subjected to the standard analysis as presented in section 4.1.1.

Simulation-wise, the main difference between AMANDA and IceCube are the different effective volumes. As the parameters of the AMANDA OMs are much less well known than those of the IceCube DOMs, we will use the average effective volume of IceCube as derived in section 2.4 and downscale it to the AMANDA case using

---

[10] Automatic Geophysical Observatories

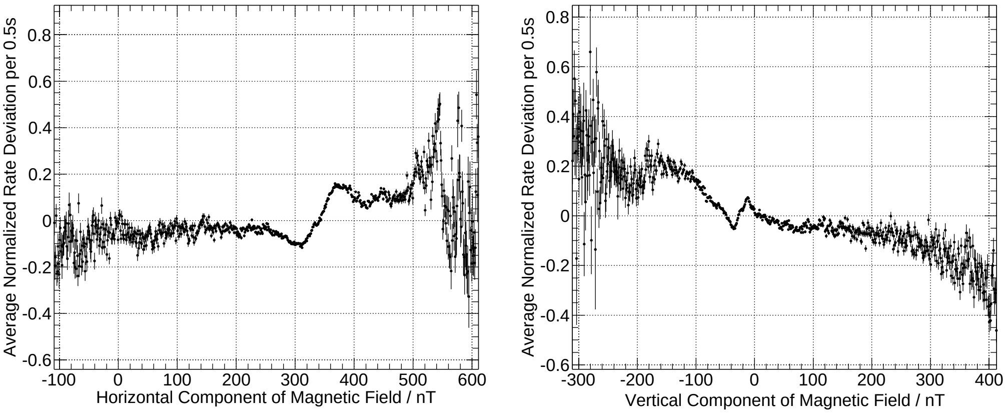

(a) Horizontal component

(b) Vertical component

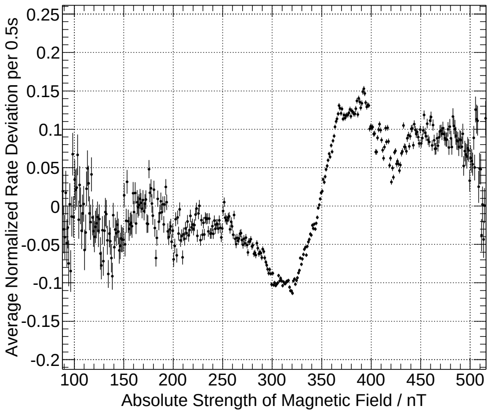

(c) Absolute field strength

Figure 4.32: Average normalized rate deviations versus the magnetic field
As for the recorded muons (see figure 4.25), the supernova data is synchronized with the external data and for each time window featuring a certain magnetic field value, the OM rate sum is averaged and plotted into a profile histogram. For all magnetic field components shown, we see a clear correlation with the summed rates. The increase in OM hits is likely induced by magnetic field related changes in the electron collection efficiency of the PMT and can therefore not be expected to be as simple as in the muon case. In IceCube the dependencies should be much smaller because the DOMs are shielded by a μ*-metal mesh.*

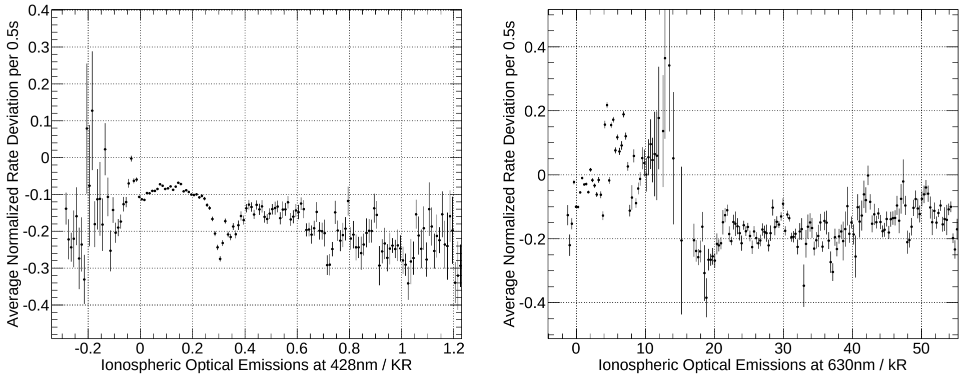

(a) 427.8 nm

(b) 630 nm

Figure 4.33: Average normalized rate deviations versus photon flux
For these plots, the same approach as in figure 4.32 was used for the photon fluxes. It is unclear, whether the rates are directly influenced by the electric fields or whether the correlation appears through a related variation of the magnetic field.

the conversion factors determined from the longterm behavior of the modules (see section 4.5).

In the case of AMANDA each dataset can feature a significantly different configuration of contributing modules. However, the effective volumes remain very similar as can be seen in table 4.4.

Time Span	2000-2001	2002-2004	2005	2006-2008
$V^e_{\mathrm{eff,B10-19}}$ / m^3/MeV	24.2 ± 2.0	24.2 ± 1.9	24.2 ± 2.0	24.0 ± 2.0

Table 4.4: Effective volumes of B10-19 modules

We will use the average value of $V^e_{\mathrm{eff,B10-19}} \approx 24.1\,\mathrm{m}^3/\mathrm{MeV}$ as an effective volume for the simulation. The respective values for the B4 generation were derived to be $V^e_{\mathrm{eff,B4}} = (18.6\pm2.1)\,\mathrm{m}^3/\mathrm{MeV}$ (with exception of the year 2007, were it was $(18.7\pm2.1)\,\mathrm{m}^3/\mathrm{MeV}$).

4.8 Supernova Search

We will now determine the optimal search parameters for the supernova search and then sift the data for signals.

4.8.1 Search Windows

To obtain the optimal sensitivity for supernova detection, it is wise to adapt the length of the search window to the model we are looking for. Implementing as many rebinnings as possible in the SNDAQ would be the best way to go. However, this approach would require reprocessing of the complete set of data and Monte Carlo and thus increase the storage requirements beyond our current capacity. Therefore, we will estimate rebinned significances using the $\Delta t_{\mathrm{raw}} = 0.5\,\mathrm{s}$ time windows.

For illustration purposes, we start with a rebinning factor of $N = 2$, i.e. we add up the data at t and $t + 0.5\,\mathrm{s}$. As μ_i and σ_i are calculated for 10 min time windows, we can assume that $\mu_i(t) \approx \mu_i(t + 0.5\,\mathrm{s})$ and $\sigma_i(t) \approx \sigma_i(t + 0.5\,\mathrm{s})$. Note that due to the exclusion window, a signal should not change this approximation. Adding up the two bins, μ_i and σ_i change as $\mu_i \rightarrow 2\mu_i$ and $\sigma_i \rightarrow \sqrt{2}\sigma_i$. From equation 4.3, we conclude that $\sigma_{\Delta\mu} \rightarrow \sqrt{2}\sigma_{\Delta\mu}$ and consequently, $\Delta\mu$ transforms as follows:

$$\begin{aligned}\Delta\mu \quad \rightarrow \quad & 2\sigma_{\Delta\mu}^2 \sum_{i=1}^{N_{\mathrm{OM}}} \frac{\epsilon_i}{2\sigma_i^2} \left[r_i(t) + r_i(t + \Delta t_{\mathrm{raw}}) - 2\mu_i\right] \\ & = \Delta\mu(t) + \Delta\mu(t + \Delta t_{\mathrm{raw}}) \quad . \end{aligned} \tag{4.22}$$

Extending this to N rebinnings is trivial. If we normalize the rate deviations to a single bin and use an average value for the error, we obtain:

$$\begin{aligned}\Delta\mu_N &= \frac{1}{N} \sum_{j=0}^{N-1} \Delta\mu(t + j\,\Delta t_{\mathrm{raw}}) \qquad \text{and} \\ \sigma_{\Delta\mu,N} &= \frac{1}{N\sqrt{N}} \sum_{j=0}^{N-1} \sigma_{\Delta\mu}(t + j\,\Delta t_{\mathrm{raw}}) \quad . \end{aligned} \tag{4.23}$$

To keep binning effects to a minimum, we use the above as a moving average.

4.8.2 Expectations

In order to examine the recorded data in a blinded way, we have to investigate the expected background and the signal Monte Carlo first.

4.8.2.1 Identification of Supernova Candidates

The optimization of the probability to detect a supernova in the Milky Way requires the reduction of false alarms while at the same time keeping the detection efficiency as high as possible.

Expected Background

First, we run the background Monte Carlo as introduced in 4.6 to produce at least 200 times the amount of data that was recorded.

If one assumes that the significance $\mathfrak{s}$ is a measure for a signal induced by a core collapse, it is reasonable to introduce a threshold ξ above which a measurement will be defined as a potential supernova. Using the background Monte Carlo, we deduce the expected number of false candidates at a given ξ and a detector uptime T to be

$$\mu_{\mathrm{BG}} = \frac{\int_{\xi}^{\infty} f(\mathfrak{s})\mathrm{d}\mathfrak{s}}{\int_{-\infty}^{\infty} f(\mathfrak{s})\mathrm{d}\mathfrak{s}} T \tag{4.24}$$

with $f(\mathfrak{s})$ being the significance distribution.

The caveat at this point is the finite amount of statistics available from the background simulation. Only few high significance events are present in the distribution which leads to steps when optimizing the discovery threshold. To circumvent this problem, Gaussian tail fits were performed to the simulated noise rate distributions.

Detection Efficiency

The detection probability for a supernova depends strongly on its distance, its type and the neutrino parameters. For this work, five different scenarios were examined:

- A scaled SN1987A flux with a signal following an exponential decay with $\tau = 3\,\mathrm{s}$,
- signatures according to the Lawrence-Livermore model for normal hierarchy,
- one-dimensional ONeMg core collapse models with full neutrino opacities for normal hierarchy and
- failed supernovae for two equations of state with inverted hierarchy and large mixing angle.

More details on the chosen models can be found in section 3.1.1.4. The scaled SN1987A flux was chosen for comparability with previous works while the Lawrence-Livermore and ONeMg simulations represent a good choice for normal supernovae as both cover a large time frame and span a good range of possible core collapses due to their large mass difference. In the case of the failed supernovae, the equations of state leads to a difference in the duration of the signal which then influences the detection probability. For all models, the neutrino oscillation parameters were chosen so that the signal is at its minimum value, thus yielding a conservative prediction. For the distances of supernovae, the distribution given in [76] was used (see also section 1.1.4).

To derive the detection probability, we simulate a supernova neutrino burst according to section 4.7 and deduce the significance $\mathfrak{s}$ expected in AMANDA. All core collapses with $\mathfrak{s}$ above the threshold ξ can be observed. The detection efficiency or Milky Way coverage ϵ at a significance threshold of ξ is given by

$$\epsilon(\xi) = \frac{\int_{\xi}^{\infty} N(\mathfrak{s})\mathrm{d}\mathfrak{s}}{\int_{0}^{\infty} N(\mathfrak{s})\mathrm{d}\mathfrak{s}} \tag{4.25}$$

with $N(\mathfrak{s})$ being the number of supernovae showing the significance $\mathfrak{s}$.

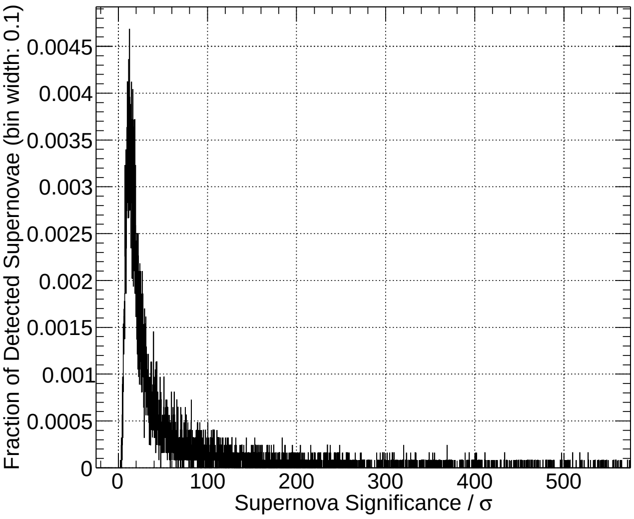

Figure 4.34: Detection probability of Lawrence-Livermore like supernovae in the Milky Way

About 12000 supernovae have been simulated for the year 2002 configuration with random distance. The x-axis denotes the significance of the bin containing most of the signal from a core collapse.

Figure 4.34 shows the distribution of the significances of Lawrence-Livermore like core collapse in the Milky Way. The detection efficiency for supernovae in our galaxy in function of the significance threshold is displayed in figure 4.35.

It immediately meets the eye that failed supernovae start out at lower efficiencies, even though their neutrino signal is much higher(see section 3.2.3.1). As already noted in section 4.4.3, the present definition of the χ^2 cut removes very strong bursts. The supernova search routine used in this analysis is optimized for small signals and does not perform as well for intense neutrino bursts (see section 4.1.1 and 4.4.3).

Obviously, a suitable choice of the χ^2 confidence interval can greatly increase the detection efficiency and therefore improve the upper limit. However, one has to be careful as a looser cut might lead to more false candidates. Figure 4.36 shows different settings for Lawrence-Livermore and failed supernovae. For common supernovae, we will use a confidence interval of 90% as it minimizes the danger of false alerts at low cost in efficiency. Failed supernovae on the other hand, lead to much higher signals which is why a large confidence interval would be best. To still be able to derive a meaningful limit for this case, we choose to restrict the χ^2 confidence to 99.999%. As the background simulation does not include strong anisotropic perturbations from single OMs, the approach used for standard supernovae is not reliable here. Instead we place a cut at $\xi = 15$ where the bulk of signals higher than 5σ resides ($> 90\%$ for the Lattimer-Swesty and $> 95\%$ for the Shen equations of state).

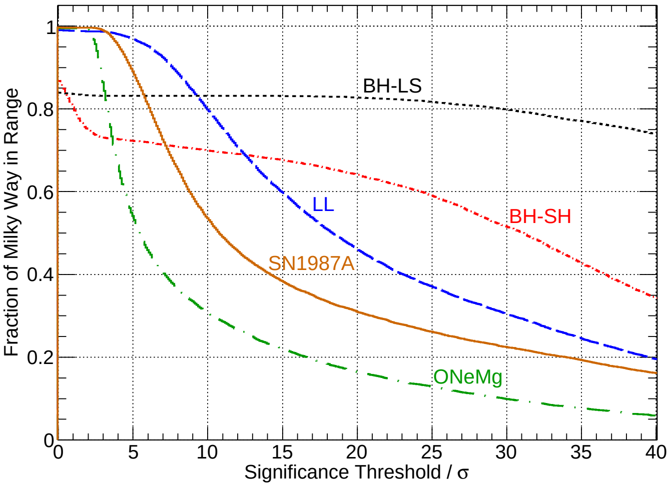

Figure 4.35: Fractions of Milky Way in range against the significance threshold ξ for each model at a χ^2 confidence of 99%.

The lines give the probability to detect a modeled core collapse of a certain type versus the significance cut ξ*. LL describes the Lawrence-Livermore model, BH-SH and BH-LS the failed supernovae with the Shen and Lattimer & Swesty equations of state. ONeMg is the one-dimensional electron capture core collapse with full neutrino opacities and SN1987A represents the scaled flux of the detected Kamiokande-II neutrinos.*

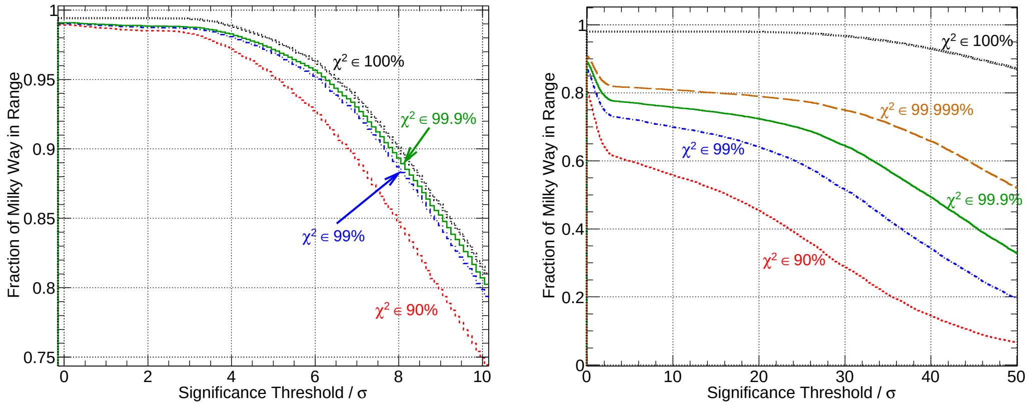

(a) Lawrence-Livermore supernova

(b) Failed supernova with Shen EoS

Figure 4.36: Supernova detection efficiency for different χ^2 confidence intervals

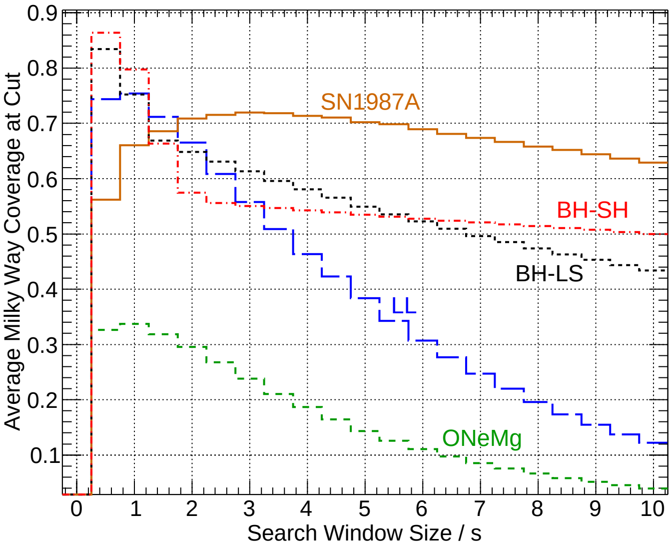

Figure 4.37: Average detection efficiencies
The average detection efficiencies for the supernova search are clearly model dependent. Depending on the supernova signal assumed in the simulation, the optimal rebinnings can be quite different.

Next, we investigate which time window is optimal for which supernova model. Figure 4.37 shows the average detection efficiencies of supernovae in the Milky Way for each rebinning with the detector configuration of 2002. It meets the eye that the optimal window sizes are smaller than expected (e.g. 3 s for the SN1987A scaling instead of 4 s). The reason is actually quite simple. When building rebinned data from the 0.5 s data stream, the requested number of adjacent bins is combined. This means that when one 0.5 s data point is disqualified, e.g. because of a bad χ^2 or wrong time stamps, all larger rebinnings holding this bin are also removed. Consequently, the larger one makes the rebinning the fewer bins are available and signal is lost; the supernova sensitivity drops.

The optimal time binnings are 1 s for the Lawrence-Livermore and the ONeMg models, 3 s for the SN1987A scaling and 0.5 s for the failed supernovae.

4.8.2.2 Best Possible Upper Limit

The derivation of an upper limit for the rate of supernovae in the Milky Way is more involved than first meets the eye. In principle, all that needs to be done is to determine a number of supernova candidates and scale it to the detection efficiency of core collapses in the Milky Way. However, the dataset represents a single measurement and thus provides only a snapshot of the supernova occurrence while we are interested in the mean rate. To place an upper limit on the expected rate of supernovae, one has to define a confidence level α at which the value is reliable.

Assume that the probability to find n supernova candidates follows the Poisson distribution

$$P(n|\mu_{\mathrm{BG}} + \mu_{\mathrm{SN}}) = \frac{(\mu_{\mathrm{BG}} + \mu_{\mathrm{SN}})^n \, e^{-(\mu_{\mathrm{BG}}+\mu_{\mathrm{SN}})}}{n!} \tag{4.26}$$

with an expectation for false alarms of μ_{BG} and the unknown supernova rate μ_{SN}. Assuming that we find n_0 candidates in our dataset, we derive the value $\mu_{\mathrm{SN}}^{\alpha}$ which describes the maximal number of expected supernova signals in our data at a confidence level of α to be:

$$\alpha \leq \sum_{n=n_0+1}^{\infty} P(n|\mu_{\mathrm{SN}}^{\alpha}) \quad . \tag{4.27}$$

As the above equation is not analytically solvable, we determine $\mu_{\mathrm{SN}}^{\alpha}$ with the Feldman-Cousins table implemented in the ROOT framework [150, 166].

Next, we scale this value to the supernova sensitivity and the detector lifetime. If we assume a galaxy coverage ϵ and an uptime T, we can translate the limit derived from the data to an overall value for the Milky Way $\mu_{\mathrm{SN,MW}}^{\alpha}$ with the relation

$$\mu_{\mathrm{SN,MW}}^{\alpha} = \mu_{\mathrm{SN}}^{\alpha} \, / \, (\epsilon \, T) \quad . \tag{4.28}$$

As the trigger threshold ξ determines the expected background as well as the efficiency, a clever choice is of the essence.

Optimal Detection Threshold

For the determination of the lowest upper limit, the trigger threshold has to be chosen in a way that combines a minimal background with a maximal detection efficiency. To this end, we calculate the expected background and the detection efficiency for different settings of ξ. Under the assumption of a null hypothesis ($\mu_{\mathrm{SN,MW}} = 0$), we perform the supernova search 10000 times for each ξ by drawing random Poisson numbers around $\mu_{\mathrm{BG}} + \mu_{\mathrm{SN}}$ and determine the theoretical upper limit. For each setting of ξ, we take the averages of these values and fill them into a profile histogram as shown in figure 4.38. The minimum is then taken as the optimal significance threshold ξ.

Note that the correct choice of the assumed background distribution is very important. It has to cover the same amount of time as the recorded data because otherwise, the expected false trigger rate would not be compatible. Unfortunately, we cannot pool the measurements of the respective years together because the distributions differ (see section 4.3). Instead, the cut optimization has to be performed for each year separately, but as the probability for a false trigger increases with uptime, the background expectations have to be scaled to the lifetime of the whole dataset.

As already stated in section 4.6.4, the simulation can only approximate the seasonal variations of muon production and does include any other external perturbations like e.g. power fluctuations or static discharges due to weather conditions. Unfortunately,

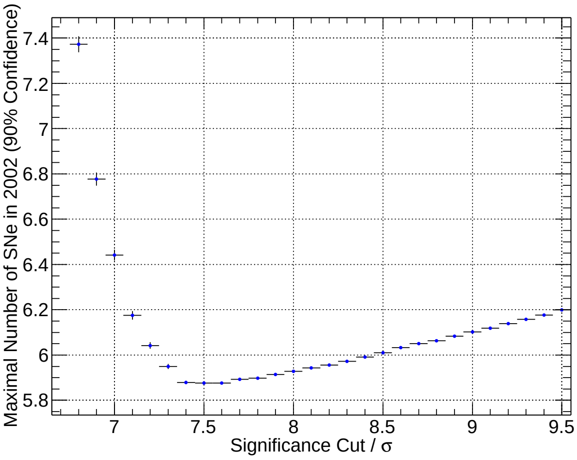

Figure 4.38: Determination of the best upper limit on the number of supernovae in the Milky Way in 2002
The significance threshold is optimized for Lawrence-Livermore like supernovae assuming the null hypothesis of noise only. Lifetime, background and detection efficiencies are those of the year 2002 configuration.

AMANDA is rather unstable with respect to these influences and there are many outliers in the distributions (see e.g. [157]). To further reduce the differences between simulated and recorded data, we modify ξ if the measured spread of the significances is different from the estimated background. This tunes the threshold only with respect to the bulk of the distribution and not the tails where the signal is expected. The adjustment is performed in the following way:

$$\xi \rightarrow \xi' = \xi + \xi\,(\sigma_{\text{data}} - \sigma_{\text{MC}}) \quad . \tag{4.29}$$

In a last step, a constant shift of 0.1 is added to ξ to ensure independence from binning effects. As evident from figure 4.38, a slight relocation to the right does not have a strong effect on the optimal limit, contrary to a relocation to the left. It has to be stressed that all these corrections were fixed before looking at the data to avoid any bias.

For the optimal significance thresholds and the respective detection efficiencies, refer to tables C.10 and C.11, respectively.

Remaining Candidates

Now, we unblind the data and apply the significance thresholds. When the significance of a data point rises above ξ, it is classified as a trigger and blanks out the data for the following 100 s. Table 4.5 shows the remaining candidates and figure 4.39 displays the one found in 1 s time resolution.

	LL	ONeMg	SN1987A	BH-LS	BH-SH
0.5s	6	7	7	**0**	**0**
1.0s	**1**	**1**	1	0	0
1.5s	0	2	0	0	0
2.0s	0	0	0	0	0
2.5s	0	0	0	0	0
3.0s	0	0	**0**	0	0

Table 4.5: Number of supernova candidates found in the data of the years 2000-2008. *The optimal search window sizes for the respective models are marked in bold.*

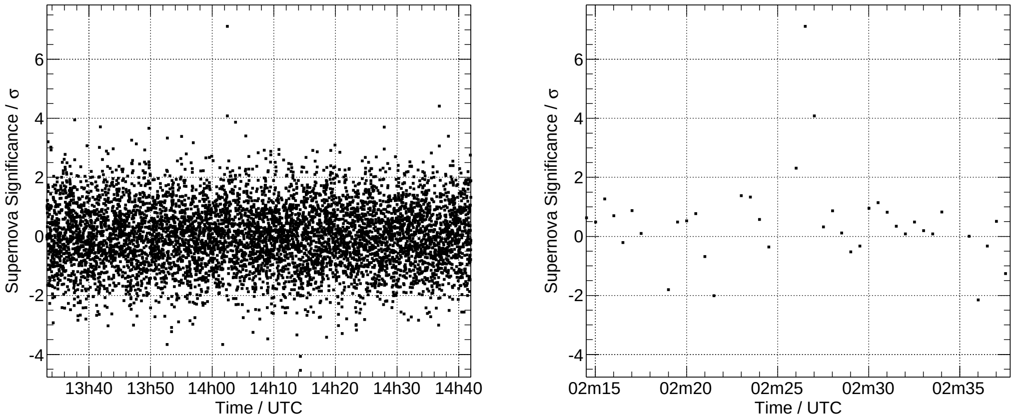

(a) May 20, 2005

(b) May 20, 2005, minutes after 14:00

Figure 4.39: Supernova candidate
The candidate features a significance just above 7σ; all qualification values are fine. The plot to the right is a closeup of the candidate.

Despite the large number of quality checks presented in section 4.4, a lot of candidates remain in the 0.5 s binning. While it may seem that the cuts are too soft, one has to remember that more than one half of the detector uptime was already rejected, and further tightening the cuts would result in even greater lifetime loss. Besides, all quality parameters previously introduced were investigated and the candidates were also correlated with the muon DAQ; no data showed any conspicuous behavior. It might have been interesting to look for power fluctuations at the time of occurrence; unfortunately, no such information was recorded by the collaboration. The number of candidates for the time binning chosen as optimal before looking at the data, however, is low.

Upper Limits

The upper limits on the average number of supernovae per year is shown in table 4.6 for each investigated model and a choice of rebinnings.

	LL	ONeMg	SN1987A	BH-LS	BH-SH
0.5s	5.1	12.7	7.4	**1.0**	**0.8**
1.0s	**2.1**	**4.8**	2.5	1.1	0.9
1.5s	1.4	7.7	1.5	1.4	1.1
2.0s	1.7	3.8	1.6	1.5	1.3
2.5s	2.1	4.7	1.8	1.6	1.4
3.0s	2.5	5.9	**2.0**	1.8	1.5

Table 4.6: Upper limits on the expected number of supernovae per year.
The optimal search window sizes for the respective models are marked in bold.

It meets the eye, that the best lowest limits do not reflect the optimal search window sizes. In the case of recorded supernova candidates, this is trivial. However, the SN1987A scaling shows its lowest upper limit at 1.5 s instead of 3 s. Again, the reason is to be found in the asymmetric data loss when discarding 0.5 s bins. In the measurements, the disqualified data points are not as uniformly distributed as they are in the Monte Carlo, and thus the uptimes for larger rebinnings drop even faster than in the simulations (see table C.9).

Systematic Uncertainties

To the systematics given in section 3.5, we have to add the uncertainties on the conversion factor between AMANDA and IceCube modules ($\sim$ 5%, see section 4.5) and the one on the supernova precursor distribution ($\sim$ 10%, see section 1.1.4).

When we look for specific model we do not assume an error because we have no benchmark. In this case, the total systematic uncertainty is $\sim {}^{+17}_{-20}\%$.

For the assumption of a scaled SN1987A flux, we have to add an uncertainty of $\sim$ 32% as given in section 2.4.4 and add a further 20% for the unknown signal shape (we assumed a signal $\sim e^{-t/3\,\mathrm{s}}$). In total, we arrive at a systematic error of $\sim {}^{+41}_{-42}\%$.

Outlook to IceCube

For IceCube, the supernova data taking started in 2007, and it is already clear from the measurements recorded with the unfinished detector that stability and data quality are much superior to AMANDA (see [93]). This is due to many reasons. First, in IceCube, the external power supply provides low voltage to the modules which then transform it to high voltage locally. This approach inhibits external power fluctuations from influencing the rates. It is not clear whether an unstable power supply is responsible for the instabilities in AMANDA, however, it seems safe to assume that this is the reason for at least some of the perturbations. Second, pulse information recorded by a DOM is digitized locally and only then sent to the surface. In AMANDA, the signals had to travel $\sim 2\,\mathrm{km}$ before being read out and could be strongly influenced by crosstalk or environmental effects on their way up (see e.g. [117]). Third, muon and supernova data acquisition are synchronized which allows the considerable effort spent on monitoring of the standard DAQ to be translated to the data taken by the SNDAQ. And last but far from least, IceCube has an order of magnitude more modules which clearly leads to a much higher stability when investigating correlated fluctuations.

Conclusion

This work focuses on the detection of supernova explosions with the AMANDA and IceCube neutrino telescopes. Even if the experiments are not designed for low energy neutrinos, they will provide interesting results if a core collapse occurs within the Milky Way.

To ensure the quantative analysis of possible supernova signatures, a Monte Carlo program which simulates core collapse neutrino bursts in the AMANDA and IceCube detectors was developed. The software so far includes 16 different supernova model predictions and can easily be extended. Furthermore, it allows to choose between many oscillation scenarios, such as MSW effects, shock wave modulations and collective oscillations induced by neutrino self-interactions. It includes settings for normal and inverted mass hierarchy and permits free choice of the θ_{13} mixing angle. Due to the object-oriented coding style, further extension of the software by additional models, new oscillation scenarios or different neutrino interactions in ice can be easily implemented.

For this thesis, the simulation results were used to investigate the IceCube detector response A likelihood method is presented which uses the shapes of the neutrino time series to distinguish quantitatively between different supernova models. IceCube performs well in discerning predictions and will certainly provide important information for the understanding of the supernova mechanism once a core collapse in the Milky Way is recorded. Depending on the kind of supernova observed, the range to reject models extends from 10 kpc for faint signals of electron capture core collapses up to the Small Magellanic Cloud for the very strong signals of failed supernovae. Distinguishing between neutrino hierarchies is more complicated as the explosion process needs to be well understood to evaluate the subtle differences. Using the shock wave propagating through the supernova envelope, the separation of inverted neutrino mass hierarchy paired with a large large θ_{13} mixing angle ($\sin^2 2\theta_{13} > 10^{-3}$) from the remaining cases is possible up to $7\,\mathrm{kpc} - 10\,\mathrm{kpc}$ with $> 5\sigma$. It has to be stressed, however, that this method relies on assumptions about the explosion process which need not be true. The effect of neutrino self-interactions on the IceCube signal can only be studied by falling back on the comparison of absolute rates. Depending on the relative ratio of neutrino luminosities in the supernova, changes induced by collective oscillations might be observable over the entire Milky Way.

The second core theme of this work was the thorough analysis of the data that was recorded by the AMANDA detector in the years 2000 to 2009. In a first step, the pulse rates were subjected to quality checks, removing unstable sensors with multiple methods. The overall stability of AMANDA turned out to be rather poor, especially when compared to IceCube. After carefully cleaning the data, it became apparent that the background contains a significant fraction of correlated noise. As the same is observed for IceCube, detector induced fluctuations can only play a minor role. The data was compared to measurements of environmental parameters such as the strength of the magnetic field and other external effects. It turned out that the correlated light production is mainly caused by atmospheric muons despite the strong suppression of the flux by the ice overburden. A Monte Carlo was developed that generates uncorrelated noise hits with lognormal functions and adds estimates of the light produced by muons.

With the signal Monte Carlo, signatures of different model predictions were simulated and added to the background. After deriving the detection efficiency for supernovae in the Milky Way and combining this information with the expected noise level, it was possible to derive an upper limit on the number of supernovae in our galaxy. Depending on the assumed supernova type and model, this limit varies between 0.8 per year for a failed supernova and 3.8 per year for the collapse of an ONeMg core. When assuming a neutrino flux modeled after SN1987A, we determine an upper limit of 2.0 core collapses per year. Note that supernovae may be hidden by dust or behind the galactic core prohibiting an optical observation.

> On n’est jamais abouti. Il y aura toujours quelque chose à faire, une autre couleur à visiter.
>
> Jean Reno

A Details on Neutrino Oscillations

A.1 Neutrinos Propagation in Matter

When propagating through matter, neutrinos are affected by forward scattering through charged and neutral current interactions. These will be considered in the following section (see [91] for a detailed discussion).

Charged Current Interactions:

As the particles $W^{\pm}$ carry charge but at the same time preserve lepton flavor, interactions are only possible between leptons of the same type. In a supernova only the interactions between electron flavors need to be taken into account:

$$\mathcal{H}_{\text{eff}}^{\text{CC}} = \frac{G_{\text{F}}}{\sqrt{2}} \left[\bar{\nu}_e(x)\gamma^{\rho}(1-\gamma^5)\nu_e(x)\right] \left[\bar{e}(x)\gamma_{\rho}(1-\gamma^5)e(x)\right] \quad . \tag{A.1}$$

The charged current potential is given as

$$V_{\text{CC}}^{e} = \sqrt{2} G_{\text{F}} N_e \quad . \tag{A.2}$$

G_{F} is the Fermi coupling constant and N_e stands for the electron number density.

Neutral Current Interactions:

The neutral current interaction, featuring the Z^0, acts on all three neutrino types in the same manner. Its effective Hamiltonian is

$$\mathcal{H}_{\text{eff}}^{\text{NC}} = \frac{G_{\text{F}}}{\sqrt{2}} \sum_{\alpha=e,\mu,\tau} \left[\bar{\nu}_{\alpha}(x)\gamma^{\rho}(\mathbb{1}-\gamma^5)\nu_{\alpha}(x)\right] \sum_{f} \left[\bar{f}(x)\gamma_{\rho}(g_V^f \mathbb{1} - g_V^f \gamma^5) f(x)\right] \quad . \tag{A.3}$$

g_V^f is the vectorial coupling of the neutrinos to a fermion f. Using the Hamiltonian, the neutral current contribution to the effective potential is determined to be:

$$V_{\text{NC}}^{\alpha} = \sqrt{2} G_{\text{F}} N_f \, g_V^f \quad . \tag{A.4}$$

with N_f standing for the density of fermions f in matter.

Because the number of electrons and protons in the star is approximately the same and $g_V^e = -g_V^p$, their contribution cancels. Thus, only neutrons have to be considered.

Combining the Interactions:

Combining charged and neutral current interactions, we get a total effective potential for the neutrinos of:

$$V^{\alpha}_{\text{eff}} = \sqrt{2}G_{\text{F}}(N_e\delta_{\alpha e} - \frac{1}{2}N_n g^n_V) \quad . \tag{A.5}$$

Note that the potential for the anti-neutrinos has the opposite sign: $\bar{V}^{\alpha}_{\text{eff}} = -V^{\alpha}_{\text{eff}}$.

Again, we define the probability for a neutrino ν_α of the flavor $\alpha = e, \mu, \tau$ at $t = 0$ to oscillate to a neutrino $\nu_\beta(t)$ as $P_{\nu_\alpha \to \nu_\beta}(t) = |\psi_{\alpha\beta}(t)|^2$ with $\psi_{\alpha\beta}(t) = \langle \nu_\beta \mid \nu_\alpha(t)\rangle$. With the Schrödinger equation, we get

$$i\frac{\mathrm{d}}{\mathrm{d}t}\psi_{\alpha\beta}(t) = \langle \nu_\beta \mid i\frac{\mathrm{d}}{\mathrm{d}t} \mid \nu_\alpha(t)\rangle = \langle \nu_\beta \mid \mathcal{H} \mid \nu_\alpha(t)\rangle \quad . \tag{A.6}$$

We split the Hamiltonian in a vacuum and an interaction term and obtain the equations

$$\mathcal{H}_0 \mid \nu_k\rangle = E_k \mid \nu_k\rangle \quad \text{and} \quad \mathcal{H}_I \mid \nu_\alpha\rangle = V_\alpha \mid \nu_\alpha\rangle \quad . \tag{A.7}$$

In the ultra-relativistic case ($E \gg m$), one can write:

$$\begin{aligned} i\frac{\mathrm{d}}{\mathrm{d}x}\psi_{\alpha\beta}(x) &= (p + \frac{m_1^2}{2E} + V_{\text{NC}})\psi_{\alpha\beta}(x) \\ &\quad + \sum_\gamma \left(\sum_k U^*_{\alpha k}\frac{\Delta m^2_{k1}}{2E}U_{\gamma k} + \delta_{\alpha e}\delta_{\gamma e}V_{\text{CC}} \right)\psi_{\alpha\gamma}(x) \quad . \end{aligned} \tag{A.8}$$

As the first part of the equation affects all neutrinos flavors the same, it is irrelevant for neutrino oscillations. Thus, it suffices to look at:

$$i\frac{\mathrm{d}}{\mathrm{d}x}\vec{\psi}_\alpha(x) = \mathcal{H}_{\text{F}}\vec{\psi}_\alpha(x) \quad , \tag{A.9}$$

with

$$\mathcal{H}_{\text{F}} = \frac{1}{2E}(UM^2U^\dagger + A) \quad , \tag{A.10}$$

$$\vec{\psi}_\alpha \equiv \begin{pmatrix} \psi_{\alpha e} \\ \psi_{\alpha\mu} \\ \psi_{\alpha\tau} \end{pmatrix} , \; M^2 \equiv \begin{pmatrix} 0 & 0 & 0 \\ 0 & \Delta m^2_{21} & 0 \\ 0 & 0 & \Delta m^2_{31} \end{pmatrix} \text{ and } A \equiv \begin{pmatrix} A_{\text{CC}} & 0 & 0 \\ 0 & 0 & 0 \\ 0 & 0 & 0 \end{pmatrix} \quad , \tag{A.11}$$

and $A_{\text{CC}} \equiv 2EV_{\text{CC}}$.

A.2 Neutrinos Self-Interactions

A.2.1 Density Matrix Formalism

The following section aims at explaining the density matrix and the NFIS picture. More details can be found in [91].

For simplicity, we will stay in the two-neutrino picture. The following considerations can be extended to three neutrinos, however, at the cost of lucidity.

A neutrino ensemble can be described by the density matrix:

$$\hat{\rho}(x) = \sum_{\alpha} \mid \nu_\alpha(x)\rangle W_\alpha \langle \nu_\alpha(x) \mid \quad . \tag{A.12}$$

W_α are statistical weights of the neutrinos in the initial ensemble and have to satisfy $\sum_\alpha W_\alpha = 1$. Summing the density matrix over all neutrino flavors gives:

$$\mathrm{tr}(\hat{\rho}(x)) \equiv \sum_{\alpha} \langle \nu_\alpha \mid \hat{\rho}(x) \mid \nu_\alpha \rangle = 1 \quad . \tag{A.13}$$

One can derive the probability to detect a neutrino of the flavor β at x to be:

$$P_\beta(x) = \mathrm{tr}(\hat{\rho}(x) \mid \nu_\beta\rangle\langle\nu_\beta \mid) = \langle \nu_\beta \mid \hat{\rho}(x) \mid \nu_\beta \rangle = \rho^{\mathrm{F}}_{\beta\beta}(x) \quad . \tag{A.14}$$

As $(\hat{\rho}^{\mathrm{F}}(x))^\dagger = \hat{\rho}^{\mathrm{F}}(x)$ and $(\mathcal{H}^{\mathrm{F}}(x))^\dagger = \mathcal{H}^{\mathrm{F}}(x)$, it follows that

$$i\frac{\mathrm{d}}{\mathrm{d}x}\hat{\rho}^{\mathrm{F}}(x) = \left[\mathcal{H}^{\mathrm{F}}(x), \hat{\rho}^{\mathrm{F}}(x)\right] \quad . \tag{A.15}$$

Like before, the Hamiltonian can be converted from the flavor eigenbasis to the matter eigenbasis $\mathcal{H}^{\mathrm{M}} = U_{\mathrm{M}}^\dagger \mathcal{H}^{\mathrm{F}} U_{\mathrm{M}}$, thus diagonalizing it. Analogously, the density matrix in the matter eigenbasis is $\hat{\rho}^{\mathrm{M}} = U_{\mathrm{M}}^\dagger \hat{\rho}^{\mathrm{F}} U_{\mathrm{M}}$. Equation A.15 becomes:

$$i\frac{\mathrm{d}}{\mathrm{d}x}\hat{\rho}^{\mathrm{M}}(x) = \left[\mathcal{H}^{\mathrm{M}}(x), \hat{\rho}^{\mathrm{M}}(x)\right] - i\left[U_{\mathrm{M}}^\dagger \frac{\mathrm{d}}{\mathrm{d}x} U_{\mathrm{M}}, \hat{\rho}^{\mathrm{M}}(x)\right] \quad . \tag{A.16}$$

Let us now go to the two flavor case. Every 2×2 matrix can be decomposed by $X = \frac{1}{2}\left(\mathrm{tr}(X)\mathbb{1} + \sum_k \mathrm{tr}(X\sigma_k)\sigma_k\right)$. Due to equation 1.30 $\mathrm{tr}(\mathcal{H}^{\mathrm{F}}) = 0$ and thereby

$$\mathcal{H}_{\mathrm{eff}} \equiv \mathcal{H}_{\mathrm{V}} + \mathcal{H}_e = -\frac{1}{2}\vec{\sigma} \cdot (\mu_{\mathrm{V}}\vec{H}_{\mathrm{V}} + \vec{H}_e) \equiv -\frac{1}{2}\vec{\sigma} \cdot \vec{H}_{\mathrm{eff}} \quad . \tag{A.17}$$

Let us now take a look at the Hamilton vectors in the flavor basis:

$$\begin{aligned} \vec{H}^{\mathrm{F}}_{\mathrm{V}} &= (-\sin 2\theta,\ 0,\ \cos 2\theta) \quad , \\ \vec{H}^{\mathrm{F}}_{e} &= (0,\ 0,\ \sqrt{2}G_{\mathrm{F}}N_e) \quad \text{and} \\ \vec{H}^{\mathrm{F}}_{\mathrm{eff}} &= \mu_{\mathrm{V}}\vec{H}_{\mathrm{V}} + \vec{H}_e \quad , \end{aligned} \tag{A.18}$$

with $\mu_{\mathrm{V}} \equiv \frac{\Delta m^2}{2E_\nu}$ and the definitions from 1.32.

Applying the same conversion for the density matrix, we obtain:

$$\hat{\rho}^{\mathrm{F}} = \frac{\mathbb{1}}{2} \pm \vec{\sigma} \cdot \vec{s}_\nu \quad \text{with} \quad \vec{s}_\nu^{\,\mathrm{F}} \equiv \pm \frac{1}{2} \begin{pmatrix} 2\,\mathrm{Re}(\rho^{\mathrm{F}}_{e\mu}) \\ 2\,\mathrm{Im}(\rho^{\mathrm{F}}_{e\mu}) \\ \rho^{\mathrm{F}}_{ee} - \rho^{\mathrm{F}}_{\mu\mu} \end{pmatrix} \quad , \tag{A.19}$$

with + describing the neutrino and − the anti-neutrino. Using the relation $\left[\vec{a} \cdot \vec{\sigma}, \vec{b} \cdot \vec{\sigma}\right] = 2i\vec{\sigma} \cdot (\vec{a} \times \vec{b})$ equation A.16 can be expressed as

$$\frac{\mathrm{d}}{\mathrm{d}x} \vec{P}_\nu = \vec{P}_\nu \times \vec{H}_{\mathrm{eff}} \quad . \tag{A.20}$$

This equation of motion is equivalent to the precession of a gyroscope with an angular momentum $\vec{P}_\nu$ around $\vec{H}_{\mathrm{eff}}$ with an angular frequency of $|\vec{H}_{\mathrm{eff}}|$. The Ehrenfest theorem tells us that the quantum mechanical description of a system is equivalent to the classical one after replacing the classical values by the expectation values of the respective operators. We define the neutrino flavor isospin:

$$\vec{s}_\nu \equiv \psi_\nu^\dagger \frac{\vec{\sigma}}{2} \psi_\nu = \frac{\vec{P}_\nu}{2} \quad \text{and} \quad \vec{s}_{\bar{\nu}} \equiv \psi_{\bar{\nu}}^\dagger \frac{\vec{\sigma}}{2} \psi_{\bar{\nu}} = -\frac{\vec{P}_{\bar{\nu}}}{2} \quad . \tag{A.21}$$

The minus sign in the second term comes from the equivalent representation in the anti-particle range. The equation of motion is the same as A.20, namely

$$\frac{\mathrm{d}}{\mathrm{d}x} \vec{s}_\nu = \vec{s}_\nu \times \vec{H}_{\mathrm{eff}} \quad . \tag{A.22}$$

It is equivalent a spin $\vec{s}_\nu$ in a magnetic field $\vec{H}_{\mathrm{eff}}$.

$\vec{s}_\nu$ is correlated to the probability of finding the respective neutrino in its flavor eigenstate by

$$\begin{aligned} P_{\nu_e}(x) &= \rho^{\mathrm{F}}_{ee}(x) = \frac{1}{2} + \vec{s}_\nu \cdot \vec{e}_3^{\,\mathrm{F}} \quad \text{and} \\ P_{\nu_\mu}(x) &= \rho^{\mathrm{F}}_{\mu\mu}(x) = \frac{1}{2} - \vec{s}_\nu \cdot \vec{e}_3^{\,\mathrm{F}} \quad . \end{aligned} \tag{A.23}$$

Let's take a look at solar neutrinos. At the point of creation $(t, x = 0)$, no neutrino mixing has yet occured, meaning that the off-diagonal elements $\rho^{\mathrm{F}}_{\eta\xi}$ are zero. This is equivalent to the initial conditions

$$\vec{s}_\nu^{\,F}(0) = \frac{1}{2} \begin{pmatrix} 0 \\ 0 \\ W_e - W_\mu \end{pmatrix} \quad \longrightarrow \quad \vec{s}_\nu^{\,M}(0) = \frac{1}{2}(W_e - W_\mu) \begin{pmatrix} \sin 2\theta_{\mathrm{M}} \\ 0 \\ \cos 2\theta_{\mathrm{M}} \end{pmatrix} \quad . \tag{A.24}$$

The equations of motion can then be solved to:

$$\vec{s}_\nu^{\,M}(x) = \frac{1}{2}(W_e - W_\mu)\begin{pmatrix}\sin 2\theta_\mathrm{M}\cos\omega x\\ \sin 2\theta_\mathrm{M}\sin\omega x\\ \cos 2\theta_\mathrm{M}\end{pmatrix} \quad . \tag{A.25}$$

The evolution of the angle between $\vec{s}_\nu$ and $\vec{H}_\mathrm{eff}$ can be derived to be

$$\frac{\mathrm{d}}{\mathrm{d}x}\left(\frac{\vec{s}_\nu\cdot\vec{H}_\mathrm{eff}}{|\vec{s}_\nu||\vec{H}_\mathrm{eff}|}\right) = \frac{\vec{s}_\nu}{|\vec{s}_\nu|}\cdot\frac{\mathrm{d}}{\mathrm{d}x}\left(\frac{\vec{H}_\mathrm{eff}}{|\vec{H}_\mathrm{eff}|}\right) = \frac{\vec{s}_\nu}{|\vec{s}_\nu|}\cdot\frac{\mathrm{d}}{\mathrm{d}x}\vec{e}_3^{\,\mathrm{M}} = \frac{\mathrm{d}}{\mathrm{d}x}\cos 2\theta_\mathrm{M} \quad . \tag{A.26}$$

The contributions to the light or heavy mass eigenstates can now be written analogously to equation A.23

$$\begin{aligned} P_\mathrm{L}(x) &= \frac{1}{2} + \vec{s}_\nu\cdot\vec{e}_3^{\,\mathrm{M}} = \frac{1+\cos 2\theta_\mathrm{M}}{2} \quad \text{and} \\ P_\mathrm{H}(x) &= \frac{1}{2} - \vec{s}_\nu\cdot\vec{e}_3^{\,\mathrm{M}} = \frac{1-\cos 2\theta_\mathrm{M}}{2} \quad . \end{aligned} \tag{A.27}$$

We now derive the adiabatic condition in the NFIS picture. Consider a timescale $\delta t \gtrsim 2\pi/|\vec{H}_\mathrm{eff}|$. During δt the NFIS $\vec{s}_\nu$ has completed at least one cycle around $\vec{H}_\mathrm{eff}$. If the change of angle of $\vec{H}_\mathrm{eff}$ is small during this time, $\delta\phi \ll 2\pi$, then $\vec{s}_\nu$ averages to $(\vec{s}_\nu\cdot\vec{e}_3^{\,\mathrm{M}})\vec{e}_3^{\,\mathrm{M}}$. Because of $\vec{e}_3^{\,\mathrm{M}}\cdot\frac{\mathrm{d}}{\mathrm{d}t}\vec{e}_3^{\,\mathrm{M}} = 0$ and equation A.26, the angle θ_M stays constant. According to equation A.27, no neutrino transitions can occur and we have adiabatic transitions. The relevant condition is:

$$\delta\phi^2 = \left(\vec{e}_3^{\,\mathrm{M}}\times(\vec{e}_3^{\,\mathrm{M}} + \frac{\mathrm{d}}{\mathrm{d}t}\vec{e}_3^{\,\mathrm{M}}\delta t)\right)^2 = \left|\frac{\mathrm{d}}{\mathrm{d}t}\vec{e}_3^{\,\mathrm{M}}\right|^2 \quad . \tag{A.28}$$

As $\vec{e}_3^{\,\mathrm{M}} = \vec{H}_\mathrm{eff}/|\vec{H}_\mathrm{eff}|$ (because it is an eigenvector of the propagation states) and $\delta t \gtrsim 2\pi/|\vec{H}_\mathrm{eff}|$

$$\left|\frac{\mathrm{d}}{\mathrm{d}t}\vec{e}_3^{\,\mathrm{M}}\right| = \frac{\dot{\vec{H}}_\mathrm{eff}\times\vec{H}_\mathrm{eff}}{|\vec{H}_\mathrm{eff}|^2} \ll |\vec{H}_\mathrm{eff}| \quad . \tag{A.29}$$

In words, this means that the rate of change of $\vec{H}_\mathrm{eff}$ is much smaller than the rotation of $\vec{s}_\nu$ around $\vec{H}_\mathrm{eff}$.

We will now qualitatively retrace the neutrino evolution in the sun using the density matrix formalism. Note that the third matter basis vector is given as $\vec{e}_3^{\,\mathrm{M}} = -\sin 2\theta_M\vec{e}_1^{\,\mathrm{F}} + \cos 2\theta_M\vec{e}_3^{\,\mathrm{F}}$.

At the creation point of the neutrinos, the density is greater than the resonance density $N_e > N_e^\mathrm{R}$ and thus $\cos 2\theta_\mathrm{M} < 0$. Here, the neutrinos are completely in their flavour eigenstate, e.g. ν_e, and thus parallel to $\vec{e}_3^{\,\mathrm{F}}$. $\vec{e}_3^{\,\mathrm{M}}$ has a negative sign on its $\vec{e}_3^{\,\mathrm{F}}$ component, meaning that the electron neutrinos would mostly consist of the heavy ν_2^M neutrinos. If $N_e \gg N_e^\mathrm{R}$, then $\cos 2\theta_\mathrm{M}$ and consequently $\theta_M \approx \pi/4$ leading to the

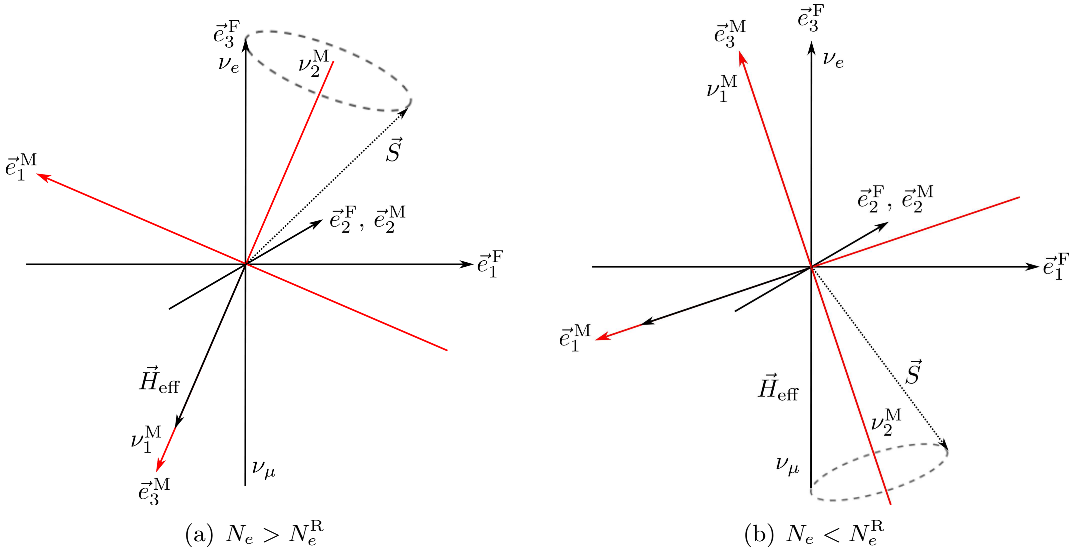

(a) $N_e > N_e^{\rm R}$ (b) $N_e < N_e^{\rm R}$

Figure A.1: Adiabatic neutrino evolution
The left picture shows the neutrino flavour isospin at high, the right at low densities. For a detailed explanation see the text.

ν_e being mostly in the $\nu_2^{\rm M}$ state. As they propagate, the $\vec{s}_\nu$ vector starts precessing around $\vec{H}_{\rm eff}$ which is parallel to $\vec{e}_3^{\rm M}$.

If $N_e < N_e^{\rm R}$ and $\cos 2\theta_{\rm M} > 0$, $\vec{e}_3^{\rm M}$ has a positive sign in front of its $\vec{e}_3^{\rm F}$ component. Consequently, ν_e are mostly made up of $\nu_1^{\rm M}$. As the neutrino leaves the star, $N_e \to 0$ and the oscillation parameters converge to their vacuum value $\theta_{\rm M} \to \theta$ and $\Delta m_{\rm M}^2 \to \Delta m^2$.

There are two possibilities to investigate, the adiabatic propagation and the maximal violation of adiabaticity.

Adiabatic neutrino evolution is schematically shown in figure A.1. If the density changes slowly, the angle between $\vec{H}_{\rm eff}$ and $\vec{s}_\nu$ changes little, while θ_M changes its sign. In the spin picture this means that the rotation speed of $\vec{s}_\nu$ around $\vec{H}_{\rm eff}$ and thus $\vec{e}_3^{\rm M}$ is much higher than the speed of change in angle between $\vec{H}_{\rm eff}$ and $\vec{e}_3^{\rm F}$. $\vec{H}_{\rm eff}$ drags $\vec{s}_\nu$ along. Neutrinos created as electron neutrinos with large contribution of the heavy state leave the star as such and will mainly be detected as muon neutrinos.

However, if the density changes rapidly, the change in $\sphericalangle(\vec{H}_{\rm eff}\vec{s}_\nu)$ is large (sketched in figure A.2). In the case of maximal violation of adiabaticity, a flip occurs and $S_3^{\rm M} \to -S_3^{\rm M}$. The change in angle between $\vec{H}_{\rm eff}$ and $\vec{e}_3^{\rm F}$ is much faster than the rotation speed of $\vec{s}_\nu$ around $\vec{H}_{\rm eff}$. In the spin picture this means that because of the slow precession, $\vec{s}_\nu$ stays in place while $\vec{H}_{\rm eff}$ and thus $\vec{e}_3^{\rm M}$ switch the sign relative to $\vec{e}_3^{\rm F}$. Consequently, neutrinos created as ν_e, consisting largely of $\nu_2^{\rm M}$, convert to the ν_1 state on their way out of the star. They will mainly be detected as electron neutrinos.

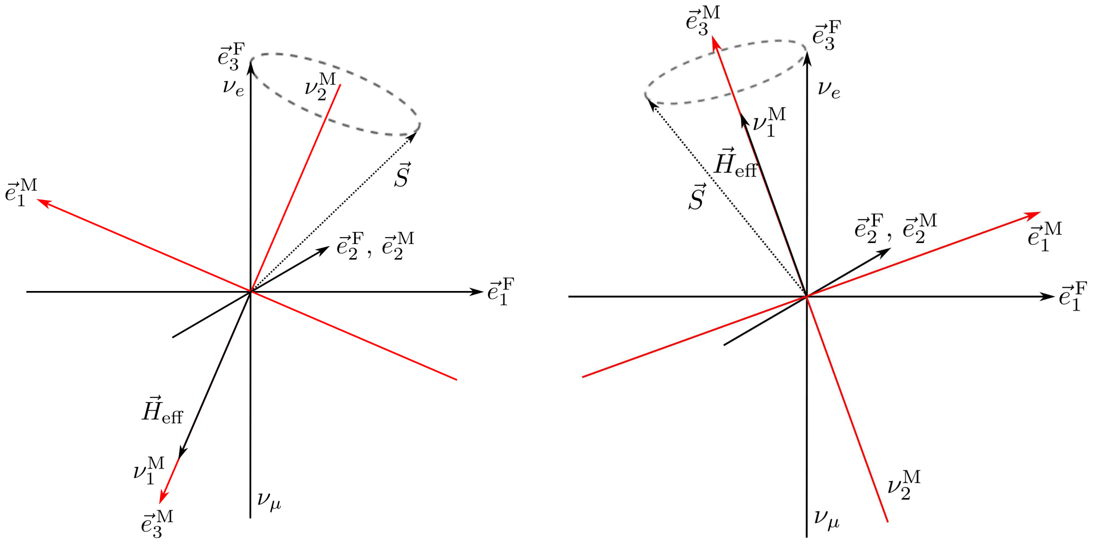

(a) $N_e > N_e^{\mathrm{R}}$ (b) $N_e < N_e^{\mathrm{R}}$

Figure A.2: Neutrino evolution in the case of maximally violated adiabaticity
The left picture shows the neutrino flavour isospin at high, the right at low densities. For a detailed explanation see the text.

A.2.2 General Synchronized Neutrino Systems

This section aims at describing the generalization of the simple case of a synchronized neutrino ensemble starting from the considerations in section 1.2.4.3. For a more complete approach refer to [102].

General Synchronized Systems in Absence of Matter

Consider a co-rotating reference frame, rotating with an angular velocity of $-\Omega\vec{H}_{\mathrm{V}}$. The e.o.m. 1.70 and 1.71 then take the form

$$\begin{aligned} \frac{\mathrm{d}}{\mathrm{d}t}\vec{\tilde{s}}_i &= \vec{\tilde{s}}_i \times (\tilde{\mu}_{\mathrm{V},i}\vec{H}_{\mathrm{V}} + \mu_\nu \vec{\tilde{S}}) \quad \text{and} \\ \frac{\mathrm{d}}{\mathrm{d}t}\vec{\tilde{S}} &= \sum_i \tilde{\mu}_{\mathrm{V},i} n_i \vec{\tilde{s}}_i \times \vec{H}_{\mathrm{V}} \quad , \end{aligned} \tag{A.30}$$

with

$$\tilde{\mu}_{\mathrm{V},i} \equiv \mu_{\mathrm{V},i} - \Omega \quad . \tag{A.31}$$

As $\vec{S}$ and $\vec{\tilde{S}}$ are the same vectors in different reference frames, synchronization in one frame entrains synchronization in all frames. Take e.g. electron anti-neutrinos with

$\vec{s} = -\frac{1}{2}\vec{e}_3^{\,f}$ and $\mu_\mathrm{V} = -\Delta m^2/2E$. By performing a rotation with $\Omega = -\Delta m^2/E$, we replace $\bar{\nu}_e$ by ν_μ.

We saw before that $|\mu_\nu \vec{S}| \gg |\mu_{\mathrm{V},i}|_\mathrm{max}$ is the condition for synchronization of a neutrino system. From the technique of co-rotating frames it becomes evident that $|\mu_{\mathrm{V},i}|_\mathrm{max}$ is not uniquely defined. The spread of the neutrino energies $\Delta\mu$, however, is a property intrinsic to all possible co-rotating frames. One can conclude that the condition for synchronization of the neutrino gas is

$$|\mu_\nu \vec{S}| \gg \Delta\mu_\mathrm{V} \quad , \tag{A.32}$$

with the spread

$$\Delta\mu_\mathrm{V} \equiv \frac{(\mu_{\mathrm{V},i})_\mathrm{max} - (\mu_{\mathrm{V},i})_\mathrm{min}}{2} \quad . \tag{A.33}$$

Synchronized Systems in Matter

If we assume a fixed matter background, the e.o.m. 1.70 and 1.71 modify to

$$\begin{aligned} \frac{\mathrm{d}}{\mathrm{d}t}\vec{s}_i &= \vec{s}_i \times (\mu_{\mathrm{V},i}\vec{H}_\mathrm{V} + \vec{H}_e + \mu_\nu \vec{S}) \quad \text{and} \\ \frac{\mathrm{d}}{\mathrm{d}t}\vec{S} &= \sum_i \mu_{\mathrm{V},i} n_i \vec{s}_i \times \vec{H}_\mathrm{V} + \vec{S} \times \vec{H}_e \quad . \end{aligned} \tag{A.34}$$

In the case where $|\vec{H}_e| \gg |\langle\mu_\mathrm{V}\rangle|$, the $\vec{H}_\mathrm{V}$-term can be neglected. If we consider a co-rotating frame with an angular frequency of $-\vec{H}_e$, we see that the total NFIS $\vec{S}$ stays fixed and the $\vec{s}_i$ precess around it. Ergo, all neutrinos remain in their initial state.

The case where $|\mu_\nu \vec{S}| \gg |\vec{H}_e| \sim |\langle\mu_\mathrm{V}\rangle|$ can be treated like the one without matter as the e.o.m. for $\vec{s}_i$ stay the same, namely equation 1.73, the individual NFIS's still precess around $\vec{S}$. However, equation 1.71 alters to

$$\frac{\mathrm{d}}{\mathrm{d}t}\vec{S} \simeq \vec{S} \times \vec{H}_\mathrm{eff} \quad , \tag{A.35}$$

with $\vec{H}_\mathrm{eff} \equiv \langle\mu_\mathrm{V}\rangle\vec{H}_\mathrm{V} + \vec{H}_e$. Because this equation is equivalent to A.22, it follows that a neutrino gas with a total NFIS $\vec{S}$ behaves just as a single NFIS with $\vec{s}_\nu = \vec{S}/2|\vec{S}|$ and $\mu_\mathrm{V} = \langle\mu_\mathrm{V}\rangle$ would in the same matter background. With definition 1.64 we conclude that for $(\Delta m^2\langle\mu_\mathrm{V}\rangle) > 0$ this behavior is equivalent to a neutrino (or an anti-neutrino for < 0) with energy $E_\mathrm{sync} \equiv |\Delta m^2/2\langle\mu_\mathrm{V}\rangle|$.

A.2.3 Bi-Polar Neutrino Systems

This section tries to provide a comprehensive approach to bi-polar systems. More details can be found in [102].

A.2.3.1 Simple System without Matter

For simplicity, we start with a system consisting of only ν_e and $\bar{\nu}_e$ in equal number densities n_ν with energies $\mu_{\mathrm{V}+} = -\mu_{\mathrm{V}-} = \mu_{\mathrm{V}}$ for all (anti-)neutrinos. We sum equation 1.63 over all neutrinos and anti-neutrinos respectively and get

$$\begin{aligned} \frac{\mathrm{d}}{\mathrm{d}t}\vec{S}_\nu &= \vec{S}_\nu \times \left(\mu_{\mathrm{V}}\vec{H}_{\mathrm{V}} + \mu_\nu \vec{S}_{\bar{\nu}}\right) \quad \text{and} \\ \frac{\mathrm{d}}{\mathrm{d}t}\vec{S}_{\bar{\nu}} &= \vec{S}_{\bar{\nu}} \times \left(-\mu_{\mathrm{V}}\vec{H}_{\mathrm{V}} + \mu_\nu \vec{S}_\nu\right) \quad . \end{aligned} \tag{A.36}$$

With the definitions of

$$\vec{S}_+ \equiv \vec{S}_\nu + \vec{S}_{\bar{\nu}} \quad \text{and} \quad \vec{S}_- \equiv \vec{S}_\nu - \vec{S}_{\bar{\nu}} \quad , \tag{A.37}$$

we arrive at the equations of motion

$$\begin{aligned} \frac{\mathrm{d}}{\mathrm{d}t}\vec{S}_+ &= \mu_{\mathrm{V}}\vec{S}_- \times \vec{H}_{\mathrm{V}} \quad \text{and} \\ \frac{\mathrm{d}}{\mathrm{d}t}\vec{S}_- &= \mu_{\mathrm{V}}\vec{S}_+ \times \vec{H}_{\mathrm{V}} + \mu_\nu \vec{S}_- \times \vec{S}_+ \quad . \end{aligned} \tag{A.38}$$

The initial conditions where no mixing has yet occurred, are given by

$$\vec{S}_\nu(0) = \frac{n_\nu}{2}\vec{e}_3^{\,\mathrm{F}} \quad , \quad \vec{S}_{\bar{\nu}}(0) = -\frac{n_\nu}{2}\vec{e}_3^{\,\mathrm{F}} \tag{A.39}$$

and thus

$$\begin{aligned} \vec{S}_+(0) &= 0 \quad \text{and} \\ \vec{S}_-(0) &= n_\nu \vec{e}_3^{\,\mathrm{F}} = n_\nu(\sin 2\theta \vec{e}_1^{\,\mathrm{V}} + \cos 2\theta \vec{e}_3^{\,\mathrm{V}}) \quad . \end{aligned} \tag{A.40}$$

From these and from equation A.38, one can derive that $\vec{S}_+$ changes only in the $\vec{e}_2^{\,\mathrm{V}}$-direction. As $\vec{e}_3^{\,\mathrm{V}} \equiv \vec{H}_{\mathrm{V}}$ we get

$$\vec{S}_+ \cdot \vec{e}_1^{\,\mathrm{V}} = \vec{S}_+ \cdot \vec{e}_3^{\,\mathrm{V}} = \vec{S}_- \cdot \vec{e}_2^{\,\mathrm{V}} = 0 \quad . \tag{A.41}$$

To understand the evolution of the neutrinos as a gas, we need to follow the development along the $\vec{e}_3^{\,\mathrm{V}}$-direction. As seen from A.41, it is given by

$$s_{\nu,3}^{\mathrm{V}} = -s_{\bar{\nu},3}^{\mathrm{V}} = \frac{\vec{S}_- \cdot \vec{e}_3^{\,\mathrm{V}}}{2n_\nu} = \frac{|\vec{S}_-|\cos\vartheta}{2n_\nu} \quad , \tag{A.42}$$

with ϑ being the angle between $\vec{S}_-$ and $\vec{H}_{\mathrm{V}} = \vec{e}_3^{\,\mathrm{V}}$.

To derive the behavior of this angle, we look at the total energy. As said before, it is constant and thus equation 1.65 simplifies to

$$\mathcal{E} = -\mu_{\mathrm{V}}\vec{S}_- \cdot \vec{H}_{\mathrm{V}} - \frac{\mu_\nu}{2}\vec{S}_+^2 = -\mu_{\mathrm{V}} n_\nu \cos 2\theta \quad . \tag{A.43}$$

From this, we derive that

$$\vec{S}_- \cdot \vec{H}_\mathrm{V} = |\vec{S}_-| \cos\vartheta = n_\nu \cos 2\theta - \frac{\mu_\nu n_\nu}{2\mu_\mathrm{V}} \vec{S}_+^2 \quad . \tag{A.44}$$

It can be seen from equations 1.79 that $\vec{S}_+^2 + \vec{S}_-^2 = n_\nu^2$ is constant. With equation A.43 and the definitions

$$\begin{aligned} s_- &\equiv \frac{|\vec{S}_-|}{n_\nu} \quad \text{and} \\ n_\nu^\mathrm{cri} &\equiv \frac{2\mu_\mathrm{V}}{\mu_\nu} \cos 2\theta \end{aligned} \tag{A.45}$$

we derive the angle ϑ:

$$\cos\vartheta = \cos 2\theta \left[\left(1 - \frac{n_\nu}{n_\nu^\mathrm{cri}} \right) \frac{1}{s_-} + \left(\frac{n_\nu}{n_\nu^\mathrm{cri}} \right) s_- \right] \quad . \tag{A.46}$$

Note that the neutrino interaction potential is delimited by $\mu_\nu < 0$ (equation 1.67). s_- describes the alignment of the system with the maximal value 1 standing for full anti-alignment of all neutrinos and anti-neutrinos and $s_- > 0$.

In case of normal mass hierarchy, $\mu_\mathrm{V} > 0$ and thus $n_\nu^\mathrm{cri} < 0$ leading to $1 \geq \cos\vartheta \geq \cos 2\theta$. Consequently, $-2\theta \leq \vartheta \leq 2\theta$, indicating that flavor mixing can maximally reach the vacuum level. For small vacuum mixing, the neutrinos stay close to their initial state.

The circumstances are much more involved for the inverted mass hierarchy where $\mu_\mathrm{V} < 0$. We have to consider three distinct cases and the different behavior of the respective derivative

$$\frac{\mathrm{d}}{\mathrm{d}s_-} \cos\vartheta = \cos 2\theta \left[-\left(1 - \frac{n_\nu}{n_\nu^\mathrm{cri}} \right) \frac{1}{s_-^2} + \frac{n_\nu}{n_\nu^\mathrm{cri}} \right] \quad . \tag{A.47}$$

$n_\nu/n_\nu^\mathrm{cri} < 1/2$: In this case, $\frac{\mathrm{d}}{\mathrm{d}s_-} \cos\vartheta \leq 0$ and thus $-2\theta \leq \vartheta \leq 2\theta$. We have the same situation as in the normal hierarchy case.

$1/2 < n_\nu/n_\nu^\mathrm{cri} < 1$: At $s_- \sim 1$ the derivative is positive but decreases to zero and below as s_- becomes smaller. We have a maximal angle ϑ_max and $\cos\vartheta_\mathrm{max} \leq \cos\vartheta \leq \cos 2\theta$. ϑ starts out at 2θ, increases to ϑ_max and then decreases again as s_- becomes smaller. This motion of $\vec{S}_-$ is mirrored in the other half of the plane defined by $\vec{e}_1^\mathrm{V}$ and $\vec{e}_3^\mathrm{V}$.

$1 \leq n_\nu/n_\nu^\mathrm{cri}$: The derivative is always positive and thus $-1 \leq \cos\vartheta \leq \cos 2\theta$. The angle oscillates around 2θ and $2\pi - 2\theta$. In the limit $n_\nu/n_\nu^\mathrm{cri} \gg 1$ the neutrinos are forced into full anti-alignment as $s_- \sim 1$ and thus full conversion of ν_e and $\bar{\nu}_e$ can occur, even if $\theta \ll 1$.

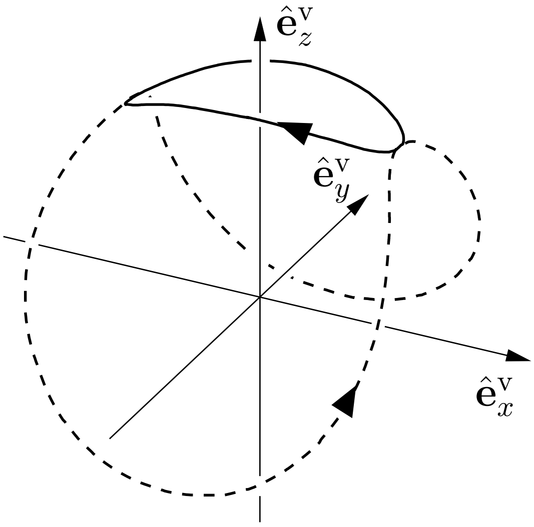

Figure A.3: Path described by $\vec{s}_\nu$ in the vacuum basis [102]
The solid line depicts the track of $\vec{s}_\nu$ *for the normal, the dashed line the inverted hierarchy for the case* $1/2 < n_\nu/n_\nu^{\mathrm{cri}} < 1$.

The track described by $\vec{s}_\nu$ is the intersection of the paraboloid surface defined equation A.43 with $\vec{H}_{\mathrm{V}} \cdot \vec{S}_- = 2n_\nu = 2n_\nu s^{\mathrm{V}}_{\nu,3}$ and $S_+^2 = 2n_\nu^2 s^2_{\nu,2}$ and the sphere defined by $\vec{S}_\nu^2 = \vec{S}_+^2 + \vec{S}_-^2 = \mathrm{const}$. It is shown in figure A.3.

With $e^{\mathrm{F}}_3 = \sin 2\theta \vec{e}^{\mathrm{V}}_1 + \cos 2\theta \vec{e}^{\mathrm{V}}_3$, equation A.42, $e^{\mathrm{F}}_1 \perp e^{\mathrm{F}}_3$ and trigonometric relations, the flavor evolution can be determined to:

$$s^{\mathrm{F}}_{\nu,3} = \vec{s}_\nu \cdot \vec{e}^{\mathrm{F}}_3 = \frac{s_-}{2} \cos(\vartheta - 2\theta) \quad . \tag{A.48}$$

The oscillation period in the bi-polar case can be estimated as follows. In the limit $n_\nu/n_\nu^{\mathrm{cri}} \gg 1$ the second equation of 1.79 tells us that $\vec{S}_-$ rotates around $\vec{S}_+$ with a frequency of $|\mu_\nu|\langle|\vec{S}_+|\rangle$. From the first equation in 1.79 one can derive that the change of $|\vec{S}_+|$ is proportional to $\vec{S}_-\vec{H}_{\mathrm{V}}$ and thus also dependent on ϑ. The maximal value $|\vec{S}_+|$ can thus reach is $T|\mu_V \vec{S}_-|$ and the minimum would be zero. Consequently, $\langle|\vec{S}_+|\rangle \sim |\vec{S}_-|T \simeq |\mu_{\mathrm{V}}|n_\nu$. For the bi-polar period we derive

$$T_{\mathrm{bi}} \sim \frac{1}{\sqrt{n_\nu |\mu_{\mathrm{V}} \mu_\nu|}} \quad . \tag{A.49}$$

A.2.3.2 General Bi-Polar Neutrino Systems

The same approach used for the generalization of synchronized systems can be used for the bi-polar case.

General Bi-Polar Systems in Absence of Matter

We consider a system having different energies for e.g. ν_e and $\bar{\nu}_e$. We define the Hamiltonian vector as

$$\vec{H}_\pm \equiv \frac{\mu_{\mathrm{V}+} \pm \mu_{\mathrm{V}-}}{2} \vec{H}_\mathrm{V} \quad , \tag{A.50}$$

with the $\mu_{\mathrm{V}+}$ the energy of the neutrino starting with $\vec{s} = +\frac{1}{2}\vec{e}_3^{\,\mathrm{F}}$ (i.e. the ν_e) and $\mu_{\mathrm{V}-}$ the energy of the neutrino starting as $\vec{s} = -\frac{1}{2}\vec{e}_3^{\,\mathrm{F}}$ (i.e. the $\bar{\nu}_e$). The equations of motion in this case are

$$\begin{aligned} \frac{\mathrm{d}}{\mathrm{d}t}\vec{S}_+ &= \vec{S}_+ \times \vec{H}_+ + \vec{S}_- \times \vec{H}_- \quad \text{and} \\ \frac{\mathrm{d}}{\mathrm{d}t}\vec{S}_- &= \vec{S}_- \times \vec{H}_+ + \vec{S}_+ \times \vec{H}_- + \mu_\nu \vec{S}_- \times \vec{S}_+ \quad . \end{aligned} \tag{A.51}$$

When going to the co-rotating frame with angular velocity of $-\vec{H}_+$, the above equations reduce to equations A.37 for $\vec{\tilde{S}}_+$ and $\vec{\tilde{S}}_-$.

All relevant of neutrino mixing e.g. $\nu_e - \bar{\nu}_e$, $\bar{\nu}_\mu - \nu_\mu$, $\nu_e - \nu_\mu$ and $\bar{\nu}_\mu - \bar{\nu}_e$ can be reduced to the simple system without matter discussed before. The governing value for this case is the energy difference between the neutrino types. The different possible mixing scenarios are shown in table A.1. The remaining mixing possibilities cannot form distinct NFIS blocks and thus no bi-polar oscillations can occur.

hierarchy	$\nu_e - \bar{\nu}_e$	$\bar{\nu}_\mu - \nu_\mu$	$\nu_e - \nu_\mu$	$\bar{\nu}_\mu - \bar{\nu}_e$
$\Delta m^2 > 0$	never	always	$E_{\nu_e} > E_{\nu_\mu}$	$E_{\bar{\nu}_\mu} < E_{\bar{\nu}_e}$
$\Delta m^2 < 0$	always	never	$E_{\nu_e} < E_{\nu_\mu}$	$E_{\bar{\nu}_\mu} > E_{\bar{\nu}_e}$

Table A.1: Conditions for bi-polar neutrino swapping of mono-energetic neutrino systems.

Bi-Polar Systems with Matter Background

If we assume a matter background, $\vec{H}_+$ modifies to

$$\vec{H}_+ \equiv \frac{\mu_{\mathrm{V}+} + \mu_{\mathrm{V}-}}{2} \vec{H}_\mathrm{V} + \vec{H}_e \quad . \tag{A.52}$$

$\vec{H}_-$ stays the same as before and is decomposed into the vectors $\vec{H}_{-\perp}$ and $\vec{H}_{-\parallel}$ which are defined as being perpendicular and parallel to $\vec{H}_+$. As we change into the co-rotating frame with angular velocity $-\vec{H}_+$, we obtain equation similar to the e.o.m. A.38, however, with time-dependent Hamiltonian vectors:

$$\begin{aligned}\frac{\mathrm{d}}{\mathrm{d}t}\vec{\tilde{H}}_{-\perp} &= \vec{\tilde{H}}_{-\perp} \times \vec{H}_{+} \quad \text{and} \\ \frac{\mathrm{d}}{\mathrm{d}t}\vec{\tilde{H}}_{-\parallel} &= 0 \quad . \end{aligned} \tag{A.53}$$

If we have a very large matter background, $\vec{\tilde{H}}_{-\perp}$ will rotate rapidly and the NFIS blocks will not be able to follow it. Its effect will thus stay small and, with the replacement of $\mu_{\mathrm{V}} \rightarrow \vec{\tilde{H}}_{-\parallel}$, it can be treated like the simple case with no matter background.

In case of a $\nu_e - \bar{\nu}_e$ system with a smaller but still large matter background, the NFIS blocks would initially be aligned with $\vec{H}_e \approx \vec{H}_{+}$. While $\vec{\tilde{H}}_{-\perp}$ acts to break this alignment its effects are small because on the one hand the effect of $\vec{\tilde{H}}_{-\perp}$ gets smaller as the angle between $\vec{\tilde{S}}$ and $\vec{\tilde{H}}_{-\parallel}$ increases and on the other hand $\vec{\tilde{H}}_{-\parallel}$ acts as a restoring force. Again, we arrive at similar conditions as in the simplified case with $\mu_{\mathrm{V}}\vec{H}_{\mathrm{V}} \rightarrow \vec{\tilde{H}}_{-\parallel}$.

B Properties of the Shifted Lognormal Function

The lognormal function describes a set of random variables x whose natural logarithm are normally distributed. In addition to the standard lognormal function, we need to include an additional parameter, a shift in x, to describe the noise hit distribution (see section 4.4.1.3):

$$p(x;\mu,\sigma,s) = \frac{1}{(x+s)\sigma\sqrt{2\pi}} \exp\left(-\frac{(\ln(x+s)-\mu)^2}{2\sigma^2}\right) \quad . \tag{B.1}$$

B.1 Derivation of the Moments

As a shifted lognormal is not commonly used, we will derive its moments in this section.

The n^{th} moment a distribution is defined as:

$$\langle x^n \rangle = \int_{-s}^{\infty} x^n \, p(x;\mu,\sigma,s) \mathrm{d}x \quad . \tag{B.2}$$

Note that the integration range is restricted by the definition range of the shifted lognormal function. In the case of $s = 0$, the moments are easily found by the substitution $y = \ln x$:

$$\begin{aligned}
\langle x^n \rangle &= \int_0^{\infty} \frac{x^n}{x\sigma\sqrt{2\pi}} \exp\left(-\frac{(\ln x - \mu)^2}{2\sigma^2}\right) \mathrm{d}x \\
&= \int_0^{\infty} \frac{1}{\sigma\sqrt{2\pi}} \exp\left(-\frac{(y-\mu)^2}{2\sigma^2} - ny\right) \mathrm{d}y \\
&= \int_0^{\infty} \frac{1}{\sigma\sqrt{2\pi}} \exp\left(-\frac{(y-(\mu+n\sigma^2)^2}{2\sigma^2} + n\mu + \frac{n^2}{2}\sigma^2\right) \mathrm{d}y \\
&= e^{n\mu + \frac{n^2}{2}\sigma^2}
\end{aligned} \tag{B.3}$$

However, a general formula for the moments is not easily defined if $s \neq 0$. We therefore consider the first three moments and derive the expectation value, the variance and the skewness:

$$\langle x \rangle = \int_{-s}^{\infty} \frac{x}{(x+s)\sigma\sqrt{2\pi}} \exp\left(-\frac{(\ln(x+s)-\mu)^2}{2\sigma^2}\right) \mathrm{d}x \tag{B.4}$$

The Substitution $y = x + s$ leads to

$$\langle x\rangle = -s + \int_0^\infty \frac{y}{y\sigma\sqrt{2\pi}} \exp\left(-\frac{(\ln y-\mu)^2}{2\sigma^2}\right) \mathrm{d}x \tag{B.5}$$

Using equation B.3 we get

$$\langle x\rangle = e^{\mu+\frac{\sigma^2}{2}} - s \tag{B.6}$$

as the expectation value. The variance results in:

$$\begin{aligned} V(x) &= \int_{-s}^\infty \frac{(x-\langle x\rangle)^2}{(x+s)\sigma\sqrt{2\pi}} \exp\left(-\frac{(\ln(x+s)-\mu)^2}{2\sigma^2}\right) \mathrm{d}x \\ &= \int_0^\infty \frac{(y-e^{\mu+\frac{\sigma^2}{2}})^2}{y\sigma\sqrt{2\pi}} \exp\left(-\frac{(\ln y-\mu)^2}{2\sigma^2}\right) \mathrm{d}x \quad . \end{aligned} \tag{B.7}$$

Which is equal to the Variance at $s = 0$:

$$V(x) = (e^{\sigma^2}-1)e^{2\mu+\sigma^2} \quad . \tag{B.8}$$

Since the skewness is defined by

$$S(x) = \frac{\langle (x-\langle x\rangle)^3\rangle}{V(x)^{\frac{3}{2}}} \quad , \tag{B.9}$$

it is obvious that the shift parameter s cancels as in equation B.7. The skewness of the shifted lognormal is found to be:

$$S(X) = (e^{\sigma^2}+2)\sqrt{e^{\sigma^2}-1} \quad . \tag{B.10}$$

B.2 Connection between Moments of Independent Distributions

When having two randomly distributed values and adding them up, the resulting expectation value and variance are well known. However, as we intend to determine the parameters of a shifted lognormal, we need three different input equations. We will therefore proceed to derive a relation between skewnesses.

We assume that the two known underlying distributions are described by the characteristic functions $\Phi_x(k)$ and $\Phi_y(k)$. We know that (see also equation 4.16)

$$\Phi_z(k) = \Phi_x(k)\Phi_y(k) \quad . \tag{B.11}$$

The moments of a probability distribution function can be derived from the characteristic function as follows:

$$\begin{aligned}\frac{d^m}{dk^m}\Phi_x(k)\Big|_{k=0} &= \int (ix)^m e^{ikx} f(x)\mathrm{d}x\Big|_{k=0} \\ &= i^m\langle x^m\rangle \quad . \qquad \text{(B.12)}\end{aligned}$$

In the general case, we get

$$\int z^m e^{ikz} f(z)dz\Big|_{k=0} = \int\int (x+y)^m e^{i(x+y)k} f(z)\mathrm{d}x\mathrm{d}y\Big|_{k=0} \qquad \text{(B.13)}$$

leading to $\langle z^m\rangle = \langle (x+y)^m\rangle$. The relationship for the expectation values $\langle z\rangle = \langle x\rangle + \langle y\rangle$ can be seen trivially, as:

$$\langle x+y\rangle = \langle x\rangle + \langle y\rangle \quad . \qquad \text{(B.14)}$$

The variance, the second central moment, is only slightly more complicated with:

$$\begin{aligned}\langle (z-\langle z\rangle)^2\rangle &= \langle (x+y-\langle x+y\rangle)^2\rangle \\ &= \langle x^2+y^2+\langle x+y\rangle^2+2xy-2x\langle x+y\rangle-2y\langle x+y\rangle\rangle \quad . \qquad \text{(B.15)}\end{aligned}$$

Using $\langle x^n y^m\rangle = \langle x^n\rangle\langle y^m\rangle$ and $\langle x+y\rangle = \langle x\rangle + \langle y\rangle$ leads to:

$$V(z) = \langle (z-\langle z\rangle)^2\rangle = \langle x^2\rangle - \langle x\rangle^2 + \langle y^2\rangle - \langle y\rangle^2 = V(x) + V(y) \quad . \qquad \text{(B.16)}$$

Finally let us consider the skewness:

$$\begin{aligned}\langle (z-\langle z\rangle)^3\rangle &= \langle z^3\rangle - 3\langle z^2\rangle\langle z\rangle + 2\langle z\rangle^3 \\ &= \langle (x+y)^3\rangle - 3\langle (x+y)^2\rangle\langle (x+y)\rangle + 2\langle (x+y)\rangle^3 \\ &= \langle x^3\rangle + 3\langle x^2\rangle\langle y\rangle + 3\langle x\rangle\langle y^2\rangle + \langle y^3\rangle \\ &\quad -3\left(\langle x^2\rangle\langle x\rangle + 2\langle x\rangle^2\langle y\rangle + \langle x\rangle\langle y^2\rangle + \langle x^2\rangle\langle y\rangle + 2\langle x\rangle\langle y\rangle^2 + \langle y^2\rangle\langle y\rangle\right) \\ &\quad +2\left(\langle x\rangle^3 + 3\langle x\rangle^2\langle y\rangle + 3\langle x\rangle\langle y\rangle^2 + \langle y\rangle^3\right) \\ &= \langle x^3\rangle - 3\langle x^2\rangle\langle x\rangle + 2\langle x\rangle^3 + \langle y^3\rangle - 3\langle y^2\rangle\langle y\rangle + 2\langle y\rangle^3 \\ &= \langle (x-\langle x\rangle)^3\rangle + \langle (y-\langle y\rangle)^3\rangle \quad . \qquad \text{(B.17)}\end{aligned}$$

Consequently, the third central moment of two randomly distributed variables simply adds up. For the skewness, this means:

$$S(z) = \frac{S(x)V(x)^{\frac{3}{2}} + S(y)V(y)^{\frac{3}{2}}}{V(x)^{\frac{3}{2}}} \quad . \qquad \text{(B.18)}$$

B.3 Derivation of the Defining Lognormal Parameters

We will now proceed to derive the parameters describing of a shifted lognormal from its statistical moments.

The expectation value, the variance and the skewness for a shifted lognormal were given in B.6, B.8 and B.10 respectively.

We will start with the skewness as it features only the σ. Taking the square of equation B.10 leads to:

$$S^2 = e^{3\sigma^2} + 3e^{2\sigma^2} - 4 \quad . \tag{B.19}$$

This is a cubic equation and theoretically be solved by 3 solutions. However, those are imaginary and as such uninteresting for our purpose. The remaining real solution is:

$$\sigma^2 = \ln\left(\sqrt[3]{\frac{S^2+2+S\sqrt{S^2+4}}{2}} + \sqrt[3]{\frac{S^2+2-S\sqrt{S^2+4}}{2}} - 1\right) \quad . \tag{B.20}$$

This leads to

$$\mu = \frac{1}{2}\left(\ln V - \ln(e^{\sigma^2}-1) - \sigma^2\right) \tag{B.21}$$

and

$$s = -E + e^{\mu+\frac{\sigma^2}{2}} \quad . \tag{B.22}$$

C AMANDA Supernova Search Tables

As dead time setting changed within the years 2005 and 2006, we tag the datasets by "dt" (data taken with dead time) and "ndt" (data taken without dead time).

Dataset	Allowed mean rates / Hz				Disqualified OMs
	B4	B10	B13	B19	
2000	200 - 400	850 - 1250	1 - 0	550 - 850	26.0%
2001	200 - 450	950 - 1400	1 - 0	600 - 900	20.4%
2002	150 - 300	550 - 800	1 - 0	350 - 550	16.6%
2003	200 - 450	1000 - 1550	800 - 1450	600 - 900	26.6%
2004	150 - 300	550 - 800	550 - 750	350 - 550	32.7%
2005 ndt	250 - 500	1000 - 1500	750 - 1500	600 - 950	27.4%
2006 ndt	250 - 450	1000 - 1500	900 - 1400	600 - 950	30.4%
2006 dt	150 - 300	550 - 850	450 - 800	350 - 550	29.3%
2007	150 - 300	500 - 750	450 - 800	300 - 550	26.0%
2008	150 - 300	550 - 750	1 - 0	350 - 550	20.4%

Table C.1: Cuts applied to the OM mean rates

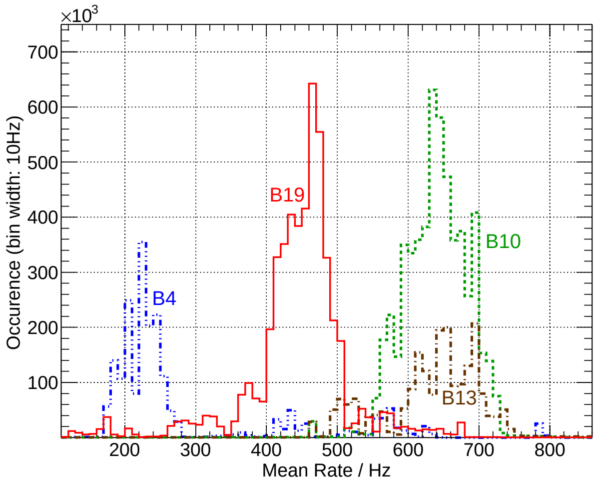

Figure C.1: OM mean rates as measured in 2007

Mean rates between February 26 and October 17, 2007, derived according to section 4.1.2.

Dataset	Binning [s]	Allowed fano factors				Loss
		B4	B10	B13	B19	
2000	0.5	1.2 - 1.8	1.3 - 2.0	0.5 - 0.0	1.4 - 2.1	0.2%
	4	1.1 - 2.0	1.2 - 2.3	0.5 - 0.0	1.3 - 2.4	0.3%
	10	0.9 - 2.2	1.0 - 2.5	0.5 - 0.0	1.0 - 2.6	0.02%
2001	0.5	1.0 - 2.1	1.0 - 2.2	0.5 - 0.0	1.0 - 2.2	0.2%
	4	0.9 - 2.3	1.1 - 2.5	0.5 - 0.0	1.0 - 2.6	0.2%
	10	0.8 - 2.5	0.9 - 2.9	0.5 - 0.0	0.9 - 2.8	0.2%
2002	0.5	0.9 - 1.3	0.8 - 1.3	0.5 - 0.0	0.8 - 1.4	0.2%
	4	0.8 - 1.6	0.7 - 1.5	0.5 - 0.0	0.8 - 1.6	0.3%
	10	0.6 - 1.7	0.6 - 1.7	0.5 - 0.0	0.6 - 1.8	0.3%
2003	0.5	1.4 - 2.1	1.5 - 2.3	1.6 - 2.3	1.5 - 2.4	0.4%
	4	1.2 - 2.3	1.4 - 2.6	1.4 - 2.6	1.4 - 2.6	0.5%
	10	1.0 - 2.6	1.1 - 2.8	1.2 - 2.8	1.1 - 2.8	0.6%
2004	0.5	0.9 - 1.5	0.8 - 1.3	0.9 - 1.3	0.8 - 1.4	1.3%
	4	0.8 - 1.6	0.7 - 1.5	0.8 - 1.5	0.8 - 1.6	1.4%
	10	0.6 - 1.7	0.6 - 1.7	0.6 - 1.7	0.7 - 1.8	1.4%
2005 ndt	0.5	1.4 - 2.1	1.5 - 2.3	1.6 - 2.3	1.4 - 2.4	1.2%
	4	1.3 - 2.4	1.4 - 2.6	1.4 - 2.6	1.3 - 2.6	1.5%
	10	1.1 - 2.7	1.1 - 2.9	1.1 - 2.9	1.1 - 2.9	1.5%
2006 ndt	0.5	1.4 - 2.1	1.5 - 2.3	1.5 - 2.3	1.5 - 2.4	1.1%
	4	1.3 - 2.7	1.3 - 2.6	1.4 - 2.6	1.4 - 2.7	1.4%
	10	1.2 - 2.8	1.2 - 2.9	1.2 - 2.9	1.2 - 2.9	1.5%
2006 dt	0.5	0.8 - 1.4	0.8 - 1.3	0.8 - 1.4	0.9 - 1.4	1.3%
	4	0.7 - 1.6	0.7 - 1.5	0.7 - 1.5	0.8 - 1.6	1.5%
	10	0.6 - 1.7	0.6 - 1.7	0.6 - 1.7	0.7 - 1.8	1.5%
2007	0.5	0.8 - 1.5	0.9 - 1.3	0.9 - 1.3	0.9 - 1.4	0.2%
	4	0.8 - 1.5	0.8 - 1.5	0.8 - 1.6	0.7 - 1.6	0.3%
	10	0.6 - 1.7	0.6 - 1.9	0.6 - 1.8	0.7 - 1.8	0.02%
2008	0.5	0.8 - 1.6	0.8 - 1.4	0.5 - 0.0	0.8 - 1.4	0.2%
	4	0.8 - 1.5	0.7 - 1.5	0.5 - 0.0	0.8 - 1.6	0.2%
	10	0.6 - 1.8	0.6 - 1.8	0.5 - 0.0	0.6 - 1.8	0.2%

Table C.2: Cuts applied to the OM fano factors

Dataset	Binning [s]	Maximal skewness				Loss
		B4	B10	B13	B19	
2000	0.5	0.6	0.5	0.0	0.5	0.3%
	4	0.8	0.8	0.0	0.8	0.1%
	10	1.1	1.1	0.0	1.1	0.4%
2001	0.5	0.7	0.5	0.0	0.5	0.3%
	4	0.8	0.8	0.0	0.8	0.1%
	10	1.1	1.1	0.0	1.1	0.1%
2002	0.5	0.5	0.4	0.0	0.4	0.1%
	4	0.7	0.7	0.0	0.7	0.1%
	10	1.0	1.0	0.0	1.0	0.1%
2003	0.5	0.7	0.5	0.5	0.5	0.3%
	4	0.9	0.8	0.8	0.8	0.1%
	10	1.1	1.1	1.0	1.1	0.1%
2004	0.5	0.5	0.4	0.4	0.5	0.1%
	4	0.8	0.8	0.8	0.8	0.05%
	10	1.1	1.1	1.1	1.1	0.1%
2005 ndt	0.5	0.7	0.6	0.6	0.6	0.3%
	4	0.9	0.8	0.8	0.8	0.1%
	10	1.1	1.1	1.1	1.1	0.1%
2006 ndt	0.5	0.7	0.5	0.5	0.6	0.4%
	4	0.9	0.8	0.8	0.8	0.2%
	10	1.1	1.1	1.1	1.1	0.1%
2006 dt	0.5	0.5	0.4	0.4	0.5	0.1%
	4	0.9	0.8	0.8	0.8	0.001%
	10	1.1	1.1	1.1	1.1	0.001%
2007	0.5	0.5	0.4	0.4	0.4	0.3%
	4	0.9	0.7	0.8	0.8	0.1%
	10	1.1	1.1	1.1	1.1	0.4%
2008	0.5	0.5	0.4	0.0	0.5	0.3%
	4	0.8	0.8	0.0	0.8	0.1%
	10	1.1	1.1	0.0	1.2	0.1%

Table C.3: Cuts applied to the absolute skewness

Year	Minimum uptime / 10^6 s	Number of OMs disqualified
2000	5.0	17
2001	6.0	34
2002	9.0	19
2003	4.0	30
2004	5.0	11
2005 ndt	9.0	20
2006 ndt	5.0	18
2006 dt	4.5	39
2007	5.5	39
2008	9.0	31

Table C.4: Cut on the OM uptime for all datasets.

Year	Maximal reduced χ^2	Number of OMs disqualified
2000	2.2	25
2001	6.0	28
2002	2.5	28
2003	2.0	24
2004	6.0	31
2005 ndt	2.4	36
2006 ndt	2.6	23
2006 dt	2.0	18
2007	3.5	33
2008	4.0	27

Table C.5: Cut on the reduced χ^2 of the lognormal fit to the OMs for each dataset.

Year	Perturbation ratio / 10^{-5}	Number of OMs disqualified
2000	2.5	16
2001	3.0	14
2002	1.0	8
2003	2.6	33
2004	3.6	32
2005 ndt	2.3	35
2006 ndt	2.5	45
2006 dt	1.7	8
2007	2.5	7
2008	1.6	14

Table C.6: Cut on the OM perturbation probability for each dataset

Year	Allowed activations per run
2000	100
2001	100
2002	90
2003	90
2004	160
2005 ndt	200
2006 ndt	180
2006 dt	90
2007	220
2008	250

Table C.7: Maximally allowed OM activations per run

Year	Minimal number of active OMs	Amount of data lost
2000	280	3.1%
2001	300	0.9%
2002	320	2.9%
2003	365	4.0%
2004	330	1.7%
2005 ndt	375	4.8%
2006 ndt	370	2.3%
2006 dt	370	1.9%
2007	365	6.3%
2008	275	2.5%

Table C.8: Minimal required number of active OMs

	$\chi^2 \in 90\%$	$\chi^2 \in 99.999\%$
$0.5s$	3.0 a	3.5 a
$1.0s$	2.7 a	3.5 a
$1.5s$	2.4 a	3.4 a
$2.0s$	2.2 a	3.4 a
$2.5s$	1.9 a	3.4 a
$3.0s$	1.7 a	3.4 a

Table C.9: Lifetimes for each rebinning and χ^2 setting.

	LL	ONeMg	SN1987A	BH-LS	BH-SH
2000	6.9	6.9	6.9	15.0	15.0
2001	7.0	6.9	7.0	15.0	15.0
2002	7.6	7.4	7.5	15.0	15.0
2003	6.7	6.9	6.8	15.0	15.0
2004	7.4	7.4	7.6	15.0	15.0
2005 ndt	6.9	6.9	6.9	15.0	15.0
2006 ndt	6.9	6.9	6.8	15.0	15.0
2006 dt	7.6	7.4	7.5	15.0	15.0
2007	7.6	7.3	7.4	15.0	15.0
2008	7.3	7.1	7.3	15.0	15.0

Table C.10: Significance cuts on the optimal rebinnings

	LL	ONeMg	SN1987A	BH-LS	BH-SH
2000	71%	25%	60%	80%	93%
2001	62%	22%	57%	68%	88%
2002	87%	38%	90%	75%	80%
2003	61%	22%	64%	59%	82%
2004	86%	37%	77%	74%	81%
2005 ndt	59%	43%	54%	63%	87%
2006 ndt	57%	21%	53%	63%	87%
2006 dt	90%	41%	91%	76%	81%
2007	89%	42%	91%	77%	82%
2008	87%	38%	79%	78%	82%
Average	75%	34%	72%	71%	84%

Table C.11: Detection efficiencies at the optimal rebinnings

Bibliography

[1] W. Baade and F. Zwicky,
Remarks on Super-Novae and Cosmic Rays,
Phys. Rev. **46**, 76 (1934).

[2] N. D. Schulz,
From Dust to Stars (Praxis Publishing Ltd, 2005).

[3] M. Hellwig,
Aufbau eines Datennahmesystems zum Supernova-Nachweis mit dem AMANDA-Detektor,
Master's thesis, Johannes Gutenberg University of Mainz, 2000.

[4] S. Woosley and H. T. Janka,
The Physics of Core-Collapse Supernovae,
Nature Physics **1**, 147 (2005).

[5] S. E. Woosley, A. Heger, and T. A. Weaver,
The evolution and explosion of massive stars,
Rev. Mod. Phys. **74**, 1015 (2002).

[6] C. E. Rolfs and W. S. Rodney,
Cauldrons in the Cosmos - Nuclear Astrophysics (The University of Chicago Press, 1988).

[7] D. Arnett,
Supernovae and nucleosynthesis. an investigation of the history of matter, from the Big Bang to the present (Princeton University Press, 1996).

[8] A. V. Filippenko,
Optical spectra of supernovae,
Ann. Rev. Astron. Astrophys. **35**, 309 (1997).

[9] D. Branch and G. A. Tammann,
Type Ia supernovae as standard candles,
Ann. Rev. Astron. Astrophys. **30**, 359 (1992).

[10] T. Nugis and H. J. G. L. M. Lamers,
Mass-loss rates of Wolf-Rayet stars as a function of stellar parameters,
A&A **360**, 227 (2000).

[11] A. Heger, C. L. Fryer, S. E. Woosley, N. Langer, and D. H. Hartmann,
How Massive Single Stars End their Life,
ApJ **591**, 288 (2003).

[12] W. Zhang, S. E. Woosley, and A. Heger,
Fallback and Black Hole Production in Massive Stars,
ApJ **679**, 639 (2008).

[13] Z. Barkat, G. Rakavy, and N. Sack,
Dynamics of Supernova Explosion Resulting from Pair Formation,
Phys. Rev. Lett. **18**, 379 (1967).

[14] S. A. Colgate and R. H. White,
The Hydrodynamic Behavior of Supernovae Explosions,
ApJ **143**, 626 (1966).

[15] K. Kotake, K. Sato, and K. Takahashi,
Explosion Mechanism, Neutrino Burst, and Gravitational Wave in Core-Collapse Supernovae,
Rept. Prog. Phys. **69**, 971 (2006).

[16] H.-T. Janka, K. Langanke, A. Marek, G. Martinez-Pinedo, and B. Mueller,
Theory of Core-Collapse Supernovae,
Phys. Rept. **442**, 38 (2007).

[17] M. Kachelriess *et al.*,
Exploiting the neutronization burst of a galactic supernova,
Phys. Rev. **D71**, 063003 (2005).

[18] A. Burrows,
Towards a synthesis of core collapse supernova theory,
Nucl. Phys. **A606**, 151 (1996).

[19] H. T. Janka,
Conditions for shock revival by neutrino heating in core- collapse supernovae,
A&A **368**, 527 (2000).

[20] H. A. Bethe and J. Wilson, R.,
Revival of a stalled supernova shock by neutrino heating,
ApJ **295**, 14 (1985).

[21] A. Burrows and J. M. Lattimer,
The birth of neutron stars,
ApJ **307**, 178 (1986).

[22] J. A. Pons, S. Reddy, M. Prakash, J. M. Lattimer, and J. A. Miralles,
Evolution of protoneutron stars,
ApJ **513**, 780 (1999).

[23] A. Marek, H. T. Janka, and E. Mueller,
Equation-of-State Dependent Features in Shock-Oscillation Modulated Neutrino and Gravitational-Wave Signals from Supernovae,
A&A **496**, 475 (2009).

[24] S. E. Woosley and J. S. Bloom,
The Supernova – Gamma-Ray Burst Connection,

Ann. Rev. Astron. Astrophys. **44**, 507 (2006).

[25] E. Waxman and J. N. Bahcall,
High energy neutrinos from cosmological gamma-ray burst fireballs,
Phys. Rev. Lett. **78**, 2292 (1997).

[26] E. Waxman and A. Loeb,
TeV neutrinos and GeV photons from shock breakout in supernovae,
Phys. Rev. Lett. **87**, 071101 (2001).

[27] M. Prakash *et al.*,
Composition and structure of protoneutron stars,
Physics Reports **280**, 1 (1997).

[28] I. Bombaci,
The maximum mass of a neutron star.,
A&A **305**, 871 (1996).

[29] W. Zhang, S. E. Woosley, and A. Heger,
Fallback and Black Hole Production in Massive Stars,
ApJ **679**, 639 (2009).

[30] K. Sumiyoshi, S. Yamada, and H. Suzuki,
Dynamics and neutrino signal of black hole formation in non-rotating failed supernovae. I. EOS dependence,
Astrophys. J. **667**, 382 (2007).

[31] K. Sumiyoshi,
Personal communication.

[32] C. S. Kochanek *et al.*,
A Survey About Nothing: Monitoring a Million Supergiants for Failed Supernovae,
Astrophys. J. **684**, 1336 (2008).

[33] S. Miyaji, K. Nomot, K. Yoko, and D. Sugimoto,
Supernova Triggered by Electron Captures,
PASJ **32**, 303 (1980).

[34] W. Hillebrandt, K. Nomoto, and R. G. Wolff,
Supernova explosions of massive stars - The mass range 8 to 10 solar masses,
A&A **133**, 175 (1984).

[35] F. S. Kitaura, H.-T. Janka, and W. Hillebrandt,
Explosions of O-Ne-Mg Cores, the Crab Supernova, and Subluminous Type II-P Supernovae,
A&A **450**, 345 (2005).

[36] A. J. T. Poelarends, F. Herwig, N. Langer, and A. Heger,
The Supernova Channel of Super-AGB Stars,
ApJ **675**, 614 (2007).

[37] L. Huedepohl, B. Mueller, H. T. Janka, A. Marek, and G. G. Raffelt,
Neutrino Signal of Electron-Capture Supernovae from Core Collapse to Cooling,
Phys. Rev. Lett. **submitted** (2009).

[38] H.-T. Janka,
Personal communication.

[39] H. A. Bethe,
Supernova mechanisms,
Rev. Mod. Phys. **62**, 801 (1990).

[40] R. Buras, H.-T. Janka, M. Rampp, and K. Kifonidis,
Two-Dimensional Hydrodynamic Core-Collapse Supernova Simulations with Spectral Neutrino Transport II. Models for Different Progenitor Stars,
A&A **457**, 281 (2006).

[41] J. M. Blondin, A. Mezzacappa, and C. DeMarino,
Stability of Standing Accretion Shocks, With an Eye Toward Core Collapse Supernovae,
ApJ **584**, 971 (2003).

[42] T. Foglizzo, P. Galletti, L. Scheck, and H. T. Janka,
Instability of a stalled accretion shock: evidence for the advective-acoustic cycle,
ApJ **654**, 1006 (2007).

[43] A. Burrows, E. Livne, L. Dessart, C. Ott, and J. Murphy,
A New Mechanism for Core-Collapse Supernova Explosions,
ApJ **640**, 878 (2006).

[44] A. Burrows, E. Livne, L. Dessart, C. D. Ott, and J. Murphy,
Features of the Acoustic Mechanism of Core-Collapse Supernova Explosions,
ApJ **655**, 416 (2007).

[45] L. Scheck, T. Plewa, H.-T. Janka, K. Kifonidis, and E. Mueller,
Pulsar Recoil by Large-Scale Anisotropies in Supernova Explosions,
Phys. Rev. Lett. **92**, 011103 (2004).

[46] L. Scheck, K. Kifonidis, H. T. Janka, and E. Mueller,
Multidimensional Supernova Simulations with Approximative Neutrino Transport I. Neutron Star Kicks and the Anisotropy of Neutrino-Driven Explosions in Two Spatial Dimensions,
A&A **457**, 963 (2006).

[47] B. M. Gaensler, P. O. Slane, E. V. Gotthelf, and G. Vasisht,
Anomalous X-ray Pulsars and Soft Gamma-Ray Repeaters in supernova remnants,
ApJ **559**, 963 (2001).

[48] A. Marek and H. T. Janka,
Delayed neutrino-driven supernova explosions aided by the standing accretion-shock instability,
ApJ **694**, 664 (2009).

[49] S. W. Bruenn *et al.*,
Mechanisms of Core-Collapse Supernovae & Simulation Results from the CHIMERA Code,
Probing Stellar Populations out to the Distant Universe: CEFALU Proceedings **1111**, 593 (2010).

[50] W. Iwakami, K. Kotake, N. Ohnishi, S. Yamada, and K. Sawada,
Three-Dimensional Simulations of Standing Accretion Shock Instability in Core-Collapse Supernovae,
ApJ **678**, 1207 (2008).

[51] J. M. Lattimer and F. D. Swesty,
A Generalized equation of state for hot, dense matter,
Nucl. Phys. **A535**, 331 (1991).

[52] H. Shen, H. Toki, K. Oyamatsu, and K. Sumiyoshi,
Relativistic Equation of State of Nuclear Matter for Supernova and Neutron Star,
Nucl. Phys. **A637**, 435 (1998).

[53] C. L. Fryer and M. S. Warren,
The Collapse of Rotating Massive Stars in Three Dimensions,
ApJ **601**, 391 (2004).

[54] M. Obergaulinger, M. A. Aloy, and E. Muller,
Axisymmetric simulations of magneto–rotational core collapse: dynamics and gravitational wave signal,
A&A **450**, 1107 (2006).

[55] F. Weber,
Strange quark matter and compact stars,
Prog. Part. Nucl. Phys. **54**, 193 (2005).

[56] I. Sagert *et al.*,
Signals of the QCD phase transition in core-collapse supernovae,
Phys. Rev. Lett. **102**, 081101 (2009).

[57] A. B. Migdal, A. I. Chernoutsan, and I. N. Mishustin,
PION CONDENSATION AND DYNAMICS OF NEUTRON STARS,
Phys. Lett. **B83**, 158 (1979).

[58] *IAU Circular No. 4316.*

[59] *IAU Circular No. 4317.*

[60] N. Panagia,
Distance to SN 1987 A and the LMC,
AU Symposium **190**, 549 (1990).

[61] P. Podsiadlowski,
The progenitor of SN 1987 A,
Astronomical Society of the Pacific **104**, 717 (1992).

[62] C. L. Fryer, S. A. Colgate, and P. A. Pinto,
Iron Opacity and the Pulsar of Supernova 1987A,
ApJ **511**, 885 (1999).

[63] T. C. Chan *et al.*,
Could the compact remnant of SN 1987A be a quark star?,
Astrophys.J. **695**, 732 (2009).

[64] R. N. Manchester,
Searching for a Pulsar in SN1987A,
AIPConf.Proc. **937**, 134 (2007).

[65] AAT 50a, D. Malin, Anglo-Australian Observatory,
`http://www.aao.gov.au/images/captions/aat050.html`.

[66] R. M. Bionta *et al.*,
Observation of a Neutrino Burst in Coincidence with Supernova SN 1987a in the Large Magellanic Cloud,
Phys. Rev. Lett. **58**, 1494 (1987).

[67] KAMIOKANDE-II, K. Hirata *et al.*,
Observation of a Neutrino Burst from the Supernova SN 1987a,
Phys. Rev. Lett. **58**, 1490 (1987).

[68] K. S. Hirata *et al.*,
Observation in the Kamiokande-II Detector of the Neutrino Burst from Supernova SN 1987a,
Phys. Rev. **D38**, 448 (1988).

[69] E. N. Alekseev, L. N. Alekseeva, I. V. Krivosheina, and V. I. Volchenko,
Detection of the Neutrino Signal from SN1987a in the LMC using the INR Baksan Underground Scintillation Telescope,
Phys. Lett. **B205**, 209 (1988).

[70] W. D. Arnett, J. N. Bahcall, R. P. Kirshner, and S. E. Woosley,
SUPERNOVA SN1987A,
Ann. Rev. Astron. Astrophys. **27**, 629 (1989).

[71] G. A. Tammann, W. Loeffler, and A. Schroder,
The Galactic supernova rate,
Astrophys. J. Suppl. **92**, 487 (1994).

[72] R. Diehl *et al.*,
Radioactive 26Al and massive stars in the Galaxy,
Nature **439**, 45 (2006).

[73] T. Feser,
Echtzeit-Suche nach Neutrinoausbrüchen von Supernovae mit dem AMANDA-II Detektor,
PhD thesis, Johannes Gutenberg University of Mainz, 2004.

[74] J. N. Bahcall and R. M. Soneira,

The Universe and faint magnitudes. I. Model for the galaxy and the predicted star counts,
ApJ Suppl. **44**, 73 (1980).

[75] I. Yusifov and I. Kucuk,
Revisiting the radial distribution of pulsars in the Galaxy,
Astron.Astrophys. **422**, 545 (2004).

[76] A. Mirizzi, G. G. Raffelt, and P. D. Serpico,
Earth matter effects in supernova neutrinos: Optimal detector locations,
JCAP **0605**, 012 (2006).

[77] J. N. Bahcall and T. Piran,
Stellar collapses in the galaxy,
Astrophys. J. **267**, L77 (1982).

[78] C. e. a. P. D. G. Amsler,
1 (2008) and 2009 partial update for the 2010 edition,
Phys. Lett. **B667** (2009).

[79] The Borexino, C. Arpesella *et al.*,
Direct Measurement of the Be-7 Solar Neutrino Flux with 192 Days of Borexino Data,
Phys. Rev. Lett. **101**, 091302 (2008).

[80] S. N. Gninenko, N. V. Krasnikov, and A. Rubbia,
Search for millicharged particles in reactor neutrino experiments: a probe of the PVLAS anomaly,
Phys. Rev. **D75**, 075014 (2007).

[81] R. R. Volkas,
Introduction to sterile neutrinos,
Prog. Part. Nucl. Phys. **48**, 161 (2002).

[82] Q. R. Ahmad *et al.* (SNO Collaboration),
Measurement of the rate of $\nu_e + d \rightarrow p + p + e^-$ interactions produced by 8B solar neutrinos at the Sudbury Neutrino Observatory,
Phys. Rev. Lett. **87**, 071301 (2001).

[83] A. B. Balantekin, J. Gava, and C. Volpe,
Possible CP-Violation effects in core-collapse Supernovae,
Phys. Lett. **B662**, 396 (2008).

[84] SNO, B. Aharmim *et al.*,
An Independent Measurement of the Total Active 8B Solar Neutrino Flux Using an Array of 3He Proportional Counters at the Sudbury Neutrino Observatory,
Phys. Rev. Lett. **101**, 111301 (2008).

[85] Super-Kamiokande, Y. Ashie *et al.*,
A Measurement of Atmospheric Neutrino Oscillation Parameters by Super-Kamiokande I,
Phys. Rev. **D71**, 112005 (2005).

[86] CHOOZ, M. Apollonio *et al.*,
Limits on Neutrino Oscillations from the CHOOZ Experiment,
Phys. Lett. **B466**, 415 (1999).

[87] MINOS, P. Adamson *et al.*,
First observations of separated atmospheric nu/mu and anti-nu/mu events in the MINOS detector,
Phys. Rev. **D73**, 072002 (2006).

[88] C. Kraus *et al.*,
Final Results from phase II of the Mainz Neutrino Mass Search in Tritium β Decay,
Eur.Phys.J.C **40**, 447 (2005).

[89] A. Goobar, S. Hannestad, E. Mortsell, and H. Tu,
The neutrino mass bound from WMAP-3, the baryon acoustic peak, the SNLS supernovae and the Lyman-alpha forest,
JCAP **06**, 019 (2006).

[90] F. De Bernardis, P. Serra, A. Cooray, and A. Melchiorri,
An improved limit on the neutrino mass with CMB and redshift-dependent halo bias-mass relations from SDSS, DEEP2, and Lyman-Break Galaxies,
Phys. Rev. **D78**, 083535 (2008).

[91] C. Giunti and C. W. Kim,
Fundamentals of Neutrino Physics and Astrophysics (Oxford University Press, 2007).

[92] S. Ando and K. Sato,
Three-generation study of neutrino spin-flavor conversion in supernova and implication for neutrino magnetic moment,
Phys. Rev. **D67**, 023004 (2003).

[93] A. Piégsa,
Supernova-Detektion mit dem IceCube-Neutrinoteleskop,
PhD thesis, Johannes Gutenberg University of Mainz, 2009.

[94] A. S. Dighe and A. Y. Smirnov,
Identifying the neutrino mass spectrum from the neutrino burst from a supernova,
Phys. Rev. **D62**, 033007 (2000).

[95] T.-K. Kuo and J. T. Pantaleone,
Nonadiabatic Neutrino Oscillations in Matter,
Phys. Rev. **D39**, 1930 (1989).

[96] G. E. Brown, H. Bethe, and G. Baym,
Supernova Theory,
Nucl. Phys. A **375**, 481 (1982).

[97] G. L. Fogli, E. Lisi, D. Montanino, and A. Palazzo,
Supernova neutrino oscillations: A simple analytical approach,
Phys. Rev. **D65**, 073008 (2002).

[98] T.-K. Kuo and J. T. Pantaleone,
Solar-Neutrino Problem and Three-Neutrino Oscillations,
Phys. Rev. Lett. **57**, 1805 (1986).

[99] R. Tomàs *et al.*,
Neutrino signatures of supernova shock and reverse shock propagation,
JCAP **09**, 015 (2004).

[100] H. T. Janka and E. Mueller,
The First Second of a Type-II Supernova: Convection, Accretion, and Shock Propagation,
ApJ **448**, L109 (1995).

[101] T.-K. Kuo and J. T. Pantaleone,
Neutrino Oscillations in Matter,
Rev. Mod. Phys. **61**, 937 (1989).

[102] H. Duan, G. M. Fuller, and Y.-Z. Qian,
Collective Neutrino Flavor Transformation In Supernovae,
Phys. Rev. **D74**, 123004 (2006).

[103] S. Hannestad, G. G. Raffelt, G. Sigl, and Y. Y. Y. Wong,
Self-induced conversion in dense neutrino gases: Pendulum in flavour space,
Phys. Rev. D **74**, 105010 (2006).

[104] G. L. Fogli, E. Lisi, A. Marrone, and A. Mirizzi,
Collective neutrino flavor transitions in supernovae and the role of trajectory averaging,
JCAP **12**, 010 (2007).

[105] G. G. Raffelt and A. Y. Smirnov,
Self-induced spectral splits in supernova neutrino fluxes,
Phys. Rev. **D76**, 081301 (2007).

[106] B. Dasgupta, A. Dighe, G. G. Raffelt, and A. Y. Smirnov,
Multiple Spectral Splits of Supernova Neutrinos,
Phys. Rev. Lett. **103**, 051105 (2009).

[107] G. Fogli, E. Lisi, A. Marrone, and I. Tamborra,
Supernova neutrinos and antineutrinos: ternary luminosity diagram and spectral split patterns,
JCAP **10**, 002 (2009).

[108] I. Tamboora and G. Fogli,
Personal communication.

[109] G. Fogli, E. Lisi, A. Marrone, and I. Tamborra,
Supernova neutrino three-flavor evolution with dominant collective effects,
JCAP **04**, 030 (2009).

[110] B. Dasgupta, A. Dighe, A. Mirizzi, and G. G. Raffelt,

Spectral split in prompt supernova neutrino burst: Analytic three-flavor treatment,
Phys. Rev. **D77**, 113007 (2008).

[111] H. Duan, G. M. Fuller, J. Carlson, and Y.-Z. Qian,
Flavor Evolution of the Neutronization Neutrino Burst from an O-Ne-Mg Core-Collapse Supernova,
Phys. Rev. Lett. **100**, 021101 (2008).

[112] G. A. Medina-Tanco, E. M. de Gouveia Dal Pino, and J. E. Horvath,
Deflection of ultra high energy cosmic rays by the galactic magnetic field: From the sources to the detector,
Astrophys. J. **492**, 200 (1997).

[113] S. Hundertmark,
Simulation und Analyse von Myonereignissen im AMANDA-B4-Neutrinoteleskop,
PhD thesis, Humboldt-Universität zu Berlin, 1999.

[114] J. E. Jacobsen,
Simulating the Detection of Muons and Neutrinos in Deep Antarctic Ice,
PhD thesis, University of Wisconsin, 1996.

[115] T. R. DeYoung,
Observation of Atmospheric Muon Neutrinos with AMANDA,
PhD thesis, University of Wisconsin, Madison, 2001.

[116] T. Kowarik,
Suche nach Supernovae und Magnetischen Monopolen mit dem AMANDA-II-Detektor,
Master's thesis, Johannes Gutenberg University of Mainz, 2005.

[117] J. C. Ahrens,
Überprüfung der Genauigkeit der Relativitätstheorie mit atmosphärischen Myonneutrinos aus den AMANDA-Daten der Jahre 2000 bis 2003,
PhD thesis, Johannes Gutenberg University of Mainz, 2006.

[118] T. Schmidt,
Aufbau und Funktionsnachweis eines Optischen Moduls mit optisch-analoger Pulsübertragung für den AMANDA-II- und ICECUBE-Detektor,
PhD thesis, Humboldt-Universität zu Berlin, 2002.

[119] O. Franzen,
Untersuchungen optischer Modules für das AMANDA- bzw. ICECUBE-Projekt,
Master's thesis, Johannes Gutenberg University of Mainz, 2003.

[120] C. Wiebusch,
Physics capabilities of the icecube deepcore detector,
in *Proceedings ICRC, Łódź, Poland*, 2009.

[121] M. V. D. Agostino,

First Evidence For Atmospheric Neutrino-Induced Cascades with the IceCube Detector,
PhD thesis, University of California, Berkeley, 2009.

[122] IceCube Gallery,
`https://gallery.icecube.wisc.edu/internal/main.php`.

[123] IceCube, R. Abbasi *et al.*,
The IceCube Data Acquisition System: Signal Capture, Digitization, and Timestamping,
Nucl. Instrum. Meth. **A601**, 294 (2009).

[124] M. Ackermann,
Searches for Signals from Cosmic Point-Like Sources of High Energy Neutrinos in 5 Years AMANDA-II Data,
PhD thesis, Humboldt-Universität zu Berlin, 2005.

[125] G. Wikström,
A Search for Solar Dark Matter with the IceCube Neutrino Telescope,
PhD thesis, Stockholm University, 2009.

[126] N. S. Martin,
Search for MeV-Antineutrinos from Gamma-Ray Bursts and Develements of a corresponding Monte Carlo simulation,
Master's thesis, Johannes Gutenberg University of Mainz, 2003.

[127] T. Griesel,
Optimierung des Nachweises von Supernovae in IceCube,
PhD thesis, Johannes Gutenberg University of Mainz, 2010.

[128] W. C. Haxton,
The Nuclear Response of Water Cherenkov Detectors to Supernova and Solar Neutrinos,
Phys. Rev. **D36**, 2283 (1987).

[129] A. Strumia and F. Vissani,
Precise quasielastic neutrino nucleon cross section,
Phys. Lett. **B564**, 42 (2003).

[130] Neutron scattering lengths and cross sections,
`http://www.ncnr.nist.gov/resources/n-lengths/`.

[131] H. M. Childers and J. D. Graves,
Bipartition Angles for Compton Scattering by Free Electrons,
Phys. Rev. **99**, 343 (1955).

[132] W. J. Marciano and Z. Parsa,
Neutrino-Electron Scattering Theory,
J. Phys. **G29**, 2629 (2003).

[133] E. Kolbe, K. Langanke, and P. Vogel,

Estimates of weak and electromagnetic nuclear decay signatures for neutrino reactions in Super-Kamiokande,
Phys. Rev. **D66**, 013007 (2002).

[134] R. Tomàs, D. Semikoz, G. G. Raffelt, M. Kachelriess, and A. S. Dighe,
Supernova pointing with low- and high-energy neutrino detectors,
Phys. Rev. **D68**, 093013 (2003).

[135] W. C. Haxton,
Personal communication.

[136] S. G. Warren,
Optical constants of ice from the ultraviolet to the microwave,
Appl. Optics **23**, 1206 (1984).

[137] K. Woschnagg,
Photonics, 2007,
`http://wiki.icecube.wisc.edu/index.php/Photonics`.

[138] J. R. Petit *et al.*,
Climate and atmospheric history of the past 420,000 years from the Vostok ice core, Antarctica,
Nature **399**, 429 (1999).

[139] M. Ackermann et al.,
Optical properties of deep glacial ice at the South Pole,
J. Geophys. Res. **111**, D13203 (2006).

[140] H. Woschnagg,
Dust logger, 2007,
`http://wiki.icecube.wisc.edu/index.php/Dust_logger`.

[141] K. Woschnagg,
Hole ice, 2007,
`http://wiki.icecube.wisc.edu/index.php/Hole_ice`.

[142] ROMEO,
`http://www.ppl.phys.chiba-u.jp/ROMEO/`.

[143] R. Maruyama,
Supernova/effectivevolume, 2007,
`http://wiki.icecube.wisc.edu/index.php/Supernova/EffectiveVolume`.

[144] K. Woschnagg,
New ice model, 2007,
`http://wiki.icecube.wisc.edu/index.php/New_ice_model`.

[145] The IceCube Collaboration),
IceCube Sensitivity for Low-Energy Neutrinos from Nearby Supernovae,
In preparation .

[146] Ahrens, Jens *et al* (the IceCube collaboration),
Search for Supernova Neutrino-Bursts with the AMANDA Detector,

Astropart.Phys. **16**, 345 (2002).

[147] P. B. Price *et al.*,
Temperature Profile for Glacial Ice at the South Pole: Implications for Life in a Nearby Subglacial Lake,
Proceedings of the National Academy of Sciences of the United States of America **99**, 7844 (2002).

[148] A. Mirizzi and G. G. Raffelt,
New analysis of the SN 1987A neutrinos with a flexible spectral shape,
Phys. Rev. **D72**, 063001 (2005).

[149] G. Pagliaroli and F. Vissani,
Features of Kamiokande-II, IMB and Baksan observations and their interpretation in a two-component model for the signal,
Astron. Lett. **35**, 1 (2009).

[150] ROOT,
`http://root.cern.ch/`.

[151] M. T. Keil,
Supernova Neutrino Spectra and Applications to Flavor Oscillations,
PhD thesis, Technische Universitaet München, 2003.

[152] T. Totani, K. Sato, H. E. Dalhed, and J. R. Wilson,
Future Detection of Supernova Neutrino Burst and Explosion Mechanism,
Astrophys.J. **496**, 216 (1998).

[153] K. Iwamoto and T. Kunugise,
Neutrino emission from type Ia supernovae,
AIP Conf. Proc. **847**, 406 (2006).

[154] R. Tomàs and G. Raffelt,
Personal communication.

[155] J. F. Beacom and P. Vogel,
Can a supernova be located by its neutrinos?,
Phys. Rev. **D60**, 033007 (1999).

[156] J. Ahrens,
Ein webbasiertes Überwachungssystem für das AMANDA-Neutrinoteleskop,
Master's thesis, Johannes Gutenberg University of Mainz, 2000.

[157] F. Rothmaier,
Atmospheric Muons in the AMANDA and IceCube Telescopes: Southpolar Stratosphere and Muon Flux Origin,
PhD thesis, Johannes Gutenberg University of Mainz, 2010.

[158] G. Cowan,
Statistical Data Analysis (Oxford Science Publications, 1998).

[159] D. A. Chirkin,

Cosmic Ray Energy Spectrum Measurement with the Antarctic Muon and Neutrino Detector Array (AMANDA),
PhD thesis, University of California at Berkeley, 2003.

[160] S. R. Gozzini,
Search for Prompt-Neutrinos with AMANDA-II,
PhD thesis, Johannes Gutenberg University of Mainz, 2008.

[161] CORSIKA, an Air Shower Simulation Program,
`http://www-ik.fzk.de/corsika/`.

[162] dCORSIKA,
`http://wiki.icecube.wisc.edu/index.php/DCorsika_releases`.

[163] D. Chirkin and W. Rhode,
Propagating leptons through matter with Muon Monte Carlo (MMC),
arxiv:hep-ph/0407075 (2008).

[164] AMASIM — Simulation tool for AMANDA,
`http://www.physto.se/~amanda/amasim/amasim.html`.

[165] AGO data archive,
`http://www.polar.umd.edu/`.

[166] G. J. Feldman and R. D. Cousins,
A Unified Approach to the Classical Statistical Analysis of Small Signals,
Phys. Rev. **D57**, 3873 (1998).